

Engineering Tunable Colloidal Nanostructures for Light Energy Harvesting

by

Ebuka S. Arinze

A dissertation submitted to The Johns Hopkins University
in conformity with the requirements for the degree of
Doctor of Philosophy

Baltimore, Maryland

October, 2018

© 2018 by Ebuka S. Arinze

All rights reserved

Abstract

Colloidal nanomaterials, such as semiconductor quantum dots and plasmonic metal nanoparticles, are of interest for various optoelectronic applications due to their size-tunable optical properties, unique electronic structures, and low-cost fabrication techniques. As the physical footprint of emerging optoelectronic device components continues to shrink, colloidal nanomaterials have the potential to enable advances in fields such as low-power computing, renewable energy generation and storage, and biosensing and medicine, due to their small size, earth-abundance, and novel functionality. This thesis focuses on engineering these nanostructures for energy harvesting technologies, such as solar cells, photodetectors and photocatalysts. This is achieved by combining modeling, nanofabrication, and advanced optical and electrical characterization techniques.

The study is implemented in three sections. The first involves engineering these nanostructures for solution processed solar cells. Using optimization algorithms combined with thin film interference modeling, we developed a method for producing arbitrary spectral profiles in solar cells structures for potential applications in building- and window-integrated power generation. Similarly, by using photonic band engineering in strongly absorbing materials,

we developed and analyzed a new strategy for tuning the spectral selectivity of optoelectronic films. Additionally we critically evaluate the prospects for plasmonic enhancements in solution-processed thin-film solar cells by developing an intuitive effective medium model for embedded plasmonic nanostructures in photovoltaic thin films.

The next section involves investigating these nanostructures for photon detection applications. One study involves using a one-step solution-based growth technique to grow antimony selenide nanowires. This enables the growth of high-quality antimony selenide nanostructures from a molecular ink directly on flexible substrates for high-performance near-infrared photodetectors thus providing a route for low-cost, flexible, and broadband photon detection. The other study demonstrates high responsivity visible blind photodetectors based on nanoheterojunction films, thus representing a viable path for building UV cost-effective optoelectronic devices

Finally, the last section includes designing, developing and characterizing new plasmonic-catalytic systems based on earth-abundant and cost-effective nanomaterials such as aluminum. We present the first photophysical characterization of plasmonic aluminum nanoparticles, and identify tuning strategies such as surface modifications for various niche applications. These three sections culminate in creating a sustainable route to building both an energy-efficient and scalable-materials platform for the next generation of nanotechnology-based optoelectronic devices for energy applications.

Thesis Committee

Primary Readers

Susanna M. Thon (Primary Advisor)
Assistant Professor
Electrical and Computer Engineering Department
Johns Hopkins University

Mark Foster
Associate Professor
Electrical and Computer Engineering Department
Johns Hopkins University

Muyinatu A. Lediju Bell
Assistant Professor
Electrical and Computer Engineering Department
Johns Hopkins University

Acknowledgments

I would like to begin by thanking my advisor and supervisor, Dr. Susanna M. Thon. I am eternally grateful to her not just for serving as a dependable resource these last few years, but also for being a mentor, and most importantly, a great friend. Her patience and flexibility with me were unlike anything I had seen before. She was flexible with my schedules, with my ideas, and with my methods. Susanna took me in at a time when I had not yet proven myself as a researcher and she patiently taught me the ropes. For that I am also grateful. Besides being deeply supportive throughout this process, I have come to realize how much she is able to connect with people, a skill that I admire and value.

I would also like to thank my wonderful lab mates, past and present, for all their hard work and dedication throughout this time. They not only facilitated the process but also made the journey enjoyable. Botong Qiu and I spent many sleepless nights together completing projects and for his contributions and friendship, I am grateful. I would like to thank Yan Cheng, who carries herself with so much grace. I am grateful for how accommodating and understanding she was throughout the process. Finally, I would like to thank Yida Lin for being so resourceful. Yida always knew when to go the extra mile. This

group of people including Arlene Chiu, Lulin Li, Nate Palmquist, Gabby Nyirjesy, Andrew Rauch, Gary Qian, Garrett Ung, Eric Tsai, Nicole Kim, and Charles Thorton made the long nights worthwhile as I thoroughly enjoyed myself while working with them and will truly miss being in their company everyday. I would like to acknowledge all the funding sources that made my research work possible. Specifically, I would like to thank the National Science Foundation (DMR-1743941), ACS Petroleum Research Fund (PRF), and Microsoft for all the support over the years.

On a different note, I am forever grateful to my closest friends from college, Alex Barthelemy, Niccolai Arenas, Nathan Abraham, and Ikenna Nwajagu, for welcoming me with open arms when I first arrived to this country. They helped me adapt to this country when I was thousands of miles away from home for the first time. I felt the need to be a part of something and they helped me feel that I was. We have been close for about a decade now and I can honestly say that their families have become my families. Their families were kind enough to welcome me during the holidays where I made countless memories with them. During the time that I have been in Baltimore, this group of friends including Castro Jean-Gilles, Zaid Khan, Anthony Mingolledo, and Sohail Sumra made a point to visit me frequently to check up on me and I am grateful for them.

I would also like to thank my high school friends namely Nonso Anyigbo, Chukwudi Ilozue, Victor Obiahu, Philip Onotu, Ochuko Efemuaye, Obinna Ngini, Uche Omegara, Tunmilara Akinlawon, Tayo Odunlami, Demilade Obayomi and Chiedu Onichabor, who I have grown to call brothers. We

learned together, fought together, and became men together. We had many trials but we succeeded together. I am very grateful to know every one of them and to have grown so close to each of them. They truly made a point to make sure we all stayed connected and throughout graduate school they made a concerted effort to make sure I always had an escape from the academic sphere of my life. Through them, I stayed connected with the outside world and this helped to preserve my sanity. I appreciate all their support as well as their efforts to push me to be a better person. My success is their success and I am grateful for that unending support. I would like to thank and dedicate this thesis to Aniefon Ekereuwem, a very dear friend and former classmate who at the age of 13 taught me the essence of hard work and the process of cultivating a strong work ethic.

I would also like to thank my Baltimore friends namely Soonen Ahua, Mamie Okodaso, Emem Okoh, Adami Osho, Kate Fischl, Patrick Barthelemy, Dolapo Fakeye, Francis Fordjour and Kayode Sanni, who made Baltimore feel very much like home away from home. So many fun experiences were shared over the years in the DMV area that made me feel comfortable and at ease throughout my graduate studies. Settling into life in Baltimore was much smoother than I could have every expected and I am forever grateful to them for that.

Of course I have to express my sincerest gratitude to my family, namely my mom (Ngozi Arinze) and sister (Ifeyinwa Arinze) who both raised me. My mother taught me what it meant to be a man. She broke many barriers that I didn't even know existed. She gave me my purpose and taught me to

never, ever settle and it is honestly because of her that I am here today. With her work ethic, her dedication, and her vision, she embodied many of the values I carried with me in the journey that was grad school. She will always be my biggest fan, even when she doesn't know exactly what I am doing. My sister has been my best friend since before she knew she was my best friend. I always looked up to her to the point where I wanted to do everything she did, down to her mannerisms and how she talked. She was the best older sibling I could have ever dreamed of. She honestly went from fighting with me to always fighting for me and for that I am thankful. Every time I have needed her she has been there for me and that is why she is my go-to person. I was not only raised by my mom and sister but also by my mom's three sisters (Chinwe Njoku, Amaka Nwokedi and Nneka Onyia) and my grandmother (Comfort Arinze). All these women who brought me up, instilled in me values that taught me how to be responsible and how to work diligently. I am grateful, also, for my cousins because they have been supportive in ways that even they are unaware of and I hope I have been a good mentor to them.

Last but not least, I want to say thank you to God for guiding my footsteps and for manifesting himself through the people he surrounds me with. God has led me through times where it might have been easier to lose hope. In those moments, where I might have wanted to give up, God led the way. He showed me love, especially in moments when I did not know if I was worthy. Without Him, none of this would have been possible.

Dedicated to my grandmother (Comfort), my mother (Ngozi) and my sister (Ifeyinwa) for paving the way for me with their embodiment of God's love.

Table of Contents

Table of Contents	x
List of Tables	xvi
List of Figures	xvii
1 Introduction and Motivation	1
1.1 Organization of this Thesis	5
2 Nanomaterials for Energy Harvesting	10
2.1 Colloidal Quantum Dots	11
2.1.1 Synthesis	13
2.1.2 Ligands	16
2.1.3 Optical Properties	17
2.2 Plasmonic Nanoparticles	21
2.2.1 Synthesis and Ligands	22
2.2.2 Optical Properties	24
2.2.2.1 SPP Dispersion Relation	25

2.2.2.2	Mie Theory	26
3	Energy Harvesting Devices	41
3.1	Photovoltaics	41
3.1.1	Device Theory	43
3.1.2	Figures of Merit	45
3.1.3	Colloidal Quantum Dot Solar Cells	46
3.1.3.1	Motivation	46
3.1.3.2	Device Architecture	48
3.1.4	Multijunction Solar Cells	50
3.2	Photodetectors	50
3.2.1	Solution-Processed Materials for Photon Detection	51
3.2.2	Figures of Merit	51
3.2.3	Solid State Photodetector Architectures	53
3.3	Photocatalysts	55
3.3.1	Background	55
3.3.2	Traditional Photocatalysts	56
3.3.3	Sensitized Plasmonic Photocatalysis	57
4	Engineering Nanostructures for Solution Processed Solar Cells	69
4.1	Limits of Plasmonic Enhancement in Solution Processed Solar Cells	69
4.1.1	Solution Processed Solar Cells	71

4.1.2	Light Trapping for Photovoltaics	73
4.1.3	Embedded Plasmonic Enhancers	74
4.1.3.1	Organic Photovoltaics	79
4.1.3.2	Perovskite Solar Cells	80
4.1.3.3	Colloidal Quantum Dot Solar Cells	81
4.1.3.4	Summary	82
4.1.4	Practical Limits of Plasmonic Enhancement	83
4.1.5	Absorption Enhancement Model	84
4.1.6	Model Evaluation	90
4.1.6.1	Comparison to Experimental Studies	90
4.1.6.2	Effect of Nanoparticle Shape	97
4.1.6.3	Effect of Nanoparticle Size and Material	99
4.1.6.4	Model Validity	103
4.1.7	Perspective and Future Directions for Solution Processed Solar Cells	105
4.2	Color-Tuned and Transparent Colloidal Quantum Dot Solar Cells	109
4.2.1	Introduction	109
4.2.2	Optimization of the photocurrent-color tradeoff	113
4.2.3	Effects of non-ideal layers on color saturation	118
4.2.4	Application in tandem structures	120
4.2.5	Experimental results and discussion	122
4.2.6	Conclusion and outlook	125

4.3	Spectral-Selection in Absorbing Optoelectronic films via Photonic Band Engineering	126
4.3.1	Introduction	127
4.3.2	Simulations	133
4.3.3	Experimental demonstration of spectral tuning using PCs in strongly absorbing materials	142
4.3.4	Summary and Outlook	147
4.4	Novel Ligand Engineering <i>via</i> Molecular Silicon	149
4.4.1	Novel Approach	150
4.4.2	Exchange Results and Discussion	152
4.4.3	Future Work and Outlook	154
4.4.3.1	Future Work	154
4.4.3.2	Outlook	156
5	Engineering Nanostructures for Photon Detection Applications	187
5.1	An Antimony Selenide Molecular Ink for Flexible Broadband Photodetectors	187
5.1.1	Introduction	188
5.1.2	Results and Discussion	191
5.1.2.1	Analytical Electron Microscopy of NWs	192
5.1.3	X-ray Diffraction and Optical Properties	195
5.1.4	Flexible Photodetectors: Figures of Merits	198
5.1.5	Conclusion	205

5.2	SnO ₂ /CuO Nanoheterojunctions for Visible-blind Photodetectors	206
5.2.1	Introduction and Background	206
5.2.2	Experimental Results and Discussion	208
5.2.3	Conclusion	217
6	Earth-Abundant Plasmonic Materials for Energy-Efficient Photocatalytic Systems	228
6.1	Introduction	228
6.2	Motivation for Aluminum	229
6.3	Dynamics of Energy Transfer in Large Plasmonic Aluminum Nanoparticles	230
6.3.1	Background	230
6.3.2	Results and Discussion	231
6.3.3	Conclusion	246
7	Conclusion and Outlook	255
7.1	Conclusion	255
7.2	Outlook	257
A	Experimental Details	259
A.1	PbS CQD Synthesis	259
A.2	Plasmonic Enhancement Project	261
A.2.1	Enhancement Model	261
A.3	Color Tuning Project	262

A.3.1	Color Computation	262
A.3.2	Optimization	263
A.4	Antimony Selenide Project	264
A.5	Aluminum Project	265
A.5.1	Two-Interface Model	265

List of Tables

1.1	Estimates of technical potential for Renewable Energy sources obtained from various studies [5, 6, 7, 8].	3
3.1	Current record efficiencies for solar cell technologies. (*Single crystal, single junction and non-concentrating systems)	49
4.1	Summary of selected plasmonic enhancement demonstrations in OPV, Perovskite, and CQD solar cells.[9]	78
4.2	Average performance characteristics of colored and transparent solar cell devices showing open-circuit voltage (V_{OC}), short-circuit current (J_{SC}), fill factor (FF) and power conversion efficiency (PCE). All measurements are for at least 5 devices.[172]	124
5.1	Quantitative EDXS and EELS analyses of Sb_2Se_3 NWs.[3] . . .	196
6.1	Heat capacities and thermal conductivities of aluminum, aluminum oxide and isopropanol.[65, 28]	243

List of Figures

1.1	Global Energy Projections	2
2.1	Quantum Dot Size-Tuning Effect	12
2.2	Synthesis of Colloidal Quantum Dots	14
2.3	PbS CQD Absorption Spectra	18
2.4	Surface Plasmon Resonance	22
2.5	Aluminum Absorbance Spectra	23
2.6	Aluminum FDTD Computation	24
3.1	Solar Illumination Spectrum	42
3.2	Basic Solar Cell Structure	44
3.3	Solar Cell Figure of Merit	45
3.4	Photograph of PbS CQD photovoltaic cell	47
3.5	CQD Solar Cell Architectures	48
3.6	Device Architecture of Photodetectors	54
3.7	Photocatalytic Process	56
3.8	Plasmonic Photocatalytic Process	57

4.1	Plasmonic Enhancement Model	86
4.2	Model: Relative Scattering Efficiency	92
4.3	Model: Photocurrent Enhancement	95
4.4	Model: Photocurrent Enhancement	98
4.5	Model: Gold vs. Silver Comparison	100
4.6	Model: 80 nm Silver Cross-Section Simulation	102
4.7	Solar Cell Interference and Optimization Technique	112
4.8	Absorption-Transparency Tradeoff	115
4.9	Photocurrent Constraint	117
4.10	Effect of Roughness	119
4.11	Multicolored Experimental Results	123
4.12	Photonic Crystal Schematic	132
4.13	Photonic Crystal FDTD calculations	136
4.14	Photonic Crystal FMM calculations	140
4.15	Photonic Crystal Experimental vs. Simulation Data	145
4.16	Design for Novel Conductive Silicon Ligands	150
4.17	Multicolored Experimental Results	152
4.18	Silicon Ligand Architecture and Exchange Schematic	153
4.19	Silicon Ligand FTIR Data	154
4.20	Silicon-Based Photovoltaic Device	154
5.1	Antimony Selenide Fabrication Scheme	191

5.2	Electron Microscopy and XRD Analysis of Antimony Selenide Nanowires	194
5.3	Optical Properties of Antimony Selenide	198
5.4	Photoconductive Device Properties	201
5.5	Figures of Merit of the PDs	203
5.6	Schematic of Nanocluster PD device	208
5.7	High-Resolution XPS Spectra	210
5.8	Nanocluster PD FDTD Simulations	213
5.9	I-V Performance for PD Devices	215
6.1	TEM Image of Aluminum NPs	233
6.2	Contour Transient Spectra	235
6.3	Time-Dependent Traces	237
6.4	Temperature Evolution Curves	245
7.1	Thesis Topics Graphic	256

Chapter 1

Introduction and Motivation

Energy access spurs innovation and advancement. It serves as a vital prerequisite for achieving economic development and attaining global sustainability. By setting a goal to ensure access to affordable, reliable, sustainable and modern energy for all by 2030 [1], the United Nations acknowledged the significance of energy access in transforming lives, economies and the planet.

Figure 1.1a illustrates the dependence of living standards on energy access. Globally, access to energy plays an important role in the growth of modern living standards. An analogous measure of energy consumption is electricity use per capita. The trend in Figure 1.1a shows a positive correlation between a country's electricity use per capita and the income level. The bottom left corner of the plot shows the small area where half of the global population lies, lagging developed countries in electricity demand by several orders of magnitudes.

Globally, about 1 billion people lack access to electricity [2] with half of this population residing in Nigeria, India, Ethiopia and Bangladesh. In addition to this, the world population is projected to grow $\sim 24\%$ from 7.4 billion today to

9.2 billion people in 2040 [3]. Figure 1.1b shows the population increase across all major regions for 3 select years (2016, 2025, and 2040) and categorized by age classes (0-14, 15-64, and 65+). Africa’s population is projected to increase at the fastest rate, resulting mainly from the growth of the working age population, with the region possessing the largest working age population across all regions by 2040.

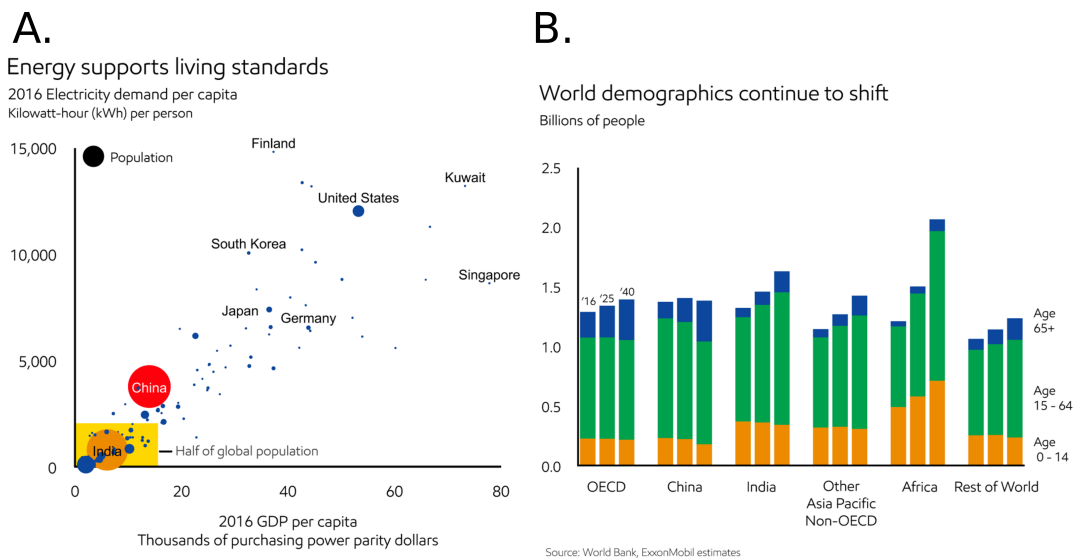


Figure 1.1: Global Energy Projections. Data depicting how:(a), Energy supports living standards (Electricity demand per capita) and (b), World demographics continue to shift.[3]

Coupling the increase in global population with the accelerating pace of technological advancement leads to a heightened increase in energy demand, thus rendering conventional sources insufficient to satisfy energy needs. Global energy demand is expected to increase $\sim 25\%$ [3], which is equivalent to adding another North America and Latin America to the world’s current energy demand. Growing living standards for expanding populations, resulting mainly from developing countries, means a projected paradigm shift to a

dependence on reliable modern energy. The increase in demand from these regions increases the need for affordable and sustainable energy. Additionally, there are environmental motivations to develop new and clean energy sources. These sources lead to minimal global warming effects, due to less carbon dioxide emissions, and reduce air and water pollution thus curbing climate change and improving public health respectively[4]. Therefore, to bridge the demand and supply gap, renewable and clean energy sources need to be evaluated, researched and implemented.

In envisioning a highly renewable-dependent future, it is imperative to understand the energy sources that have the greatest realistic potential to bridge the impending deficit. For example, let's take solar energy. Despite over 120,000 TW of sunlight hitting the earth, a large percentage of this cannot be utilized. The practical limit, a percentage of the total potential, takes

Source	Potential (TW)
Solar	1.9-82
Wind	1.0-19
Ocean	0.06-1.1
Hydro	1.0-3.0
Biomass	0.9-48
Geothermal	0.03-0.7

Table 1.1: Estimates of technical potential for Renewable Energy sources obtained from various studies [5, 6, 7, 8].

into account the energy conversion losses and land restrictions. This technical potential for renewable energy sources has been assessed [5, 6, 7, 8] and is summarized in Table 1.1.

With global energy consumption currently at ~ 19.2 TW [9], the various potentials indicate solar as the renewable energy source that can most comfortably satisfy both current and future global energy demands. This identifies solar energy as the most viable component of energy generation moving

forward.

About 65 years ago, the first practical solar cell was demonstrated to the public (Bell Solar Cell). While the industry has since matured, these silicon based devices still suffer from bulkiness, inflexibility, intensive manufacturing processes, poor band gap tunability, and relatively high associated costs. Similarly, photon detection has historically been enabled over the past few decades via inorganic semiconductors such as silicon or III-V compound materials. However, the expensive lithographic fabrication techniques coupled with broad spectral photoresponses render these materials non-optimal for wavelength-specific applications. Another light harvesting mechanism is photocatalysis. To harvest sunlight and subsequently drive chemical reactions, photocatalysts typically employ wide band gap semiconductors. These materials, however, suffer from poor spectral utilization as they typically only absorb ultraviolet light, which composes only $\sim 4\%$ of sunlight.

Materials for light harvesting technologies should ideally be low-cost, lightweight and flexible, relatively easy to manufacture, and possess band gap tunability for niche applications. Despite significant progress, many technologies still need a strong push to achieve their full potential and deliver a sustainable energy future. A viable route to achieving this goal is via solution processed nanomaterials. As the physical footprint of emerging optoelectronic device components continues to shrink and quantum effects become important, colloidal nanomaterials (such as semiconductor quantum dots and plasmonic metal nanoparticles) have the potential to enable advances in fields such as low-power computing, renewable energy generation and storage, and

biosensing and medicine, due to their small size, earth-abundance, and novel functionality.

With increasing demands in energy, computing, and infrastructure, novel materials and devices based on sustainable, energy-efficient, and scalable platforms will be critical to maintaining a competitive edge. This thesis focuses on engineering nanostructures for energy harvesting by combining modeling, nanofabrication, and advanced optical and electrical characterization techniques to address these 21st century challenges. It focuses on developing and tuning new semiconducting and metallic colloidal nanoparticle-based materials for various optoelectronic device applications, such as solar cells and photodetectors, and to better understand nanoscale energy transfer and light-matter interaction.

1.1 Organization of this Thesis

The following is a brief outline of this thesis. Chapter 1 provides a brief context of the energy landscape while motivating the need for colloidal nanomaterials in optoelectronic devices to address energy demands and protect the environment. Chapter 2 delves into the two main nanomaterials investigated in this study; colloidal quantum dots and plasmonic nanomaterials. Chapter 3 provides some understanding of the device physics as well as gives a historical perspective of some nanostructured energy harvesting devices; photovoltaics, photodetectors, and photocatalysts. Chapters 4, 5 and 6 go into details on various studies I have been a part of that investigated and engineered nanostructures for solution-processed solar cells, photon detection

applications and photocatalytic systems. Chapter 7 provides a conclusion from the various studies as well as offers an outlook for scalable nanomaterials for energy harvesting applications. Experimental procedures for all projects can be found in the appendix.

The main objectives of the present work are to:

1. Provide a context of the energy landscape and motivate the need for sustainable materials, such as colloidal nanomaterials, to address global energy demands efficiently.
2. Provide a foundation for understanding the role of nanomaterials in energy harvesting devices such as solar cells, photodetectors, and photocatalysts.
3. Demonstrate the systems that I have modeled, fabricated and characterized based on these colloidal nanostructures, and provide an outlook on the future of these technologies moving forward.

The studies and results reported on in this thesis work represent the collaborative work of many people, some of which are listed below:

- In Section 4.1, Botong Qiu assisted in creating and testing the developed model for different solution processed solar cell systems.
- In Section 4.2, Nate Palmquist and Yida Lin helped with fine-tuning the presented optimization technique by accounting for various practical factors. Botong Qiu also assisted with the fabrication and testing of the solar cell devices.

- In Section 4.3, Botong Qiu primarily led the fabrication and characterization of the optoelectronic films. Yida Lin and Arlene Chiu assisted with the FDTD simulations of the photonic-band engineered systems.
- Section 4.4 was a collaboration with Prof. Rebekka Klausen's group including Heidi van de Wouw and Carlton Foster who synthesized the Si-based ligands.
- Section 5.1 was a collaboration with Dr. Ratan Debnath's group and Dr. Nhan Nyugen at National Institute of Standards and Technology, Prof. Mulpuri Vao's group at George Mason University, and Prof. Mona Zaghoul's group at George Washington University. These groups led the synthesis, and fabrication of the nanostructures.
- Section 5.2 was a collaboration with Dr. Ratan Debnath's group and Dr. Nhan Nyugen at National Institute of Standards and Technology. They led the fabrication and characterization efforts of the optoelectronic films while Botong Qiu assisted with the FDTD simulation efforts.
- Section 6.3 was a collaboration with Prof. Art Bragg's group including Ken Smith who led the ultrafast laser measurements. Yan Cheng also synthesized the aluminum nanoparticles used in this study.

References

- [1] United Nations. “Transforming our world: The 2030 agenda for sustainable development”. In: *Resolution adopted by the General Assembly* (2015).
- [2] World Bank. *World Development Indicators 2016*. World Development Indicators. World Bank Publications, 2016. ISBN: 9781464806841. URL: <https://books.google.com/books?id=yqAeDAAAQBAJ>.
- [3] ExxonMobil. *2018 Outlook for Energy: A View to 2040*. 2018. URL: <https://cdn.exxonmobil.com/~media/global/files/outlook-for-energy/2018/2018-outlook-for-energy.pdf>.
- [4] Ottmar Edenhofer, Ramon Pichs-Madruga, Youba Sokona, Kristin Seyboth, Patrick Matschoss, Susanne Kadner, Timm Zwickel, Patrick Eickemeier, Gerrit Hansen, Steffen Schlömer, et al. “IPCC special report on renewable energy sources and climate change mitigation”. In: *Prepared By Working Group III of the Intergovernmental Panel on Climate Change*, Cambridge University Press, Cambridge, UK (2011).
- [5] Patrick Moriarty and Damon Honnery. “What is the global potential for renewable energy?” In: *Renewable and Sustainable Energy Reviews* 16.1 (2012), pp. 244–252.
- [6] Carlos De Castro, Margarita Mediavilla, Luis Javier Miguel, and Fernando Frechoso. “Global wind power potential: Physical and technological limits”. In: *Energy Policy* 39.10 (2011), pp. 6677–6682.
- [7] Carlos De Castro, Margarita Mediavilla, Luis Javier Miguel, and Fernando Frechoso. “Global solar electric potential: A review of their technical and sustainable limits”. In: *Renewable and Sustainable Energy Reviews* 28 (2013), pp. 824–835.
- [8] Vaclav Smil. *Energy transitions: history, requirements, prospects*. ABC-CLIO, 2010.

REFERENCES

- [9] International Energy Agency. *Key World Energy Statistics*. 2017. URL: <https://www.iea.org/publications/freepublications/publication/KeyWorld2017.pdf>.

Chapter 2

Nanomaterials for Energy Harvesting

Nanomaterials, materials that are structured on nanometer-scale dimensions, have emerged in the last decades as a useful material and are currently deployed in a wide range of optoelectronic technologies, with applications in light emission [1, 2, 3], biological sensing [4, 5, 6, 7], communication [8, 9, 10, 11], information and computing technology [12, 13, 14, 15], and energy harvesting and storage[16, 17, 18].

Colloidal nanomaterials, nanomaterials stabilized in a solvent *via* anchoring ligands, are of interest for these optoelectronic applications due to their size-tunable optical properties, unique electronic structures, relative earth-abundance, and low-cost fabrication techniques.

The miniaturization of emerging device components has magnified the relevance of colloidal nanomaterials and their potential to enable further advances in a number of fields. The nanostructured nature of these materials leads to emergent behavior on the macroscale. Examples of colloidal

nanomaterials include semiconductor quantum dots and plasmonic metal nanoparticles.

2.1 Colloidal Quantum Dots

This section is adapted (in part) from Ref. [16]. Reprinted with permission from *Nanophotonics*, Volume 5, Issue 1, Pages 31-54, "Advancing colloidal quantum dot photovoltaic technology," by Y. Cheng, E. S. Arinze, N. Palmquist and S. M. Thon, copyright © 2016.

Colloidal quantum dots (CQDs) are semiconducting nanocrystals with typical diameters of approximately 2-20 nm that exhibit quantum confinement effects. These CQDs are frequently composed of II-VI, III-V, and IV-VI semiconductors. The most common types of CQD materials used in solar cell applications are PbS, PbSe, CdS, and CdSe.

PbS and PbSe possess small bulk band gaps, 0.41 eV and 0.27 eV respectively [19, 20], making them ideal candidates for tuning the associated nanoparticle absorption spectra throughout the near-infrared portion of the sun's spectrum. CdS and CdSe, with larger bulk band gaps of 2.38 eV and 1.78 eV respectively are of more interest for visible-wavelength applications [21].

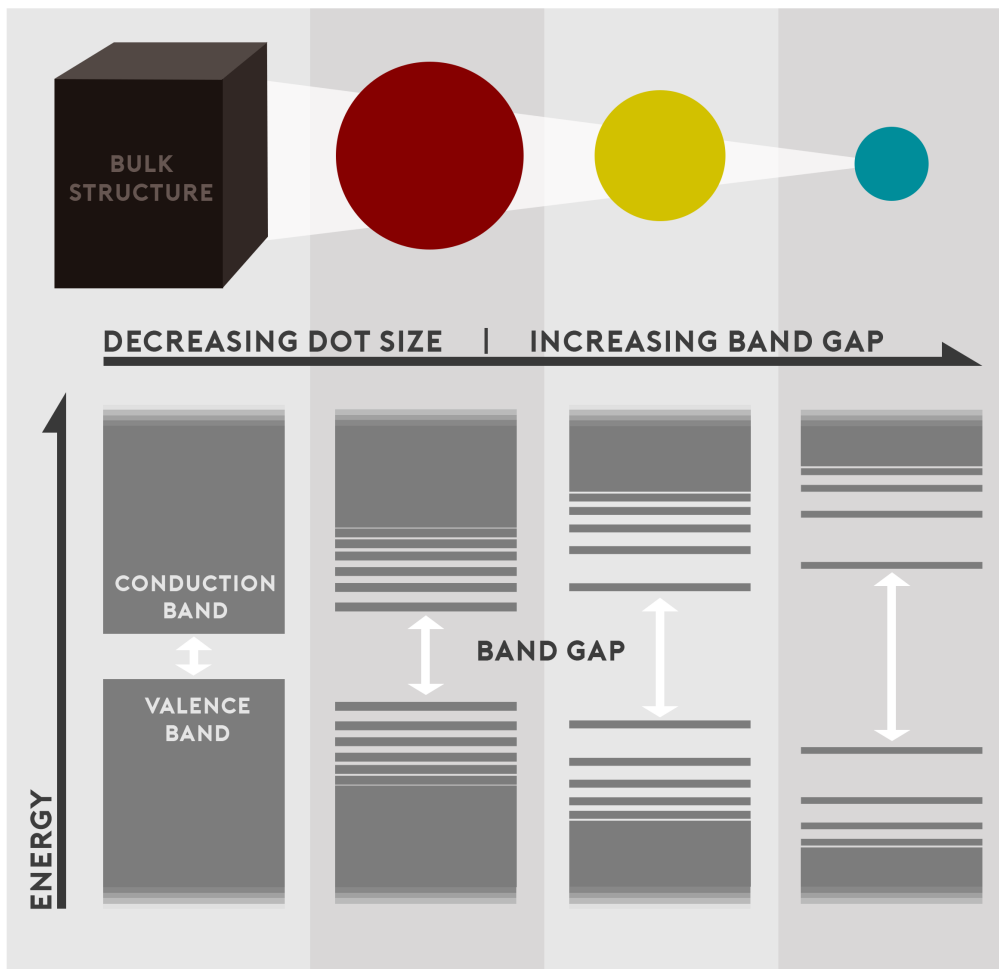


Figure 2.1: Quantum Dot Size-Tuning Effect. Illustration of quantum confinement, the effect that enables tuning of the optical properties of quantum dots through tuning of their size. A decrease in the quantum dot size leads to an increase in the band gap as well energy level quantization.

This widespread interest in QDs stems from their desirable properties including their solution-phase processing and spectral tuning via the quantum size effect, which in turn facilitates the manipulation of their optical and electrical properties. Figure 2.1 illustrates the quantum confinement effect that

differentiates CQDs from their corresponding bulk materials. Energetically, the conduction and valence bands are separated by the band gap, a region of forbidden electronic states. Instead of a bulk-like continuum of energy bands below and above the valence and conduction bands respectively, structuring the semiconductor into QDs with characteristic sizes smaller than the Bohr exciton radius in the bulk material generate discrete states with the corresponding symmetry and energy dependent on QD parameters (including size and shape). This quantum mechanical effect thus enables the energy gap between the highest occupied state and the lowest unoccupied states to be directly related to the CQD size [22, 23, 24].

CQDs are a particularly promising optoelectronic device material for several reasons. They offer the potential for the realization of low-cost devices [25, 26] through their ease of manufacturing [27], air stability [28], and film flexibility [29, 30, 31], thus making them compatible with roll-to-roll and other scalable fabrication techniques.

2.1.1 Synthesis

A critical factor for most CQD device applications is the synthesis of highly monodisperse quantum dots. CQD size is controlled during synthesis by a number of factors, including temperature, precursor concentration and rate of conversion [32, 33], and degree of saturation. The synthesis of CQDs typically involves precursor decomposition forming monomers that undergo rapid nucleation followed by a slow growth phase [34, 35]. The synthesis reaction is initiated at a particular temperature, when the room temperature

precursor is injected into a hot non-coordinating solvent (called the "hot injection method") [36]. The nucleation and growth processes are influenced by factors including monomer concentration and reactivity, solution viscosity and reaction temperature.

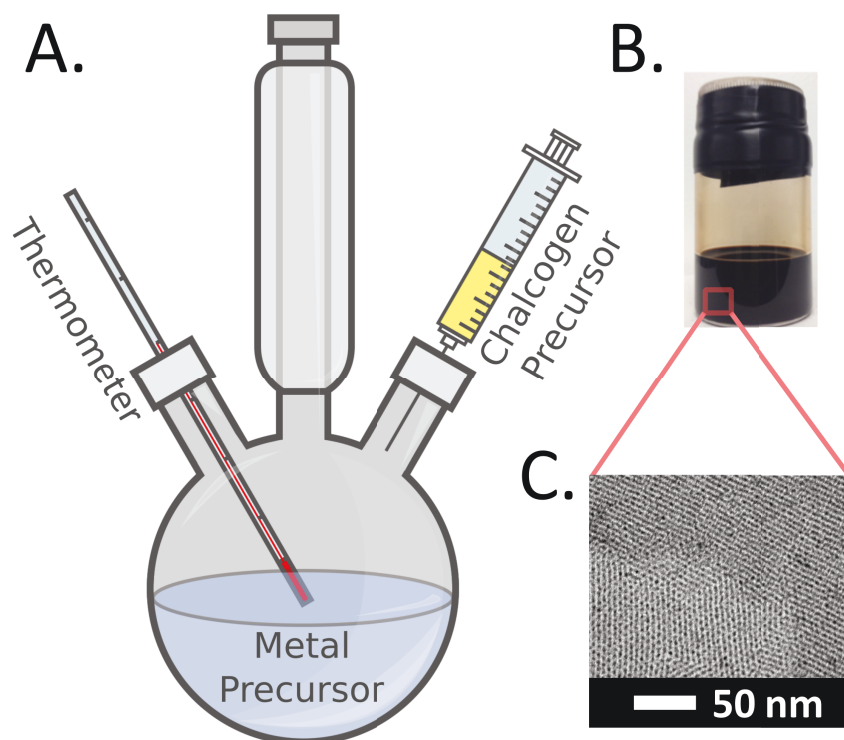


Figure 2.2: (a) Setup showing synthesis of colloidal quantum dots with component precursors and temperature controller. (b) Photograph of as-synthesized PbS CQD solution with excitonic peak at ~ 950 nm. (c) Transmission electron microscope (TEM) image of a large ensemble of PbS CQDs with excitonic peak wavelength of ~ 950 nm.

By varying the injection temperature, the size of the quantum dots can be tuned over a relatively large range [37]. Figure 2.2a illustrates the typical setup of the synthesis of CQDs using this hot-injection approach. An alternative synthesis method, known as the "heating-up" method, involves mixing all precursors, reagents, and solvent together at a low temperature and heating

the mixture to a specific temperature [38]. This method yields similar size dispersion as the hot injection method, but may offer greater scalability potential due to its simplicity. Single-shot synthesis yields of up to 40 g of nanocrystals have been reported using this method [39]; typical syntheses utilizing the "hot injection" method yield about 0.5 g of nanocrystal material [39].

The most common precursors used for PbS and PbSe syntheses are PbO, oleic acid, and bis(trimethylsilyl)sulfide ((TMS)₂S) or bis(trimethylsilyl)selenide ((TMS)₂Se) [34, 40]. However, (TMS)₂S and (TMS)₂Se are flammable and toxic, and they readily hydrolyze with water to form toxic H₂S and H₂Se. This has led to the development of methods based on alternative precursors, including PbCl₂ instead of PbO as the lead precursor to improve the surface passivation of the resulting CQDs [37, 41], and elemental sulfur instead of ((TMS)₂S) [42, 43]. Additional novel growth methods have been proposed, including the synthesis of PbSe in a phosphate glass host [44]. The advantage of crystallizing QDs from the porous glass is that more homogeneous, larger crystal sizes exhibiting quantum confinement effects could be achieved versus those achieved in the conventional colloidal growth methods [45].

There are many other colloidal nanocrystal materials that have been synthesized using variations of these methods, including single element materials, such as graphene [46], Si, and Ge, and compound materials, as well as ternary and quaternary compounds [47, 48, 49, 50].

The detailed synthesis procedures for the CQDs used in later chapters of this thesis are described in the Appendix.

2.1.2 Ligands

Ligands play an important role in CQD synthesis and electronic film properties [51]. Their main function is to maintain colloidal stability in the solution phase and prevent CQDs from aggregating during the nucleation stage of synthesis. Pb- and Cd-chalcogenide CQDs as-synthesized typically have Pb- and Cd-rich surfaces [52, 53, 54, 55]. There, the ligands also play an important role in passivating electronic trap states that are otherwise present due to the presence of under-coordinated surface atoms. Additionally, ligands help to protect CQDs from oxidative degradation, and can facilitate electronic coupling between neighboring CQDs in the film phase. Long organic ligands, however, can act as electronic tunneling barriers, where the rate of charge transport through the barrier decreases exponentially with the barrier width and the square root of the barrier height [56, 57, 58, 59].

Ligand selection can therefore have a large impact on CQD solar cell performance, and much effort has been directed in the field towards engineering ligands for better device operation. Popular ligands for CQD electronic film applications include alkane and aromatic thiols, amines, and carboxylic acids [60, 51, 61, 62, 63, 64]; metal chalcogenide complexes [57]; and halogen atoms [65]. Most organic ligands consist of three parts: an inner anchor to the quantum dot, a middle hydrophilic segment, and an outer functional group. The freedom in choosing a functional group gives ligated CQD materials versatility for different applications.

Metal chalcogenides and metal halides are alternatives to organic ligands commonly used for CQDs in solar cells. Treatment with metal chalcogenide

complexes, such as $\text{In}_2\text{Se}_2^{2-}$ [66, 67], $\{\text{In}_2\text{Cu}_2\text{Se}_4\text{S}_3\}^{3-}$ [66], and $\text{Sn}_2\text{S}_6^{4-}$ [57], has been shown to improve interparticle coupling over the use of organic ligands [57] in CQD thin film field effect transistors.

Metal halide ligands are well suited for trap state passivation, as their small size allows them to access and passivate exposed surface sites inaccessible to longer organic ligands. Studies have shown that device air stability and efficiency are greatly increased when the CQD active material is treated with Cl-containing ligands [60, 41]. Several specific methods have been developed that take advantage of the properties of halogen ligands. These include a PbS CQD treatment procedure that deployed iodine-based materials to create an air-stable ink [68], and a PbS/CdS core/shell CQD synthesis method that used chlorine-based ligands to create a to achieve a high open-circuit voltage through the large band gap of CdS and the passivating effects of the Cl [69]. The highest performing CQD solar cells today incorporate some halide-based ligands into their CQD films [70, 71, 72].

The CQDs used in the experiments described in later chapters of this thesis primarily employed oleic acid, MPA, EDT and halide ligands.

2.1.3 Optical Properties

The optical properties of CQDs are determined by the size, composition, ligand structure, and shape of the individual quantum dots [73, 74, 75, 76, 77]. Figure 2.3 shows absorption spectra for several PbS CQD solutions synthesized via the hot injection method with exciton peaks in the range of 730 nm to 1600 nm, corresponding to CQD diameters of approximately 2.3 to 6.5 nm [24].

The solar spectral irradiance is also plotted to indicate the range that can be potentially captured by PbS CQDs.

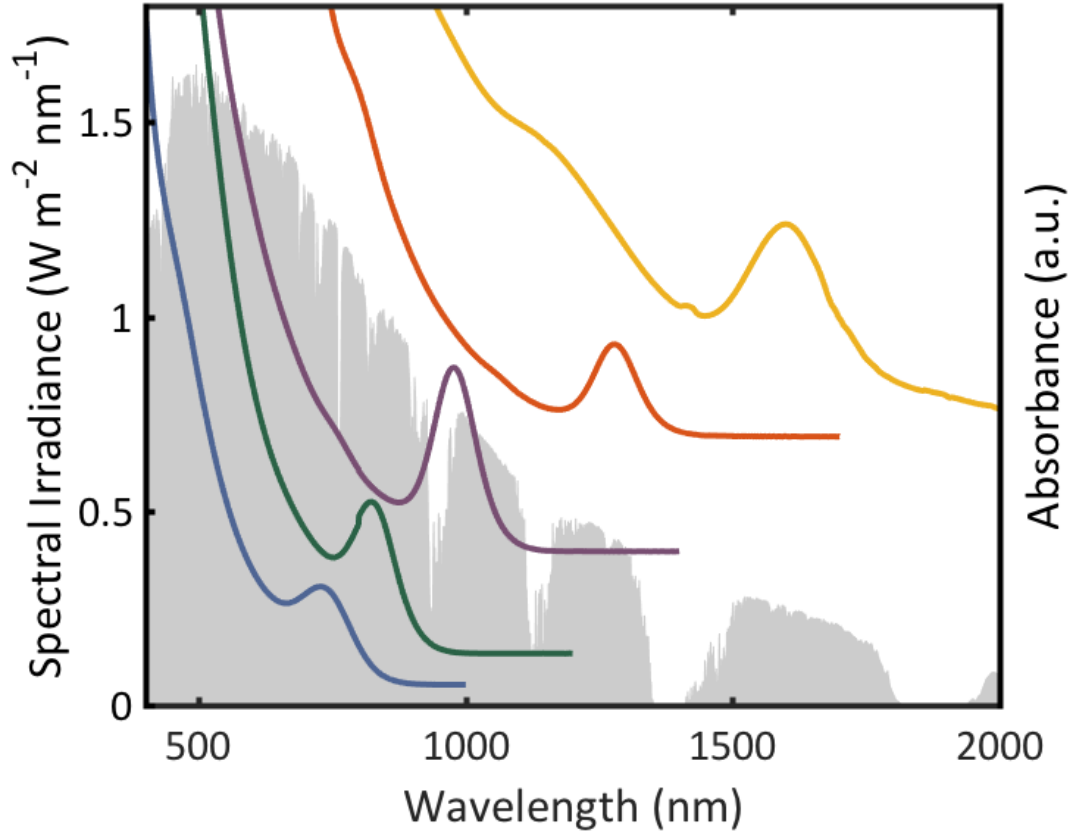


Figure 2.3: PbS CQD Absorption Spectra. Solution-phase absorption spectra of PbS CQDs with exciton peaks at wavelengths of 730, 820, 980, 1280 and 1600 nm. Spectra are offset for clarity. Additionally, the AM1.5G standard solar spectral irradiance (grey) is plotted

The size of the CQD has a direct impact on the apparent band gap, with smaller quantum dots exhibiting higher excitation energies. This is quantitatively shown via the Brus Equation [78]:

$$E^* = E_g + \frac{\hbar^2 \pi^2}{2R^2} \left[\frac{1}{m_e} + \frac{1}{m_h} \right] - \frac{1.8e^2}{\epsilon_0 \epsilon_p R} \quad (2.1)$$

Here, E^* is the apparent band gap, E_g is the bulk band gap, m_e and m_h are the respective effective electron and hole masses, ϵ_p is the dielectric constant of the nanoparticle, and R is the nanoparticle radius. This formula includes the additive component of the quantum confinement of the excitons as well as the subtractive component of the electron-hole repulsion. For PbS CQDs, a prevalent material for CQD solar cells due to its optimal band gap tuning range, Moreels et. al. showed that the following empirical equation is a good approximation of the relationship between the effective band gap (in eV) of the CQD and its diameter, d (nm) [24]:

$$E^* = 0.41 + \frac{1}{0.0252d^2 + 0.283d} \quad (2.2)$$

Particle size influences optical properties beyond tuning the absorption onset. The ambient stability of PbS CQDs has also been demonstrated to be dependent on the nanoparticle size [79]. The first exciton wavelength of larger CQDs (diameter > 4 nm) experiences a blue shift when stored in air, as the un-passivated (100) surface becomes oxidized and the effective optical particle diameter decreases [79]. It was also shown that the molar extinction coefficient increases with the CQD volume as d^3 (where d is particle diameter) at higher energies, but only increases as $d^{1.3}$ near the band gap [24].

Electroluminescence efficiency is an important metric for optoelectronic nanomaterial-based films, since it depends on both electronic transport efficiency and radiative recombination efficiency. It is therefore an indirect measure of the electronic trap state density[80] and carrier mobility, and is correlated with optoelectronic properties such as the open-circuit voltage of

a solar cell; thus, achieving large luminescence yields is a requirement in photovoltaic materials. Typical as-synthesized CQD solutions possess photoluminescence quantum efficiencies (PLQE) around 50%, and treatments such as the CdCl_2 metal-halide passivation strategy have been shown to help CQD solutions maintain these efficiencies even after the washing steps necessary to prepare the CQDs for film deposition [81]. Film-phase PLQEs are much lower, substantiating the view that CQD film transport is limited by non-radiative recombination processes induced by large electronic trap state densities.

Additionally, emission in CQDs is red-shifted with respect to the first (1S) excitonic absorption peak [82]. This difference between the luminescence energy and the absorption energy is referred to as the Stokes shift, and it decreases with increasing quantum dot size. The relatively large Stokes shifts observed in CQDs have been partially attributed to the surface properties of the nanoparticles [83].

Ligands play an important role in the optical properties of CQDs. Better passivated surfaces can increase radiative recombination efficiency, leading to higher photoluminescence quantum yields. Ligands can also facilitate coupling between quantum dots, which can have the effect of red-shifting the absorption and emission spectra and increasing exciton dissociation rates, thereby lowering radiative recombination rates. One study showed that photoluminescence quantum yields could be increased by a factor of 2 when using glutathione (GSH) over tiopronin (TP) ligands due to the presence of an inner thiol group in the GSH ligand [84]. Silvia et al. later showed that the partial hydrolysis of GSH caused some of the sulfur to react with the CdTe

to create a CdS shell that provided better surface passivation [85]. Another study found that when comparing bifunctional carboxylic acid molecules, the more acidic and shorter chains performed the best optically, leading to an exciton absorption peak red shift due to greater electronic coupling between neighboring quantum dots [86]. This electronic coupling, also seen in the study of 1,3-benzenedithiol (1,3-BDT), EDT, mercaptopropionic acid (MPA), and ammonium sulfide $((\text{NH}_4)_2\text{S})$, was attributed to the extension of the electron wavefunction outside the individual CQDs [87]. This resulted in a reduction of the quantum confinement of the particles, decreasing the apparent band gap of the CQDs.

2.2 Plasmonic Nanoparticles

The collective oscillations of the free electrons at the surface of a conductor are known as surface plasmons. These excitations couple strongly to incident electromagnetic radiation and are able to propagate along a metal-dielectric interface as surface plasmon polaritons. Surface plasmons can be excited at optical frequencies in materials such as gold and silver. Figure 2.4 illustrates the surface plasmon resonance resulting from the match between the incident field energy and the oscillating electrons on the nanoparticle surface. In nanoscale structures, these excitations are known as localized surface plasmon resonances (LSPRs), and can facilitate strong local field enhancement.

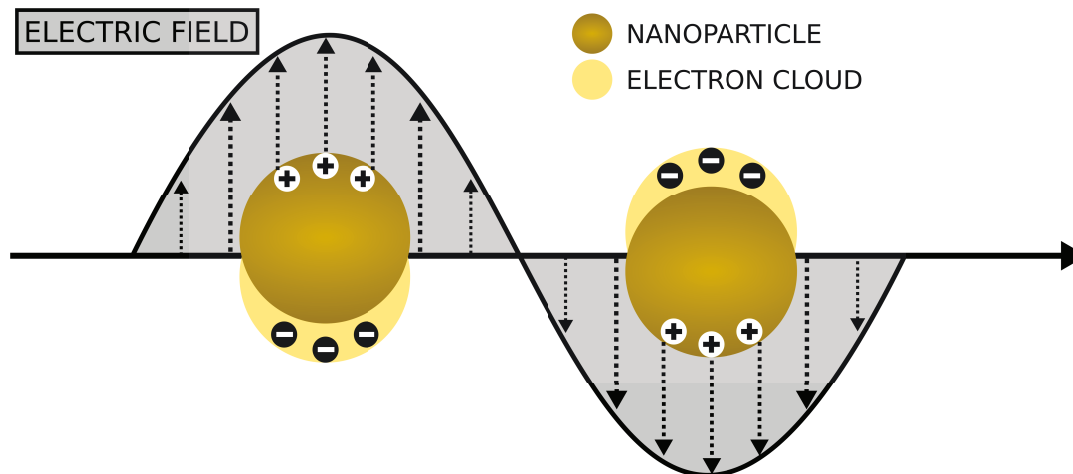


Figure 2.4: Schematic illustrating the surface plasmon resonance on the surface of a metal nanoparticle.

In recent years, metal nanoparticles (MNPs) have gained attention as a result of their unique properties and potential applications when compared to their bulk phases. A critical property of these nanoparticles is their optical spectrum. In the 10-100 nm size regime, they exhibit strong absorption that can be tuned from the ultraviolet (UV) to the near-infrared (NIR) spectral regions, depending on the properties of the metallic band structure. The optical properties of MNPs can be tuned via parameters such as the size, shape, material, and surrounding medium. Examples of metal nanoparticle materials that exhibit LSPRs include gold[88, 89], silver [90, 91], copper [92, 93] and aluminum [94, 95].

2.2.1 Synthesis and Ligands

There are various demonstrated pathways to synthesize plasmonic nanoparticles. Some of these synthesis routes include chemical reduction [96, 97], decomposition [98], radiolysis [99, 100], sol-gel method [101, 102], seed-mediated

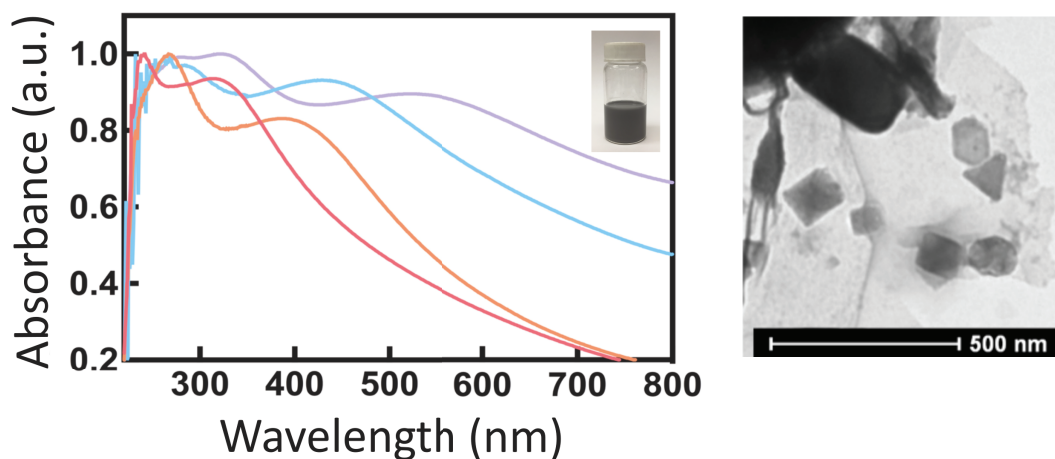


Figure 2.5: Aluminum Absorbance Spectra. (a) Solution-phase absorbance spectra of aluminum nanoparticles with dipolar plasmonic resonances at wavelengths of 317, 389, 440, and 525 nm (red, orange, blue, and purple curves, respectively). Inset shows a vial containing a colloidal aluminum nanoparticle solution. (b) TEM Image showing variation in shapes of synthesized aluminum nanoparticles.

growth [102, 103], and biosynthesis [104, 105]. These techniques have been employed to synthesize plasmonic nanoparticles of various shapes and sizes.

Ligands serve multiple roles in the synthesis of plasmonic nanoparticles. First, they provide colloidal stabilization of the nanoparticles in the dispersal solvent. Second, they can potentially assist with facet stabilization thus providing a route to synthesize nanoparticles of different shapes. Lastly, they occasionally serve as reducing agents themselves in the synthesis process. Examples of common ligands used in plasmonic nanoparticle synthesis are poly(vinyl pyrrolidone) (PVP) [104], citrate [105], oleic acid [106] and cetyltrimethylammonium bromide (CTAB) [107].

Figure 2.5 (a) shows absorbance spectra for several aluminum nanoparticle solutions synthesized with dipolar plasmonic resonance peaks in the range of 317 nm to 525 nm, corresponding to nanoparticle diameters of approximately

66 to 130 nm. The aluminum nanoparticles are synthesized using modifications of established procedures [98]. Briefly, the particles were formed through decomposition of dimethylethylamine alane under mild heating using titanium(IV) isopropoxide as a catalyst. A sample TEM image is shown in figure 2.5 (b) with the aluminum solution exhibiting different synthesized shapes.

2.2.2 Optical Properties

The optical properties of plasmonic nanoparticles can be calculated using Mie theory [108, 109] or numerically via finite-difference time-domain (FDTD) simulations [110, 111] or finite element methods [112, 113]. FDTD simulations solve the Maxwell equations on a discrete grid in time and space.

By injecting a plane wave source, field components are

iteratively computed until a converged steady-state solution is obtained. These calculated fields can be translated to absorption, scattering and extinction cross-sections.

FDTD computations were employed to calculate the optical properties

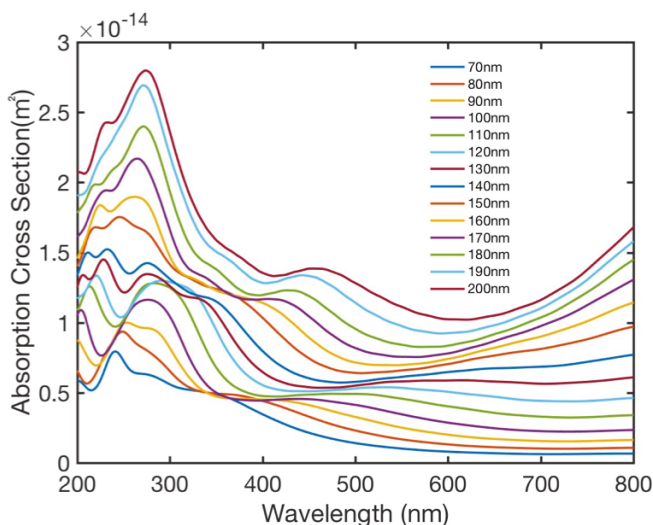


Figure 2.6: FDTD-calculated absorption cross sections for a single bare aluminum nanosphere in a 2-propanol background.

of different sized aluminum nanospheres. Figure 2.6 shows the computed absorption spectra for aluminum nanospheres, varying in size from 70 to 200 nm in diameter, in an isopropanol medium. The data shows a red-shift in the surface plasmon resonance peak with an increase in nanoparticle size, as well as the emergence of higher order modes. These simulations provide a platform through which plasmonic nanoparticle-systems can be designed and experimental results can be investigated or verified.

2.2.2.1 SPP Dispersion Relation

As discussed earlier, the surface plasmon polaritons result from strong coupling of free space electromagnetic wave and surface plasmon excitation. By solving Maxwell's equations, the dispersion relation of propagating SPPs is given as [114]:

$$\beta = \beta' + i\beta'' \quad (2.3)$$

where

$$\beta' = \frac{\omega}{c} \left(\frac{\epsilon'_1 \epsilon_2}{\epsilon'_1 + \epsilon_2} \right)^{1/2} \quad (2.4)$$

$$\beta'' = \frac{\omega}{c} \left(\frac{\epsilon'_1 \epsilon_2}{\epsilon'_1 + \epsilon_2} \right)^{3/2} \frac{\epsilon''_1}{2(\epsilon'_1)^2} \quad (2.5)$$

where the real metal has a complex dielectric function $\epsilon_1 = \epsilon'_1 + i\epsilon''_1$, ϵ_2 is the relative permittivity of the dielectric material, $\frac{\omega}{c}$ refers to the propagating wave vector in vacuum. The real component, β' , is the dispersion of the surface plasmon and the imaginary component, β'' , assesses the propagation

loss of SPPs along the metal-dielectric interface (mode damping factor). In the limit of negligible damping and at large wave vectors, the SPP frequency converges to the surface plasmon frequency and is given by:

$$\omega_{sp} = \frac{\omega_p}{\sqrt{1 + \epsilon_2}} \quad (2.6)$$

where ω_{sp} and ω_p are the surface plasmon frequency and the plasma frequency respectively.

2.2.2.2 Mie Theory

In 1908, G. Mie investigated the scattering of light from an object with a spherical shape.[115] This theory, known as the Mie theory (also known as the Mie-Debye theory or Lorentz-Mie theory), over the next few decades has become a useful tool in understanding the behaviors of spherical particles in non-absorbing media. The solution assumes that the particle is illuminated by a plane wave source and is embedded in a homogeneous and isotropic medium.

The scattering, extinction, and absorption cross-sections can be expressed as a function of the Mie coefficients as[116]:

$$C_{sca} = \frac{2\pi}{k^2} \sum_{n=1}^{\infty} (2n + 1) (|a_n|^2 + |b_n|^2) \quad (2.7)$$

$$C_{ext} = \frac{2\pi}{k^2} \sum_{n=1}^{\infty} (2n + 1) \text{Re}(a_n^2 + b_n) \quad (2.8)$$

$$C_{abs} = C_{ext} - C_{sca} \quad (2.9)$$

where a_n and b_n are the Mie coefficients for the scattered field, n is the complex refractive index of the material, and k ($2\pi/\lambda$) is the in-medium wavenumber. By dividing these parameters by the geometrical cross section of the sphere, we can obtain the scattering (Q_{sca}), extinction (Q_{ext}) and absorption (Q_{abs}) efficiencies respectively.

References

- [1] Yasuhiro Shirasaki, Geoffrey J Supran, Mounqi G Bawendi, and Vladimir Bulović. “Emergence of colloidal quantum-dot light-emitting technologies”. In: *Nature Photonics* 7.1 (2013), p. 13.
- [2] Xingliang Dai, Zhenxing Zhang, Yizheng Jin, Yuan Niu, Hujia Cao, Xiaoyong Liang, Liwei Chen, Jianpu Wang, and Xiaogang Peng. “Solution-processed, high-performance light-emitting diodes based on quantum dots”. In: *Nature* 515.7525 (2014), p. 96.
- [3] Xingliang Dai, Yunzhou Deng, Xiaogang Peng, and Yizheng Jin. “Quantum-Dot Light-Emitting Diodes for Large-Area Displays: Towards the Dawn of Commercialization”. In: *Advanced materials* 29.14 (2017), p. 1607022.
- [4] Yucheng Wang, Rui Hu, Guimiao Lin, Indrajit Roy, and Ken-Tye Yong. “Functionalized quantum dots for biosensing and bioimaging and concerns on toxicity”. In: *ACS applied materials & interfaces* 5.8 (2013), pp. 2786–2799.
- [5] IV Martynenko, AP Litvin, F Purcell-Milton, AV Baranov, AV Fedorov, and YK Gun’ko. “Application of semiconductor quantum dots in bioimaging and biosensing”. In: *Journal of Materials Chemistry B* 5.33 (2017), pp. 6701–6727.
- [6] Jeffrey N Anker, W Paige Hall, Olga Lyandres, Nilam C Shah, Jing Zhao, and Richard P Van Duyne. “Biosensing with plasmonic nanosensors”. In: *Nanoscience And Technology: A Collection of Reviews from Nature Journals*. World Scientific, 2010, pp. 308–319.
- [7] Xiaoling Wu, Changlong Hao, Jatish Kumar, Hua Kuang, Nicholas A Kotov, Luis M Liz-Marzán, and Chuanlai Xu. “Environmentally responsive plasmonic nanoassemblies for biosensing”. In: *Chemical Society Reviews* (2018).

REFERENCES

- [8] P Michler, A Kiraz, C Becher, WV Schoenfeld, PM Petroff, Lidong Zhang, E Hu, and A Imamoglu. “A quantum dot single-photon turnstile device”. In: *science* 290.5500 (2000), pp. 2282–2285.
- [9] A Vardi, N Akopian, G Bahir, L Doyennette, M Tchernycheva, L Nevou, FH Julien, F Guillot, and E Monroy. “Room temperature demonstration of Ga N/ Al N quantum dot intraband infrared photodetector at fiber-optics communication wavelength”. In: *Applied physics letters* 88.14 (2006), p. 143101.
- [10] Holger Schmeckeber and Dieter Bimberg. “Quantum-dot semiconductor optical amplifiers for energy-efficient optical communication”. In: *Green Photonics and Electronics*. Springer, 2017, pp. 37–74.
- [11] Josep Miquel Jornet and Ian F Akyildiz. “Graphene-based plasmonic nano-antenna for terahertz band communication in nanonetworks”. In: *IEEE Journal on selected areas in communications* 31.12 (2013), pp. 685–694.
- [12] Ji-Hyuk Choi, Han Wang, Soong Ju Oh, Taejong Paik, Pil Sung, Jinwoo Sung, Xingchen Ye, Tianshuo Zhao, Benjamin T Diroll, Christopher B Murray, et al. “Exploiting the colloidal nanocrystal library to construct electronic devices”. In: *Science* 352.6282 (2016), pp. 205–208.
- [13] Daniel Loss and David P DiVincenzo. “Quantum computation with quantum dots”. In: *Physical Review A* 57.1 (1998), p. 120.
- [14] Yan Wang, Ziyu Lv, Jinrui Chen, Zhanpeng Wang, Ye Zhou, Li Zhou, Xiaoli Chen, and Su-Ting Han. “Photonic Synapses Based on Inorganic Perovskite Quantum Dots for Neuromorphic Computing”. In: *Advanced Materials* (2018), p. 1802883.
- [15] Tengfeng Zhu, Yihan Zhou, Yijie Lou, Hui Ye, Min Qiu, Zhichao Ruan, and Shanhui Fan. “Plasmonic computing of spatial differentiation”. In: *Nature communications* 8 (2017), p. 15391.
- [16] Yan Cheng, Ebuka S Arinze, Nathan Palmquist, and Susanna M Thon. “Advancing colloidal quantum dot photovoltaic technology”. In: *Nanophotonics* 5.1 (2016), pp. 31–54.
- [17] Anna Douglas, Rachel Carter, Landon Oakes, Keith Share, Adam P Cohn, and Cary L Pint. “Ultrafine iron pyrite (FeS₂) nanocrystals improve sodium–sulfur and lithium–sulfur conversion reactions for efficient batteries”. In: *ACS nano* 9.11 (2015), pp. 11156–11165.

REFERENCES

- [18] Changlong Wang and Didier Astruc. "Nanogold plasmonic photocatalysis for organic synthesis and clean energy conversion". In: *Chemical Society Reviews* 43.20 (2014), pp. 7188–7216.
- [19] Steven A McDonald, Gerasimos Konstantatos, Shiguo Zhang, Paul W Cyr, Ethan JD Klem, Larissa Levina, and Edward H Sargent. "Solution-processed PbS quantum dot infrared photodetectors and photovoltaics". In: *Nature materials* 4.2 (2005), p. 138.
- [20] Chinedu E Ekuma, David J Singh, Juana Moreno, and Mark Jarrell. "Optical properties of PbTe and PbSe". In: *Physical Review B* 85.8 (2012), p. 085205.
- [21] SJ Lade, MD Uplane, and CD Lokhande. "Photoelectrochemical properties of CdX (X= S, Se, Te) films electrodeposited from aqueous and non-aqueous baths". In: *Materials chemistry and physics* 68.1-3 (2001), pp. 36–41.
- [22] Louis E Brus. "Electron–electron and electron-hole interactions in small semiconductor crystallites: The size dependence of the lowest excited electronic state". In: *The Journal of chemical physics* 80.9 (1984), pp. 4403–4409.
- [23] Alexey I Ekimov, Al L Efros, and Alexei A Onushchenko. "Quantum size effect in semiconductor microcrystals". In: *Solid State Communications* 56.11 (1985), pp. 921–924.
- [24] Iwan Moreels, Karel Lambert, Dries Smeets, David De Muynck, Tom Nollet, José C Martins, Frank Vanhaecke, Andre Vantomme, Christophe Delerue, Guy Allan, et al. "Size-dependent optical properties of colloidal PbS quantum dots". In: *ACS nano* 3.10 (2009), pp. 3023–3030.
- [25] Joel Jean, Patrick R Brown, Robert L Jaffe, Tonio Buonassisi, and Vladimir Bulović. "Pathways for solar photovoltaics". In: *Energy & Environmental Science* 8.4 (2015), pp. 1200–1219.
- [26] Cyrus Wadia, A Paul Alivisatos, and Daniel M Kammen. "Materials availability expands the opportunity for large-scale photovoltaics deployment". In: *Environmental science & technology* 43.6 (2009), pp. 2072–2077.

REFERENCES

- [27] Anna Loiudice, Aurora Rizzo, Michela Corricelli, M Lucia Curri, Maria R Belviso, P Davide Cozzoli, Giulia Grancini, Annamaria Petrozza, and Giuseppe Gigli. "Room-temperature treatments for all-inorganic nanocrystal solar cell devices". In: *Thin Solid Films* 560 (2014), pp. 44–48.
- [28] Zhijun Ning, Oleksandr Voznyy, Jun Pan, Sjoerd Hoogland, Valerio Adinolfi, Jixian Xu, Min Li, Ahmad R Kirmani, Jon-Paul Sun, James Minor, et al. "Air-stable n-type colloidal quantum dot solids". In: *Nature materials* 13.8 (2014), p. 822.
- [29] Illan J Kramer, Gabriel Moreno-Bautista, James C Minor, Damir Kopilovic, and Edward H Sargent. "Colloidal quantum dot solar cells on curved and flexible substrates". In: *Applied Physics Letters* 105.16 (2014), p. 163902.
- [30] Huan Liu, Min Li, Oleksandr Voznyy, Long Hu, Qiuyun Fu, Dongxiang Zhou, Zhe Xia, Edward H Sargent, and Jiang Tang. "Physically flexible, rapid-response gas sensor based on colloidal quantum dot solids". In: *Advanced Materials* 26.17 (2014), pp. 2718–2724.
- [31] Matthew E Cryer and Jonathan E Halpert. "300 nm Spectral Resolution in the Mid-Infrared with Robust, High Responsivity Flexible Colloidal Quantum Dot Devices at Room Temperature". In: *ACS Photonics* (2018).
- [32] Kuo-Feng Lin, Hsin-Ming Cheng, Hsu-Cheng Hsu, Li-Jiaun Lin, and Wen-Feng Hsieh. "Band gap variation of size-controlled ZnO quantum dots synthesized by sol-gel method". In: *Chemical Physics Letters* 409.4-6 (2005), pp. 208–211.
- [33] Jonathan S Owen, Emory M Chan, Haitao Liu, and A Paul Alivisatos. "Precursor conversion kinetics and the nucleation of cadmium selenide nanocrystals". In: *Journal of the American Chemical Society* 132.51 (2010), pp. 18206–18213.
- [34] Margaret A Hines and Gregory D Scholes. "Colloidal PbS nanocrystals with size-tunable near-infrared emission: observation of post-synthesis self-narrowing of the particle size distribution". In: *Advanced Materials* 15.21 (2003), pp. 1844–1849.
- [35] Jongnam Park, Jin Joo, Soon Gu Kwon, Youngjin Jang, and Taeghan Hyeon. "Synthesis of monodisperse spherical nanocrystals". In: *Angewandte Chemie International Edition* 46.25 (2007), pp. 4630–4660.

REFERENCES

- [36] CBea Murray, David J Norris, and Mounji G Bawendi. "Synthesis and characterization of nearly monodisperse CdE (E= sulfur, selenium, tellurium) semiconductor nanocrystallites". In: *Journal of the American Chemical Society* 115.19 (1993), pp. 8706–8715.
- [37] Iwan Moreels, Yolanda Justo, Bram De Geyter, Katrien Haestraete, José C Martins, and Zeger Hens. "Size-tunable, bright, and stable PbS quantum dots: a surface chemistry study". In: *ACS nano* 5.3 (2011), pp. 2004–2012.
- [38] Soon Gu Kwon, Yuanzhe Piao, Jongnam Park, Subramanian Angappane, Younghun Jo, Nong-Moon Hwang, Je-Geun Park, and Taeghwan Hyeon. "Kinetics of monodisperse iron oxide nanocrystal formation by "heating-up" process". In: *Journal of the American Chemical Society* 129.41 (2007), pp. 12571–12584.
- [39] Jongnam Park, Kwangjin An, Yosun Hwang, Je-Geun Park, Han-Jin Noh, Jae-Young Kim, Jae-Hoon Park, Nong-Moon Hwang, and Taeghwan Hyeon. "Ultra-large-scale syntheses of monodisperse nanocrystals". In: *Nature materials* 3.12 (2004), p. 891.
- [40] Wanli Ma, Sarah L Swisher, Trevor Ewers, Jesse Engel, Vivian E Ferry, Harry A Atwater, and A Paul Alivisatos. "Photovoltaic performance of ultrasmall PbSe quantum dots". In: *ACS nano* 5.10 (2011), pp. 8140–8147.
- [41] Jianbing Zhang, Jianbo Gao, Elisa M Miller, Joseph M Luther, and Matthew C Beard. "Diffusion-controlled synthesis of PbS and PbSe quantum dots with in situ halide passivation for quantum dot solar cells". In: *ACS nano* 8.1 (2013), pp. 614–622.
- [42] Mingjian Yuan, Kyle W Kemp, Susanna M Thon, Jin Young Kim, Kang Wei Chou, Aram Amassian, and Edward H Sargent. "High-performance quantum-dot solids via elemental sulfur synthesis". In: *Advanced Materials* 26.21 (2014), pp. 3513–3519.
- [43] Martin R McPhail and Emily A Weiss. "Role of organosulfur compounds in the growth and final surface chemistry of PbS quantum dots". In: *Chemistry of Materials* 26.11 (2014), pp. 3377–3384.
- [44] A Lipovskii, E Kolobkova, V Petrikov, I Kang, A Olkhovets, T Krauss, M Thomas, J Silcox, F Wise, Q Shen, et al. "Synthesis and characterization of PbSe quantum dots in phosphate glass". In: *Applied physics letters* 71.23 (1997), pp. 3406–3408.

REFERENCES

- [45] NF Borrelli and DW Smith. "Quantum confinement of PbS microcrystals in glass". In: *Journal of non-crystalline solids* 180.1 (1994), pp. 25–31.
- [46] Xin Yan, Xiao Cui, and Liang-shi Li. "Synthesis of large, stable colloidal graphene quantum dots with tunable size". In: *Journal of the American Chemical Society* 132.17 (2010), pp. 5944–5945.
- [47] Katsuhiko Nose, Takahisa Omata, and Shinya Otsuka-Yao-Matsuo. "Colloidal synthesis of ternary copper indium diselenide quantum dots and their optical properties". In: *The Journal of Physical Chemistry C* 113.9 (2009), pp. 3455–3460.
- [48] Danielle K Smith, Joseph M Luther, Octavi E Semonin, Arthur J Nozik, and Matthew C Beard. "Tuning the synthesis of ternary lead chalcogenide quantum dots by balancing precursor reactivity". In: *ACS nano* 5.1 (2010), pp. 183–190.
- [49] Zhengtao Deng, Hao Yan, and Yan Liu. "Band gap engineering of quaternary-alloyed ZnCdS₂ quantum dots via a facile phosphine-free colloidal method". In: *Journal of the American Chemical Society* 131.49 (2009), pp. 17744–17745.
- [50] Bin-Long Wu, Hsi-Jung Chao, Chih-Ping Chen, Cheng-Hsien Yang, and Jia-Yaw Chang. "One-pot synthesis of colloidal Cd_x:CuInS₂ quaternary quantum dots used as sensitizers in photovoltaic cells". In: *RSC Advances* 5.46 (2015), pp. 36605–36613.
- [51] Mark Green. "The nature of quantum dot capping ligands". In: *Journal of Materials Chemistry* 20.28 (2010), pp. 5797–5809.
- [52] Jiang Tang, Lukasz Brzozowski, D Aaron R Barkhouse, Xihua Wang, Ratan Debnath, Remigiusz Wolowiec, Elenita Palmiano, Larissa Levina, Andras G Pattantyus-Abraham, Damir Jamakosmanovic, et al. "Quantum dot photovoltaics in the extreme quantum confinement regime: the surface-chemical origins of exceptional air-and light-stability". In: *ACS nano* 4.2 (2010), pp. 869–878.
- [53] Jason Taylor, Tadd Kippeny, and Sandra J Rosenthal. "Surface stoichiometry of CdSe nanocrystals determined by Rutherford backscattering spectroscopy". In: *Journal of Cluster Science* 12.4 (2001), pp. 571–582.

REFERENCES

- [54] Jacek Jasieniak and Paul Mulvaney. "From Cd-rich to Se-rich- the manipulation of CdSe nanocrystal surface stoichiometry". In: *Journal of the American Chemical Society* 129.10 (2007), pp. 2841–2848.
- [55] Iwan Moreels, Bernd Fritzing, José C Martins, and Zeger Hens. "Surface chemistry of colloidal PbSe nanocrystals". In: *Journal of the American Chemical Society* 130.45 (2008), pp. 15081–15086.
- [56] Dmitri V Talapin, Jong-Soo Lee, Maksym V Kovalenko, and Elena V Shevchenko. "Prospects of colloidal nanocrystals for electronic and optoelectronic applications". In: *Chemical reviews* 110.1 (2009), pp. 389–458.
- [57] Maksym V Kovalenko, Marcus Scheele, and Dmitri V Talapin. "Colloidal nanocrystals with molecular metal chalcogenide surface ligands". In: *Science* 324.5933 (2009), pp. 1417–1420.
- [58] Philippe Guyot-Sionnest. "Electrical transport in colloidal quantum dot films". In: *The Journal of Physical Chemistry Letters* 3.9 (2012), pp. 1169–1175.
- [59] Amir Zabet-Khosousi and Al-Amin Dhirani. "Charge transport in nanoparticle assemblies". In: *Chemical reviews* 108.10 (2008), pp. 4072–4124.
- [60] Jiang Tang, Kyle W Kemp, Sjoerd Hoogland, Kwang S Jeong, Huan Liu, Larissa Levina, Melissa Furukawa, Xihua Wang, Ratan Debnath, Dongkyu Cha, et al. "Colloidal-quantum-dot photovoltaics using atomic-ligand passivation". In: *Nature materials* 10.10 (2011), p. 765.
- [61] H Tetsuo Uyeda, Igor L Medintz, Jyoti K Jaiswal, Sanford M Simon, and Hedi Mattoussi. "Synthesis of compact multidentate ligands to prepare stable hydrophilic quantum dot fluorophores". In: *Journal of the American Chemical Society* 127.11 (2005), pp. 3870–3878.
- [62] Ethan JD Klem, Harnik Shukla, Sean Hinds, Dean D MacNeil, Larissa Levina, and Edward H Sargent. "Impact of dithiol treatment and air annealing on the conductivity, mobility, and hole density in PbS colloidal quantum dot solids". In: *Applied Physics Letters* 92.21 (2008), p. 212105.
- [63] Carlo Giansante, Luigi Carbone, Cinzia Giannini, Davide Altamura, Zoobia Ameer, Giuseppe Maruccio, Anna Loiudice, Maria R Belviso, P Davide Cozzoli, Aurora Rizzo, et al. "Colloidal arenethiolate-capped

REFERENCES

- PbS quantum dots: optoelectronic properties, self-assembly, and application in solution-cast photovoltaics". In: *The Journal of Physical Chemistry C* 117.25 (2013), pp. 13305–13317.
- [64] D Aaron R Barkhouse, Andras G Pattantyus-Abraham, Larissa Levina, and Edward H Sargent. "Thiols passivate recombination centers in colloidal quantum dots leading to enhanced photovoltaic device efficiency". In: *ACS nano* 2.11 (2008), pp. 2356–2362.
- [65] Matthew J Greaney, Elsa Couderc, Jing Zhao, Benjamin A Nail, Matthew Mecklenburg, William Thornbury, Frank E Osterloh, Stephen E Bradforth, and Richard L Brutchey. "Controlling the trap state landscape of colloidal CdSe nanocrystals with cadmium halide ligands". In: *Chemistry of Materials* 27.3 (2015), pp. 744–756.
- [66] Chengyang Jiang, Jong-Soo Lee, and Dmitri V Talapin. "Soluble Precursors for CuInSe₂, CuIn_{1-x}Ga_xSe₂, and Cu₂ZnSn(S, Se)₄ Based on Colloidal Nanocrystals and Molecular Metal Chalcogenide Surface Ligands". In: *Journal of the American Chemical Society* 134.11 (2012), pp. 5010–5013.
- [67] Jong-Soo Lee, Maksym V Kovalenko, Jing Huang, Dae Sung Chung, and Dmitri V Talapin. "Band-like transport, high electron mobility and high photoconductivity in all-inorganic nanocrystal arrays". In: *Nature nanotechnology* 6.6 (2011), p. 348.
- [68] Zhijun Ning, Haopeng Dong, Qiong Zhang, Oleksandr Voznyy, and Edward H Sargent. "Solar cells based on inks of n-type colloidal quantum dots". In: *ACS nano* 8.10 (2014), pp. 10321–10327.
- [69] Darren CJ Neo, Cheng Cheng, Samuel D Stranks, Simon M Fairclough, Judy S Kim, Angus I Kirkland, Jason M Smith, Henry J Snaith, Hazel E Assender, and Andrew AR Watt. "Influence of shell thickness and surface passivation on PbS/CdS core/shell colloidal quantum dot solar cells". In: *Chemistry of Materials* 26.13 (2014), pp. 4004–4013.
- [70] Mengxia Liu, Oleksandr Voznyy, Randy Sabatini, F Pelayo García de Arquer, Rahim Munir, Ahmed Hesham Balawi, Xinzheng Lan, Fengjia Fan, Grant Walters, Ahmad R Kirmani, et al. "Hybrid organic-inorganic inks flatten the energy landscape in colloidal quantum dot solids". In: *Nature materials* 16.2 (2017), p. 258.

REFERENCES

- [71] Erin M Sanehira, Ashley R Marshall, Jeffrey A Christians, Steven P Harvey, Peter N Ciesielski, Lance M Wheeler, Philip Schulz, Lih Y Lin, Matthew C Beard, and Joseph M Luther. “Enhanced mobility CsPbI₃ quantum dot arrays for record-efficiency, high-voltage photovoltaic cells”. In: *Science advances* 3.10 (2017), eaao4204.
- [72] 2018. URL: <https://www.nrel.gov/pv/assets/images/efficiency-chart.png>.
- [73] VA Fonoberov, EP Pokatilov, and AA Balandin. “Exciton states and optical transitions in colloidal CdS quantum dots: Shape and dielectric mismatch effects”. In: *Physical Review B* 66.8 (2002), p. 085310.
- [74] Anusorn Kongkanand, Kevin Tvrdy, Kensuke Takechi, Masaru Kuno, and Prashant V Kamat. “Quantum dot solar cells. Tuning photoreponse through size and shape control of CdSe- TiO₂ architecture”. In: *Journal of the American Chemical Society* 130.12 (2008), pp. 4007–4015.
- [75] David J Norris and MG Bawendi. “Measurement and assignment of the size-dependent optical spectrum in CdSe quantum dots”. In: *Physical Review B* 53.24 (1996), p. 16338.
- [76] Robert E Bailey and Shuming Nie. “Alloyed semiconductor quantum dots: tuning the optical properties without changing the particle size”. In: *Journal of the American Chemical Society* 125.23 (2003), pp. 7100–7106.
- [77] Jie Zheng, Caiwei Zhang, and Robert M Dickson. “Highly fluorescent, water-soluble, size-tunable gold quantum dots”. In: *Physical Review Letters* 93.7 (2004), p. 077402.
- [78] Louis Brus. “Electronic wave functions in semiconductor clusters: experiment and theory”. In: *The Journal of Physical Chemistry* 90.12 (1986), pp. 2555–2560.
- [79] Hyekyoung Choi, Jae-Hyeon Ko, Yong-Hyun Kim, and Sohee Jeong. “Steric-hindrance-driven shape transition in PbS quantum dots: understanding size-dependent stability”. In: *Journal of the American Chemical Society* 135.14 (2013), pp. 5278–5281.
- [80] Owen D Miller, Eli Yablonovitch, and Sarah R Kurtz. “Strong internal and external luminescence as solar cells approach the Shockley–Queisser limit”. In: *IEEE Journal of Photovoltaics* 2.3 (2012), pp. 303–311.

REFERENCES

- [81] Alexander H Ip, Susanna M Thon, Sjoerd Hoogland, Oleksandr Voznyy, David Zhitomirsky, Ratan Debnath, Larissa Levina, Lisa R Rollny, Graham H Carey, Armin Fischer, et al. "Hybrid passivated colloidal quantum dot solids". In: *Nature nanotechnology* 7.9 (2012), p. 577.
- [82] VI Klimov, AA Mikhailovsky, Su Xu, A Malko, JA Hollingsworth, a CA Leatherdale, H-J Eisler, and MG Bawendi. "Optical gain and stimulated emission in nanocrystal quantum dots". In: *Science* 290.5490 (2000), pp. 314–317.
- [83] Oleksandr Voznyy. "Mobile surface traps in CdSe nanocrystals with carboxylic acid ligands". In: *The Journal of Physical Chemistry C* 115.32 (2011), pp. 15927–15932.
- [84] Ying-Fan Liu and Jun-Sheng Yu. "Selective synthesis of CdTe and high luminescence CdTe/CdS quantum dots: the effect of ligands". In: *Journal of Colloid and Interface Science* 333.2 (2009), pp. 690–698.
- [85] Carvalho MS Silva FO, Macedo WA Mendonça R, and Reis Balzuweit K. "Effect of surface ligands on the optical properties of aqueous soluble CdTe quantum dots". In: *Nanoscale Research Letters* 7 (2012).
- [86] Anthony R Smith, Woojun Yoon, William B Heuer, Sophie IM Baril, Janice E Boercker, Joseph G Tischler, and Edward E Foos. "Effect of ligand structure on the optical and electronic properties of nanocrystalline PbSe films". In: *The Journal of Physical Chemistry C* 116.10 (2012), pp. 6031–6037.
- [87] Fan Xu, Luis Felipe Gerlein, Xin Ma, Chelsea R Haughn, Matthew F Doty, and Sylvain G Cloutier. "Impact of different surface ligands on the optical properties of PbS quantum dot solids". In: *Materials* 8.4 (2015), pp. 1858–1870.
- [88] Nikhil R Jana, Latha Gearheart, and Catherine J Murphy. "Seed-mediated growth approach for shape-controlled synthesis of spheroidal and rod-like gold nanoparticles using a surfactant template". In: *Advanced Materials* 13.18 (2001), pp. 1389–1393.
- [89] Xiaohua Huang, Prashant K Jain, Ivan H El-Sayed, and Mostafa A El-Sayed. "Plasmonic photothermal therapy (PPTT) using gold nanoparticles". In: *Lasers in medical science* 23.3 (2008), p. 217.

REFERENCES

- [90] Matthew Rycenga, Claire M Cobley, Jie Zeng, Weiyang Li, Christine H Moran, Qiang Zhang, Dong Qin, and Younan Xia. "Controlling the synthesis and assembly of silver nanostructures for plasmonic applications". In: *Chemical reviews* 111.6 (2011), pp. 3669–3712.
- [91] Claire M Cobley, Sara E Skrabalak, Dean J Campbell, and Younan Xia. "Shape-controlled synthesis of silver nanoparticles for plasmonic and sensing applications". In: *Plasmonics* 4.2 (2009), pp. 171–179.
- [92] Thi My Dung Dang, Thi Tuyet Thu Le, Eric Fribourg-Blanc, and Mau Chien Dang. "Synthesis and optical properties of copper nanoparticles prepared by a chemical reduction method". In: *Advances in Natural Sciences: Nanoscience and Nanotechnology* 2.1 (2011), p. 015009.
- [93] George H Chan, Jing Zhao, Erin M Hicks, George C Schatz, and Richard P Van Duyne. "Plasmonic properties of copper nanoparticles fabricated by nanosphere lithography". In: *Nano Letters* 7.7 (2007), pp. 1947–1952.
- [94] Mark W Knight, Nicholas S King, Lifei Liu, Henry O Everitt, Peter Nordlander, and Naomi J Halas. "Aluminum for plasmonics". In: *ACS nano* 8.1 (2013), pp. 834–840.
- [95] Xianmao Lu, Matthew Rycenga, Sara E Skrabalak, Benjamin Wiley, and Younan Xia. "Chemical synthesis of novel plasmonic nanoparticles". In: *Annual review of physical chemistry* 60 (2009), pp. 167–192.
- [96] Asta Šileikaitė, Igoris Prosyčėvas, Judita Puišo, Algimantas Juraitis, and Asta Guobienė. "Analysis of silver nanoparticles produced by chemical reduction of silver salt solution". In: *Mater. Sci* 12.4 (2006), pp. 1392–1320.
- [97] Maribel G Guzmán, Jean Dille, and Stephan Godet. "Synthesis of silver nanoparticles by chemical reduction method and their antibacterial activity". In: *Int J Chem Biomol Eng* 2.3 (2009), pp. 104–111.
- [98] Michael J McClain, Andrea E Schlather, Emilie Ringe, Nicholas S King, Lifei Liu, Alejandro Manjavacas, Mark W Knight, Ish Kumar, Kenton H Whitmire, Henry O Everitt, et al. "Aluminum nanocrystals". In: *Nano letters* 15.4 (2015), pp. 2751–2755.
- [99] Nilanjali Misra, Virendra Kumar, Lalit Borde, and Lalit Varshney. "Localized surface plasmon resonance-optical sensors based on radiolytically synthesized silver nanoparticles for estimation of uric acid". In: *Sensors and Actuators B: Chemical* 178 (2013), pp. 371–378.

REFERENCES

- [100] Carmen M Doudna, Massimo F Bertino, Frank D Blum, Akira T Tokuhira, Debdutta Lahiri-Dey, Soma Chattopadhyay, and Jeff Terry. "Radiolytic synthesis of bimetallic Ag- Pt nanoparticles with a high aspect ratio". In: *The Journal of Physical Chemistry B* 107.13 (2003), pp. 2966–2970.
- [101] Yoshio Kobayashi, Miguel A Correa-Duarte, and Luis M Liz-Marzán. "Sol- gel processing of silica-coated gold nanoparticles". In: *Langmuir* 17.20 (2001), pp. 6375–6379.
- [102] Mauro Epifani, Cinzia Giannini, Leander Tapfer, and Lorenzo Vasanelli. "Sol-gel synthesis and characterization of Ag and Au nanoparticles in SiO₂, TiO₂, and ZrO₂ thin films". In: *Journal of the American Ceramic Society* 83.10 (2000), pp. 2385–2393.
- [103] Babak Nikoobakht and Mostafa A El-Sayed. "Preparation and growth mechanism of gold nanorods (NRs) using seed-mediated growth method". In: *Chemistry of Materials* 15.10 (2003), pp. 1957–1962.
- [104] Jiale Huang, Qingbiao Li, Daohua Sun, Yinghua Lu, Yuanbo Su, Xin Yang, Huixuan Wang, Yuanpeng Wang, Wenyao Shao, Ning He, et al. "Biosynthesis of silver and gold nanoparticles by novel sundried *Cinnamomum camphora* leaf". In: *Nanotechnology* 18.10 (2007), p. 105104.
- [105] Rajesh Ramanathan, Anthony P O'ÁZMullane, Rasesh Y Parikh, Peter M Smooker, Suresh K Bhargava, and Vipul Bansal. "Bacterial kinetics-controlled shape-directed biosynthesis of silver nanoplates using *Morganella psychrotolerans*". In: *Langmuir* 27.2 (2010), pp. 714–719.
- [106] Yong Wang, Jian Feng Wong, Xiaowei Teng, Xue Zhang Lin, and Hong Yang. "Pulling nanoparticles into water: phase transfer of oleic acid stabilized monodisperse nanoparticles into aqueous solutions of α -cyclodextrin". In: *Nano Letters* 3.11 (2003), pp. 1555–1559.
- [107] Nancy Ortiz and Sara E Skrabalak. "On the dual roles of ligands in the synthesis of colloidal metal nanostructures". In: *Langmuir* 30.23 (2014), pp. 6649–6659.
- [108] Hendrik Christoffel Hulst and Hendrik C van de Hulst. *Light scattering by small particles*. Courier Corporation, 1981.
- [109] Qiang Fu and Wenbo Sun. "Mie theory for light scattering by a spherical particle in an absorbing medium". In: *Applied Optics* 40.9 (2001), pp. 1354–1361.

REFERENCES

- [110] M Futamata, Y Maruyama, and M Ishikawa. "Local electric field and scattering cross section of Ag nanoparticles under surface plasmon resonance by finite difference time domain method". In: *The Journal of Physical Chemistry B* 107.31 (2003), pp. 7607–7617.
- [111] Weihai Ni, Xiaoshan Kou, Zhi Yang, and Jianfang Wang. "Tailoring longitudinal surface plasmon wavelengths, scattering and absorption cross sections of gold nanorods". In: *Acs Nano* 2.4 (2008), pp. 677–686.
- [112] Bruce T Draine and Piotr J Flatau. "Discrete-dipole approximation for scattering calculations". In: *JOSA A* 11.4 (1994), pp. 1491–1499.
- [113] J-M Jin and Valdis V Liepa. "Application of hybrid finite element method to electromagnetic scattering from coated cylinders". In: *IEEE transactions on antennas and propagation* 36.1 (1988), pp. 50–54.
- [114] Stefan Alexander Maier. *Plasmonics: fundamentals and applications*. Springer Science & Business Media, 2007.
- [115] Gustav Mie. "Beiträge zur Optik trüber Medien, speziell kolloidaler Metallösungen". In: *Annalen der physik* 330.3 (1908), pp. 377–445.
- [116] Craig F Bohren and Donald R Huffman. *Absorption and scattering of light by small particles*. John Wiley & Sons, 2008.

Chapter 3

Energy Harvesting Devices

Colloidal nanomaterials have potential applications in light emission [1, 2, 3], biological sensing [4, 5, 6, 7], communication [8, 9, 10, 11], information and computing technology [12, 13, 14, 15], and energy harvesting and storage [16, 17, 18]. Over the past decade, there has been a lot of interest in employing colloidal nanomaterials such as colloidal quantum dots and plasmonic nanoparticles in energy harvesting devices such as photovoltaics [16, 19], photodetectors [20, 21] and photocatalytic systems [22, 23].

3.1 Photovoltaics

Solar cells are two-terminal optoelectronic devices that convert solar energy to electricity via the photovoltaic effect. The emission spectrum of the sun is broad and spans different ranges of the electromagnetic spectrum. Figure 3.1 plots the AM 1.5 G standard solar illumination spectrum [24]. The AM 1.5 G is the standard spectrum employed for all testing and rating of terrestrial solar cell devices with an integrated power of 1000 W/m^2 (or 100 mW/cm^2).

Peaking in the visible portion of the spectrum, the plot shows the solar energy distribution of $\sim 5\%$ in the ultraviolet region, $\sim 45\%$ in the visible region and $\sim 50\%$ in the infrared region. The band gap of silicon, the most ubiquitous absorbing material for solar cells, is indicated in figure 3.1.

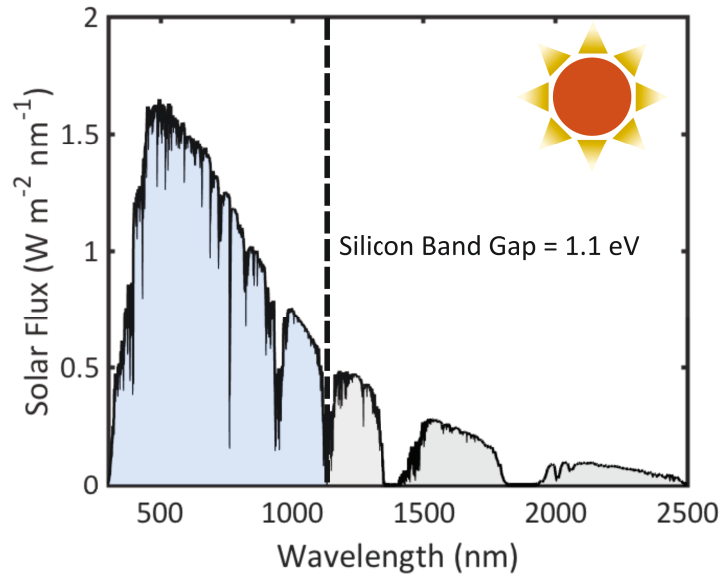


Figure 3.1: The AM1.5 G standard solar spectral flux as a function of wavelength. The dotted line indicates the band gap of crystalline silicon. .

The blue shaded region under the curve is absorbed by the silicon material and subsequently converted to electricity, whereas the gray shaded region is unabsorbed.

To calculate the maximum theoretical efficiency of a solar cell (from a single p-n junction), the Shockley-Queisser limit or detailed balanced limit is employed.[25] The theory utilizes fundamental thermodynamic principles in assessing solar cell device performance. For a single junction solar cell device, a later study identifies both the optimal band gap of the absorbing material (1.34 eV or 930 nm) and the highest attainable efficiency (33.7%).[26] These results were calculated from a few parameters including the temperature of

the sun's surface (T_s), the ambient temperature, and the electronic band gap of the semiconductor material. It is important to note that the results based on the detailed balance model is based on a few assumptions namely:

1. Every absorbed photon generates a single electron-hole pair (exciton).
2. No absorption occurs with photons possessing energies less than the band gap of the semiconductor.
3. Radiative recombination is the only recombination process accounted for.
4. Resistive losses are zero.
5. The solar cell temperature is kept at ambient temperature (300K).
6. Incident sunlight is not concentrated ("one" sun case)

At smaller band gap energies, more photons can be absorbed leading to potentially high extracted current, however the realized voltage is low. Conversely, at higher band gap energies, high voltages can be realized, however, fewer photons can be absorbed. This is the current-voltage trade-off that is observed in solar cells. Despite the band gap of silicon falling close to the optimal band gap (1.34 eV) for single junction solar cell devices [25, 26], much of the near infrared region is still underutilized. Using different materials development techniques and architectural optimization schemes, more of the solar spectrum could be efficiently harvested.

3.1.1 Device Theory

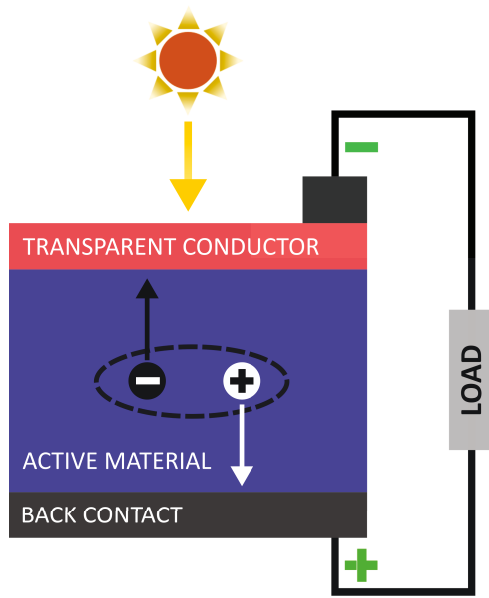


Figure 3.2: Schematic showing the basic solar cell structure composed of an absorbing active (photogenerative) material, front and back contacts, and the connection to an external load.

In its simplest form, a solar cell is composed of a light absorbing medium asymmetrically connected to an external load to do work. Absorption of photons via solar illumination results in the generation of excitons (electron-hole pairs). The charge carriers are then separated and preferentially channeled to different contacts, resulting in a net current.

Fig 3.2 illustrates these basic components of a solar cell structure. The role of the transparent conductor is to allow photons to pass through to the absorbing medium while serving as a collecting contact for one charge carrier type. The role of the back contact, typically a reflective metal, is to reflect unabsorbed light through the medium for a higher probability of absorption while also collecting the other charge carrier type. Charge carrier separation, which can be induced by thermal dissociation for materials with small binding energies or by charge-separating junctions created within the active material, generates a photovoltage (at open circuit) and a photocurrent (at short circuit). Useful work, from the combination of these two parameters, can be extracted via connection to an external load. Ideally, a good solar cell should absorb all incident photons, separate excitons into charge carriers quickly that maintain separate quasi-Fermi distributions

for high photovoltage, and transport charge carriers to collecting electrodes efficiently.

3.1.2 Figures of Merit

The operation of solar cells is typically parametrized by several figures of merit. The short-circuit current, I_{SC} , is the current that flows through a photovoltaic device at zero bias. I_{SC} depends on the generation and collection of charge carriers, and the area-independent short-circuit current density, or J_{SC} , is often employed in its place.

The open-circuit voltage, V_{OC} , is the maximum photovoltage obtained from a solar cell device at zero current. The V_{OC} is largely dependent on the band

gap or absorption edge of the photovoltaic material and can be reduced by recombination processes. The fill factor, FF , is a measure of the "squareness" of the current-voltage curve and is defined as the ratio of the current times the voltage at the maximum power point of operation to $I_{SC} \times V_{OC}$. The power conversion efficiency, PCE , is the ratio of the maximum power generated from the device to the input power from the sun, and is usually calculated as:

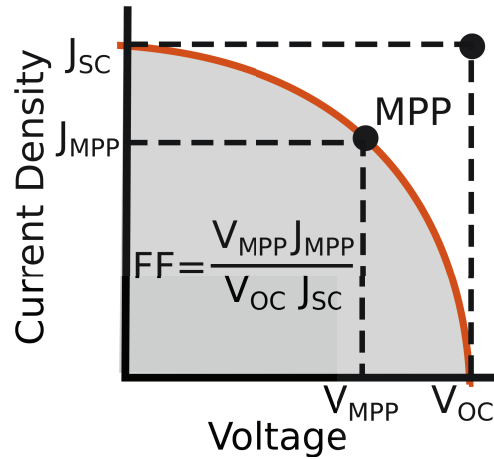


Figure 3.3: Plot showing the current density-voltage characteristic observed in photovoltaic devices. The short-circuit current, open-circuit voltage, and the maximum power point are indicated on the J-V curve.

$$PCE = \frac{J_{SC} \times V_{OC} \times FF}{100 \text{ mW/cm}^2}$$

where 100 mW/cm^2 is the AM1.5G standard terrestrial solar irradiance.

3.1.3 Colloidal Quantum Dot Solar Cells

This subsection is adapted (in part) from Ref. [16]. Reprinted with permission from *Nanophotonics*, Volume 5, Issue 1, Pages 31-54, "Advancing colloidal quantum dot photovoltaic technology," by Y. Cheng, E. S. Arinze, N. Palmquist and S. M. Thon, copyright © 2016.

The search for sustainable and cost-competitive alternatives to fossil fuel-based energy sources has driven developments in solution-processed solar cells. These technologies seek to reduce manufacturing and processing costs as well as improve device efficiencies over traditional and thin-film bulk semiconductor platforms. The low-temperature roll-to-roll production methods, solution-based fabrication techniques and high efficiency potential make materials such as polymers [27, 28, 29], hybrid perovskites [30, 31, 32], and colloidal quantum dots (CQDs) [33, 16] attractive technologies.

3.1.3.1 Motivation

There are several specific motivations for pursuing CQD-based solar cell technology. First, though the true costs of scaling up CQD solar cell manufacturing to the GW power scale are unknown, they are expected to be low and similar to those for organic photovoltaics [34] because of the similarities in materials, synthesis, and growth processes involved in the two technologies. Secondly,

the steady rise in device efficiencies may indicate that CQD films combine the benefits of bulk semiconductors with those of solution-processed molecular materials [35, 36]. Thirdly, CQDs possess unique optical and electrical properties that could potentially be harnessed in strategies for overcoming the single junction Shockley-Queisser efficiency limit [25].

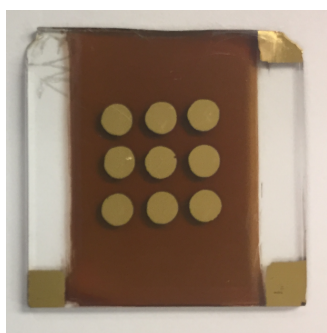


Figure 3.4: Top-view photograph of a 3 x 3 array of PbS CQD photovoltaic cells (full substrate is 1 inch x 1 inch).

This last property is of particular interest for a number of advanced photovoltaic concepts. The band gap tunability of CQD materials creates a pathway through which tandem solar cells can be fabricated using a single materials system, thus eliminating the difficulty of finding a combination of materials with appropriate band gaps and suitable lattice matching for optimized multijunction cells [37, 38, 39]. Solution-based fabrication methods and infrared (IR) responsivity enable CQD films to be effectively combined with other materials in hybrid multijunction devices and serve as IR sensitizers. Lastly, CQDs may have the potential to overcome the Shockley-Queisser limit through multiple-exciton generation (MEG). MEG can occur in semiconductors when a photon of energy greater than twice the band gap energy is absorbed, resulting in the generation of multiple charge carriers per single photon absorbed through impact ionization. MEG rates are predicted to be higher in CQDs than in traditional bulk semiconductors due to the discretization of the CQD energy spectrum [40, 41]. Figure 3.4 shows a CQD solar cell array in which the PbS CQD film was

spin-cast using a layer-by-layer deposition process to build up a thick film.

3.1.3.2 Device Architecture

Early photovoltaic devices that used CQDs as the absorbing layer employed a Schottky or metal-semiconductor junction for operation [42]. They relied primarily on the difference in work functions between the transparent conductive oxide (TCO), and the top metal electrode to generate a built-in field and promote the flow of a photocurrent across the absorbing medium. This absorbing medium was initially a polymer-CQD composite layer; however, after further studies on the electronic impact of the polymer [43], the composite was replaced with a pure CQD layer. Figure 3.5a shows the structure of a CQD Schottky junction solar cell. The CQD Schottky architecture has several advantages, such as functional simplicity and ease of fabrication, and has achieved PCEs exceeding 5% [44]. The major drawback of this architecture is Fermi level pinning at the rectifying junction which limits the V_{OC} to well under the band gap of the material [45, 46].

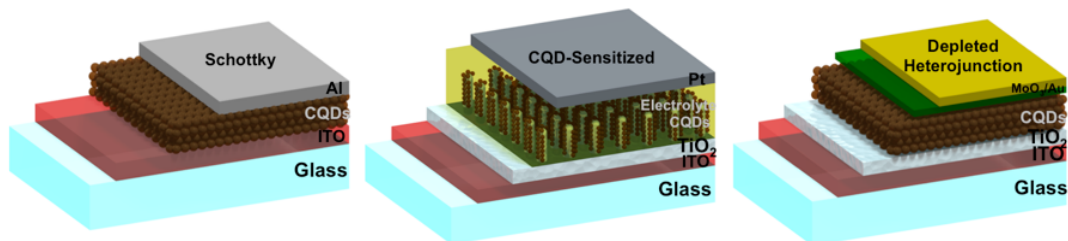


Figure 3.5: CQD photovoltaics device architectures. Schematics of different CQD solar cell architectures employing: (a) a Schottky junction, (b) CQDs as sensitizers, (c) a Depleted Heterojunction.[16]

The infrared sensitivity and high absorptivity of CQDs makes them attractive materials for use as sensitizers in electrochemical solar cell architectures [47, 48]. In these sensitized solar cell (SSC) devices, a monolayer of CQDs coats a porous electron acceptor (usually TiO_2 or ZnO), and hole transport and extraction is provided by an infiltrated electrolyte. Although performances continue to rise in these device architectures, efficient deposition of high-performing pre-synthesized CQDs into the nanoporous electrodes is a challenge. The highest power conversion efficiency to date achieved in a CQD-SSC device is 8.21% [49]. In this study, a novel sequential double layer treatment on the CQD-sensitized photoanode was demonstrated to suppress interfacial recombination while enhancing cell stability.

As a means to overcoming the limitations of the Schottky junction architecture, as well as to combine the merits of the Schottky and CQD-SSC architectures, the depleted heterojunction (DH) CQD solar cell was developed [33]. The DH architecture consists of an n-type electron acceptor forming a heterojunction with a p-type CQD film. The highest certified power conversion efficiency to date of $\sim 13\%$ has been achieved in a modified depleted heterojunction architecture incorporating some halide-based ligand treatment strategies in the CQD films [54, 50, 51]. This performance value is compared

Technology	Efficiency (%)
CQD [50]	13.43%
Perovskite [51]	23.3%
Dye-sensitized [52]	11.9%
Organic [51]	12.6%
Crystalline Si* [53]	26.1%
GaAs* [51]	27.8%

Table 3.1: Current record efficiencies for solar cell technologies. (*Single crystal, single junction and non-concentrating systems)

to other solution processed solar cells as well as traditional photovoltaic technologies, and summarized in Table 3.1

3.1.4 Multijunction Solar Cells

Multijunction solar cells, devices composed of multiple single junction cells, are able to overcome the Shockley-Queisser limit. By dividing up the solar spectrum into spectral ranges suitable to separate solar cells, higher efficiencies are able to be realized. This spectral splitting is achieved by stacking the materials with the highest band gap material on top. In a 2-terminal configuration, current matching between component solar cell devices is required for optimal performance.

The intrinsic ability to tune the band gap of colloidal quantum dots via the quantum confinement effect make them a suitable materials system for multijunction applications. In these multijunction systems, the performance limit on the solar cell performance jumps from 33.7% (single-junction) to 42% (tandem) and 49% (triple-junction)[46, 55]. Various studies have demonstrated the practicality of CQDs in these multijunction devices[56, 57, 58, 59, 60, 37].

3.2 Photodetectors

Photodetectors are optoelectronic devices that transduce photons from electromagnetic radiation into electric signals. These devices are present in our day-to-day activities with applications in cameras [61, 62], remote-control [63], medical imaging [64, 65] and optical communication [66, 67]. Solid state

photodetectors possess an absorbing semiconductor material that is responsible for absorbing incident electromagnetic radiation and converting that to electric charge.

3.2.1 Solution-Processed Materials for Photon Detection

Traditionally, photon detection devices are made from single crystalline inorganic semiconductors such as silicon [68, 69] or semiconductor compounds such as III-V compounds [70, 71]. The miniaturization and integration of semiconductor device components into with read-out integrated circuits (ROICs) makes device design more complex and imposes bounds on device size and sensitivity [72, 73]. Additionally, traditional inorganic semiconducting materials are broadband absorbers, and as a result, narrow-band sensing requires the use of filters thus further complicating device architecture.

Over the past decade, solution-processed nanomaterials (such as polymers, hybrid perovskites, colloidal quantum dots and nanowires) are emerging as potential photon detection materials because of their favorable spectral tunability, relative cost, and facile manufacturing and processing techniques [74, 75, 21, 42]. More specifically, the versatility of the fabrication technique makes it possible for relatively easy integration of the active material with read-out integrated circuits [76].

3.2.2 Figures of Merit

There are several figures of merit employed in the performance assessment of photon detection devices. These assessment parameters are not only used

to compare different photodetectors but also in the selection of appropriate photodetectors for specific applications.

Incident electromagnetic energy on a photodetector results in the generation of free carriers and subsequently, the conversion to photocurrent. The *responsivity* (R), used to quantify the amplitude of an induced electrical signal from the detector, is defined as:

$$R = \frac{I_{ph}}{P_{opt}}$$

where I_{ph} is the photoinduced current (A) and P_{opt} is the incident power (W) [77]. The *quantum efficiency* (QE), used to evaluate the probability that an incident photon will be converted to an electrical charge, is defined as:

$$QE = \frac{n_{phq}}{n_p}$$

where n_{phq} is the number of photoinduced charge carriers and n_p is the number of incident photons. The number of incident photons can be defined as the total number of photons incident on the detector (external QE) or the number of incident photons absorbed by the semiconducting material (internal QE).

Another important parameter for accurately determining the sensitivity of a photodetector is *noise*. Types of noise relevant to photodetector operation include Johnson (thermal) noise, shot noise, flicker noise and generation-recombination noise [78]. The *noise current* determines the smallest value of the detectable optical signal. The *noise equivalent power* (NEP) locates the

minimum detectable signal for a photodetector. This incident power, which produces a photocurrent equal to the noise current, is defined as:

$$NEP = \frac{i_n}{R}$$

where i_n is the noise current and R is the responsivity value. However, NEP is dependent on surface area and is not used in direct comparisons between different types of detectors. An area-independent parameter, *specific detectivity* (D^*), is used to evaluate the sensitivity of photodetectors and allows for comparison among detectors [79]. It is defined as:

$$D^* = \frac{\sqrt{A_d B}}{NEP} = \frac{\sqrt{A_d B R}}{i_n}$$

where A_d is the area of the detector (cm^2), B is the electrical bandwidth (Hz), R is the responsivity value (A/W), i_n is the noise current (A), and NEP is the noise equivalent power (W).

3.2.3 Solid State Photodetector Architectures

Semiconductor-based photodetectors are grouped into three main classes based on their primary working principle [80];

- Photoconductors
- Phototransistors
- Photodiodes

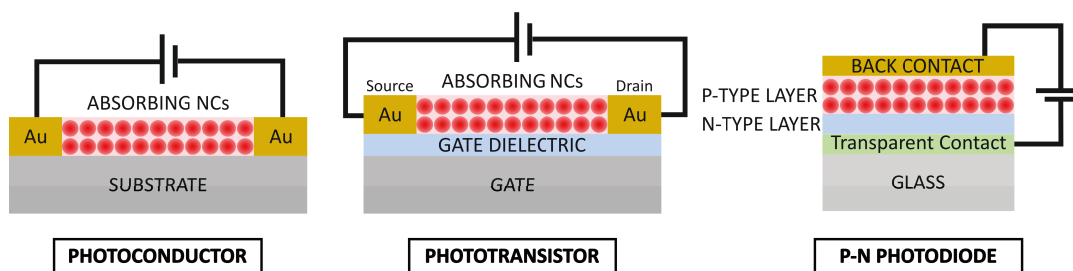


Figure 3.6: Device architecture of solution-processed photodetectors. Schematic of (a) a photoconductor device architecture, (b) a phototransistor device and (c) a p-n junction photodiode device.

Figure 3.6 depicts the three different classes of photodetectors. The *photoconductor* is composed of a semiconducting material and two ohmic metallic contacts thus forming a two-terminal optoelectronic device. Illumination on the device results in the generation of electron-hole pairs and subsequently an increase in conductivity. One charge carrier type is circulated externally through the metal contacts and then recombines with the opposing charge carrier type. This architecture provides photoconductive gain, with a ratio of re-circulated charge carriers to absorbed incident photons of greater than unity.

The *phototransistor* is a three-terminal optoelectronic amplifying switch with a semiconducting channel that can be modulated with the application of a gate or drain bias. To control current flow and amplify electrical signals, this optoelectronic modulation can assist or impede transport of certain charge carrier types. The *photodiode*, on the other hand, relies on a built-in potential provided by a junction to efficiently assist with the extraction of photoinduced carriers. The formed junction can exist between a semiconductor with different doping levels (a p-n homojunction), two different semiconductors (a p-n

heterojunction), or a semiconductor and a rectifying metal contact (a Schottky junction). Photodiode-based photodetectors typically operate in reverse bias, and charge collection efficiency typically depends to some extent on the strength of the bias.

3.3 Photocatalysts

Photocatalysts are increasingly expected to play a significant role in solving some critical problems of the 21st century including energy deficits and environmental pollution. The chemical industry currently uses about 6% of all energy consumed in the United States [81]. Reducing this footprint through the development of more efficient synthetic processes would have far-reaching direct and indirect consequences for the energy landscape, because of the influence of the chemical industry on the fuels and manufacturing sectors.

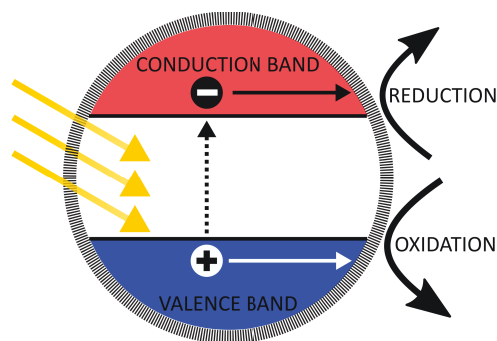
3.3.1 Background

Photocatalysis is of particular interest as a sustainable alternative to conventional methods of organic synthesis. Photochemistry, in which a species in the reaction mixture is promoted to an excited state through the absorption of a photon, is a "green" process which has light as the only energy input and typically outputs no chemical waste by-products. In addition, it can be driven in theory by a variety of inexpensive light sources, including solar radiation.

3.3.2 Traditional Photocatalysts

To drive chemical reactions, semiconducting nanoparticles such as TiO_2 [82, 83], ZnO [84, 85], Fe_2O_3 [86, 87], and WO_3 [88, 89] have been traditionally employed as photocatalysts.

Figure 3.7 shows the basic processes involved in a semiconductor nanoparticle-based photocatalytic cycle. Photon illumination leads to absorption by the semiconductor and subsequently, the promotion of electrons from the valence band to the conduction band (leaving behind holes) within the semiconductor photocatalyst. The next step involves the transport of the charge carriers to the



surface of the nanostructure. Lastly, the electrons and holes react with acceptors (reduction) and donors (oxidation), respectively, within the reaction medium.

Figure 3.7: Schematic illustrating the basic principle of semiconductor nanoparticle-based photocatalytic processes.

The main challenges facing large-scale implementation of photocatalytic synthesis are poor light utilization efficiency and the reliance on rare and expensive catalyst materials. The most common and efficient photocatalysts, due to their wide band gaps, only absorb ultraviolet (UV) photons, limiting the spectral utilization to costly and high energy sources. Previous solutions to this problem have focused on either the development of new photocatalytic materials, such as those based on rare transition metal complexes which can

absorb visible light directly [90], or sensitization with noble metal plasmonic materials which can absorb visible radiation and transfer hot electrons to the semiconducting nanoparticle [91].

3.3.3 Sensitized Plasmonic Photocatalysis

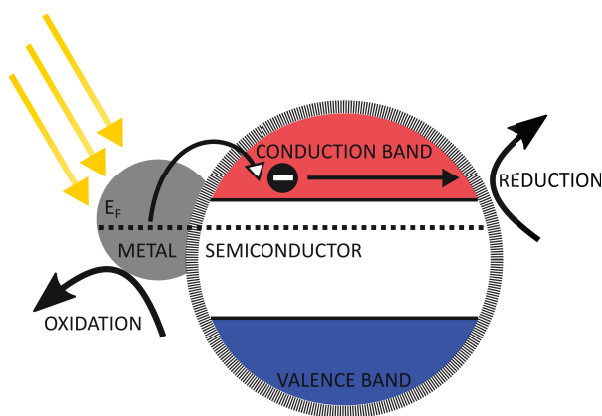


Figure 3.8: Schematic illustrating the basic principle of a plasmonically enhanced photocatalytic system.

Sensitized plasmonic photocatalytic systems, typically composed of a metal nanoparticle that acts as a "sensitizer" for a semiconducting nanostructure, are emerging as promising systems for highly efficient photocatalysis. Figure 3.8 shows the basic processes involved in a plasmonically enhanced photocatalytic system. Upon excitation

of the LSPR of the metal nanoparticles, energetic 'hot' electrons are generated at the plasmon resonance, which is usually designed to occur in a portion of the electromagnetic spectrum where the semiconductor otherwise would not absorb (i.e. below the semiconductor band gap). These hot electrons are then able to cross the Schottky barrier created at the metal-semiconductor interface. Consequently, the semiconductor gains high energy electrons in its conduction band leading to improved photocatalytic activity stemming from utilization of the otherwise unabsorbed visible or near-infrared region of the

electromagnetic spectrum.

Development of scalable photocatalysts requires identifying or designing plasmonic materials that can be used to effectively harness radiation in the visible and near infrared regions of the solar spectrum, but must also utilize materials that have a large natural abundance. Indeed, many photocatalysts developed for chemical reductions rely on rare elements such as noble/precious metals (gold, silver, platinum) and transition metals (e.g. ruthenium), and thus are limited by raw material supply.

Taking advantage of their high natural abundance, low toxicity, and spectral tunability for sustainable implementation, the development and characterization of aluminum-based materials for plasmonically enhanced photocatalytic reductions will be described in Chapter 6 of this thesis.

References

- [1] Yasuhiro Shirasaki, Geoffrey J Supran, Mounqi G Bawendi, and Vladimir Bulović. “Emergence of colloidal quantum-dot light-emitting technologies”. In: *Nature Photonics* 7.1 (2013), p. 13.
- [2] Xingliang Dai, Zhenxing Zhang, Yizheng Jin, Yuan Niu, Hujia Cao, Xiaoyong Liang, Liwei Chen, Jianpu Wang, and Xiaogang Peng. “Solution-processed, high-performance light-emitting diodes based on quantum dots”. In: *Nature* 515.7525 (2014), p. 96.
- [3] Xingliang Dai, Yunzhou Deng, Xiaogang Peng, and Yizheng Jin. “Quantum-Dot Light-Emitting Diodes for Large-Area Displays: Towards the Dawn of Commercialization”. In: *Advanced materials* 29.14 (2017), p. 1607022.
- [4] Yucheng Wang, Rui Hu, Guimiao Lin, Indrajit Roy, and Ken-Tye Yong. “Functionalized quantum dots for biosensing and bioimaging and concerns on toxicity”. In: *ACS applied materials & interfaces* 5.8 (2013), pp. 2786–2799.
- [5] IV Martynenko, AP Litvin, F Purcell-Milton, AV Baranov, AV Fedorov, and YK Gun’ko. “Application of semiconductor quantum dots in bioimaging and biosensing”. In: *Journal of Materials Chemistry B* 5.33 (2017), pp. 6701–6727.
- [6] Jeffrey N Anker, W Paige Hall, Olga Lyandres, Nilam C Shah, Jing Zhao, and Richard P Van Duyne. “Biosensing with plasmonic nanosensors”. In: *Nanoscience And Technology: A Collection of Reviews from Nature Journals*. World Scientific, 2010, pp. 308–319.
- [7] Xiaoling Wu, Changlong Hao, Jatish Kumar, Hua Kuang, Nicholas A Kotov, Luis M Liz-Marzán, and Chuanlai Xu. “Environmentally responsive plasmonic nanoassemblies for biosensing”. In: *Chemical Society Reviews* (2018).

REFERENCES

- [8] P Michler, A Kiraz, C Becher, WV Schoenfeld, PM Petroff, Lidong Zhang, E Hu, and A Imamoglu. "A quantum dot single-photon turnstile device". In: *science* 290.5500 (2000), pp. 2282–2285.
- [9] A Vardi, N Akopian, G Bahir, L Doyennette, M Tchernycheva, L Nevou, FH Julien, F Guillot, and E Monroy. "Room temperature demonstration of Ga N/ Al N quantum dot intraband infrared photodetector at fiber-optics communication wavelength". In: *Applied physics letters* 88.14 (2006), p. 143101.
- [10] Holger Schmeckeber and Dieter Bimberg. "Quantum-dot semiconductor optical amplifiers for energy-efficient optical communication". In: *Green Photonics and Electronics*. Springer, 2017, pp. 37–74.
- [11] Josep Miquel Jornet and Ian F Akyildiz. "Graphene-based plasmonic nano-antenna for terahertz band communication in nanonetworks". In: *IEEE Journal on selected areas in communications* 31.12 (2013), pp. 685–694.
- [12] Ji-Hyuk Choi, Han Wang, Soong Ju Oh, Taejong Paik, Pil Sung, Jinwoo Sung, Xingchen Ye, Tianshuo Zhao, Benjamin T Diroll, Christopher B Murray, et al. "Exploiting the colloidal nanocrystal library to construct electronic devices". In: *Science* 352.6282 (2016), pp. 205–208.
- [13] Daniel Loss and David P DiVincenzo. "Quantum computation with quantum dots". In: *Physical Review A* 57.1 (1998), p. 120.
- [14] Yan Wang, Ziyu Lv, Jinrui Chen, Zhanpeng Wang, Ye Zhou, Li Zhou, Xiaoli Chen, and Su-Ting Han. "Photonic Synapses Based on Inorganic Perovskite Quantum Dots for Neuromorphic Computing". In: *Advanced Materials* (2018), p. 1802883.
- [15] Tengfeng Zhu, Yihan Zhou, Yijie Lou, Hui Ye, Min Qiu, Zhichao Ruan, and Shanhui Fan. "Plasmonic computing of spatial differentiation". In: *Nature communications* 8 (2017), p. 15391.
- [16] Yan Cheng, Ebuka S Arinze, Nathan Palmquist, and Susanna M Thon. "Advancing colloidal quantum dot photovoltaic technology". In: *Nanophotonics* 5.1 (2016), pp. 31–54.
- [17] Anna Douglas, Rachel Carter, Landon Oakes, Keith Share, Adam P Cohn, and Cary L Pint. "Ultrafine iron pyrite (FeS₂) nanocrystals improve sodium–sulfur and lithium–sulfur conversion reactions for efficient batteries". In: *ACS nano* 9.11 (2015), pp. 11156–11165.

REFERENCES

- [18] Changlong Wang and Didier Astruc. "Nanogold plasmonic photocatalysis for organic synthesis and clean energy conversion". In: *Chemical Society Reviews* 43.20 (2014), pp. 7188–7216.
- [19] Ebuka S Arinze, Botong Qiu, Gabrielle Nyirjesy, and Susanna M Thon. "Plasmonic nanoparticle enhancement of solution-processed solar cells: practical limits and opportunities". In: *ACS Photonics* 3.2 (2016), pp. 158–173.
- [20] F Pelayo García de Arquer, Ardalan Armin, Paul Meredith, and Edward H Sargent. "Solution-processed semiconductors for next-generation photodetectors". In: *Nature Reviews Materials* 2.3 (2017), p. 16100.
- [21] Md Rezaul Hasan, Ebuka S Arinze, Arunima K Singh, Vladimir P Oleshko, Shiqi Guo, Asha Rani, Yan Cheng, Irina Kalish, Mona E Zaghloul, Mulpuri V Rao, et al. "An Antimony Selenide Molecular Ink for Flexible Broadband Photodetectors". In: *Advanced electronic materials* 2.9 (2016), p. 1600182.
- [22] Suljo Linic, Phillip Christopher, and David B Ingram. "Plasmonic-metal nanostructures for efficient conversion of solar to chemical energy". In: *Nature materials* 10.12 (2011), p. 911.
- [23] Kenneth J Smith, Yan Cheng, Ebuka S Arinze, Nicole E Kim, Arthur E Bragg, and Susanna M Thon. "Dynamics of Energy Transfer in Large Plasmonic Aluminum Nanoparticles". In: *ACS Photonics* 5.3 (2017), pp. 805–813.
- [24] ASTM ASTM. *G173: Standard Tables for Reference Solar Spectral Irradiance at Air Mass 1.5: Direct Normal and Hemispherical for a 37 Degree Tilted Surface*. 2008.
- [25] William Shockley and Hans J Queisser. "Detailed balance limit of efficiency of p-n junction solar cells". In: *Journal of applied physics* 32.3 (1961), pp. 510–519.
- [26] Sven Rühle. "Tabulated values of the Shockley–Queisser limit for single junction solar cells". In: *Solar Energy* 130 (2016), pp. 139–147.
- [27] Dieter Wöhrle and Dieter Meissner. "Organic solar cells". In: *Advanced Materials* 3.3 (1991), pp. 129–138.
- [28] Serap Günes, Helmut Neugebauer, and Niyazi Serdar Sariciftci. "Conjugated polymer-based organic solar cells". In: *Chemical reviews* 107.4 (2007), pp. 1324–1338.

REFERENCES

- [29] Harald Hoppe and Niyazi Serdar Sariciftci. "Organic solar cells: An overview". In: *Journal of materials research* 19.7 (2004), pp. 1924–1945.
- [30] Martin A Green, Anita Ho-Baillie, and Henry J Snaith. "The emergence of perovskite solar cells". In: *Nature Photonics* 8.7 (2014), nphoton–2014.
- [31] Huanping Zhou, Qi Chen, Gang Li, Song Luo, Tze-bing Song, Hsin-Sheng Duan, Ziruo Hong, Jingbi You, Yongsheng Liu, and Yang Yang. "Interface engineering of highly efficient perovskite solar cells". In: *Science* 345.6196 (2014), pp. 542–546.
- [32] Mingzhen Liu, Michael B Johnston, and Henry J Snaith. "Efficient planar heterojunction perovskite solar cells by vapour deposition". In: *Nature* 501.7467 (2013), p. 395.
- [33] Andras G Pattantyus-Abraham, Illan J Kramer, Aaron R Barkhouse, Xihua Wang, Gerasimos Konstantatos, Ratan Debnath, Larissa Levina, Ines Raabe, Mohammad K Nazeeruddin, Michael Gratzel, et al. "Depleted-heterojunction colloidal quantum dot solar cells". In: *ACS nano* 4.6 (2010), pp. 3374–3380.
- [34] Joseph Kalowekamo and Erin Baker. "Estimating the manufacturing cost of purely organic solar cells". In: *Solar Energy* 83.8 (2009), pp. 1224–1231.
- [35] Victor I Klimov. "Detailed-balance power conversion limits of nanocrystal-quantum-dot solar cells in the presence of carrier multiplication". In: *Applied Physics Letters* 89.12 (2006), p. 123118.
- [36] Sotirios Baskoutas and Andreas F Terzis. "Size-dependent band gap of colloidal quantum dots". In: *Journal of applied physics* 99.1 (2006), p. 013708.
- [37] Xihua Wang, Ghada I Koleilat, Jiang Tang, Huan Liu, Illan J Kramer, Ratan Debnath, Lukasz Brzozowski, D Aaron R Barkhouse, Larissa Levina, Sjoerd Hoogland, et al. "Tandem colloidal quantum dot solar cells employing a graded recombination layer". In: *Nature Photonics* 5.8 (2011), p. 480.
- [38] Andrew S Brown and Martin A Green. "Detailed balance limit for the series constrained two terminal tandem solar cell". In: *Physica E: Low-dimensional Systems and Nanostructures* 14.1-2 (2002), pp. 96–100.

REFERENCES

- [39] Joshua J Choi, Whitney N Wenger, Rachel S Hoffman, Yee-Fun Lim, Justin Luria, Jacek Jasieniak, John A Marohn, and Tobias Hanrath. "Solution-Processed Nanocrystal Quantum Dot Tandem Solar Cells". In: *Advanced Materials* 23.28 (2011), pp. 3144–3148.
- [40] Randy J Ellingson, Matthew C Beard, Justin C Johnson, Pingrong Yu, Olga I Micic, Arthur J Nozik, Andrew Shabaev, and Alexander L Efros. "Highly efficient multiple exciton generation in colloidal PbSe and PbS quantum dots". In: *Nano letters* 5.5 (2005), pp. 865–871.
- [41] Arthur J Nozik. "Multiple exciton generation in semiconductor quantum dots". In: *Chemical Physics Letters* 457.1-3 (2008), pp. 3–11.
- [42] Steven A McDonald, Gerasimos Konstantatos, Shiguo Zhang, Paul W Cyr, Ethan JD Klem, Larissa Levina, and Edward H Sargent. "Solution-processed PbS quantum dot infrared photodetectors and photovoltaics". In: *Nature materials* 4.2 (2005), p. 138.
- [43] Ahmed Maria, Paul W Cyr, Ethan JD Klem, Larissa Levina, and Edward H Sargent. "Solution-processed infrared photovoltaic devices with > 10% monochromatic internal quantum efficiency". In: *Applied Physics Letters* 87.21 (2005), p. 213112.
- [44] Claudia Piliago, Loredana Protesescu, Satria Zulkarnaen Bisri, Maksym V Kovalenko, and Maria Antonietta Loi. "5.2% efficient PbS nanocrystal Schottky solar cells". In: *Energy & Environmental Science* 6.10 (2013), pp. 3054–3059.
- [45] Jenny Nelson. *The physics of solar cells*. World Scientific Publishing Company, 2003.
- [46] Charles H Henry. "Limiting efficiencies of ideal single and multiple energy gap terrestrial solar cells". In: *Journal of applied physics* 51.8 (1980), pp. 4494–4500.
- [47] Neil C Greenham, Xiaogang Peng, and A Paul Alivisatos. "Charge separation and transport in conjugated-polymer/semiconductor-nanocrystal composites studied by photoluminescence quenching and photoconductivity". In: *Physical review B* 54.24 (1996), p. 17628.
- [48] Wendy U Huynh, Janke J Dittmer, and A Paul Alivisatos. "Hybrid nanorod-polymer solar cells". In: *science* 295.5564 (2002), pp. 2425–2427.

REFERENCES

- [49] Ke Zhao, Zhenxiao Pan, Iva An Mora-Sero, Enrique Callejas, Hai Wang, Ya Song, Xueqing Gong, Jin Wang, Mischa Bonn, Juan Bisquert, et al. "Boosting power conversion efficiencies of quantum-dot-sensitized solar cells beyond 8% by recombination control". In: *Journal of the American Chemical Society* 137.16 (2015), pp. 5602–5609.
- [50] Erin M Sanehira, Ashley R Marshall, Jeffrey A Christians, Steven P Harvey, Peter N Ciesielski, Lance M Wheeler, Philip Schulz, Lih Y Lin, Matthew C Beard, and Joseph M Luther. "Enhanced mobility CsPbI₃ quantum dot arrays for record-efficiency, high-voltage photovoltaic cells". In: *Science advances* 3.10 (2017), eaao4204.
- [51] 2018. URL: <https://www.nrel.gov/pv/assets/images/efficiency-chart.png>.
- [52] R Komiya, A Fukui, N Murofushi, N Koide, R Yamanaka, and H Katayama. "Improvement of the conversion efficiency of a monolithic type dye-sensitized solar cell module". In: *Technical Digest of the 21st International Photovoltaic Science and Engineering Conference, 2C-5O-08, Fukuoka, Japan*. 2011.
- [53] Felix Haase, Christina Hollemann, Sören Schäfer, Agnes Merkle, Michael Rienäcker, Jan Krügener, Rolf Brendel, and Robby Peibst. "Laser contact openings for local poly-Si-metal contacts enabling 26.1%-efficient POLO-IBC solar cells". In: *Solar Energy Materials and Solar Cells* 186 (2018), pp. 184–193.
- [54] Mengxia Liu, Oleksandr Voznyy, Randy Sabatini, F Pelayo García de Arquer, Rahim Munir, Ahmed Hesham Balawi, Xinzheng Lan, Fengjia Fan, Grant Walters, Ahmad R Kirmani, et al. "Hybrid organic-inorganic inks flatten the energy landscape in colloidal quantum dot solids". In: *Nature materials* 16.2 (2017), p. 258.
- [55] Edward H Sargent. "Infrared photovoltaics made by solution processing". In: *Nature Photonics* 3.6 (2009), p. 325.
- [56] Zhenyu Jiang, Guanjun You, Li Wang, Jie Liu, Wenjia Hu, Yu Zhang, and Jian Xu. "Solution-processed high-performance colloidal quantum dot tandem photodetectors on flexible substrates". In: *Journal of Applied Physics* 116.8 (2014), p. 084303.

REFERENCES

- [57] Zhenyu Jiang, Wenjia Hu, Chen Mo, Yan Liu, Wenjun Zhang, Guanjun You, Li Wang, Mahmoud RM Atalla, Yu Zhang, Jie Liu, et al. "Ultra-sensitive tandem colloidal quantum-dot photodetectors". In: *Nanoscale* 7.39 (2015), pp. 16195–16199.
- [58] Havid Aqoma, Randi Azmi, Seung-Hwan Oh, and Sung-Yeon Jang. "Solution-processed colloidal quantum dot/organic hybrid tandem photovoltaic devices with 8.3% efficiency". In: *Nano energy* 31 (2017), pp. 403–409.
- [59] Arfa Karani, Le Yang, Sai Bai, Moritz H Futscher, Henry J Snaith, Bruno Ehrler, Neil C Greenham, and Dawei Di. "Perovskite/Colloidal Quantum Dot Tandem Solar Cells: Theoretical Modeling and Monolithic Structure". In: *ACS Energy Letters* 3.4 (2018), pp. 869–874.
- [60] Yu Bi, Santanu Pradhan, Mehmet Zafer Akgul, Shuchi Gupta, Alexandros Stavrinadis, Jianjun Wang, and Gerasimos Konstantatos. "Colloidal Quantum Dot Tandem Solar Cells Using Chemical Vapor Deposited Graphene as an Atomically Thin Intermediate Recombination Layer". In: *ACS Energy Letters* 3.7 (2018), pp. 1753–1759.
- [61] Albrecht Poglitsch, Christoffel Waelkens, Norbert Geis, Helmut Feuchter, Bart Vandenbussche, Louis Rodriguez, Oliver Krause, Etienne Renotte, Christiaan Van Hoof, P Saraceno, et al. "The photodetector array camera and spectrometer (PACS) on the Herschel space observatory". In: *Astronomy & astrophysics* 518 (2010), p. L2.
- [62] Eric R Fossum. "CMOS image sensors: Electronic camera-on-a-chip". In: *IEEE transactions on electron devices* 44.10 (1997), pp. 1689–1698.
- [63] O Kelly and I Nemhauser. "Techniques for using the position sensitivity of silicon photodetectors to provide remote machine control". In: *Soviet Journal of Quantum Electronics* 4.9 (1975), p. 1072.
- [64] D Cavouras, I Kandarakis, A Bakas, D Triantis, CD Nomicos, and GS Panayiotakis. "An experimental method to determine the effective luminescence efficiency of scintillator-photodetector combinations used in X-ray medical imaging systems." In: *the british journal of radiology* 71.847 (1998), pp. 766–772.
- [65] Tiziano Agostinelli, M Campoy-Quiles, JC Blakesley, R Speller, DDC Bradley, and J Nelson. "A polymer/fullerene based photodetector with extremely low dark current for x-ray medical imaging applications". In: *Applied Physics Letters* 93.20 (2008), p. 419.

REFERENCES

- [66] Andreas Pospischil, Markus Humer, Marco M Furchi, Dominic Bachmann, Romain Guider, Thomas Fromherz, and Thomas Mueller. “CMOS-compatible graphene photodetector covering all optical communication bands”. In: *Nature Photonics* 7.11 (2013), p. 892.
- [67] Hans Melchior, Mahlon B Fisher, and Frank R Arams. “Photodetectors for optical communication systems”. In: *Proceedings of the IEEE* 58.10 (1970), pp. 1466–1486.
- [68] Rudolph H Dyck and Gene P Weckler. “Integrated arrays of silicon photodetectors for image sensing”. In: *IEEE Transactions on Electron Devices* 15.4 (1968), pp. 196–201.
- [69] Matthew K Emsley, Olufemi Dosunmu, and M Selim Unlu. “High-speed resonant-cavity-enhanced silicon photodetectors on reflecting silicon-on-insulator substrates”. In: *IEEE Photonics Technology Letters* 14.4 (2002), pp. 519–521.
- [70] SR Forrest, M DiDomenico Jr, RG Smith, and HJ Stocker. “Evidence for tunneling in reverse-biased III-V photodetector diodes”. In: *Applied Physics Letters* 36.7 (1980), pp. 580–582.
- [71] Robert J Deri. “Monolithic integration of optical waveguide circuitry with III-V photodetectors for advanced lightwave receivers”. In: *Journal of lightwave technology* 11.8 (1993), pp. 1296–1313.
- [72] Tomoyuki Suzuki. “Challenges of image-sensor development”. In: *Solid-State Circuits Conference Digest of Technical Papers (ISSCC), 2010 IEEE International*. IEEE. 2010, pp. 27–30.
- [73] Paul S Peercy. “The drive to miniaturization”. In: *Nature* 406.6799 (2000), p. 1023.
- [74] Letian Dou, Yang Micheal Yang, Jingbi You, Ziruo Hong, Wei-Hsuan Chang, Gang Li, and Yang Yang. “Solution-processed hybrid perovskite photodetectors with high detectivity”. In: *Nature communications* 5 (2014), p. 5404.
- [75] Xiong Gong, Minghong Tong, Yangjun Xia, Wanzhu Cai, Ji Sun Moon, Yong Cao, Gang Yu, Chan-Long Shieh, Boo Nilsson, and Alan J Heeger. “High-detectivity polymer photodetectors with spectral response from 300 nm to 1450 nm”. In: *Science* 325.5948 (2009), pp. 1665–1667.

REFERENCES

- [76] Ethan JD Klem, Chris Gregory, Dorota Temple, and Jay Lewis. "PbS colloidal quantum dot photodiodes for low-cost SWIR sensing". In: *Infrared Technology and Applications XLI*. Vol. 9451. International Society for Optics and Photonics. 2015, p. 945104.
- [77] Silvano Donati. *Photodetectors*. Vol. 1. Prentice Hall PTR, 1999.
- [78] Eustace L Dereniak and Glenn D Boreman. *Infrared detectors and systems*. Vol. 306. Wiley New York, 1996.
- [79] R Clark Jones. "A method of describing the detectivity of photoconductive cells". In: *Review of Scientific Instruments* 24.11 (1953), pp. 1035–1040.
- [80] Simon M Sze and Kwok K Ng. *Physics of semiconductor devices*. John wiley & sons, 2006.
- [81] R Wells. "Statement for the Record by Rich Wells for the US Congress Select Committee on Energy Independence and Global Warming". In: *Hearing on What's Cooking with Natural Gas in Energy Independence and Global Warming Solutions* (2008).
- [82] Akira Fujishima, Xintong Zhang, and Donald A Tryk. "TiO₂ photocatalysis and related surface phenomena". In: *Surface Science Reports* 63.12 (2008), pp. 515–582.
- [83] Jenny Schneider, Masaya Matsuoka, Masato Takeuchi, Jinlong Zhang, Yu Horiuchi, Masakazu Anpo, and Detlef W Bahnemann. "Understanding TiO₂ photocatalysis: mechanisms and materials". In: *Chemical reviews* 114.19 (2014), pp. 9919–9986.
- [84] SR Morrison and T Freund. "Chemical role of holes and electrons in ZnO photocatalysis". In: *The Journal of chemical physics* 47.4 (1967), pp. 1543–1551.
- [85] Di Li and Hajime Haneda. "Morphologies of zinc oxide particles and their effects on photocatalysis". In: *Chemosphere* 51.2 (2003), pp. 129–137.
- [86] Shao-Wen Cao and Ying-Jie Zhu. "Hierarchically nanostructured α -Fe₂O₃ hollow spheres: preparation, growth mechanism, photocatalytic property, and application in water treatment". In: *The Journal of Physical Chemistry C* 112.16 (2008), pp. 6253–6257.

REFERENCES

- [87] Bruce C Faust, Michael R Hoffmann, and Detlef W Bahnemann. "Photocatalytic oxidation of sulfur dioxide in aqueous suspensions of α -iron oxide (Fe_2O_3)". In: *The Journal of Physical Chemistry* 93.17 (1989), pp. 6371–6381.
- [88] Di Chen and Jinhua Ye. "Hierarchical WO_3 hollow shells: dendrite, sphere, dumbbell, and their photocatalytic properties". In: *Advanced Functional Materials* 18.13 (2008), pp. 1922–1928.
- [89] S-H Baeck, K-S Choi, Thomas F Jaramillo, Galen D Stucky, and Eric W McFarland. "Enhancement of photocatalytic and electrochromic properties of electrochemically fabricated mesoporous WO_3 thin films". In: *Advanced Materials* 15.15 (2003), pp. 1269–1273.
- [90] Tehshik P Yoon, Michael A Ischay, and Juana Du. "Visible light photocatalysis as a greener approach to photochemical synthesis". In: *Nature chemistry* 2.7 (2010), p. 527.
- [91] Cesar Clavero. "Plasmon-induced hot-electron generation at nanoparticle/metal-oxide interfaces for photovoltaic and photocatalytic devices". In: *Nature Photonics* 8.2 (2014), p. 95.

Chapter 4

Engineering Nanostructures for Solution Processed Solar Cells

The search for sustainable and cost-competitive alternatives to fossil fuel-based energy sources has driven developments in solution-processed solar cells. The low-temperature roll-to-roll production methods, solution-based fabrication techniques and high efficiency potential make materials such as polymers [1, 2, 3], hybrid perovskites [4, 5, 6], and colloidal quantum dots (CQDs) [7, 8] attractive technologies.

4.1 Limits of Plasmonic Enhancement in Solution Processed Solar Cells

This section is adapted from Ref. [9]. Reprinted with permission from ACS Photonics 3, no. 2, 158-173, "Plasmonic Nanoparticle Enhancement of Solution-Processed Solar Cells: Practical Limits and Opportunities," by E. S. Arinze, B. Qiu, G. Nyirjesy and S. M. Thon, copyright © 2016.

The search for sustainable and cost-competitive alternatives to fossil fuel-based energy sources has driven developments in solution-processed solar cells. These technologies seek to reduce manufacturing and processing costs as well as improve device efficiencies over traditional and thin-film bulk semiconductor platforms. The low temperature roll-to-roll production methods, solution-based fabrication techniques and high efficiency potential make materials such as polymers, hybrid perovskites, and colloidal quantum dots attractive technologies. However, the electronic transport lengths in most solution-processed materials are smaller than the photon absorption lengths, especially at near infrared wavelengths, due to their nanostructured nature and associated interface-related defects and impurities. This is referred to as the "absorption-extraction compromise" whereby the material thickness required for complete absorption results in incomplete extraction of the photogenerated charge carriers.

Attempts to improve the efficiencies of solution-processed devices have included engineering of the absorbing material,[10, 11, 12, 13] design of new device architectures,[14, 15, 16, 17, 18] and incorporation of light trapping techniques to decrease the effective film absorption lengths.[19, 20, 21, 22, 23, 24] Introducing plasmonic elements, which enhance the interaction of light with matter in metallic structures on the nanoscale, has been of particular interest to the field due to their minimum perturbation of the device structure and successful deployment for related optoelectronic device applications.[25, 26, 27, 27, 28, 29, 30]

Various efforts to introduce plasmonic enhancers into solution-processed

photovoltaic cells have been tested, some of which will be reviewed in the following section. However, absolute photocurrent and power conversion efficiency improvements have been relatively limited thus far, partially due to the difficulty in systematic evaluation of the optimum plasmonic nanoparticle design for integration with specific photovoltaic materials. Here, we provide an overview of the field of embedded plasmonic-enhanced solution processed solar cells. We then develop an analytical model to systematically evaluate the practical potential of plasmonic enhancements in thin film materials. We compare the photocurrent enhancements predicted by our model to simulation and experimental results for three different systems. Finally, we use our model to make specific suggestions for the field moving forward, focusing on the optimum plasmonic nanoparticle material type, material shape, and concentration for realizing maximum potential enhancements for different systems.

4.1.1 Solution Processed Solar Cells

Compared to traditional bulk semiconductors, solution-processed solar cell materials typically have shorter charge transport lengths, stronger exciton binding energies, and larger electronic trap state densities due to the heterogeneity of their structures arising from the low-energy fabrication and processing procedures. Additionally, flexibility in doping of the materials is generally lacking. Therefore, solution-processed solar cell architectures have been designed to engineer around these issues. Taking inspiration from electrochemical cells, most solution-processed photovoltaic devices employ

heterointerfaces, which can be structured to enhance charge separation and collection while minimizing the thickness of the active material.

Initial OPV architectures involving a bilayer donor-acceptor planar heterojunction[31] suffered from the "exciton-diffusion" bottleneck that resulted from the small diffusion lengths.[32, 33, 34, 35, 36] This led to the development of the bulk heterojunction architecture, in which the acceptor and donor phases are blended to form a high interfacial area mixture.[37, 38] This architecture is limited by the ability to optimally distribute charge separation interfaces and facilitate appropriate conduction channels.[39, 40, 41]

The highest-performing CQD photovoltaic devices use a heterojunction architecture in which the CQD medium forms a junction with an n-type wide band gap semiconductor such as TiO₂ or ZnO.[7] Control over the CQD film doping,[42] band alignment,[43] and structuring of the electrodes[10] have led to the development of advanced architectures that utilize multiple CQD film types, although high electronic trap state densities still limit performance.[44]

In the case of perovskite solar cells, sensitizing-type architectures produced most of the initial results in the field. The perovskite material is infiltrated into an electron-extracting[18, 45, 46, 47, 48] or insulating[13, 49, 50] mesoporous layer (usually TiO₂ and Al₂O₃ respectively) and topped with a hole transporting material. With advances in the growth of long-diffusion-length large-domain single crystal perovskites,[51, 52] the field is trending towards more conventional planar cell designs in which the perovskite film is sandwiched between electron- and hole-extracting electrodes.

The limited carrier transport lengths necessitate careful engineering of

solution processed solar cell device architectures in order to maximize absorption and achieve the highest possible efficiencies. This problem is magnified at longer photon wavelengths near the band gap energy where absorption lengths can exceed carrier transport lengths by more than an order of magnitude in OPV and CQD materials, making light trapping a vital component of successful device designs.

4.1.2 Light Trapping for Photovoltaics

As a technique for absorption enhancement, the idea of light trapping in thick and thin optical films has been studied for decades.[53, 54, 55, 56] Conventionally, light trapping employs total internal reflection as the primary confinement mechanism and is achieved through structural manipulation of the device layers. The maximum absorption enhancement factor (Yablonovitch Limit or Lambertian Limit [53, 54, 55]) for conventional thin-film light-trapping strategies is $4n^2 / \sin^2\theta$, where n is the refractive index of the absorbing medium, and θ is the angle of the emission cone in the medium surrounding the cell (also known as the acceptance angle). For normal incidence radiation ($\theta = \pi/2$), this upper limit can be further simplified to $4n^2$.

Recent theoretical work on light trapping has focused on the ultra sub-wavelength regime for optical film thicknesses. On the nanoscale, where light-matter interactions beyond the classical ray optics limit take place, it is theoretically possible to surpass the traditional Lambertian limit over specific wavelength ranges.[48] Using a rigorous electromagnetic approach, Yu et al. developed a statistical temporal coupled-mode theory of light trapping,[57]

demonstrating that the enhancement factor can in theory be increased to $12 \times 4n^2$ over a virtually unlimited spectral bandwidth when optical modes exhibit deep-subwavelength-scale field confinement. Callahan et al. proposed that an elevated local density of optical states (LDOS) for the absorber is the key design element, and they demonstrated several nanostructured solar cell architectures that exceeded the Yablonovitch limit in simulation.[58]

Beyond evaluating the absorption enhancement factor, Schuster et al. proposed a figure of merit called light trapping efficiency (LTE), which is the ratio of the total current gain achieved in a device to the theoretical maximum current gain achievable in an ideal Lambertian scattering system.[59] Using LTE as a metric, they demonstrated that multiple theoretical and experimental photonic structures could be used to approach the enhancement limit.[59] Plasmonic enhancement strategies ideally fall under the category of approaches that can be used exceed the Lambertian limit.

4.1.3 Embedded Plasmonic Enhancers

The collective oscillations of the free electrons at the surface of a conductor are known as surface plasmons. These excitations couple strongly to incident electromagnetic radiation and are able to propagate along a metal-dielectric interface as surface plasmon polaritons. Plasmons can be excited at optical frequencies in materials such as gold and silver. In nanoscale structures, localized surface plasmon resonances (LSPRs) result in strong local field enhancement. This nanophotonic effect can be used to circumvent the traditional diffraction limits, and can result in the scattering of incoming light into guided modes in

a thin film material with embedded plasmonic nanoparticles. Plasmonic elements have been applied in diverse applications such as nanoscale sensing,[60, 61, 62] light emitting diodes,[63, 64, 65] lasers,[66, 67, 68] photon detection,[69] information processing,[70] and photovoltaics.[23, 71, 72, 73, 74, 75]

Embedded plasmonic structures are of particular interest for solution-processed photovoltaic devices, such as those based on organic, hybrid inorganic-organic perovskite, and colloidal quantum dot thin film materials. Several reports study the integration of plasmonic structures into such devices with demonstrated increases in optical absorption.[71, 72, 74, 76] Embedded plasmonic structures within the absorbing medium are of particular interest for solution-processed technologies since the materials growth techniques are uniquely compatible with hybrid inclusions, whereas bulk semiconductor systems must rely on surface-based plasmonic in-couplers or scatterers.[77, 78, 79, 80, 81, 82]

Plasmonic nanostructures can be spatially placed at the top of, within, or at the base of solution-processed devices. Placing the plasmonic nanoparticles within the active layer rather than in or on top of contact or buffer layers has several advantages. Mixing the plasmonic materials into the active layer of the cell can help to reduce reflection losses that occur before the light reaches the active layer and increase wave-guiding within the absorbing medium.[83, 84, 85] Finally, the near-field effects associated with LSPRs can be used to enhance absorption within the active layer if there is a strong spatial-field overlap with the absorbing medium. Embedded plasmonic schemes make use of this strong local field enhancement without significantly disrupting the device

structure as in conventional light trapping designs. While this perspective focuses on embedded nanoparticle plasmonic enhancement strategies, non-embedded plasmonic strategies have been explored in-depth in the field, due to the ease of design and fabrication associated with integrating top- and bottom-device structures without disrupting the active layers. These schemes include placing metallic nanoparticles and nanostructured gratings outside the active layers for light in-coupling and trapping.[86, 87, 88, 89, 90, 91, 92, 93, 94, 95] Symmetric metallic nanostructured gratings, either 1D or 2D nanostructures, can be designed for effective light coupling to surface plasmon polariton (SPP) modes that strongly confine light at the interface, resulting in light concentration or preferential scattering into the active layer.

Examples of these methods include the design and integration of 2D SPP gratings for incident light coupling at the exciton peak wavelength in a CQD optoelectronic device.[95] A peak absorption enhancement factor of 3 was observed at the target wavelength. Additionally, the short-circuit current in the light trapping spectral range (640 nm to 1100 nm) was observed to increase by 41%. In another study for OPVs,[92] a 14.8% improvement in efficiency was observed due to the integration of Ag nanoparticle films at the front electrode for preferential forward scattering into the active layer. In this plasmonic scheme, the Ag nanoparticle film was self-assembled via thermal evaporation and subsequent annealing.

In general, the propensity of plasmonic nanoparticles embedded within the active layer itself to serve as recombination sites for exciton quenching[96] has led to extensive exploration of plasmonic enhancement schemes that

take advantage of scattering and light coupling from the electrode layers. However, the potential for high near-field enhancements from plasmonic particles embedded within the active layer provides motivation for further exploring embedded nanoparticle schemes.

The field of embedded plasmonic enhancement schemes for solution processed solar cells has advanced rapidly in recent years. Plasmonic particles of different shapes and sizes have been studied in organic photovoltaic (OPV), colloidal quantum dot (CQD), and perovskite solar cells. Large photocurrents have been demonstrated, although relative power conversion efficiency (PCE) enhancements have remained under 16% for films with PCE values of over 5%.

Table 4.1 summarizes the progress so far in embedded plasmonic enhancement schemes for solution-processed solar cells. Gold and silver are the most commonly used plasmonic materials, and they have also been combined with oxide cores or shells.[24, 97, 98] The nanoparticles in the summarized studies ranged in size from 5 - 150 nm and were embedded at concentrations of 1 - 15 wt.%. The maximum PCE of 16.3% was achieved in a perovskite solar cell.[98] Maximum PCEs of 7.1% and 6.9% were achieved through plasmonic enhancement in OPVs and CQD solar cells, respectively.[84, 97] Although many potential nanoplasmonic enhancement schemes have been explored,[25, 74, 75, 77, 98, 99, 100, 101, 102, 103, 104, 105] experimental realizations of integrated plasmonic designs have yet to lead to record device efficiencies.[106, 57, 107, 108, 109]

Plasmonic Material (Shape)	Plasmonic Nanoparticle Size (nm)	Plasmonic Nanoparticle Concentration	Max. J_{SC} (mA/cm ²)	J_{SC} Enhancement	Max. PCE (%)	PCE Enhancement
Au (Octahedron)[110]	45	$2 \times 10^{11} \text{cm}^{-3}$	10.22	11.6%	4.24	18.8%
Au (Sphere)[101]	30-40	20% by vol.	10.18	13.7%	4.19	20.4%
Au (Truncated Octahedron)[83]	70	5 wt. %	11.16	8.3%	6.45	11.8%
Ag (Nanocluster)[84]	40	1 wt. %	11.61	7.6%	7.1	12.7%
Au (Sphere)[85]	18	0.5 wt. %	4.8	15.7%	2.17	32.3%
Ag (Sphere)[111]	5-15	1:16 wt. ratio (Ag:P3HT)	8.9	1.1%	3.3	-2.9%
Ag (Truncated Octahedron)[112]	80	15 wt. %	8.7	19.2%	3.2	88.2%
Au (Sphere and Prism)[113]	20 and 60x10	2 wt. %	10.61	18%	4.3	19.4%
Au (Sphere)[114]	30	1 wt. %	15.3	-0.1%	7.02	6.7%
Au-Ag (Popcorn Alloy)[115]	150 ± 50	0.7 wt. % TiO_2	16.46	6.1%	10.3	15.7%
Au-SiO ₂ (Sphere)[116]	80/8 (core/shell)	0.9 wt. %	15.3	13.5%	9.5	13%
Au-TiO ₂ (Sphere)[98]	40/2 (core/shell)	2.2 wt. %	22	8.9%	16.3	12.4%
Au (Sphere)[117]	5	0.3% by vol.	29.45	42.2%	4.5	12.5%
Ag (Hemisphere)[118]	40	33% surface coverage	8.5	19.4%	0.68	58.1%
SiO ₂ -Au (Sphere)[97]	15/60 (core/shell)	$10 \mu\text{m}^{-2}$	24.5	13%	6.9	11%

Table 4.1: Summary of selected plasmonic enhancement demonstrations in OPV, Perovskite, and CQD solar cells.[9]

4.1.3.1 Organic Photovoltaics

Plasmonic particles have been embedded within or between the active layers and selective contacts in OPV devices.[83, 84, 85, 101, 110, 111, 112, 113, 114] Typical OPVs have an active layer that consists of electron-donor and electron-acceptor materials.

One study[84] incorporated chemically-synthesized 40 nm silver nanoclusters into the active layer of a poly[N-9"-hepta-decanyl-2,7-carbazole-alt-5,5-(4',7'-di-2-thienyl-2',1',3'-benzothiadiazole) (PCDTBT): [6,6]-phenyl-C70-butyric acid methyl ester (PC70BM) bulk heterojunction (BHJ) solar cell to improve the efficiency. The nanoclusters exhibited a maximum absorbance peak near 420 nm. A 12.7% improvement in PCE was obtained by optimizing the weight percentage of the nanoclusters in the active layer. This enhancement was mainly due to a 7.6% increase in the short-circuit current density (J_{SC}) and an associated reduction in the cell series resistance.

The addition of 70 nm truncated gold octahedral nanoparticles at optimized concentrations (5 wt.%) to the BHJ active layer in another study[83] resulted in consistent PCE improvements in fabricated devices. Other shapes, including Ag nanoparticles and nanoprisms mixed into the buffer layer of an OPV cell, [113] have also been used to realize wide-band absorption enhancements. Generally, relative PCE improvements on the order of 10% have been demonstrated in plasmonically enhanced OPV devices, mainly due to increases in J_{SC} . Associated compromises in the open-circuit voltage (V_{OC}) and fill factor (FF) are the prime reasons why these systems have been unable to rival the record efficiencies in the field.

4.1.3.2 Perovskite Solar Cells

Embedded plasmonic schemes have been explored only recently in perovskite solar cells, due to the relative novelty of this technology.[24, 98, 115] One demonstration enhanced the PCE of a perovskite solar cell by 12.4% by incorporating 40 nm silver-core nanoparticles with 2 nm TiO₂ shells through a low-temperature processing route.[98] The nanoparticles were added to the mesoporous Al₂O₃ scaffold layer, which was infiltrated with methylammonium lead iodide perovskite material.

Another study in the perovskite material system achieved a relative PCE enhancement of 15.7%.[115] A broadband absorption enhancement was demonstrated through the addition of Au-Ag alloy popcorn-shaped nanoparticles to the device. These nanoparticles were synthesized through a co-reduction of HAuCl₄ and AgNO₃ and had an average size of 150 ± 50 nm. The nanoparticles were embedded in the mesoporous TiO₂ at a concentration of 0.7 wt%.[115]

Higher efficiencies have been achieved in perovskite solar cells compared to OPV devices, and therefore these devices have less to gain from plasmonic enhancement schemes. The high efficiency is due to both substantial absorptivity near the band gap energy and superior charge transport. However, plasmonic enhancements could potentially enable materials savings even in high efficiency systems.

4.1.3.3 Colloidal Quantum Dot Solar Cells

Several different device architectures have been employed to make high-performing CQD solar cells.[119, 97, 120, 121, 122, 116, 123, 124, 117, 118, 125] All consist of close-packed CQD films sandwiched between selective transparent and reflective contacts.[123] Like OPV devices, CQD cells must overcome an absorption-extraction compromise to reach high performance, and several plasmonic enhancement strategies have been deployed to address this compromise.

To enhance the absorption specifically in the infrared regime, a study[97] added 120 nm diameter core-15 nm shell SiO₂-Au core-shell nanoparticles to the active layer of a depleted heterojunction cell. In the lead sulfide (PbS) matrix, the nanoshells exhibit an LSPR peak at 820 nm. An enhancement in infrared photocurrent led to an 11% PCE improvement over a control device. [97]

Absorption enhancements in the active layer of a CQD solar cell have also been achieved by using the near field enhancement associated with small (5 nm-diameter) Au nanoparticles instead of focusing on far-field scattering gains.[117] The study demonstrated evidence of hot-electron transfer directly from the excited metal particles to the PbS semiconductor nanocrystals. The best performing cell had a 12.5% PCE improvement over a non-plasmonic device. [117]

Plasmonic particles can play electronic as well as optical roles in CQD solar cells. One study built an Ag nanoparticle - PbS CQD nano-Schottky junction device by depositing self-assembled 40 nm diameter Ag hemispheres that

covered 33% of the ITO contact.[118] The PCE was enhanced by 58.1% compared to the fabricated control devices, which used a planar silver architecture. The improved performance was attributed to the modified absorption profile due to the enhanced optical field around the nanoparticles. This ensured that carriers were generated close to the metal-semiconductor interface within the depletion region.

Generally, plasmonically enhanced CQD devices have benefited from absorption improvements near the weakly-absorbing quantum dot band gap edge. The overall PCE enhancements have generally been weakened by mild loss in V_{OC} and FF.

4.1.3.4 Summary

The largest relative improvements in all three materials systems were achieved in cells with low starting efficiencies and device absorption.[112, 118] Incorporating plasmonic particles generally increased film absorption, although none of the plasmonically enhanced devices achieved record efficiencies in their respective classes, nor approached the theoretical photocurrent limits based on the photovoltaic material band gaps. Addressing the question of whether the full parameter space has yet to be explored in these systems or if plasmonic enhancement schemes are fundamentally limited in practical devices remains an important research challenge.

4.1.4 Practical Limits of Plasmonic Enhancement

There are several practical obstacles to using plasmonic structures as photocurrent enhancers, which need to be taken into account for plasmonic solar cell design. The biggest barrier is the presence of parasitic absorption in the nanoparticles.[73, 126, 127, 128, 129] Parasitic absorption refers to the loss of photocarriers excited in the metal particles themselves that decay via non-radiative channels to produce heat. This process competes with useful absorption in the photovoltaic material. The relative amount of parasitic absorption vs. useful near- and far-field scattering in the metal can be manipulated to some extent by controlling the size, morphology, material, and placement of the metallic nanoparticles.

Another practical limitation is that embedded plasmonic nanostructures can act as carrier recombination centers in the absorbing medium,[111, 130, 131] often leading to a reduction in device open-circuit voltage as well as current.[132] Including a small insulating barrier in the form of a ligand or dielectric shell around the plasmonic nanostructure can suppress this effect but can also reduce the evanescent spatial field overlap with the photovoltaic absorber, thereby limiting the potential for absorption enhancement.

Other practical issues that arise in plasmonic solar cell design include chemical and physical compatibility of the solvents associated with the plasmonic and photovoltaic materials, and materials costs of the precious metals employed as nanoparticles (primarily gold and silver). Finally, there is the issue of resulting spectral trade-offs. Plasmonic structures have the ability to enhance a spectral regime where there is incomplete absorption in the

photovoltaic material. However, in regimes where absorption is substantially complete, introducing plasmonic structures has the potential to degrade the system. Therefore, it is important to be tactical both in understanding the associated spectra[133, 134] and in choosing the type, size, shape and placement within the device of the plasmonic nanostructures.[135, 136, 137]

4.1.5 Absorption Enhancement Model

Taking into account the practical enhancement limitations described above, it is clear that questions remain about the potential for using plasmonic nanoparticles as enhancers in real photovoltaic systems. Specifically, given a set of photovoltaic and plasmonic nanomaterials of interest, it would be useful to be able to quantitatively evaluate the potential photocurrent enhancement using an intuitive model that takes into account the experimental degrees of freedom present in the system. These parameters include the metal nanoparticle material, size and shape; the thickness and identity of the photovoltaic active layer; and the relative concentration or number density of the embedded plasmonic particles. Adjusting and optimizing these factors experimentally is time- and materials-intensive, given the large parameter space.

We have developed an analytical model that can be used to evaluate the potential absorption enhancement in embedded plasmonic nanoparticle systems over a large parameter space. The results can be translated into potential photocurrent (J_{SC}) enhancement with the assumption of perfect carrier collection. The model determines the effective absorption coefficient and thickness of a photovoltaic film embedded with plasmonic nanoparticles based on the

physical and optical properties of the constituent materials. These calculated effective parameters are in turn, translated to an effective absorption, taking inspiration from effective medium approaches for estimating the optical properties of mixed media.

Effective Medium Approximations (EMAs), such as the Bruggeman Model [138] and the Maxwell-Garnett Theory (MGT)[139], treat a heterogeneous medium as one that is homogeneous by effectively averaging the properties of the individual constituent materials. In the MGT, the model medium is composed of spherical particles embedded in a host material. This theory assumes that the composite material is electrodynamically isotropic and possesses a linear response to incident light. Other assumptions include that the mixture parameters are static (non-parametric), the nanoparticle inclusions are separated by distances that surpass their individual sizes, and the sizes of the inclusions are small in comparison to the wavelength of light in the integrated medium. The Bruggeman model is an extension of the MGT that facilitates the inclusion of polydisperse particles.

Our proposed model is an intuitive extension and approximation of an effective medium theory for a specific system: plasmonically enhanced thin-film photovoltaics. The model makes similar assumptions as the MGT, including the isotropic nature of the materials and the monodispersity of the nanoparticle inclusions, but accounts for the plasmonic response by using simulated nanoparticle scattering and absorption cross-sections.

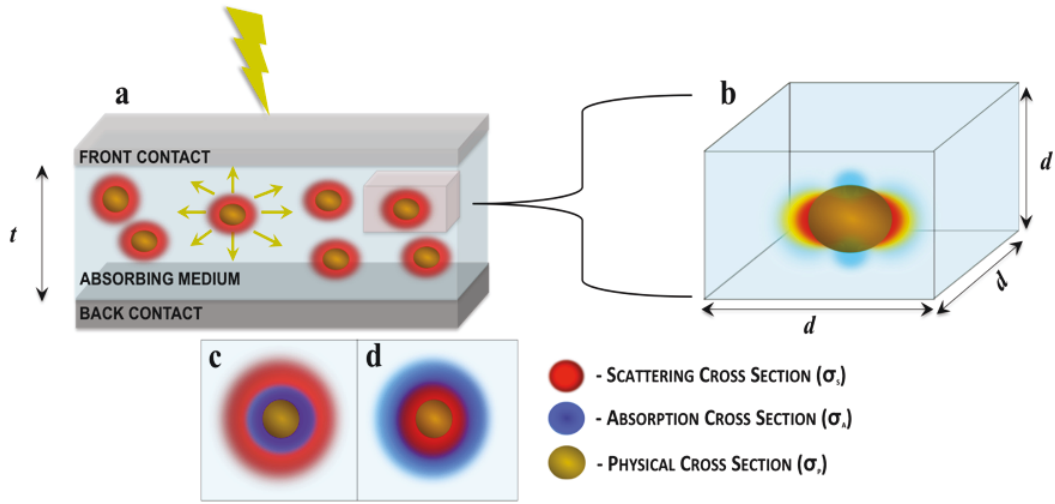


Figure 4.1: (a) Photovoltaic absorbing medium sandwiched between top and bottom contacts with randomly distributed embedded plasmonic nanoparticles. (b) Unit cube with side length d based on the average particle spacing used to evaluate the effect of a single plasmonic nanoparticle on the film. (c) Cross-section of the unit cell illustrating the case where the nanoparticle scattering cross-section exceeds the absorption cross-section. (d) Cross-section of the unit cell illustrating the case where the nanoparticle absorption cross-section exceeds the scattering cross-section.[9]

The model takes as inputs the absorption coefficient, α [m^{-1}], of the photovoltaic material; the photovoltaic film thickness, t [m], along the illumination direction; the physical cross-section, σ_p [m^2]; the scattering cross-section, σ_s [m^2]; and the absorption cross-section, σ_a [m^2] of the embedded plasmonic nanoparticles. The physical cross-section is usually defined as the 2D projection of the physical volume occupied by the nanoparticle. The absorption cross-section quantifies the rate at which energy is removed through absorption from an incident field, and the scattering cross-section quantifies the net power reflected from the nanoparticle. The scattering and absorption cross-sections can be calculated using Mie Theory[140, 141] or numerically

via finite-difference time-domain (FDTD) simulations[142, 143] or finite element methods[144, 145] with the absorbing medium used as the background. Scattering and absorption efficiencies, Q_s and Q_a , are defined as the ratios of the scattering and absorption cross-sections, respectively, to the physical cross-section of the plasmonic nanoparticles ($Q_s = \sigma_s / \sigma_p$; $Q_a = \sigma_a / \sigma_p$). The absorption cross-section, scattering cross-section, absorption efficiency, scattering efficiency and absorption coefficient are all wavelength-dependent in general.

Our model assumes that the nanoparticles are randomly and uniformly distributed within the photovoltaic film with an average number density. We use the concept of a unit cell to represent the concentration (number density), ρ [m^3], of the nanoparticles within the absorbing medium. The unit cell is a cube with one nanoparticle at the center, such that the side length, d [m], is related to the concentration as:

$$\rho = \frac{1}{d^3} \quad (4.1)$$

In addition, we define a unitless variable C to represent the relative separation between the nanoparticles:

$$C = \frac{d}{D} \quad (4.2)$$

where D is the diameter [m] (or length for non-spherical particles) of the nanoparticles. Neglecting reflection at the photovoltaic absorber surface, we use the Beer-Lambert Law[146] to calculate the absorption, A_1 , in the

unmodified photovoltaic film and the absorption, A_2 , in the film with the embedded plasmonic particles:

$$A_1 = 1 - e^{-\alpha t} \quad (4.3)$$

$$A_2 = 1 - e^{-\alpha_{plasmonic} t_{plasmonic}} \quad (4.4)$$

$$\alpha_{plasmonic} = \alpha \left[1 + \frac{\sigma_p}{d^2} (Q_s - Q_a) \right] \quad (4.5)$$

$$t_{plasmonic} = t \sqrt{1 - \frac{\sigma_p}{d^2}} \quad (4.6)$$

Equations 4.5 and 4.6 relate the new effective absorption coefficient ($\alpha_{plasmonic}$) and the new effective film thickness ($t_{plasmonic}$), respectively, to the materials system parameters. In Equation 4.5, $\alpha_{plasmonic}$ represents the effect that a single plasmonic nanoparticle has on the surrounding medium. The MGT uses a cubic lattice of nanoparticles in a medium to approximate the effective dielectric constant by accounting for the volume fraction taken up by the inclusions as well as the relative permittivities of the medium and inclusions. In a similar fashion, we use the plasmonic properties of a single nanoparticle and the optical properties of the medium to approximate the effective absorption coefficient. $\alpha_{plasmonic}$ can be larger or smaller than the absorption coefficient of the bare medium, depending on the relative values of the scattering, absorption and physical cross-sections of the plasmonic nanoparticle inclusions, as well as the number density of the nanoparticles, represented by their average

2D spacing, d^2 . The scattering cross-section effectively adds to the absorptivity of the medium while the absorption cross-section effectively subtracts from the absorptivity of the medium. Also, the physical loss of absorbing medium caused by replacing a fraction of the material with nanoparticles is accounted for in Equation 4.6, which subtracts the projection of the physical area occupied by the nanoparticles from the cross-section of the unit cell.

This model accounts for the parasitic absorption that takes place within the metal nanoparticles, which is a source of photocarrier loss, by subtracting a term proportional to Q_a in the expression for $\alpha_{plasmonic}$. It requires input from numerical electrodynamic simulations in the form of single particle absorption and scattering cross-sections. The total-field scattered-field (TFSF) source method[147] in the FDTD simulations yields an effective scattering cross-section that can account for both the near- and far-field scattering associated with the nanoparticle. Thus both conventional far-field scattering and "local field" effects are incorporated in the model.

Using Equations 4.3-4.6, we can define a quantitative figure of merit, M , which is a measure of the absorption enhancement in the photovoltaic system due to adding the embedded plasmonic nanostructures:

$$M = \frac{A_2}{A_1} - 1 \quad (4.7)$$

By integrating M over all wavelengths, the net absorption enhancement ($M_{total} > 0$) or loss ($M_{total} < 0$) factor can be calculated. Assuming perfect carrier collection (100% internal quantum efficiency, IQE), we can use this model to calculate the expected photocurrent enhancement in a photovoltaic device by

integrating the product of the enhanced (A_2) or control absorptions (A_1), solar photon flux, and the elementary electric charge over all wavelengths.

This model requires only the calculation of the single-particle plasmonic optical properties as a prerequisite for estimating the properties of the bulk mixed media systems over a large range of parameters. This method is computationally fast compared to full numerical modeling of entire film structures with randomly embedded nanoparticles. In the following section, we will use the above model to make realistic predictions for achievable photocurrents in plasmonically enhanced photovoltaic devices and compare the results to previous experimental studies.

4.1.6 Model Evaluation

4.1.6.1 Comparison to Experimental Studies

Previous demonstrations of embedded plasmonic nanoparticle enhancements in organic, hybrid organic-inorganic perovskite and colloidal quantum dot solar cells provide test systems for evaluating our model. We will examine one specific example from each of these three systems to analyze in detail: (1) Silver nanoclusters embedded in a poly [N-9"-hepta-decanyl-2,7-carbazole-alt-5,5-(4',7'-di-2-thienyl-2',1',3'-benzothiadiazole) (PCDTBT): [6,6]-phenyl C-71-butyric acid methyl ester (PC₇₀BM) mixture,[84] (2) Au/Ag alloy popcorn shaped nanoparticles embedded in mesoporous TiO₂ and infiltrated with methylammonium lead iodide (CH₃NH₃PbI₃) perovskite,[115] and (3) SiO₂-Au core-shell nanospheres embedded in a PbS CQD thin film.[97] Absorption coefficients for the three photovoltaic materials were extracted from reported

values in the literature.[97, 148, 149]

We employed FDTD simulations to calculate Q_s and Q_a for single plasmonic nanoparticles in the three examples using the total-field/scattered-field source method.[147, 150, 151, 152, 153] We used the average value of the real part of the refractive index of the three materials over a wavelength range of 300-800 nm for the PCDTBT: PC₇₀BM mixture and CH₃NH₃PbI₃ perovskite material and 300-1200 nm for the PbS CQDs as the background in the simulations. The silver nanoclusters were represented by closely-packed 40 nm diameter nanospheres with spacing extrapolated from Figure 4.3 of Reference [57] and total diameter of 600 nm. The popcorn-shaped Au/Ag nanoparticles were modeled as nanospheres with diameters equal to the reported size of the alloyed particles (150 nm) and refractive indices given by the molar average of the refractive indices of Au and Ag based on the reported weight ratio.[115] The average real part of the refractive index of a PbS CQD film with the first exciton peak at 959 nm was used as the background for the 120 nm SiO₂ core/15 nm Au shell particles.[97]

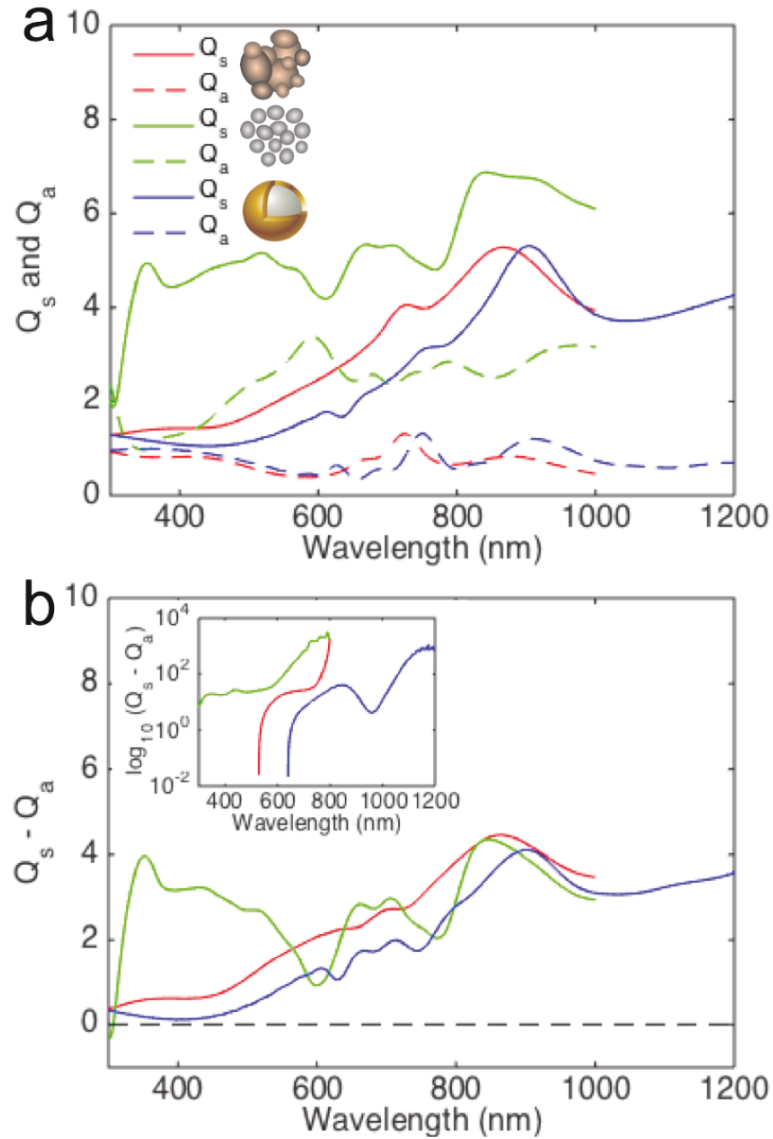


Figure 4.2: (a) Scattering efficiency (Q_s) and absorption efficiency (Q_a) vs. wavelength for the three different plasmonic nanoparticle types calculated using single-particle FDTD simulations. Solid lines: scattering efficiency. Dashed lines: absorption efficiency. Red: 150 nm Au/Ag alloy popcorn nanoparticles embedded in a perovskite-infiltrated-TiO₂ background. Green: 40 nm silver nanoclusters embedded in a PCDTBT:PC70BM mixture. Blue: nanoshells with 120 nm SiO₂ core and 15 nm Au shell thickness embedded in PbS CQD film background. (b) Relative scattering efficiency ($Q_s - Q_a$) vs. wavelength for the systems plotted in (a). Inset: relative scattering efficiency ($Q_s - Q_a$) required to achieve 90% absorption as a function of wavelength the three systems at a relative nanoparticle separation $C = 3$. [9]

Figure 4.2 shows that the relative scattering efficiency ($Q_s - Q_a$) for all three types of plasmonic nanoparticles is positive over most of the relevant wavelength ranges (the absorption of the organic and perovskite materials cuts off near 800 nm). Therefore, these three types of plasmonic nanoparticles are all predicted to be enhancers in their respective absorbing media. The inset in Figure 4.2b shows the relative scattering efficiencies required to achieve 90% absorption in the three systems at relative nanoparticle separations of $C = 3$. The fact that Q_s and Q_a are small compared to C in each study indicates that using single-particle simulations as the basis for calculating the optical properties of the system is a reasonable approximation. This validity condition can be written as:

$$\text{Max}(\sqrt{Q_s}, \sqrt{Q_a}) < C \quad (4.8)$$

Equation 4.8 requires that there is no spatial overlap of the optical influences of adjacent nanoparticles. The number density of the embedded plasmonic particles is an important experimental free parameter. There is an inherent trade-off in an embedded nanoparticle system: increasing the nanoparticle concentration can yield more scattering enhancement of the absorption in the photovoltaic material; however, the nanoparticles occupy physical volume that subtracts from the ability of the photovoltaic material to absorb light. Our model can be used to calculate the optimum nanoparticle density for each of the three test systems given the photovoltaic film thicknesses used in each case (80 nm for the PCDTBT:PC₇₀BM film; 200 nm as an

approximation of the average optical thickness of the perovskite-infiltrated-TiO₂ film; and 400 nm for the PbS CQD film).

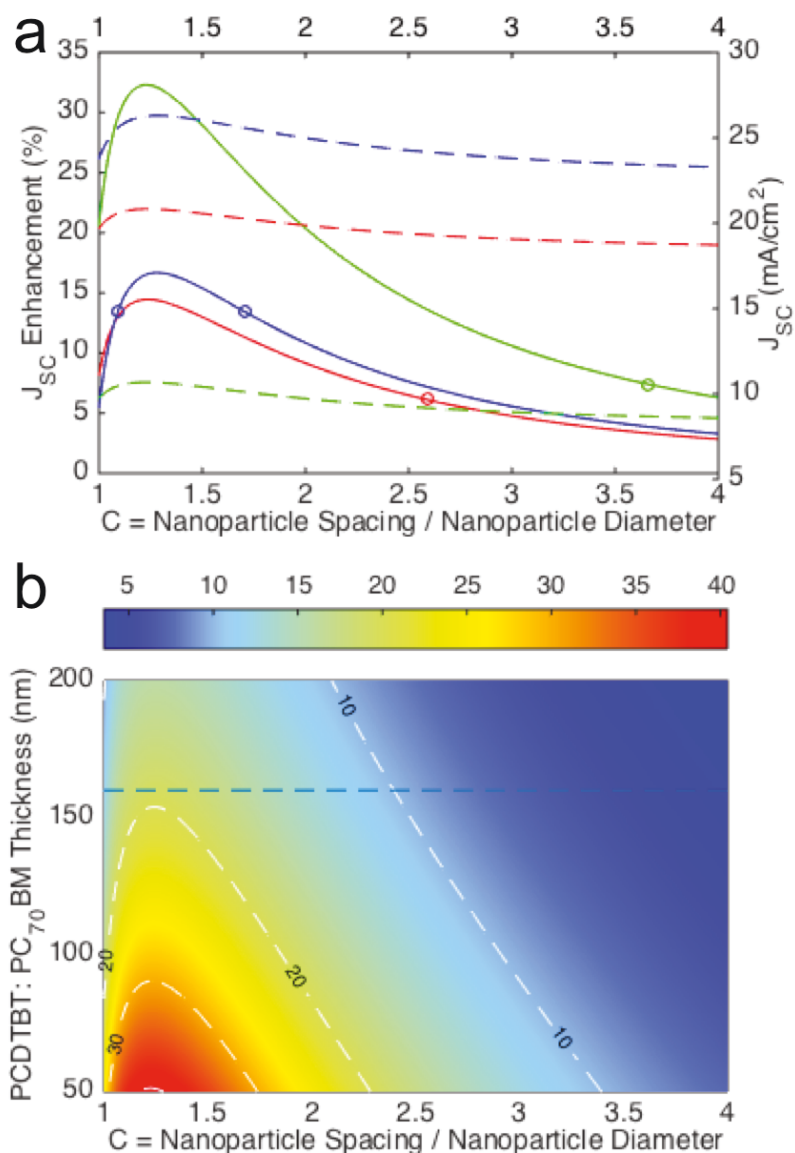


Figure 4.3: (a) Solid lines: predicted J_{SC} enhancement (%) vs. relative nanoparticle separation. The circles are experimental J_{SC} enhancement for the best-performing cells in each study. Dashed lines: predicted J_{SC} values (mA/cm^2) vs. relative nanoparticle separation. Red: 150 nm Au/Ag alloy popcorn embedded in perovskite-infiltrated-TiO₂. Green: 40 nm silver nanoclusters embedded in PCDTBT:PC₇₀BM. Blue: 120 nm SiO₂ core/15 nm Au shell nanospheres in PbS CQD film. (b) Percent J_{SC} enhancement (color scale) as a function of film thickness and nanoparticle separation. The white dashed lines are contours at 10%, 20%, 30% and 40% J_{SC} enhancement to guide the eye. The blue line indicates a thickness of 160 nm, twice the reported thickness in Reference [57].[9]

Figure 4.1a is a plot of the predicted photocurrent and photocurrent enhancement as a function of relative nanoparticle separation. There is an optimum separation, or number density, of embedded plasmonic nanoparticles in each case, and the predicted J_{SC} enhancement has a long tail extending to the limit of large nanoparticle separation. The circles correspond to the J_{SC} enhancement for the best-performing cells in each study and estimated experimental values of C for the three systems were approximately 2-5, which lie in the large separation/low density range.[84, 97, 115] Generally, due to the difficulty in achieving precise control of the synthetic and deposition processes, there are multiple sources of error in the estimations of nanoparticle size and density; however, all experimentally observed enhancements fell within the range predicted by our model.

The largest relative photocurrent enhancements are predicted for the system composed of Ag nanoclusters embedded in PCDTBT:PC₇₀BM. This is primarily due to the small thickness (80 nm) of the absorbing film; intuitively, larger relative enhancements should be possible for thinner active layers in which initial absorption is less complete. We examined the effect of the thickness of the PCDTBT:PC₇₀BM layer by varying it simultaneously with the effective nanoparticle separation to determine the potential J_{SC} enhancement as shown in Figure 4.1b. The maximum J_{SC} enhancement requires a thickness-independent high density of embedded plasmonic nanoparticles. The blue dashed line indicates a thickness of 160 nm, which is double the reported thickness in Reference [57]. If the organic layer thickness could be doubled, the predicted J_{SC} enhancement in the organic system is very close to that

predicted in the other two systems. This reinforces the idea that plasmonic enhancements are potentially more useful in extremely thin films, even independent of photovoltaic material type, and that OPV cells in particular may have more to gain from embedded plasmonic enhancement schemes.

4.1.6.2 Effect of Nanoparticle Shape

Since our model uses calculated plasmonic absorption and scattering cross-sections as inputs, it can incorporate non-spherical nanoparticles, many of which have been used in embedded photovoltaic enhancement schemes.[83, 113] Shape plays an important role in plasmonic nanoparticle properties.[135, 154, 155, 156, 157, 158, 159, 160, 161] Sharp edges can drastically increase local field intensity while simultaneously introducing strong parasitic absorption.[155, 156, 158, 159, 161] We applied our model to systems composed of octahedral and truncated octahedral Au nanoparticles (70 nm in length) embedded in PCDTBT:PC₇₀BM [83], and compared them to a system with similarly-sized Au nanospheres as the plasmonic material in the same matrix. The simulation results are shown in Figure 4.4.

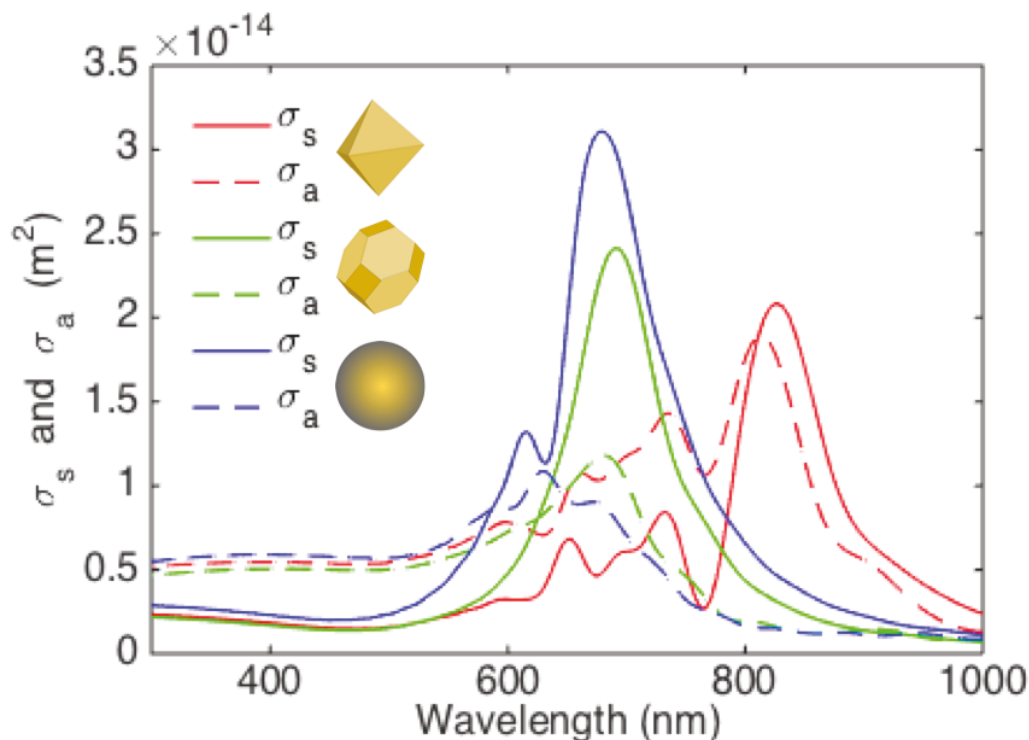


Figure 4.4: Scattering (solid lines) and absorption (dashed lines) cross-section vs. wavelength for different shaped plasmonic nanoparticles of similar size embedded in a PCDTBT:PC₇₀BM background. Red: 70 nm octahedral Au nanoparticles. Green: 70 nm truncated octahedral Au nanoparticles. Blue: 70 nm Au nanospheres.[9]

The octahedral particles contain sharp points, while the truncated octahedra are much closer to spherical in shape. FDTD simulations indicate that gold nanospheres and truncated octahedra of similar size have similar optical properties. The truncated octahedra exhibit a slight red shift and a decrease of the scattering cross-section peak amplitude compared to the nanospheres. The regular octahedral nanoparticles exhibit smaller scattering amplitudes and an increase in absorption with a large red shift compared to the other particles. The absorption cross-section exceeds the scattering cross-section in the 300-800 nm spectral range, indicating that this particle type will not

enhance absorption in a PCDTBT:PC₇₀BM film.

Both the truncated octahedra and the nanospheres have scattering cross-sections larger than their absorption cross-sections near 700 nm in wavelength, indicating that both nanoparticle types have the potential to enhance photovoltaic absorption in this spectral range. However, at wavelengths shorter than 600 nm, the absorption cross-sections are generally larger than the scattering cross-sections, meaning that parasitic absorption will exceed any useful scattering enhancement in this range. This test case illustrates the need to engineer nanoparticle shape for a specific application, and, generally, that shapes with sharp corners often introduce more parasitic absorption than useful scattering enhancements.

4.1.6.3 Effect of Nanoparticle Size and Material

The size-dependence of the scattering and absorption properties of plasmonic nanoparticles is another useful tuning knob for optoelectronic applications.[159, 162, 163, 164] We studied the size-dependent behavior of systems composed of Au and Ag nanospheres embedded in PCDTBT:PC₇₀BM. The results are shown in Figure 4.5. We used a fixed nanoparticle separation of $C = 2$ and a photovoltaic layer thickness of $t = 80$ nm for these calculations.

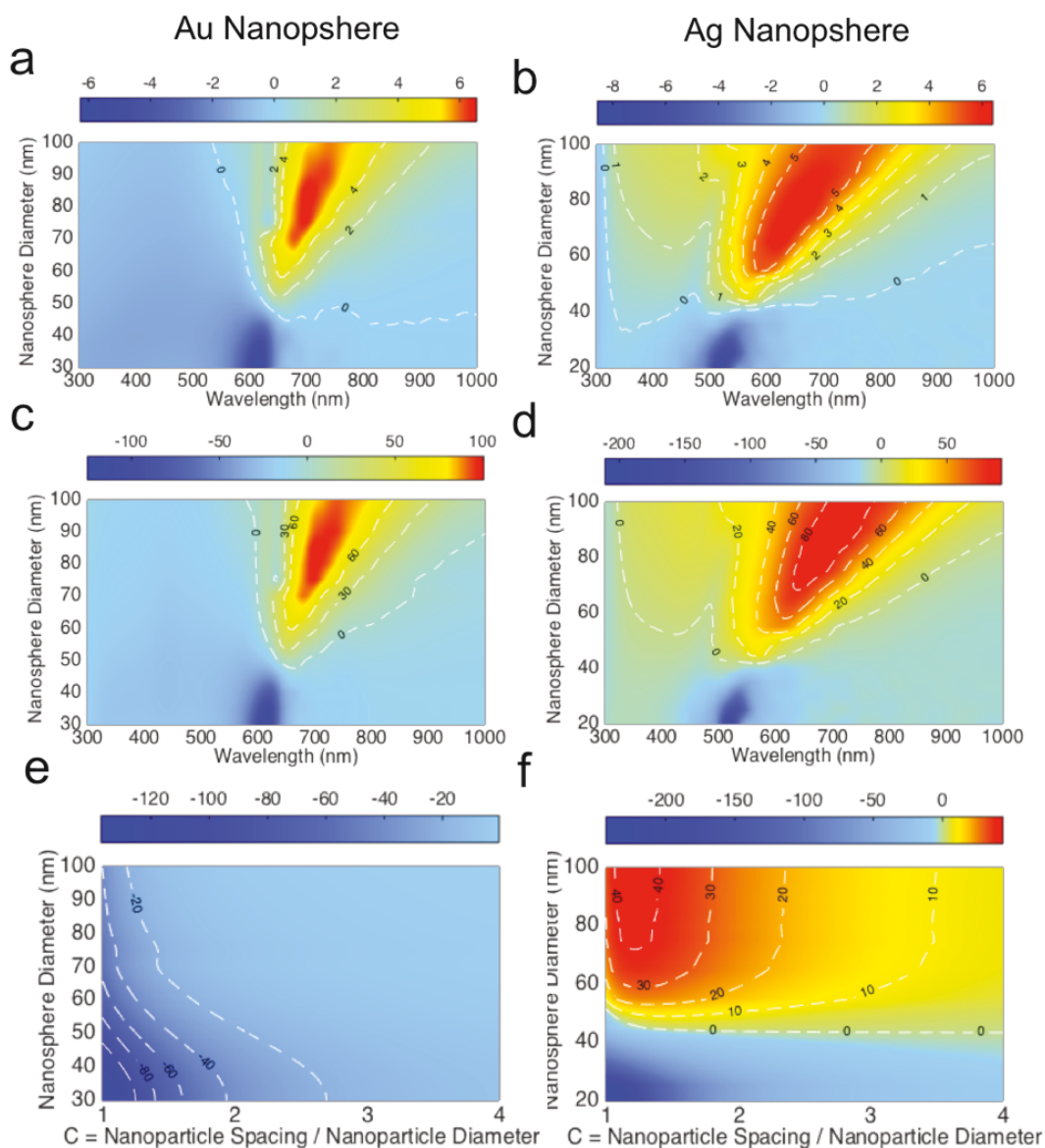


Figure 4.5: (a), (b) Relative scattering efficiency ($Q_s - Q_a$) vs. wavelength and particle size for Au (a) and Ag (b) nanospheres embedded in an organic film. The dashed contour lines represent $Q_s - Q_a$ as labeled. (c), (d) Percent absorption enhancement or loss vs. wavelength and particle size for Au (c) and Ag (d) nanospheres embedded in an organic film. The dashed contour lines represent relative percentage changes as labeled. (e), (f) Percent J_{SC} loss or enhancement vs. relative particle separation and particle size for Au (e) and Ag (f) nanospheres embedded in an organic film. The dashed contour lines represent relative percentage changes as labeled.[9]

The relative scattering efficiency and the absorption enhancement red-shift as a function of nanoparticle size, as can be seen in Figure 4.5. The Au system exhibits significant parasitic absorption in the shorter wavelength regime. Figure 4.5c demonstrates that embedding these types of particles in the OPV film is predicted to result in no net J_{SC} enhancement. This is because parasitic absorption is predicted to dominate within the AM1.5G peak power range and relevant absorption window for PCDTBT:PC₇₀BM of 300-800 nm.

One potential method for avoiding nanoparticle parasitic absorption in the strongly absorbing spectral ranges of the photovoltaic material is to embed nanoparticles at selective locations along the illumination direction of a device. Au nanoparticles such as those modeled in Figure 5 could be embedded at the back of a PCDTBT:PC₇₀BM layer (farther from the illumination plane) so that shorter wavelength photons can be substantially absorbed before reaching the nanoparticle locations within the film. Only photons with wavelengths in the more weakly-absorbing spectral region of PCDTBT:PC₇₀BM and the more strongly-scattering spectral region of the nanoparticles (600-800 nm) would have a high probability of interacting with the plasmonic elements, thereby enhancing total absorption in the device.

The system composed of Ag nanospheres embedded in PCDTBT:PC₇₀BM behaves both qualitatively and quantitatively differently from the Au nanosphere system. As can be seen in Figure 5d, Ag nanospheres with diameters larger than 35 nm can be strong enhancers in PCDTBT:PC₇₀BM at wavelengths near 650 nm. The spectral range of enhancement displays a red shift with increasing nanoparticle size. The main spectral peak corresponds to the dipole

LSPR mode of the Ag nanospheres, and the overall enhancement is a result of competition between the scattering and parasitic absorption. The calculated electric field profile of the LSPR mode at 680 nm and scattering and absorption cross-sections vs. wavelength for an 80 nm diameter Ag nanosphere embedded in a PCDTBT:PC₇₀BM film can be seen in Figure 4.6.

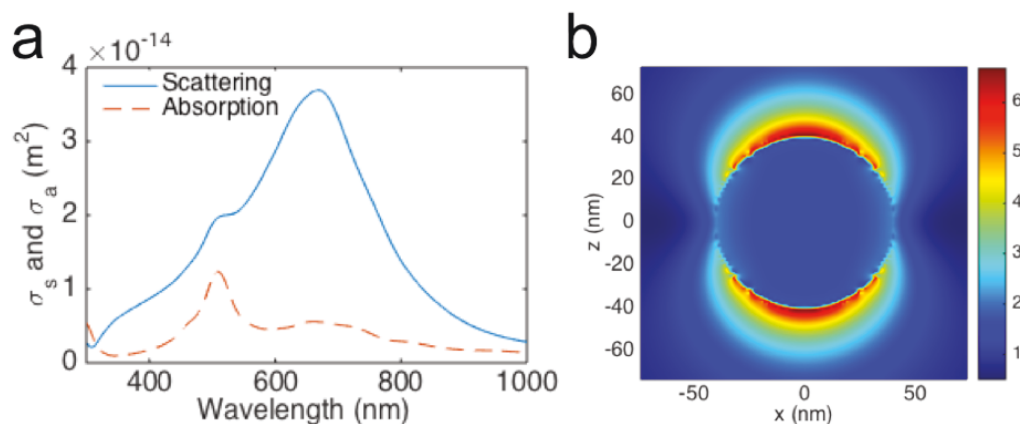


Figure 4.6: (a) Scattering and absorption cross-section vs. wavelength for an 80 nm diameter Ag nanosphere embedded in a PCDTBT:PC₇₀BM background. (b) Calculated normalized electric field intensity ($\lambda = 680 \text{ nm}$) for a single Ag nanosphere at the plane normal to the incident illumination.[9]

Figure 4.5e shows the wavelength-dependent absorption enhancement for different sized Ag nanospheres. Due to the high absorptivity of PCDTBT:PC₇₀BM below 500 nm, most of the light in this range is absorbed in 80 nm of material without the integration of plasmonic nanoparticles. Since the absorptivity of PCDTBT:PC₇₀BM between 600 nm and 800 nm is low, exploiting nanoparticles with strong scattering in this spectral range results in an absorption enhancement, with the peak enhancement exhibiting a red-shift as a function of nanoparticle size.

Using the AM1.5G spectrum as our input, we calculated the predicted J_{SC}

enhancement as a function of Ag nanosphere size and number density. The results are shown in Figure 4.5f; significant J_{SC} enhancements can be achieved for Ag nanospheres with diameters larger than 45 nm. Larger Ag nanospheres and higher number densities result in larger predicted J_{SC} enhancements. For all sizes of embedded Ag nanospheres, the predicted J_{SC} enhancement has a long and relatively flat tail in the large nanoparticle separation limit and becomes very sensitive to separation changes in the high number density limit.

4.1.6.4 Model Validity

The above model estimates the effective absorption in an absorbing photovoltaic layer using the Beer-Lambert law, which describes bulk absorption in a homogeneous medium. However, in a typical multi-layer solution-processed thin-film solar cell, the layer thicknesses are on the scale of the wavelengths of interest, and, as a result, interference effects can play an influential role in real device absorption. These interference effects could be included in our model by embedding the expression for absorption within a thin film interference calculation framework such as the Transfer Matrix Method (TMM) for a multi-layered structures.[165] Such methods take as inputs the thicknesses and the wavelength-dependent complex indices of refraction of the different optical material layers. Our model predicts the new effective absorption coefficient of the modified absorbing medium in a system containing embedded plasmonic nanoparticles. This absorption coefficient is directly related to the imaginary part of the refractive index function; however, estimating an effective real part is more complicated due to the surface plasmon condition that the real part of

the dielectric function change signs across an interface.

In order to test the effect of thin film interference on the sample device absorption results described above, we input the modified imaginary part of the refractive index from our model into a TMM solver[166] and varied the real part by using small perturbations around the original values for a given set of CQD device layer thicknesses.[97] The main effect on total device absorption was due to the addition of a back reflective contact and was less sensitive to variations in the thickness of the front illuminated side transparent contact layers. Due to interference effects, the predicted photocurrents calculated using the TMM were slightly higher (by less than 10%) than the predictions using the Beer-Lambert-based model above, but the overarching trends associated with relative nanoparticle concentration were preserved. A $\pm 10\%$ perturbation of the real part of the refractive index of the active layer resulted in a $\pm 8\%$ shift in the original predicted photocurrents.

Although calculations that take thin film interference effects into account must be used to make accurate predictions of the photocurrent in a real device structure, our enhancement model can be used to evaluate the total absorption enhancement potential associated with an embedded plasmonic nanoparticle strategy as a function of particle type, size, and concentration. Specific device designs can then be fine-tuned by using thin film interference and other light trapping effects.

As previously mentioned, the model described above is a good approximation for real systems when Equation 4.8 is satisfied, i.e. the average nanoparticle concentration is relatively small. This is borne out by the close match of

the predicted J_{SC} enhancements with the reported experimental results. When Equation 4.8 is not satisfied, the model can still be used, but coupling effects between the nanoparticles must be taken into account via simulation of the optical properties of a larger system.[163, 164] In addition, at higher nanoparticle concentrations, our model becomes less accurate due to strong nanoparticle scattering effects and the break down of the plane-wave condition for the Beer-Lambert law.

The model predicts absorption enhancement and corresponding JSC enhancement by assuming perfect carrier collection (IQE) in the photovoltaic systems. However, it is possible to include carrier loss induced by the nanoparticle inclusions into the model, and models that account for both optical and electrical effects have been developed for other proposed systems. [167, 168, 169, 170] This could be achieved, for example, by calculating the effective nanoparticle electronic trap capture cross-section and subtracting the trapping efficiency from the Q terms in the calculation of $\alpha_{plasmonic}$ (Equation 4.5). Other carrier loss mechanisms in real devices could be included through experimental IQE measurements.

4.1.7 Perspective and Future Directions for Solution Processed Solar Cells

General strategies for designing an effective plasmonic enhancement scheme for a specific photovoltaic system can be based on the following two steps:

1. Choose an appropriate material, shape and size in which the scattering cross-section is larger than the absorption cross-section within the

photovoltaic material of interest for the intended spectral enhancement range.

2. An effective medium approach, such as the model described here, can be used to select the optimum embedded nanoparticle density for maximum plasmonic absorption enhancement of the photovoltaic medium.

As has been demonstrated through successful experiments, this strategy can lead to absorption and consequent photocurrent enhancements in real devices. Careful analysis of the model described above, however, indicates that the absolute magnitude of the potential enhancements may be limited. Specifically, in CQD and perovskite solar cells, the model predicts that the maximum achievable plasmonic photocurrent enhancements can probably only improve upon the current best performing devices by about 15%, corresponding to 1 - 4 mA/cm² of additional photocurrent. Given these results and the history of steady transport improvements in these materials, we recommend that the fields concentrate instead on improving fundamental materials properties such as decreasing electronic trap state densities and increasing charge carrier diffusion lengths through improved passivation and growth methods. Plasmonic enhancements are of most interest for applications where external considerations limit the thickness of the active material to less than that already utilized in the best performing devices.

In contrast, the outlook for plasmonic enhancements in organic photovoltaics may be much brighter. Active layer thicknesses are smaller in the best performing OPV classes due to limitations on exciton dissociation and diffusion. Therefore, plasmonic photocurrent enhancements of up to 40% are

predicted by our model, as can be seen in Figure 4.5. Specifically, the field should concentrate on using large (up to 100 nm) silver particles for OPV films due to the LSPR spectral overlap and reduced parasitic absorption at shorter wavelengths, and nanoparticle shapes with pointed vertices should be avoided due to the parasitic absorption induced by the sharp edges. From a practical standpoint, care must be taken in using large nanoparticles for thin film enhancement to avoid the formation of detrimental shunt paths in devices. Critically, further absorption and photocurrent enhancements are predicted to be possible at larger embedded nanoparticle densities than have previously been explored. However, the density must be fine-tuned in order to achieve optimum performance due to the sharply peaked nature of the predicted enhancement curves, as seen in Figure 4.3. In recent years, there have been improvements in achieving thicker absorbing layers for OPVs,[171] and the maturation of these improvements would render plasmonic enhancements less applicable.

In addition to emphasizing work on plasmonically enhanced OPV, we propose two relatively unexplored plasmonic enhancement paths. The first is aggressively pursuing new plasmonic materials strategies. Gold and silver have been the most commonly used plasmonic materials in photovoltaics due to their low-loss behavior in the visible wavelength range resulting from the relatively small values of the imaginary parts of the dielectric function. Alternatives such as aluminum, copper and indium tin oxide also have the potential for low loss in specific spectral ranges. New strategies that take advantage of these materials could include spatially integrating ITO nanoparticles at the

base of a tandem device to enhance infrared absorption, or using aluminum nanoparticles for ultraviolet absorption enhancement in thin absorbing active layers. Additionally, alloying different metals to achieve "averaging" of the spectral properties for broadband enhancement is an attractive potential strategy.

The second path of interest is pursuing electronic coupling to make true hybrid plasmonic-excitonic materials. Instead of considering only the optical properties of plasmonic enhancers in forming an effective medium, full treatment of the electronic effects of these materials could make plasmonic materials of interest for multiple classes of solution processed solar cells. The goal would be to use coherent electronic coupling of plasmonic particles to semiconducting media in order to engineer the excitonic structure. This material hybridization strategy could be used to extend the spectral sensitivity of organic materials to infrared wavelengths, e.g. or could be used modify the band structure CQD films to increase absorption near the exciton wavelengths while aiding in transport.

In conclusion, as the field of plasmonically-enhanced solar cells matures, focusing on strategies with the highest potential for enabling real performance advances is of increasing interest. We believe this entails adjusting nanoparticle concentration as the most crucial tuning knob in embedded plasmonically-enhanced photovoltaic devices, working on the specific silver-based strategy outlined for OPV and pursuing the advanced methods described above that go beyond the traditional gold/silver optical enhancement paradigm.

4.2 Color-Tuned and Transparent Colloidal Quantum Dot Solar Cells

This section is adapted (in part) from Ref. [172]. Reprinted with permission from Optics Express 24, no. 4, A101-A112, "Color-tuned and transparent colloidal quantum dot solar cells via optimized multilayer interference," by E. S. Arinze, B. Qiu, N. Palmquist, Y. Cheng, Y. Lin, G. Nyirjesy, G. Qian, and S. M. Thon, copyright © 2017.

4.2.1 Introduction

Multi-colored solar cells, solar cells with controlled, tunable spectral reflection and absorption profiles, are of significant interest due to their potential to be coated on exterior surfaces of urban infrastructures, such as building facades, rooftops and automotive skins, to serve both aesthetic and functional purposes.[173, 174] In tandem cell applications, there is also a need to systematically control absorption and, in turn, achieve the required current-matching in cells that possess different spectral absorption profiles. Additionally, semi-transparent solar cells are attractive for integration into portable electronics [175] and for window coatings to help with building and vehicular heat management.[176, 177] Solar cells based on solution-processed materials are especially promising for these large-area applications because of their thin-film and lightweight nature, ease and flexibility of fabrication, associated low costs, and high efficiency potential.

Past examples of colored solution-processed solar cell technologies include using combinations of dyes,[178] photonic filters,[179] physically- or

chemically-modified absorbing/transport layers,[180, 181, 182, 183, 184, 185] integrated liquid/photonic crystals,[186, 187] embedded optical microcavities and dielectric mirrors,[182, 188, 189] and modified top/bottom electrodes [190, 191, 192] in dye-sensitized, organic, and perovskite solar cells. Although multi-colored and semitransparent solar cells based on perovskites and organic materials have been demonstrated, their narrow spectral absorbing ranges, which lie mainly within the visible portion of the spectrum, represent a significant drawback for achieving high photocurrents. As a result, light management strategies to produce cell colors or achieve transparency come with an unavoidable loss of device efficiency.

Colloidal quantum dots (CQDs), semiconducting nanocrystals stabilized in solution, are a promising candidate material for achieving multicolored and semitransparent solar cells [193, 194] due to their band gap tunability, which is enabled by the quantum size effect.[195] Specifically, lead sulfide and lead selenide (PbS, bulk band gap energy of 0.41 eV,[196] and PbSe, bulk band gap energy of 0.27 eV [197]) CQDs have band gaps that can be tuned from the near-infrared to the visible portion of the spectrum. As a result, visible absorption losses induced by the design of multicolored or semitransparent cells can potentially be compensated for by enhanced absorption in the infrared region.

Standard CQD film-based devices [193, 194, 198](Figure 4.7) employ different electronic layers that have thicknesses on the order of the optical wavelengths of interest. The layer thicknesses and design are typically optimized for their electrical properties, but optical thin-film interference plays a large role in these devices as well, as demonstrated by efforts to utilize interference

effects to achieve semitransparency and absorption enhancement via electrode modification [199, 200] and microcavity structuring.[200, 201] Traditionally, transparency in CQD-based devices is induced by employing thin absorbing layers.[202, 203] In this study, we design, optimize and fabricate multicolored and transparent CQD solar cells based on thin-film interference engineering concepts to customize both optical and electrical device properties.[204] Using physical and mathematical modeling techniques, including Transfer Matrix Method (TMM) calculations [166] and multiobjective optimization algorithms,[205, 206] we have developed an optimization method for the custom-design of multicolored and transparent CQD solar cells that could be generalized to other materials systems. The optimization sequence is depicted in Figure 4.7c. The method maximizes reflection and transmission at specific wavelengths, creating a desired cell color, while simultaneously requiring high photocarrier generation rates in a solar cell device.

Our multi-layer thin film calculations were based on a depleted heterojunction architecture [7] design for CQD photovoltaics, but could be generalized to include any optoelectronic layer structure. Figure 4.7 shows an example of this architecture, which consists of an optically thick glass substrate, followed by indium tin oxide (ITO, the bottom contact), TiO_2 (the n-type layer), PbS CQD film (the p-type layer), MoO_3 (buffer layer), and Ag (the top electrode).

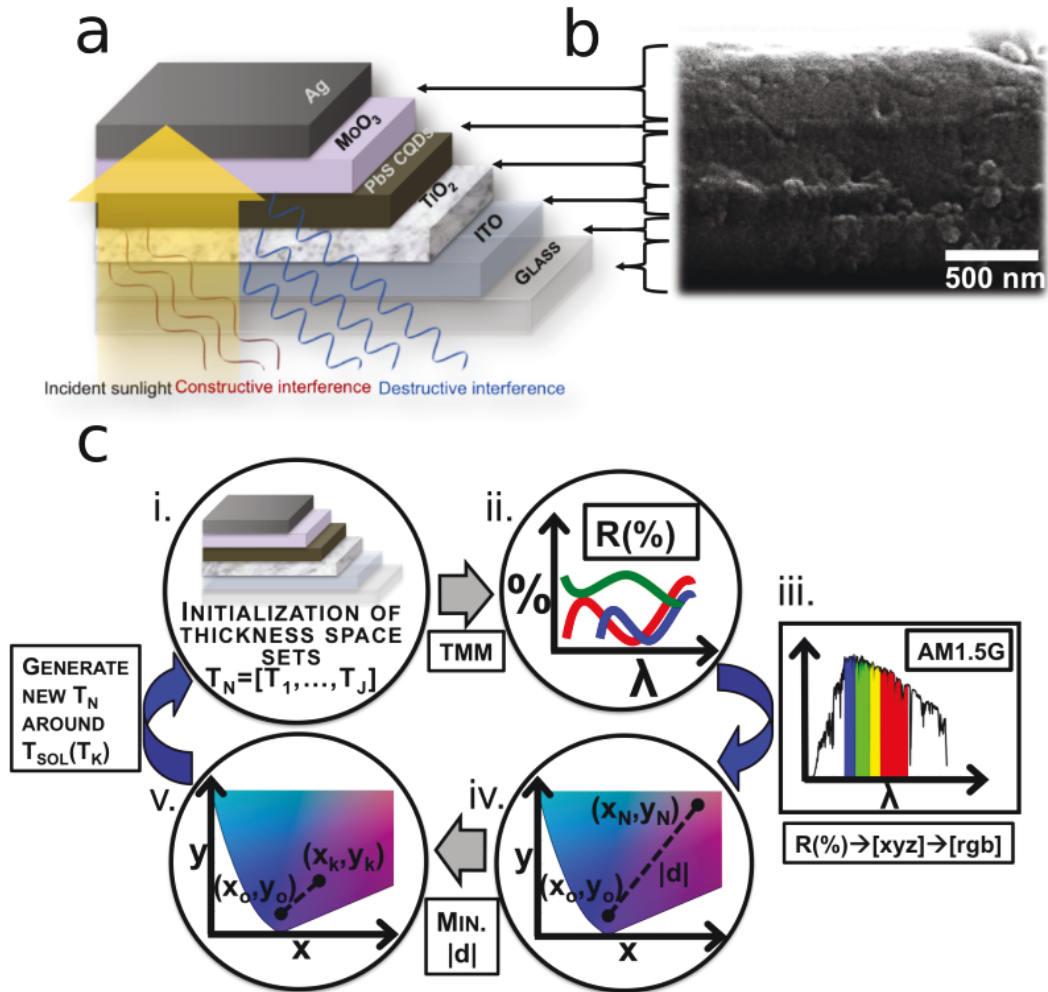


Figure 4.7: (a) Schematic of a CQD-based solar cell illustrating the spectrally-dependent optical interference patterns that can result from tuning the thicknesses of the different cell layers. As incident broadband sunlight passes through the device, constructive or destructive interference occurs at certain wavelengths, resulting in wavelength-dependent reflectivity and transmission, giving the cell its apparent color or semitransparency. (b) Cross-sectional scanning electron microscope (SEM) image of the structure shown in (a) with the layers labeled. (c) Graphic representation of the optimization technique to produce cells with defined color characteristics. Space set of thickness combinations is (i) initialized and each combination is transformed to (ii) a reflection spectrum via TMM. These spectra in combination with incident (iii) AM1.5G and color matching functions are translated to rgb colors on (iv) chromaticity plots where the distance to the intended color is (v) minimized. This optimization cycle repeats until a global minimum is realized.[172]

4.2.2 Optimization of the photocurrent-color tradeoff

We use the TMM, which takes the thicknesses and complex refractive indices of all layers as inputs, and calculates normalized electrical field profiles within the multi-layer structure. In our simulations, the materials models are composed of complex refractive index data from the literature and experimental ellipsometry measurements, and we consider a broadband illumination source with a wavelength range of 300 - 1800 nm. In the case of opaque reflective colored solar cells, Ag is used as the back contact, and ITO is used as the back contact for the semitransparent solar cells. We calculate the reflection spectrum of the device, and predict the expected "color" by combining this spectrum with an appropriate set of color matching functions (1931 CIE [207]) and an illuminating spectrum (AM1.5G). The predicted color can be represented on a 2-dimensional chromaticity plot, as shown in Figure 4.93a Cell "transparency" is calculated by averaging transmittance data over the visible wavelength range (420 nm - 680 nm) output by the TMM calculations.

In order to optimize the color response of our cells, we use particle swarm optimization (PSO), a population-based algorithm, [205] tailored for our specific application, as illustrated in Figure 4.7c. A "swarm size" of solution thickness sets is initialized and fed into the TMM to generate associated reflection spectra, which are then transformed to apparent color. These [rgb] co-ordinates are then optimized for a specific reflected color/wavelength response by minimizing the distance between the target point and solution point on the chromaticity plot, yielding a global solution via multiple iterations. The presence of two different populations (pbest and pcurrent) and

particle movements in PSO allows for both greater degrees of exploration and faster convergence when compared to other optimization methods, such as genetic algorithms. Due to the multilayer architecture of our device and highly multidimensional search space involved, a semi-periodic reflectivity landscape with multiple local minima emerges. Therefore, employing a PSO with a relatively large "swarm size" provides an efficient route to identifying the global minimum for our highly multidimensional optimization problem.

Despite the infrared responsivity of the PbS CQDs, there still exists a trade-off between the available photocurrent and visible transparency in device designs. This trade-off can be partially mitigated by taking the advantage of multi-layer interference effects to reduce visible field overlap with the CQD layer while maintaining absorption in the infrared. In order to achieve high photocurrent with minimum loss of visible transparency, we used PSO to perform single-objective optimizations on the layer thicknesses, keeping the PbS layer thickness constant. The three optimization targets chosen to explore the entire parameter space involved with the trade-off were high transparency, high photocurrent, and low transparency. The available photocurrent and average transparency of each solution to the three optimization problems are shown in Figure 4.8.

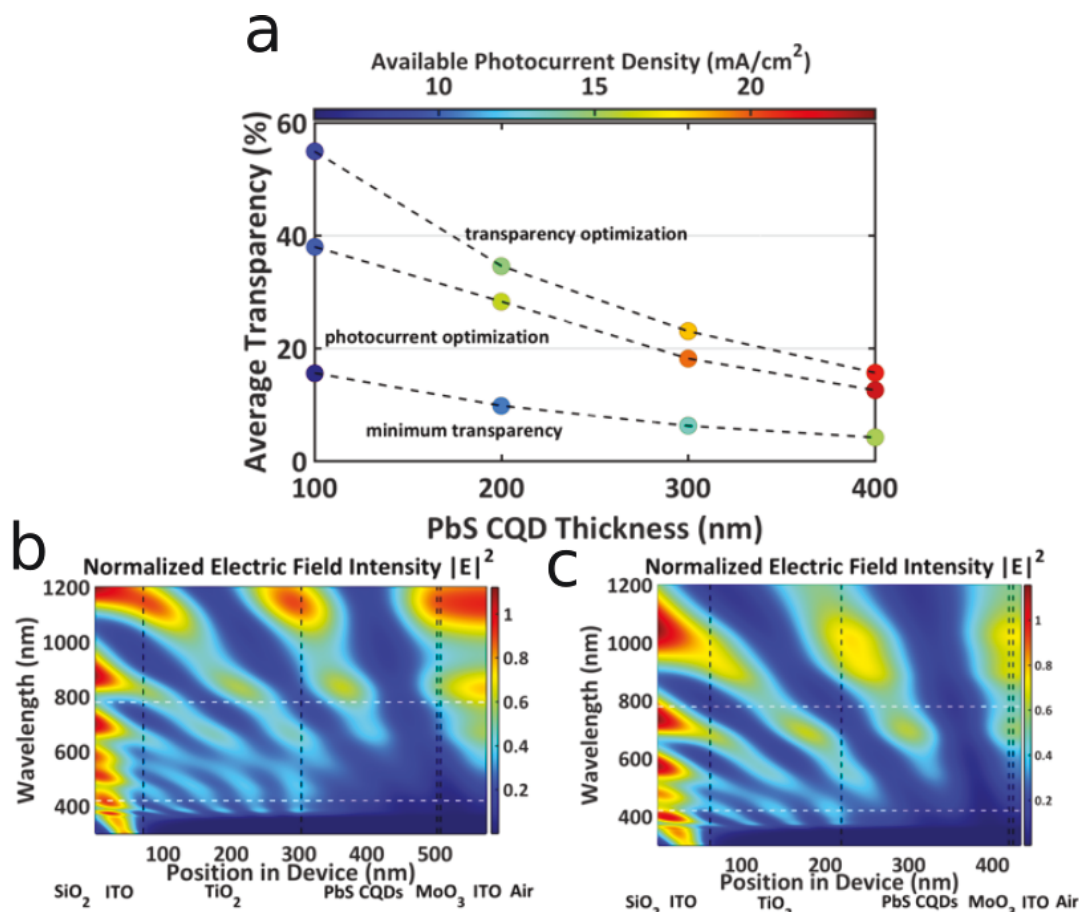


Figure 4.8: (a) Calculated average transparency (%) and corresponding available photocurrent density (mA/cm², color bar) versus PbS CQD film thickness (nm). Top curve: optimized for maximum average visible transparency. Middle curve: optimized for maximum available photocurrent density. Bottom curve: calculated for minimum average transparency. Calculated electric field intensity as a function of wavelength and position in the transparent device structure (ITO back contact) with a PbS CQD layer thickness of 200 nm for: (b) transparency-optimized case; (c) photocurrent-optimized case.[172]

In Figure 4.8a, the average transparency is plotted as a function of CQD layer thickness, and the available photocurrent is represented by the color. The top curve is the set of solutions at each given PbS CQD film thickness optimized for the highest transparency. The middle curve is optimized for the

highest photocurrent at each film thickness. Higher photocurrent comes with the expected trade-off of lower transparency. The bottom curve is calculated for the lowest transparency, and it has the lowest available photocurrent of the three sets of solutions. The difference between the bottom curve and the middle curve represents both the photocurrent and degree of transparency that can be gained for a given active layer thickness by doing a rational layer thickness optimization via our method.

The high photocurrent for the middle curve is achieved by maximizing the electric field intensity within the absorbing layer. The high transparency of the top curve is achieved by employing multi-layer interference to minimize the electric field intensity at visible wavelengths within the absorbing layer. The difference between these two cases is visualized in Figures 4.8b and c. In the optimized photocurrent case (Figure 4.8c), there is an intensity peak at a wavelength near 700 nm within the CQD film, allowing more longer wavelength light to be absorbed within this layer. In the optimized transparency case (Figure 4.8b), there is no electric field intensity peak at the edge of the visible spectral range; instead, there is a peak closer to 800 nm at the NIR edge, allowing visible light to be transmitted and maintaining a relatively high photocurrent through NIR photon absorption.

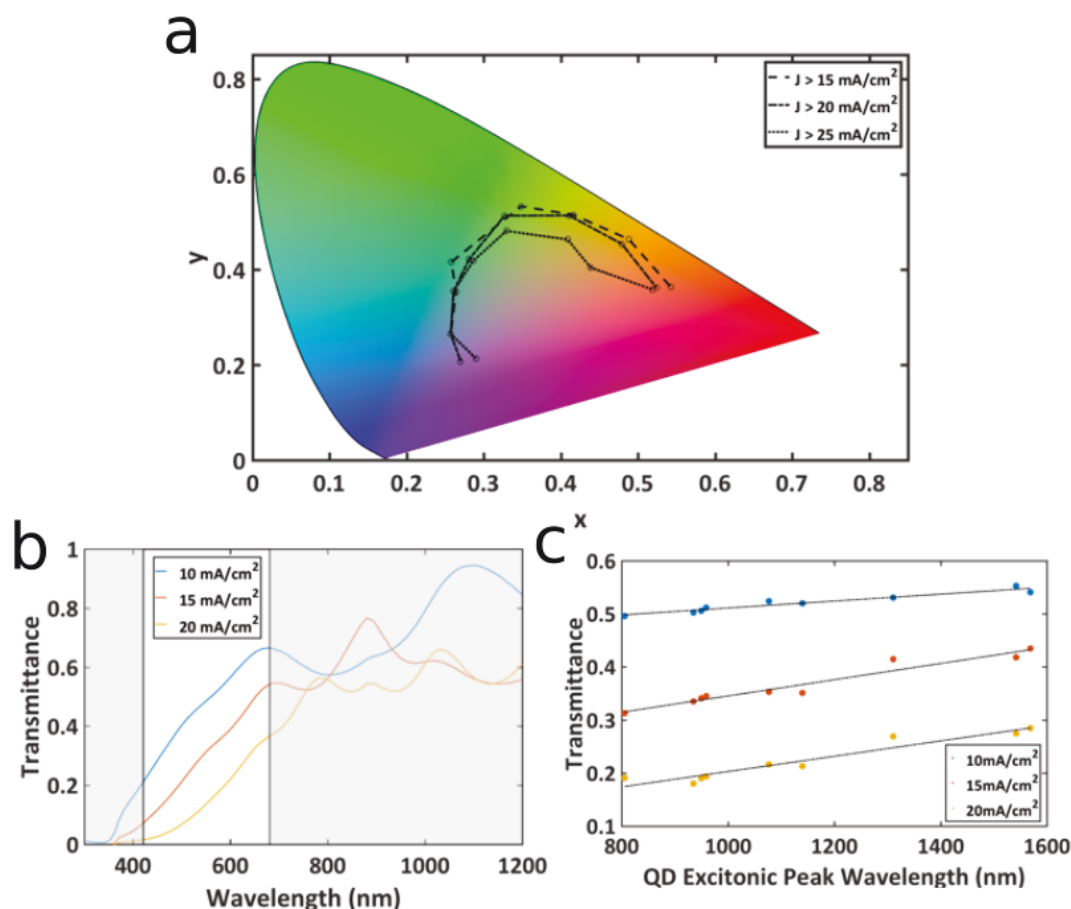


Figure 4.9: (a) Chromaticity plot showing achievable colors given minimum photocurrent requirements ($J > 15 \text{ mA/cm}^2$, $J > 20 \text{ mA/cm}^2$, and $J > 25 \text{ mA/cm}^2$). Calculated Transmittance plots showing: (b) trade-off between transparency and photocurrent (for CQDs with 950 nm exciton peak wavelength), and (c) achievable transparency given minimum photocurrent requirements for different CQD excitonic peak wavelengths.[172]

The tradeoffs between attainable color or transparency and minimum device photocurrent are illustrated in Figure 4.9a. From this plot, it is apparent that photocurrent requirements more strongly affect "redder" colors, whereas the range of "bluer" colors that can be achieved shows little correlation with achievable photocurrent. Figure 4.9b shows transmittance plots

for devices optimized for their transparency based on photocurrent restrictions. As expected, lower required device photocurrents result in higher potential visual transparency levels. Figure 4.9c shows the dependence of the photocurrent/transparency tradeoff on the CQD excitonic peak wavelength.

4.2.3 Effects of non-ideal layers on color saturation

In evaluating the prospects for real devices, it is important to take into account non-ideal effects, such as interface roughness, non-uniformity of the layer physical properties, and the presence of scattering centers formed by impurities and contaminants. We can incorporate these effects into our model by using another parameter, the effective "optical roughness" of each layer. We create a sufficiently large number of samples with random thicknesses by adding the standard deviation of a Gaussian distribution based on the measured or assumed roughness to the mean thickness for each layer. We then calculate the reflectance curve of each sample in the distribution and statistically average the reflectance from all samples to derive the effective reflectance curves.

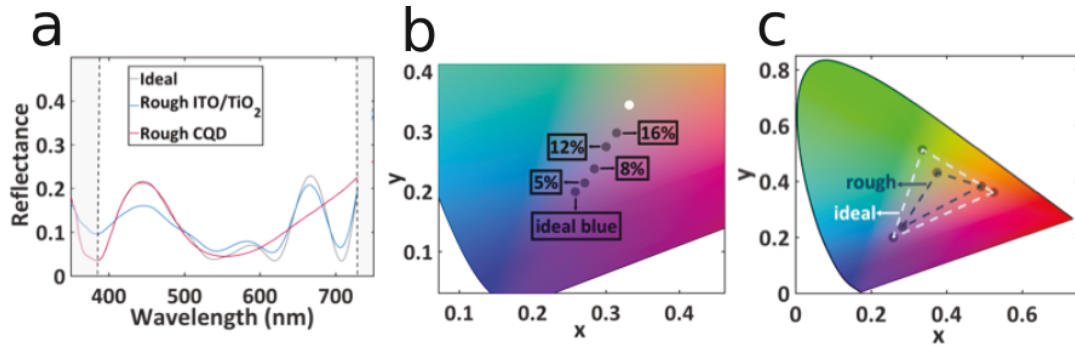


Figure 4.10: (a) Simulated reflectance curves for a specific color objective with and without an effective optical roughness of 10% for the ITO/TiO₂ layers and 10% for the CQD layer. (b) Effects of different levels of roughness on the chromaticity of a "blue" device. Percentages refer to the ratio of the standard deviation to the ideal thickness of the ITO/TiO₂ layer. The white point of the standard illuminant is also plotted as a reference point. (c) Roughness (10%) has the effect of moving the vertices on the largest achievable triangle of color profiles closer to the white point.[172]

Due to the nanostructured nature of the material itself as well as the deposition technique, the CQD layer typically has a geometrical roughness of 3-10 nm.[122] The geometrical roughness of the underlying electrodes and oxide layers deposited by evaporation, which can be determined from surface profilometry, is usually smaller than that of the CQD films. However, the effective optical roughness can be significantly greater than the geometrical roughness. One possible origin of optical inhomogeneity in the ITO and TiO₂ layers is the compositional and structural non-uniformity introduced during the deposition and processing steps, which can be seen as a spatial variation in the refractive index profile of the electrode films.

Figure 4.10 shows the effects of non-ideal interference on the reflectance curves as well as the effective colors of the devices. As can be seen in Figure 4.10a, the reflectance from devices with rough CQD layers is smoothed in the red spectral region, while the shorter-wavelength region is mostly unaffected

by the roughness. For rough TiO_2 and ITO layers, the deviations from the ideal case are greater in the blue region. The changes in the reflectance curves reduce the wavelength selectivity, and make the apparent color less saturated. The chromaticity plot in Figure 4.10b demonstrates this effect for a device that is designed to be blue in color. As the effective optical roughness of the ITO/ TiO_2 layer increases, the chromaticity point moves towards the white point, decreasing the saturation, and shifting the color towards brown-grey. In Figure 4.10c, after accounting for the optical roughness, all 3 points corresponding to the maximum achievable saturation of red, blue and green, are closer to the white point. This approach to considering the effects of non-ideal interference is particularly useful for understanding color in real devices.

4.2.4 Application in tandem structures

Our proposed method for color-tuning CQD solar cells is of particular interest for applications in all-CQD and hybrid tandem photovoltaics, where current-matching is critical to series-connected device performance. CQDs are particularly suited to tandem applications because of their band gap tunability, infrared responsivity, and compatibility with a variety of materials systems afforded by their solution-processing. This flexibility effectively eliminates the difficulty of finding a materials combination possessing both appropriate band gaps and suitable lattice matching for optimized multijunction cells.[208] Proof-of-principle studies have demonstrated tandem structures utilizing all-CQD materials systems [209, 210, 211] and CQDs in conjunction with polymer materials.[212, 213]

In these series-connected CQD tandem structures, current matching is essential to obtain high efficiency devices. Generally, this is achieved by empirically adjusting the layer thicknesses until approximately equal photon absorption occurs in the two active layers. Here, we use our optimization algorithm to take into account the effects of interference in a multilayered stack to design optimum absorbing layer thicknesses.

For our optimization simulation, we employed a PbS CQD system comprised of 1.55 eV and 0.95 eV dots which are both within 5% of the optimum band gaps for the maximum efficiency in a two-junction tandem structure.[214] In addition, our simulated tandem structure integrated a graded recombination layer as demonstrated in a previous study.[209] Calculating absorption using only the Beer-Lambert law [146] in the active layers, not taking into account reflection, gave optimum thicknesses of 350 nm and 247 nm for the front and back cells, respectively, predicting a maximum photocurrent of 18.1 mA/cm². Using our optimization process, we obtained optimum thicknesses of 350 nm and 196 nm for the front and back cells, respectively, achieving an output-matched photocurrent of 18.6 mA/cm². We achieved a ~3% increase in expected photocurrent using our optimized approach, even though it takes into account reflection and the detrimental parasitic absorptions in the electrodes and the other non-active layers in the 9 layer tandem stack, whereas the control case does not. Our optimization method, accounting for both interference and reflection, provides an efficient route for tandem layer designs in both CQD and hybrid systems.

4.2.5 Experimental results and discussion

We fabricated several proof-of-principle CQD solar cell devices based on our optimization method designs for different colors using PbS CQDs with exciton peak wavelengths near 950 nm. To minimize the fabrication uncertainty in the layer thicknesses, we used commercial ITO-coated glass substrates with ITO thicknesses of 28 nm for our "red" and "green" cell designs. For the "blue" cell, we deposited ITO on a glass substrate via e-beam evaporation, followed by an annealing process, to obtain our target optical thickness. The TiO₂ layer was also deposited using e-beam evaporation for precise thickness control, and a TiCl₄ solution treatment was applied afterwards.[97] The PbS CQD layer was built up using a layer-by-layer solid state ligand exchange process.[97] Two or three drops of oleic acid capped PbS CQD solution at a concentration of 50 mg/mL per layer were deposited through a 0.22 μm pore filter and spin-cast on the substrate. 0.5% mercaptopropionic acid (MPA) in methanol was used to soak the film for 3 seconds to replace the oleic acid, then the film was spin-cast dry. Lastly, the films were washed with methanol twice to remove the unbound ligands, completing the deposition of one CQD film layer. The total CQD film thickness was controlled through the acceleration, spin speed, spin time and number of layers and verified using profilometry measurements. We were able to control the thickness of the CQD layers to within ±15 nm. The top contact was composed of a thin MoO₃ buffer layer and Ag, which were both deposited via e-beam evaporation.

Photographs of the colored and transparent cells are shown in Figure 4.11a.

We measured the reflectance of each solar cell using an Agilent Cary 5000 UV-Vis-NIR spectrophotometer with an integrating sphere insert, calculated the corresponding xyz color values by integrating over the AM1.5G spectrum, and plotted them in a chromaticity diagram. The reflectance spectra are plotted in Figure 4.11b, and the calculated color of the fabricated devices is shown in Figure 4.11d.

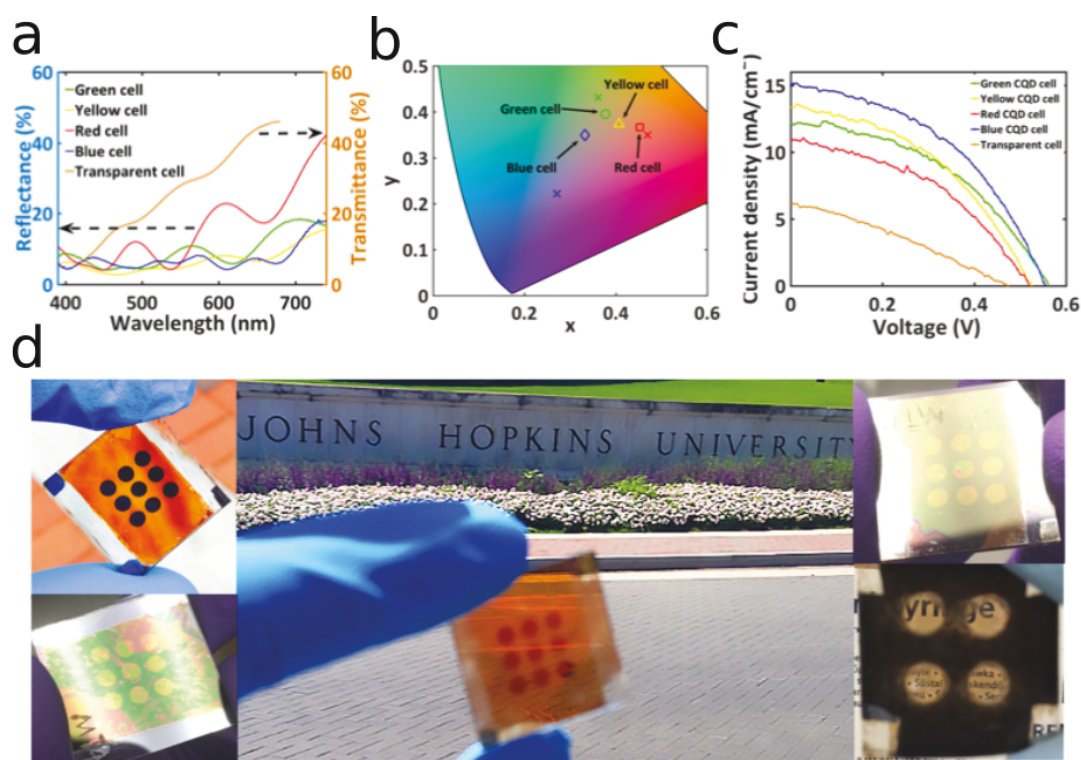


Figure 4.11: (a) Experimental reflectance and transmittance spectra for colored and semi-transparent solar cells, respectively. (b) Chromaticity plot showing the calculated coordinates for different colored devices. Crosses indicate design points while corresponding colored shapes indicate experimental points. (c) J-V characteristics taken under simulated solar illumination for colored and semi-transparent devices. (d) Photographs of blue (upper left), green (lower left), red (center), yellow (upper right), and semi-transparent (lower right) CQD solar cells.[172]

We also fabricated semi-transparent devices based on our optimization

CHAPTER 4. SOLUTION PROCESSED SOLAR CELLS

Cell Type	V_{OC} (V)	J_{SC} (mA/cm ²)	FF	PCE(%)	Design Parameters ITO/TiO ₂ /PbS/MoO ₃ /Ag (nm)
Blue	0.56±0.01	14.6±0.6	0.44±0.01	3.6±0.1	240/113/400/100/475
Green	0.55±0.02	12.1±0.7	0.42±0.02	2.8±0.1	28/150/297/12/60
Yellow	0.53±0.01	12.6±0.5	0.41±0.01	2.7±0.2	28/150/297/12/60
Red	0.50±0.03	10.3±0.8	0.41±0.03	2.1±0.3	28/166/222/22/274
Transparent	0.46±0.05	5.2±0.7	0.31±0.01	0.8±0.1	28/349/170/17/85(ITO)

Table 4.2: Average performance characteristics of colored and transparent solar cell devices showing open-circuit voltage (V_{OC}), short-circuit current (J_{SC}), fill factor (FF) and power conversion efficiency (PCE). All measurements are for at least 5 devices.[172]

method. The top contact of these devices was a composite electrode consisting of spin-coated Ag nanowires and ITO nanoparticles. Our test devices had measured visible transparencies ranging from 27.3% to 32.2%. The measured transmittance spectrum of the highest efficiency device is plotted in Figure 4.11c.

All current density-voltage measurements were carried out in a nitrogen-purged environment. Current density-voltage curves were measured using a Keithley 2400 source meter with illumination provided by a Sciencetech solar simulator with an irradiance of 1000 W/m². The active area of the solar cell was illuminated through a circular aperture with an area of 0.044 cm² ± 0.003 cm². The power through the aperture, measured using a Thorlabs broadband power meter, was used to calibrate the power density. The measured short circuit current (J_{SC}), open circuit voltage (V_{OC}), fill factor (FF), and power conversion efficiency (PCE) for the different cells are summarized in Table 4.2.

The differences in performance between the devices are related to their

different design parameters, which are determined by the need to optimize reflection and transmission over specific wavelength ranges. Blue is a relatively difficult color to produce using this method, since the reflections are minimized due to the strong absorption of the CQD film in the blue region of the spectrum. The optimal design included a very thick CQD film layer. The lower FF of the semi-transparent device is related to the difficulty in making a strongly conducting top transparent contact without heat-processing due to the presence of the temperature-sensitive underlying CQD film.

Generally, the experimental photocurrents were smaller than those predicted by the simulations by approximately 50-60%, due to experimental deviations from the model assumptions. The simulations make the assumption of perfect carrier collection (IQE = 100%), whereas CQD solar cell IQE is typically on the order of 50-90% above the band gap.[97, 215] Additionally, experimental variations in the device layer thicknesses can contribute to lower average photocurrents. On average, the ITO, TiO₂, and PbS CQD layer thicknesses in our devices were within 15 nm, 10 nm, and 15 nm, respectively, of the design thicknesses.

4.2.6 Conclusion and outlook

We developed a method for producing arbitrary spectral profiles in layered solar cell structures using thin film interference modeling techniques combined with optimization algorithms. At selected wavelengths, our model maximizes reflection and/or transmission to create a target color and transparency level while simultaneously maximizing photocarrier generation rates. Our study

revealed that designs with minimum transparency do not necessarily correspond to the highest attainable device photocurrent, providing a pathway for high efficiency colored devices. Although effective optical roughness in the films decreases the color saturation, CQD solar cell devices with well-defined color profiles can still be produced. Our optimization method produced layer designs for tandem solar cell applications, with increases in expected photocurrent over conventional designs despite taking into account optical losses. Experimentally, we fabricated proof-of-principle blue, green, yellow, red and semi-transparent devices. The measured reflectance and transmittance spectra agreed well with the perceived color and transparency levels.

Future work will focus on broadening the application of our model to hybrid materials systems (single junction and tandem design structures based on non-CQD-based films) and explicitly including additional loss mechanisms. Additionally, the overall device performance could be improved by employing the current best CQD device architecture strategies with graded doped CQD layers involving solution-based halide passivation treatments.[216, 217] Finally, this work, coupled with the development of more efficient room-temperature-processed transparent electrode materials, should extend the range of functionalities of flexible optoelectronic devices.

4.3 Spectral-Selection in Absorbing Optoelectronic films via Photonic Band Engineering

This section is adapted (in part) from Ref. [218]. Reprinted with permission from Optics Express 26, no. 21, pp. 26933-26945, "Photonic band engineering

in absorbing media for spectrally selective optoelectronic films," by B. Qiu, Y. Lin, E. S. Arinze, A. Chiu, L. Li and S. M. Thon, copyright © 2018.

4.3.1 Introduction

Spectrally selectivity is critical in many optoelectronic applications, such as optical imaging [219, 220], target recognition [221, 222], chemical detection [221, 223, 224, 225] and solar energy harvesting [226, 214, 227, 228], but is difficult to achieve in traditional semiconductors which typically absorb at all energies above their band gaps. Specific examples of technologies requiring fine-tuned spectral responsivity include finite bandwidth photodetectors and materials with controlled transparency windows for multijunction and transparent photovoltaics [226, 214]. Spectral-selectivity can be employed for heat management in solar cells or other optoelectronic devices by reflecting unwanted wavelengths that would otherwise be parasitically absorbed in the contacts or other device layers. [229, 230, 231, 232] Common solutions to this problem include using external filters for photodetectors [223], which come with the cost of adding complexity to the system, and empirically controlling the thicknesses of each absorbing material in tandem solar cells to realize current matching, which often sacrifices photocurrent output [233, 209, 234]. Here, we propose a solution that achieves controlled spectral selectivity within the absorbing material itself, i.e. the photogenerative material that is responsible for energy conversion or transfer of the absorbed photon energy: using photonic crystals to engineer the photonic band structure in absorbing media to directly control the wavelength-dependent absorption, reflectivity

and transmissivity.

Photonic crystals (PCs) are materials with periodic variations in their dielectric functions, potentially creating a photonic band gap, a range of frequencies in which photons are forbidden to propagate. This compelling mechanism enables PCs to be used to manipulate light flow in many applications including optical communications [235, 236, 237], computing [238, 239, 240, 241], and optoelectronics [242, 243, 244, 245, 246]. In addition to artificial structures, many examples of PCs can be found in the natural world, enabling effects such as the structural colors of butterfly wings and beetles [247, 248, 249].

Most of these examples use PCs with photonic band gaps lying in the naturally non-absorbing range of the materials, i.e. below the electronic band gap where the material behaves like a simple dielectric, although photonic band structures can be straight-forwardly tuned in frequency by adjusting the length scale of the dielectric function periodicity (lattice constant). [250] Positioning the photonic band gap of a PC in the absorbing region of a material presents complications due to absorption being viewed as a loss mechanism for many applications. However, optoelectronic applications such as photovoltaics or photodetectors rely on semiconductor absorption and photogeneration as vital operating mechanisms, and the possibility of using photonic band engineering within the absorbing region represents a potential new spectral tuning mechanism. The concept is illustrated in Figures 4.12a and b. Previous work on engineering photonic band gaps in lossy materials includes forming PCs from metals that have shown diminished reflection peaks with increasing absorption [251]. Initial work on forming PCs within

the photoactive layers for solar cells has been proposed, focusing on utilizing the PC structures for spectrally-selective light trapping [252] and absorption enhancement [252, 253, 254] based on density of states modulation. For wavelength selective-absorption, band-pass absorbers made from dye-glass [255] have been widely implemented for decades, and in recent years, metamaterials based on periodic plasmonic structures have been demonstrated with very high absorbance within the visible range for solar-thermal applications [256]. These implementations typically focus on extending the spectral response in their respective systems by combining structures with engineered responses in different spectral ranges. However, rather than focusing on absorption alone, a comprehensive method for inducing spectral-selectivity that aims to enable wavelength-dependent absorption, reflectivity and transmittivity simultaneously, including not just absorption enhancement but also suppression through the use of controlled transparency windows, has yet to be demonstrated. Here, we describe how embedding PCs in photogenerative materials could offer a handle for controlling spectral features across multiple wavelength bands and dynamic ranges in complicated optoelectronic applications such as multi-junction solar cells.

Spectral-selectivity is particularly applicable for the design of color-tuned materials with controlled transparency windows for multijunction and transparent photovoltaics. Infrared (IR) sensitive materials, such as small-bandgap semiconductors, absorb strongly at all energies above their band gaps. Molecular materials, such as organic semiconductors, [257] typically have finite-bandwidth absorption peaks in the visible and UV, but IR-only responsive

materials are rare. To incorporate IR-sensitive materials into multijunction solar cells, they must be positioned at the back side of a standard solar cell device to permit the absorption of visible radiation by the front cell, and the thicknesses of both cells must be fine-tuned to achieve current-matching. An ideal material for incorporating multijunction functionality into current single junction photovoltaic technology would have an absorption profile that was both spectrally tunable and finite in bandwidth, thus offering flexibility for both current-matching and device design.

The concept of using the photonic band structure in a slab-type PC to control the reflection and transmission of external propagating fields is illustrated in Figure 4.12. In Figure 4.12, we present a system consisting of a 2D PC "slab" structure in which a periodic lattice of air holes is drilled in a semiconductor. The "out-of-plane" incident, reflected, and transmitted fields are highlighted and interact with the "in-plane" resonant field with properties determined by the PC structure. Here we use "in-plane" to describe physical structures or fields and states that are bound by or mostly concentrated in the slab itself, and "out-of-plane" to describe fields and waves that propagate indefinitely outside of the slab structure. The "in-plane" fields and states compose the band structure of the slab, and they can couple to the "out-of-plane" incident waves at the point of the Brillouin Zone, shown on the right side of the Figure. We sketch hypothetical reflection and transmission spectra at normal incidence alongside a hypothetical (generic) in-plane band diagram for a structure such as that shown in Figure 4.12 to illustrate the coupling between the in-plane photonic bands and the out-of-plane reflection and transmission profiles. The

transmission and reflection spectra should consist of a smoothly varying background that resembles a Fabry-Perot interference spectrum, [258] with sharp and asymmetric resonance features on top. As will be discussed in the next section, the coupling between incident waves and the photonic bands sharing a lateral wave-vector results in resonance features in the transmission and reflection spectra of the slab. This coupling gives rise to the potential for tuning the "out-of-plane" spectral selectivity by tailoring the band structure of the PC slab, to achieve desired absorption, reflection and transmission profiles.

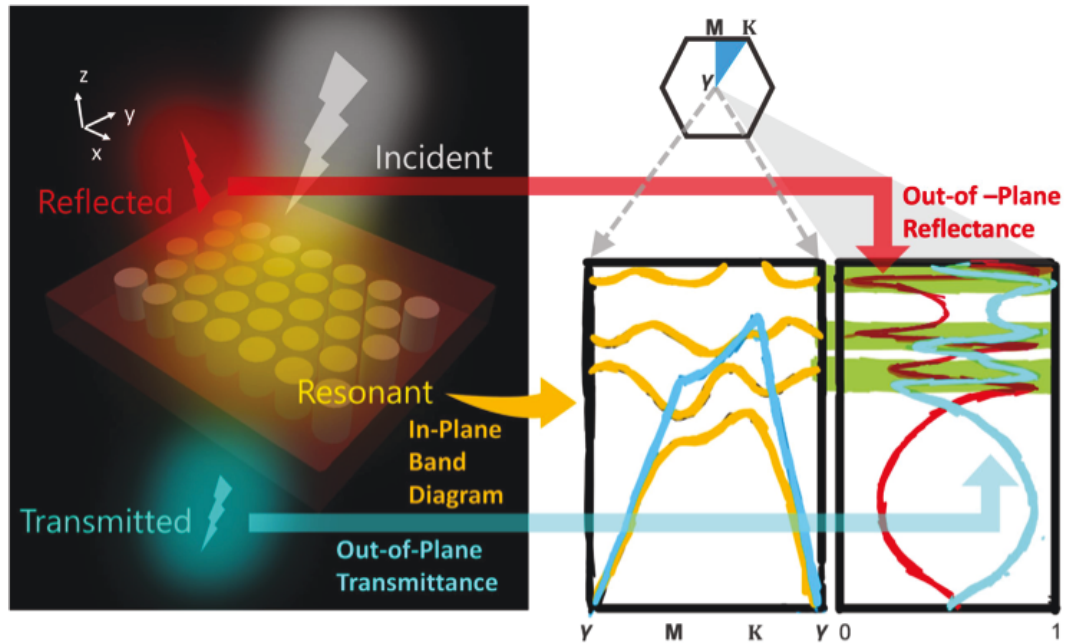


Figure 4.12: Schematic of a generic 2D slab photonic crystal illustrating the spectral tuning concept (left). The "in-plane" photonic band structure is used to generate spectrally-selective reflectivity, transmissivity and absorption for target optoelectronic applications. Broadband light (white in color) is incident on the slab, with specific frequency components strongly coupled to the resonance modes of the slab (yellow), resulting in spectrally-selective transmission (blue) and reflection (red). A hypothetical photonic band diagram for the generic slab structure (photonic bands are shown in yellow; the light line is shown in blue in the center panel) and "out-of-plane" transmittance (blue) and reflectance (red) spectra at normal incidence are sketched on the right side of the Fig.. The green stripes show direct correlations (coupling) between the sharp resonance features in the transmittance and reflectance spectra and the photonic band states at the γ -point. A Brillouin Zone diagram for the hypothetical structure is shown above the photonic band diagram sketch.

In this work, we use finite-difference time-domain (FDTD) simulations and Fourier modal methods [259, 260, 261] to quantify the effect of material absorption on a slab PC with relevant photonic bands that fall above the electronic band gap of the semiconductor slab material. We then use the

insights gained from the simulations to design a PC structure in a solution-processed semiconductor, based on a PbS colloidal quantum dot (CQD) thin film, that strongly absorbs in the infrared but transmits visible light more strongly than in the non-structured semiconductor. This type of material could enable visible-blind infrared photodetectors without external filters, and it could also allow for flexibility in current-matching in a tandem solar cell.

4.3.2 Simulations

To study the effect of material absorption on photonic band structure, we based our simulations on the well-studied 2D GaAs slab PC structure, [242] which consists of a triangular lattice of air pillars in a semiconductor slab of finite thickness. In FDTD simulations, we are able to artificially adjust the strength of the absorption through control of the imaginary part of the dielectric constant (ϵ_I) as long as we keep the real part (ϵ_R) constant, which is equivalent to varying the real and imaginary parts of the refractive index (n, k). Dispersion is not explicitly considered in the test-case model since it results in difficulty in satisfying the Kramers-Kronig relations [262]. The completely non-absorbing control case uses a material that has ϵ_R set to 13, meant to approximate the average value of n for GaAs across the relevant frequency range, and ϵ_I set to zero. We then gradually increase the value of ϵ_I in the simulations, keeping ϵ_R constant, in order to systematically quantify the effect of dissipation on the photonic band structure.

We use FDTD simulations to calculate the frequencies of the modes that

can exist in the structure beyond the initial transient phase in our artificial materials to reconstruct their photonic band structures. The broadband field profile of the excitation source is chosen to ensure that all modes of interest are excited. Randomly distributed time monitors collect the time-resolved field data. Destructive interference causes rapid decay of non-resonant fields, while the excited modes of the structure resonate with varying decay rates for the bulk of the simulation time. The frequencies of these modes are extracted via fast Fourier transform (FFT).

Details of the FDTD simulation method for band structure simulations [263] are as follows: The simulation volume consists of an integer number of unit cells of the 2D periodic structure, and the volume is extended in the z-direction symmetrically above and below the slab by approximately 10 lattice constants. Bloch boundary conditions are used for the x and y (in-plane) directions and perfectly matched layers (PMLs) with symmetric or anti-symmetric boundary conditions are used in the simulations corresponding to the even (TE-like) or odd (TM-like) mode polarizations, respectively, for the z-direction. Identical broadband dipole sources with random polarizations are used to excite the modes and randomly distributed throughout the simulation volume. Conformal meshing is used near material interfaces, and Maxwell's integral Eqs are used to account for structural variations within a single mesh cell. We apodize the loaded time signals from each time monitor for each field component, with a Gaussian-shaped windowing function used to only consider the portion of the time signal following the source pulse injection and before the simulation is cut off. The resulting FFT of the apodized signal

is a spectrum with peaks at the resonant mode frequencies, corresponding to allowed photonic bands. The energy spectra of Fourier-transformed time signals for each field component of every time monitor are summed to ensure that we identify all of the resonant frequencies even if some of the randomly placed time monitors are located at the node of a mode. The simulations are repeated for each Bloch vector value, K , and frequency peaks for each K that meet the threshold tolerance are retained.

In our simulations, we chose a semiconductor slab thickness of 125 nm and tuned the lattice constant ($a = 250$ nm) and radius ($r = 60$ nm) of the air holes to produce a number of relevant photonic bands within the visible regime, or above the electronic band gap of GaAs. The model structure is shown in the inset of Figure 4.13c. The simulated band structure for the non-absorbing control case with both even and odd modes is shown in the top left panel of Figure 4.13a, followed by a series of photonic band structures with increasing k . The photonic band structure for a GaAs PC slab including full dispersion [264] in the refractive index model is shown in Figure 4.13b.

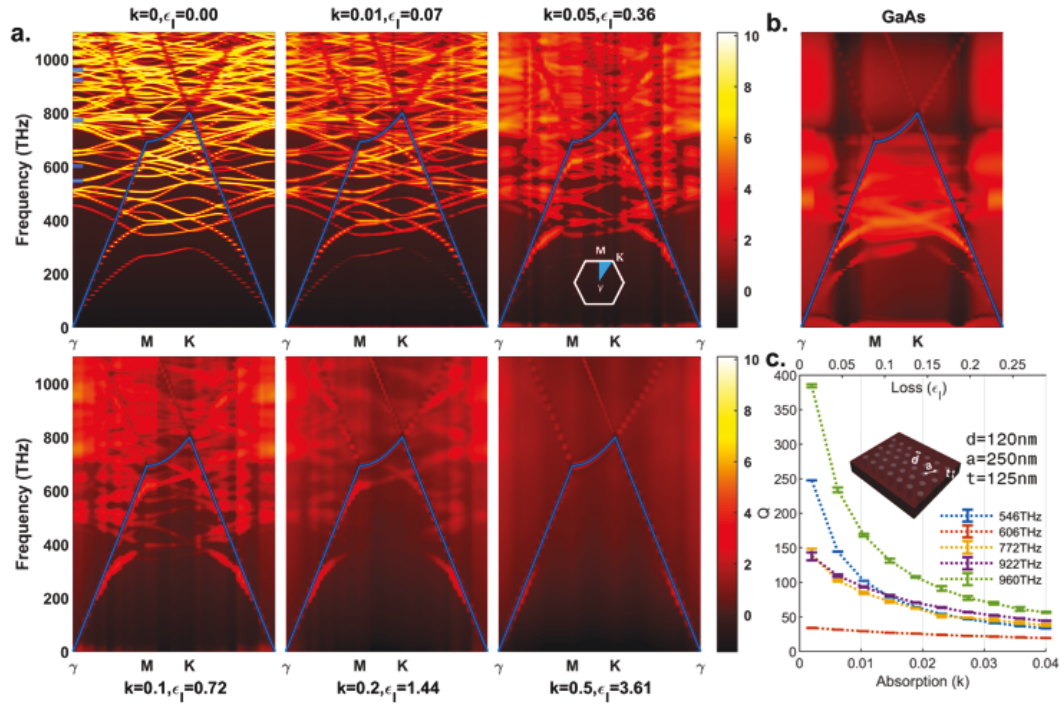


Figure 4.13: (a) FDTD-calculated photonic band diagrams for the structure shown in (c) with media loss (absorption) varying from $\epsilon_I=0$ to $\epsilon_I=3.61$ and constant $\epsilon_R=13$, with corresponding imaginary part of the refractive index also indicated. The light lines are plotted in blue. The color scale is in arbitrary logarithmic units corresponding to the field intensity. (b) FDTD-calculated photonic band diagram for the same structure for a GaAs slab medium (the dielectric constant includes dispersion in this case). (c) Quality factor for 5 selected modes, indicated by the blue markings at the point in the top left panel of (a), as a function of loss in the material. Inset: model of the simulated structure, a triangular lattice of air holes in a semiconductor slab with 120 nm diameter, 250 nm lattice constant, and 125 nm slab thickness.

As can be seen from Figure 4.13a, the frequencies of the photonic bands are almost unchanged as dissipation is added to the optical model, if ϵ_I remains small compared to ϵ_R , although the relative band strengths are reduced with increasing material absorption. As material loss increases, the widths of the bands are broadened, and the clarity of the higher order bands decreases faster than that of the lower order bands, which is expected from the shorter

absorption lengths at higher frequencies present in the model. The rough maintenance of the photonic band frequencies in the presence of weak material loss can be understood using perturbation theory applied to the PC master Eq. [242] Adding a small imaginary part to the dielectric function, ϵ , results in the addition of an imaginary part to the resonance frequency, $\omega_0 = \omega_0 - i\gamma$, which consequently adds to the linewidth of the Lorentzian resonance profile and reduces the resonance peak height.

To quantitatively study the properties of photonic bands in dissipative structures, we calculated quality factors, Q , for the individual bands in the structure shown in Figure 4.13: $Q_i = \omega_0/\Gamma_i$, where Γ_i is the energy decay rate, or the band resonance linewidth, of the i th photonic band at the γ point of the periodic structure. Modes at the point are above the light line, and because of the finite thickness of the PC slab, they are radiating modes at that point that can couple to external propagating fields. Here, we chose five modes capable of coupling to plane waves at normal incidence angles, i.e. they can be excited by incident plane waves and radiate energy to reflected and transmitted plane waves. For this reason, these bands dissipate energy from the slab and have finite Q even without the presence of material absorption. Figure 4.13c shows the quality factors for the five bands as a function of increasing ϵ_I or k in the material. All quality factors exhibit similar decays as a function of ϵ_I and can be well fitted by the function $Q_i = \frac{Q_0\Gamma_0}{\Gamma_0 + \alpha_i\epsilon_I}$, where Q_0 is the quality factor of the lossless structure, and α_I is a constant that depends on the spatial distribution of the i th mode [26]. As loss in the material (ϵ_I) increases, the differences in Q between different modes decrease, corresponding to a "smearing" and

overlapping of the photonic bands until they eventually become indistinct at the limit of very high material absorption.

Understanding the interactions of external propagating fields with the in-plane photonic band structure of a slab-like PC, specifically the spectral reflection and transmission of a PC thin film, is a critical step in using them for absorbing optoelectronic applications. These interactions involve power transfer from external fields to radiating modes within the slab and vice versa. Such systems can be modeled as resonators interacting with external ports using coupled-resonator theories [265]. In PC thin films of interest for optoelectronic applications, the periodicities are always smaller than the wavelengths of interest; therefore, for plane wave sources, no diffraction orders exist. Consequently, all fields and modes that interact with an incident wave are contained in the reflected and transmitted waves with the same in-plane wave vector as the incident wave, and the in-resonance slab radiating modes. Waves impinging at normal incidence on a slab-PC therefore compose a system that can be fully and concisely modeled.

Figure 4.14 shows transmission and reflection spectra for absorbing and non-absorbing PC structures calculated via Fourier modal methods [259, 260, 261] at a fixed in-plane wave vector with polarization along one of the reciprocal lattice vectors. The smoothly-varying background curve resembles the spectrum from a simple Fabry-Perot cavity consisting of a uniform continuous media sandwiched between two mirrors, with additional sharp resonance features added on top. The resonances occur at the same frequencies as the in-plane PC radiating modes and are asymmetric with negative and positive

features due to the nature of Fano resonance behavior [265]; these features include dramatic increases in transmission on one side of the resonance, even in the case with material absorption. The transmitted and reflected fields directly couple to the incident field while simultaneously indirectly coupling to the radiating mode of the photonic crystal excited by the incident field. Such resonance phenomena are well explained by temporal-coupled wave theory [265, 266, 267]. We note that not all modes in the photonic band structure can be excited with incident plane waves, due to restrictions in symmetry and polarization [265].

In the absence of absorption, the Fano resonance features are narrow and sharp, due to the intrinsic long lifetimes of the lossless radiating modes. When absorption is added to the model, the lifetimes of the radiating modes are reduced, resulting in broader and weaker resonance features, which originate from the same effects as the reduction in Q factor seen for the modes in the band structures. The resonance frequencies for the same structure with a non-zero ϵ_I , set to 2% of ϵ_R , are almost unchanged, in accordance with the FDTD photonic band structure simulations. The FDTD-calculated photonic band structure for the $\epsilon_R=0$ case is plotted next to the reflection and transmission spectra in Figure 4.14 to illustrate direct spectral correspondence between the out-of-plane Fano resonance features and the in-plane photonic crystal bands. The overall reflection and transmission are both slightly reduced in the case with absorption compared to the case without absorption, as would be expected for a uniform lossy slab.

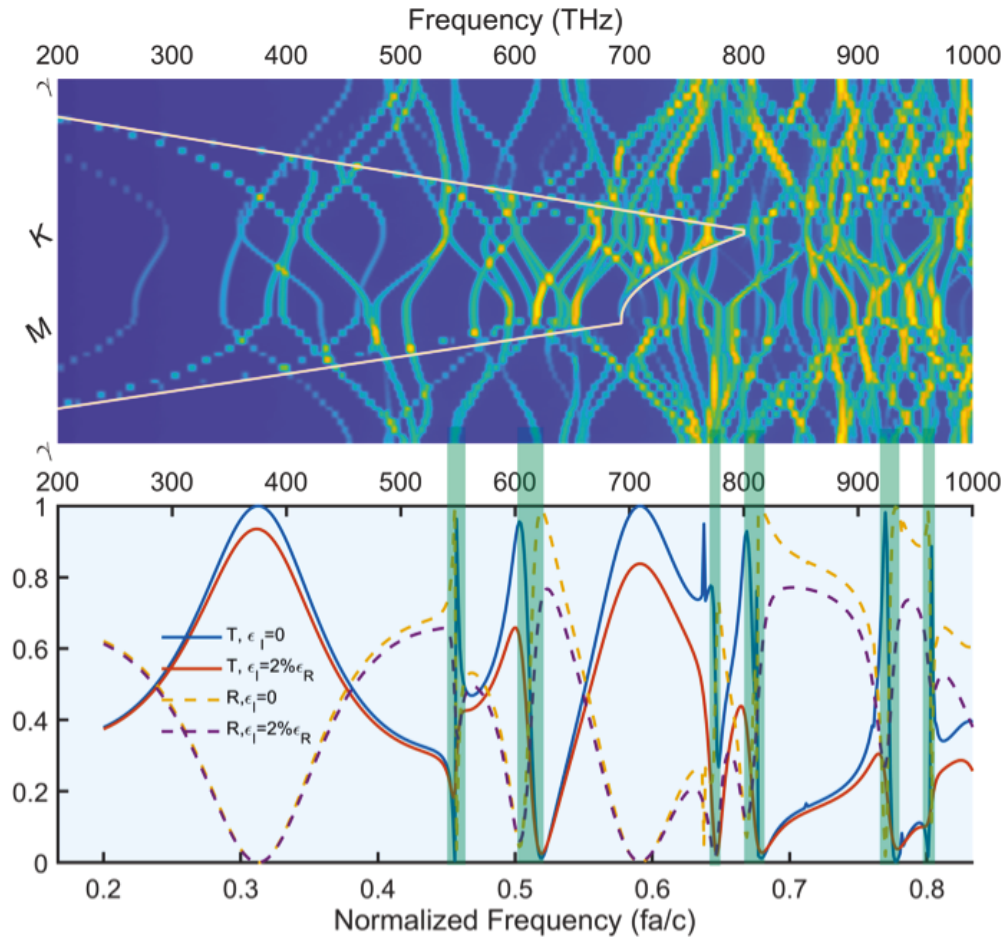


Figure 4.14: FMM-calculated transmission (solid lines) and reflection (dashed lines) spectra (bottom) for a triangular lattice slab photonic crystal with $r = 0.24a$, $t = 0.5a$ and $\epsilon = 13$ (blue and yellow spectra) and $\epsilon = 13 + 0.3i$ (red and purple spectra). The incident field is perpendicular to the slab structure. The corresponding FDTD-calculated band structure for the $\epsilon = 13$ case is shown in the top panel (light line plotted in white). The resonance regions are highlighted and associated with the modes at the Γ point in the band structure.

Although the resonance features are less apparent in the transmission and reflection spectra of the absorptive structure, the interactions of the PC medium with the radiating resonance modes are not necessarily weakened.

Applications such as photovoltaics and photocatalysis that depend on absorption of the photoactive material could benefit from this phenomenon of increased absorption of the resonance modes. The amplitude of the i th steady-state resonance mode in the presence of material absorption can be approximated from temporal-coupled wave theory as shown in Equation 4.9 [266, 268]:

$$a_i = \frac{gs}{i(\omega - \omega_0) + \Gamma_{rad,i} + \Gamma_{abs,i}} \quad (4.9)$$

where g and s are the coupling strength and the amplitude of the incident field, respectively; ω_0 is the resonance frequency; and Γ_{rad} and Γ_{abs} are the decay rates, i.e., the reciprocals of the radiation and absorption lifetimes. The power absorbed in the i th mode is therefore approximated as:

$$P_{abs} \propto \Gamma_{abs} |a_i|^2 = \frac{\Gamma_{abs} |g|^2 |s|^2}{(\omega - \omega_0)^2 + (\Gamma_{rad,i} + \Gamma_{abs,i})^2} \quad (4.10)$$

which can be maximized at the resonance frequency ω_0 , if the absorption strength is comparable to the radiative strength. In the presence of material absorption, the widths of the resonances are also broadened so that a larger range of frequencies is capable of inducing stronger absorption in the media. Additionally, the integrated absorbed power associated with a specific resonance (photonic band) always increases with increasing material absorption strength.

Based on this analysis, using 2D PC slabs in absorptive materials should enable spectral modulation, including absorption and transmission tuning, with

careful control of the PC parameters. Broadband transmission and reflection selectivity is controlled primarily by the average optical properties of the slab, i.e. the effective refractive index. The smoothly varying background in the reflection spectra can be very accurately fitted assuming an optically uniform slab with slight dispersion in the dielectric constant that varies around the average dielectric constant of the PC slab. Broadband transmission and reflection tuning is therefore effectively only dependent on the volume ratio of the periodic voids (low-index inclusions), the slab thickness, and the properties of the high-index material. The spectral locations of the sharp resonant features corresponding to the photonic bands within the material, on the other hand, are highly dependent on the PC structural properties, such as the periods and shapes of the voids, not on the slab thickness and high-to-low index material volume ratio. Additionally, due to the optical scalability of PC structures in the absence of strong dispersion, specific spectral features can be easily shifted to preferred frequency ranges simply by scaling the structure accordingly. The addition of material absorption allows abrupt spectral features to be smoothed and broadened without significant shifts in frequency or decreases in the absorbed incident power, an additional tool that can be used to tailor transmission and reflection profiles.

4.3.3 Experimental demonstration of spectral tuning using PCs in strongly absorbing materials

Our simulation results indicate that the photonic band structure can be at least partially preserved in a PC fabricated in a strongly absorbing medium and

that this in-plane band structure has a strong effect on the out-of-plane transmission and reflection spectra. We sought to experimentally demonstrate this spectral tuning mechanism by fabricating a proof-of-principle PC structure in a strongly absorbing material with response in the infrared portion of the spectrum.

We chose to use a PbS CQD thin film as the absorbing media because of the demonstrated infrared absorption, facile solution processability, and applicability in many optoelectronic applications, including photodetectors, [269] LEDs [270] and solar cells [194, 172]. We used nanosphere self-assembly [271, 272] to construct a monolayer triangular lattice structure out of polystyrene beads, which served as the low-index material, and infiltrated them with PbS CQDs as the high-index absorbing material to form a photonic crystal-CQD (PC-CQD) structure. We optimized the PC-CQD film for transmittance in the visible regime using FDTD simulations. Our simulations aimed to mimic the realistic system by incorporating slight non-uniformity in the large-scale film thicknesses. We calculated the transmission by averaging the simulation results for 11 different film thicknesses for the PC-CQD case (250 ± 50 nm) and 3 different film thicknesses for the CQD control case (200 ± 10 nm), based on our experimental thickness measurements. As shown in Figures 4.15a-b, the PC-CQD film consisting of 250 nm beads in a monolayer triangular lattice array infiltrated with PbS CQDs displays a slight enhancement in visible transparency and a slight decrease in near-infrared (NIR) transparency compared to the control CQD film in both the simulation and experimental spectra. The electrical field profiles at the transmittance peak and valley of the 250 nm

PC-CQD film are shown in Figures 4.15 c and d, respectively. At the transmittance peak, the field is mainly confined within the low-index dielectric material, whereas at the transmittance valley, the field interacts more with the high-index absorbing media and thus more energy is absorbed at that wavelength.

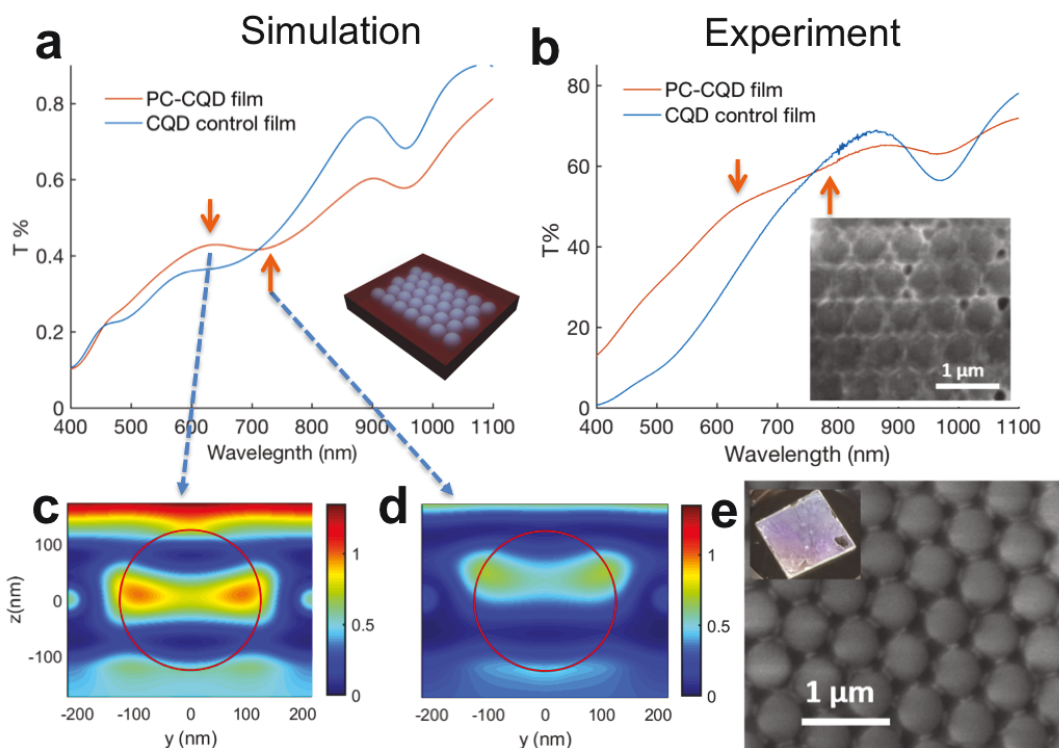


Figure 4.15: (a) FDTD-calculated transmittance for a control CQD film and a PC-CQD film. The inset is the PC-CQD structure: a triangular lattice monolayer of polystyrene beads infiltrated with PbS CQDs. The control CQD film is 200 nm thick on average, and the PC-CQD film consists of 250 nm diameter beads in a triangular array with a lattice constant of 250 nm; the space around the beads is filled with CQDs to form a 250 nm thick film on average. The spectra are averaged over several thicknesses to simulate roughness. The PC-CQD film shows a slight enhancement in visible transparency compared to the control CQD film. (b) UV-Vis-NIR spectrophotometric transmittance spectra of the PC-CQD film and the control CQD film, showing qualitative agreement with the FDTD calculations. Absolute difference in transmittance can be attributed to large-area non-uniformities in the films. Inset: Top-view SEM image of the PC-CQD structure consisting of mildly-etched self-assembled polystyrene beads infiltrated with PbS CQDs. (c) FDTD-calculated cross-section of the spatial electric field profile at the transmittance peak (d) valley. (e) Top-view SEM image of the etched bead array before CQD infiltration. The inset is a photo of the 1 inch x 1 inch bead array on a glass substrate before CQD infiltration. Large-scale order can be inferred from the strong iridescence of the structure.

To fabricate the PC-CQD film, we started by treating glass substrates with an O_2 plasma to make them hydrophilic and spin-cast 50 μL of an aqueous

solution of polystyrene beads at a concentration of 10% w/v purchased from Magsphere at a speed of 500 rpm for 10 seconds, followed by a 2-minute 700 rpm drying step. The beads self-assemble to form a close-packed triangular array with a lattice constant equal to the bead diameter. We then applied an O_2 plasma etching step at 120 W for a few minutes to open up space between the beads, adjusting the time to control the ratio of the bead radius-to-lattice constant. A scanning electron microscope (SEM) image of the bead array after etching is shown Figure 4.15e, and the inset contains a photograph of the 1 inch x 1 inch sample, which shows strong iridescence from the beads, indicating large-scale order. We synthesized oleic-acid capped PbS CQDs following previously published methods [273] and deposited the control CQD films from octane at a concentration of 50 mg/mL via a layer-by-layer spin-casting and 3-mercaptopropionic acid (MPA) ligand exchange process [273] to build up a film of the desired thickness. We used a lower concentration CQD solution (10 mg/mL) while keeping the concentration of the MPA-in-methanol solution at 1% by volume, to promote infiltration of the CQDs into the bead array. An SEM image of the PC-CQD film is shown in the inset of Figure 4.15b, showing preservation of the bead array and infiltration of the CQDs. Optical transmittance spectra of the PC-CQD and control films are shown in Figure 4.15b and were measured by placing samples at the entrance of an integrating sphere in a UV-Vis-NIR spectrophotometer. The experimental data is in rough qualitative agreement with the FDTD simulation results: the PC-CQD film shows a slight enhancement in visible transparency with a peak visible in both the experimental and simulation spectra at approximately 630 nm. The peaks and valleys of the experimental spectra are broadened and reduced in

intensity compared to the simulated spectra, most likely due to non-uniformity across the films and significant surface roughness that results in reduction of interference effects. Although preliminary, these results demonstrate that photonic structuring in strongly absorbing materials can result in significant modulation of the optical spectra which could be a useful tuning knob for optoelectronic applications. Future work will involve complete photonic band structure calculations to identify optimal structures that can be fabricated using CQD materials with targeted spectral properties for specific device applications.

4.3.4 Summary and Outlook

We developed and analyzed a new strategy for tuning the spectral selectivity of optoelectronic thin films: using photonic band engineering in strongly absorbing materials in which in-plane photonic bands are used to control the spectral properties of the out-of-plane reflection and transmission spectra. We analyzed a model system composed of a semiconductor-based slab photonic crystal in which the photonic bands of interest are located in the absorbing region of the material. By artificially varying k in FDTD and FMM simulations, we were able to quantify the impact of absorption on the photonic band structure. Specifically, adding absorption had little impact on the frequency of the photonic bands, although the widths of the bands were broadened and the quality factors of the in-plane modes decreased and saturated with increasing material absorption. Our FMM analysis showed that coupling between the

photonic bands at the γ point and normal-incidence wave induces sharp resonance features over the smoothly varying background in the reflection and transmission spectra, which can lead to strong frequency-dependent variations in the reflectivity and transmissivity associated with Fano resonances, even in the presence of material absorption. These results indicate that PC structures in strongly absorbing media can be used to produce spectrally selective optoelectronic thin films for targeted applications by careful adjustment of the lattice parameters.

Experimentally, we demonstrated the use of photonic structuring to tune the transmission spectrum of a strongly absorbing material by fabricating a proof-of-principle structure consisting of a self-assembled polystyrene bead monolayer infiltrated with PbS CQDs. The PC-CQD structure showed both near-infrared absorption enhancement and visible transparency enhancement over a control homogeneous CQD film of the same thickness, qualitatively matching predictions.

Future work will focus on extending these results by calculating full photonic band structures for solution-processed systems and including realistic dispersion in the optical models. We will use the insights gained from this study to design spectrally-selective photoactive optoelectronic films for targeted applications such as narrow-band infrared photodetectors and infrared solar cell materials for multijunction photovoltaics. The platform described here should form the basis for a new way to think about using photonic band structure engineering to control the spectral selectivity of strongly absorbing materials.

4.4 Novel Ligand Engineering *via* Molecular Silicon

The development of new renewable energy technologies as alternatives to costly, polluting, and unsustainable fossil fuels is an urgent priority for sustaining an energy-dependent civilization and improving human health. Solar technologies hold great promise because the radiant solar energy arriving at Earth's surface is approximately 10,000 times what is needed to fulfill current human demands; however, today's photovoltaics (solar cells) are still too costly to compete with fossil fuels. These costs are associated with energy-intensive manufacturing, transportation, and installation of bulky conventional semiconductor technologies, making development of new, lightweight, cheap, and flexible solar materials a critical need.

This project identifies an innovative solution to a paradox in cutting-edge third-generation solar-cell materials that would address limitations in their efficiency for solar-energy capture and could enable widespread adoption of solar power generation. Solar cells absorb sunlight and convert it to electrical energy; the ideal device combines broadband light absorption with efficient electrical conduction. Unlike conventional bulk semiconductors, colloidal quantum dots (CQDs), nanometer-sized fragments of semiconductors synthesized in solution, are inexpensive light-absorbing materials for solar cells. Importantly, CQD size can be adjusted to tune the optical bandgap, enabling harvesting of the sun's broad emission spectrum.[8] However, this property leads to a paradox: the nanoscale dimensions that control the attractive

light-absorption characteristics of CQDs result in poor electrical conductivity, limiting device efficiency. In CQD films, charge must be transported through the inter-particle medium, which is composed of insulating (not conductive) carbon-based CQD ligands. Ligands, small molecules that bind to CQD surfaces, play a crucial role in device performance: they prevent surface defect-related losses in efficiency due to formation of charge-carrier traps, solubilize CQDs for material processing, and maintain their nanoscale dimensions in films. Resolving this absorption-conductivity paradox for CQD materials is essential to progress in engineering nanostructured solar cells as the energy technology of the future.

4.4.1 Novel Approach

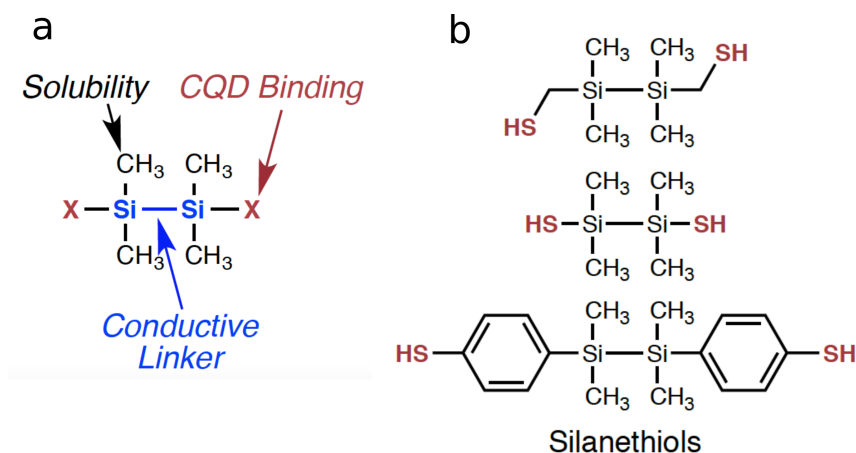


Figure 4.16: (a) Design for novel conductive silicon ligands showing different components. (b) Diverse architectures for bifunctionalized silicon based ligands

Our solution to the challenge of enhancing charge transport in CQD films is to replace insulating carbon-based ligands with conductive silicon-based ligands to form a novel solar cell material. Successful past ligand strategies

for CQD thin film devices were based on organic molecules, such as alkyl [274] and aromatic thiols,[275] alkylamines,[276] and mercaptocarboxylic acids,[273] and inorganic passivants such as single halogen atoms⁶ and metal chalcogenide complexes.[277] However, CQD films formed from these ligands are either poor conductors or non-photovoltaic.

While it is well appreciated on the macroscopic scale that diamond is an insulator and silicon is a semiconductor, we briefly outline the evidence for enhanced conductance in molecular-scale silicon. Both carbon and silicon form cyclic and acyclic chains, called alkanes and oligosilanes respectively.[278] A previous study showed in single molecule studies that tunneling conductance is much more efficient through silanes than alkanes.[279] The conclusions from the single molecule Si studies translate to bulk thin films: Klausen and Katz report record-setting mobilities in crystalline oligosilane films and observe no charge transport in alkane films.[280] These experiments are directly relevant to the proposed work because a similar mechanism (variable range hopping) is considered the dominant charge transport mechanism in both molecular silicon and CQD materials,[281] whereby device mobility exponentially decreases with increasing ligand length, portending electrical compatibility of these components within the hybrid materials proposed here.

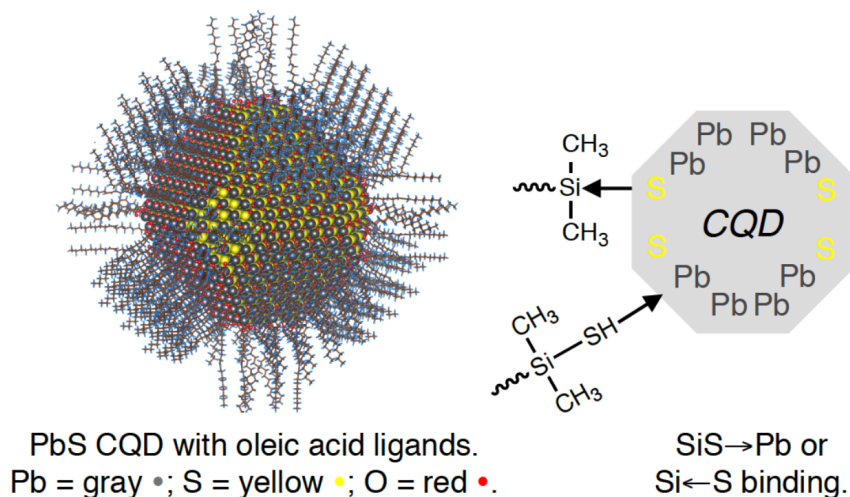


Figure 4.17: Schematic of colloidal quantum dot showing Pb-rich surfaces and ligand binding sites.

Our design for novel conductive ligands is a chain of Si atoms capped at one or both termini with a chemical group (thiol, or SH, Figure 4.16) designed to bind more strongly to Pb on the CQD surfaces than organic oleates. Ligands capped at only one end should maintain isolated CQDs, while difunctionalized ligands could yield a network of cross-linked quantum dots.[279] Difunctionalized ligands and ligands with different numbers of Si atoms are the focus of ongoing work. Molecular silicon is often considered unstable due to a propensity for oxidation; our novel approach to this issue is to coat the Si atoms with methyl (CH₃) groups for solubility and protection from oxidation.[282]

4.4.2 Exchange Results and Discussion

PbS CQDs are synthesized following previously established procedures.[195] These procedures yield size-tuned nanocrystals (with exciton peak ~950) that

have Pb-rich surfaces capped with oleic acid ligands (Figure 4.17). We perform solution-phase a ligand exchange to replace the oleic acid ligands with silicon ligands. We achieve this using a biphasic solution ligand exchange.

Figure 4.18a shows the monofunctionalized silicon ligand employed in this exchange procedure. Figure 4.18b shows the biphasic solutions with octane and DMSO as the component solvents in the exchange. Initially, the oleate-capped CQDs are in the octane phase and the silicon ligands are in the DMSO phase. After vortexing, the CQDs migrate to the DMSO phase and are stabilized by the silicon ligands. The oleic acid is left behind in the octane phase. Subsequent addition of toluene and centrifugation are performed to precipitate the CQDs, and the precipitate was redispersed in DMSO.

Figure 4.20 shows the FTIR spectroscopy data comparing the as-synthesized PbS CQDs to the Si-exchanged QDs. The silicon ligands and oleic acid ligands are plotted for comparison as well. Different spectral bands for molecular bonds are highlighted to emphasize differences in the spectra. Most importantly, the Si-CH₃ and Si-C bands show significant differences in the QDs before and after the ligand exchange. These signatures, unique to the silicon ligands, are seen in the post-exchanged QDs thus providing evidence of the exchange occurring.

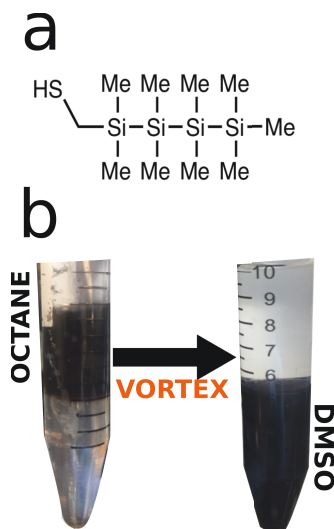


Figure 4.18: Architecture of colloidal quantum dot solar cell device employing silicon-based ligands.

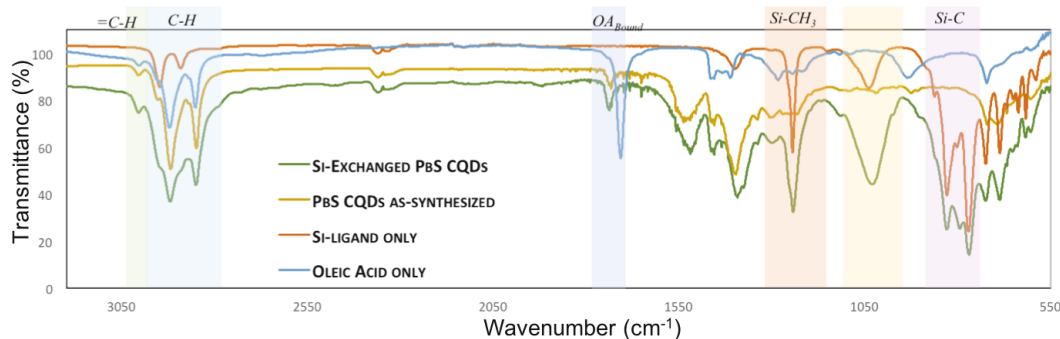


Figure 4.19: FTIR spectra of PbS nanocrystals before and after silicon ligand exchange, as well as reference silicon ligand and oleic acid ligand reference spectra.

4.4.3 Future Work and Outlook

4.4.3.1 Future Work

Absorbance and photoluminescence studies will characterize optical properties of solutions and films. The composite materials will also be characterized by X-ray photoelectron spectroscopy (XPS) to confirm elemental composition. Electron and atomic force microscopy will be used to characterize film structure. In addition to their crucial role in charge transport, ligands can modify CQD energy levels and absorptivity. While alkanes do not strongly absorb ultraviolet or visible light, oligosilanes do. Both the position of maximum absorbance and the extinction coefficient increase with the number of Si atoms in the chain, evidence that molecular silicon has a smaller optical band gap than carbon

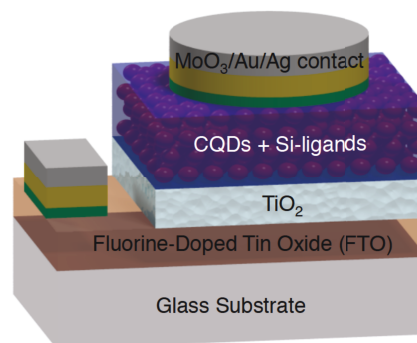


Figure 4.20: Architecture of colloidal quantum dot solar cell device employing silicon-based ligands.

which could beneficially increase absorptivity in the composite films. Ultraviolet photoelectron spectroscopy (UPS) will measure the valence band edge and Fermi level in composite films to determine ligand influence on electronic structure, a critical parameter for photovoltaic device engineering.

To test our hypothesis, we will fabricate and characterize solar cells based on Si-CQD films as the absorbing material. Their performance will be compared to CQD solar cells employing traditional carbon-based ligands. Our solar cells will be based on a typical solar cell architecture[7] (Figure 4.20). The solar cell figures of merit will be measured, with the long-term goal of achieving record power conversion efficiency for a CQD solar cell.

Fundamental characterization of performance-limiting charge-carrier traps, their effects on charge-carrier lifetimes, and how they are determined by material architecture is critical to diagnosing and improving CQD photovoltaic device performance. Bragg's lab will use a combination of transient electronic absorption and "pump-push" photocurrent spectroscopies[283, 284] to probe fundamental charge-transfer processes and charge-carrier trapping. Both techniques use an ultrafast laser pulse to initiate charge transfer that underlies photovoltaic behavior and a second pulse to interrogate the kinetics and properties of charges. Transient changes in absorption of free and trapped charge carriers (as probed by evolution in photoinduced reflectance of infrared pulses, R) will be used to deduce their lifetimes. Impacts on the photocurrent, I , to the action of photoinduced detrapping of charge carriers will be measured over the lifetime of charge carriers in order to interrogate the formation and depth of charge traps.

4.4.3.2 Outlook

This project, based on an entirely new concept in ligand design, demonstrates nanostructured optically active and electronically conductive thin films for photovoltaics. It has the potential to resolve a performance-limiting factor in CQD photovoltaics by breaking a compromise between film conductivity and absorption, thereby enabling widespread cost-effective implementation of solar energy harvesting. The relevance of such an advance is not limited to solar cells, but could be extended to other optoelectronic technologies in the future, including light emitting diodes, lasers, and photodetectors. Developing tunable, highly conductive materials in which light emission efficiency does not have to be sacrificed for charge injection efficiency could have a potentially transformative effect on display technologies. The long-term vision of combining semiconductor-like charge transport with the tunable optical properties of nanomaterials would be a paradigm-shifting advancement in the fields of flexible electronics and renewable energy generation.

References

- [1] Dieter Wöhrlé and Dieter Meissner. “Organic solar cells”. In: *Advanced Materials* 3.3 (1991), pp. 129–138.
- [2] Serap Günes, Helmut Neugebauer, and Niyazi Serdar Sariciftci. “Conjugated polymer-based organic solar cells”. In: *Chemical reviews* 107.4 (2007), pp. 1324–1338.
- [3] Harald Hoppe and Niyazi Serdar Sariciftci. “Organic solar cells: An overview”. In: *Journal of materials research* 19.7 (2004), pp. 1924–1945.
- [4] Martin A Green, Anita Ho-Baillie, and Henry J Snaith. “The emergence of perovskite solar cells”. In: *Nature Photonics* 8.7 (2014), nphoton–2014.
- [5] Huanping Zhou, Qi Chen, Gang Li, Song Luo, Tze-bing Song, Hsin-Sheng Duan, Ziruo Hong, Jingbi You, Yongsheng Liu, and Yang Yang. “Interface engineering of highly efficient perovskite solar cells”. In: *Science* 345.6196 (2014), pp. 542–546.
- [6] Mingzhen Liu, Michael B Johnston, and Henry J Snaith. “Efficient planar heterojunction perovskite solar cells by vapour deposition”. In: *Nature* 501.7467 (2013), p. 395.
- [7] Andras G Pattantyus-Abraham, Illan J Kramer, Aaron R Barkhouse, Xihua Wang, Gerasimos Konstantatos, Ratan Debnath, Larissa Levina, Ines Raabe, Mohammad K Nazeeruddin, Michael Gratzel, et al. “Depleted-heterojunction colloidal quantum dot solar cells”. In: *ACS nano* 4.6 (2010), pp. 3374–3380.
- [8] Yan Cheng, Ebuka S Arinze, Nathan Palmquist, and Susanna M Thon. “Advancing colloidal quantum dot photovoltaic technology”. In: *Nanophotonics* 5.1 (2016), pp. 31–54.

REFERENCES

- [9] Ebuka S Arinze, Botong Qiu, Gabrielle Nyirjesy, and Susanna M Thon. "Plasmonic nanoparticle enhancement of solution-processed solar cells: practical limits and opportunities". In: *ACS Photonics* 3.2 (2016), pp. 158–173.
- [10] D Aaron R Barkhouse, Andras G Pattantyus-Abraham, Larissa Levina, and Edward H Sargent. "Thiols passivate recombination centers in colloidal quantum dots leading to enhanced photovoltaic device efficiency". In: *ACS nano* 2.11 (2008), pp. 2356–2362.
- [11] Sung Heum Park, Anshuman Roy, Serge Beaupré, Shinuk Cho, Nelson Coates, Ji Sun Moon, Daniel Moses, Mario Leclerc, Kwanghee Lee, and Alan J Heeger. "Bulk heterojunction solar cells with internal quantum efficiency approaching 100%". In: *Nature photonics* 3.5 (2009), p. 297.
- [12] Yongye Liang, Danqin Feng, Yue Wu, Szu-Ting Tsai, Gang Li, Claire Ray, and Luping Yu. "Highly efficient solar cell polymers developed via fine-tuning of structural and electronic properties". In: *Journal of the American Chemical Society* 131.22 (2009), pp. 7792–7799.
- [13] Michael M Lee, Joël Teuscher, Tsutomu Miyasaka, Takuro N Murakami, and Henry J Snaith. "Efficient hybrid solar cells based on meso-structured organometal halide perovskites". In: *Science* (2012), p. 1228604.
- [14] Paul Heremans, David Cheyns, and Barry P Rand. "Strategies for increasing the efficiency of heterojunction organic solar cells: material selection and device architecture". In: *Accounts of chemical research* 42.11 (2009), pp. 1740–1747.
- [15] Jin Young Kim, Sun Hee Kim, H-H Lee, Kwanghee Lee, Wanli Ma, Xiong Gong, and Alan J Heeger. "New architecture for high-efficiency polymer photovoltaic cells using solution-based titanium oxide as an optical spacer". In: *Advanced materials* 18.5 (2006), pp. 572–576.
- [16] Illan J Kramer and Edward H Sargent. "The architecture of colloidal quantum dot solar cells: materials to devices". In: *Chemical reviews* 114.1 (2013), pp. 863–882.
- [17] Jeong-Hyeok Im, Chang-Ryul Lee, Jin-Wook Lee, Sang-Won Park, and Nam-Gyu Park. "6.5% efficient perovskite quantum-dot-sensitized solar cell". In: *Nanoscale* 3.10 (2011), pp. 4088–4093.

REFERENCES

- [18] Jin Hyuck Heo, Sang Hyuk Im, Jun Hong Noh, Tarak N Mandal, Choong-Sun Lim, Jeong Ah Chang, Yong Hui Lee, Hi-jung Kim, Arpita Sarkar, Md K Nazeeruddin, et al. "Efficient inorganic-organic hybrid heterojunction solar cells containing perovskite compound and polymeric hole conductors". In: *Nature photonics* 7.6 (2013), p. 486.
- [19] Ali Dabirian and Nima Taghavinia. "Theoretical study of light trapping in nanostructured thin film solar cells using wavelength-scale silver particles". In: *ACS applied materials & interfaces* 7.27 (2015), pp. 14926–14932.
- [20] Michael Niggemann, Moritz Riede, Andreas Gombert, and Karl Leo. "Light trapping in organic solar cells". In: *physica status solidi (a)* 205.12 (2008), pp. 2862–2874.
- [21] Seung-Bum Rim, Shanbin Zhao, Shawn R Scully, Michael D McGehee, and Peter Peumans. "An effective light trapping configuration for thin-film solar cells". In: *Applied Physics Letters* 91.24 (2007), p. 243501.
- [22] Albert Polman and Harry A Atwater. "Photonic design principles for ultrahigh-efficiency photovoltaics". In: *Nature materials* 11.3 (2012), p. 174.
- [23] Chun-Hsien Chou and Fang-Chung Chen. "Plasmonic nanostructures for light trapping in organic photovoltaic devices". In: *Nanoscale* 6.15 (2014), pp. 8444–8458.
- [24] Wei Zhang, Michael Saliba, Samuel D Stranks, Yao Sun, Xian Shi, Ulrich Wiesner, and Henry J Snaith. "Enhancement of perovskite-based solar cells employing core-shell metal nanoparticles". In: *Nano letters* 13.9 (2013), pp. 4505–4510.
- [25] Harry A Atwater. "The promise of plasmonics". In: *Scientific American* 296.4 (2007), pp. 56–62.
- [26] Dmitri K Gramotnev and Sergey I Bozhevolnyi. "Plasmonics beyond the diffraction limit". In: *Nature photonics* 4.2 (2010), p. 83.
- [27] Jon A Schuller, Edward S Barnard, Wenshan Cai, Young Chul Jun, Justin S White, and Mark L Brongersma. "Plasmonics for extreme light concentration and manipulation". In: *Nature materials* 9.3 (2010), p. 193.
- [28] Stefan A Maier and Harry A Atwater. "Plasmonics: Localization and guiding of electromagnetic energy in metal/dielectric structures". In: *Journal of applied physics* 98.1 (2005), p. 10.

REFERENCES

- [29] Ekmel Ozbay. "Plasmonics: merging photonics and electronics at nanoscale dimensions". In: *science* 311.5758 (2006), pp. 189–193.
- [30] Stefan Alexander Maier. *Plasmonics: fundamentals and applications*. Springer Science & Business Media, 2007.
- [31] Ching W Tang. "Two-layer organic photovoltaic cell". In: *Applied Physics Letters* 48.2 (1986), pp. 183–185.
- [32] Wade A Luhman and Russell J Holmes. "Investigation of energy transfer in organic photovoltaic cells and impact on exciton diffusion length measurements". In: *Advanced Functional Materials* 21.4 (2011), pp. 764–771.
- [33] Oleksandr V Mikhnenko, Hamed Azimi, Markus Scharber, Mauro Morana, Paul WM Blom, and Maria Antonietta Loi. "Exciton diffusion length in narrow bandgap polymers". In: *Energy & Environmental Science* 5.5 (2012), pp. 6960–6965.
- [34] Thomas Stübinger and Wolfgang Brütting. "Exciton diffusion and optical interference in organic donor–acceptor photovoltaic cells". In: *Journal of Applied Physics* 90.7 (2001), pp. 3632–3641.
- [35] Richard R Lunt, Noel C Giebink, Anna A Belak, Jay B Benziger, and Stephen R Forrest. "Exciton diffusion lengths of organic semiconductor thin films measured by spectrally resolved photoluminescence quenching". In: *Journal of Applied Physics* 105.5 (2009), p. 053711.
- [36] Paul E Shaw, Arvydas Ruseckas, and Ifor DW Samuel. "Exciton diffusion measurements in poly (3-hexylthiophene)". In: *Advanced Materials* 20.18 (2008), pp. 3516–3520.
- [37] Masahiro Hiramoto, Hiroshi Fujiwara, and Masaaki Yokoyama. "p-i-n like behavior in three-layered organic solar cells having a co-deposited interlayer of pigments". In: *Journal of applied physics* 72.8 (1992), pp. 3781–3787.
- [38] JJM Halls, CA Walsh, Neil C Greenham, EA Marseglia, Richard H Friend, SC Moratti, and AB Holmes. "Efficient photodiodes from interpenetrating polymer networks". In: *Nature* 376.6540 (1995), p. 498.
- [39] Jeffery Peet, C Soci, RC Coffin, TQ Nguyen, A Mikhailovsky, Daniel Moses, and Guillermo C Bazan. "Method for increasing the photoconductive response in conjugated polymer/fullerene composites". In: *Applied physics letters* 89.25 (2006), p. 252105.

REFERENCES

- [40] Jeffery Peet, Jin Young Kim, Nelson E Coates, Wang Li Ma, Daniel Moses, Alan J Heeger, and Guillermo C Bazan. "Efficiency enhancement in low-bandgap polymer solar cells by processing with alkane dithiols". In: *Nature materials* 6.7 (2007), p. 497.
- [41] Wei Chen, Maxim P Nikiforov, and Seth B Darling. "Morphology characterization in organic and hybrid solar cells". In: *Energy & Environmental Science* 5.8 (2012), pp. 8045–8074.
- [42] Jiang Tang, Huan Liu, David Zhitomirsky, Sjoerd Hoogland, Xihua Wang, Melissa Furukawa, Larissa Levina, and Edward H Sargent. "Quantum junction solar cells". In: *Nano letters* 12.9 (2012), pp. 4889–4894.
- [43] Chia-Hao M Chuang, Patrick R Brown, Vladimir Bulović, and Mounsi G Bawendi. "Improved performance and stability in quantum dot solar cells through band alignment engineering". In: *Nature materials* 13.8 (2014), p. 796.
- [44] David Zhitomirsky, Oleksandr Voznyy, Larissa Levina, Sjoerd Hoogland, Kyle W Kemp, Alexander H Ip, Susanna M Thon, and Edward H Sargent. "Engineering colloidal quantum dot solids within and beyond the mobility-invariant regime". In: *Nature communications* 5 (2014), p. 3803.
- [45] Hui-Seon Kim, Chang-Ryul Lee, Jeong-Hyeok Im, Ki-Beom Lee, Thomas Moehl, Arianna Marchioro, Soo-Jin Moon, Robin Humphry-Baker, Jun-Ho Yum, Jacques E Moser, et al. "Lead iodide perovskite sensitized all-solid-state submicron thin film mesoscopic solar cell with efficiency exceeding 9%". In: *Scientific reports* 2 (2012), p. 591.
- [46] Dongqin Bi, Soo-Jin Moon, Leif Häggman, Gerrit Boschloo, Lei Yang, Erik MJ Johansson, Mohammad K Nazeeruddin, Michael Grätzel, and Anders Hagfeldt. "Using a two-step deposition technique to prepare perovskite (CH₃NH₃PbI₃) for thin film solar cells based on ZrO₂ and TiO₂ mesostructures". In: *Rsc Advances* 3.41 (2013), pp. 18762–18766.
- [47] Jun Hong Noh, Sang Hyuk Im, Jin Hyuck Heo, Tarak N Mandal, and Sang Il Seok. "Chemical management for colorful, efficient, and stable inorganic–organic hybrid nanostructured solar cells". In: *Nano letters* 13.4 (2013), pp. 1764–1769.

REFERENCES

- [48] Lioz Etgar, Peng Gao, Zhaosheng Xue, Qin Peng, Aravind Kumar Chandiran, Bin Liu, Md K Nazeeruddin, and Michael Gratzel. "Mesoscopic CH₃NH₃PbI₃/TiO₂ heterojunction solar cells". In: *Journal of the American Chemical Society* 134.42 (2012), pp. 17396–17399.
- [49] Matthew J Carnie, Cecile Charbonneau, Matthew L Davies, Joel Troughton, Trystan M Watson, Konrad Wojciechowski, Henry Snaith, and David A Worsley. "A one-step low temperature processing route for organolead halide perovskite solar cells". In: *Chemical communications* 49.72 (2013), pp. 7893–7895.
- [50] James M Ball, Michael M Lee, Andrew Hey, and Henry J Snaith. "Low-temperature processed meso-superstructured to thin-film perovskite solar cells". In: *Energy & Environmental Science* 6.6 (2013), pp. 1739–1743.
- [51] Dong Shi, Valerio Adinolfi, Riccardo Comin, Mingjian Yuan, Erkki Alarousu, Andrei Buin, Yin Chen, Sjoerd Hoogland, Alexander Rothenberger, Khabiboulakh Katsiev, et al. "Low trap-state density and long carrier diffusion in organolead trihalide perovskite single crystals". In: *Science* 347.6221 (2015), pp. 519–522.
- [52] Wanyi Nie, Hsinhan Tsai, Reza Asadpour, Jean-Christophe Blancon, Amanda J Neukirch, Gautam Gupta, Jared J Crochet, Manish Chhowalla, Sergei Tretiak, Muhammad A Alam, et al. "High-efficiency solution-processed perovskite solar cells with millimeter-scale grains". In: *Science* 347.6221 (2015), pp. 522–525.
- [53] Eli Yablonovitch. "Statistical ray optics". In: *JOSA* 72.7 (1982), pp. 899–907.
- [54] Adolf Goetzberger. "Optical confinement in thin Si-solar cells by diffuse back reflectors". In: *15th Photovoltaic Specialists Conference*. 1981, pp. 867–870.
- [55] Patrick Campbell and Martin A Green. "The limiting efficiency of silicon solar cells under concentrated sunlight". In: *IEEE Transactions on Electron Devices* 33.2 (1986), pp. 234–239.
- [56] Carl Halgglund, S Peter Apell, and Bengt Kasemo. "Maximized optical absorption in ultrathin films and its application to plasmon-based two-dimensional photovoltaics". In: *Nano letters* 10.8 (2010), pp. 3135–3141.

REFERENCES

- [57] Zongfu Yu, Aaswath Raman, and Shanhui Fan. "Fundamental limit of nanophotonic light trapping in solar cells". In: *Proceedings of the National Academy of Sciences* 107.41 (2010), pp. 17491–17496.
- [58] Dennis M Callahan, Jeremy N Munday, and Harry A Atwater. "Solar cell light trapping beyond the ray optic limit". In: *Nano letters* 12.1 (2012), pp. 214–218.
- [59] Christian S Schuster, Angelo Bozzola, Lucio C Andreani, and Thomas F Krauss. "How to assess light trapping structures versus a Lambertian Scatterer for solar cells?" In: *Optics Express* 22.102 (2014), A542–A551.
- [60] Surbhi Lal, Stephan Link, and Naomi J Halas. "Nano-optics from sensing to waveguiding". In: *Nature photonics* 1.11 (2007), p. 641.
- [61] AV Kabashin, P Evans, S Pastkovsky, W Hendren, GA Wurtz, R Atkinson, R Pollard, VA Podolskiy, and AV Zayats. "Plasmonic nanorod metamaterials for biosensing". In: *Nature materials* 8.11 (2009), p. 867.
- [62] Na Liu, Thomas Weiss, Martin Mesch, Lutz Langguth, Ulrike Eigenthaler, Michael Hirscher, Carsten Sonnichsen, and Harald Giessen. "Planar metamaterial analogue of electromagnetically induced transparency for plasmonic sensing". In: *Nano letters* 10.4 (2009), pp. 1103–1107.
- [63] Min-Ki Kwon, Ja-Yeon Kim, Baek-Hyun Kim, Il-Kyu Park, Chu-Young Cho, Clare Chisu Byeon, and Seong-Ju Park. "Surface-plasmon-enhanced light-emitting diodes". In: *Advanced Materials* 20.7 (2008), pp. 1253–1257.
- [64] Koichi Okamoto, Isamu Niki, Alexander Shvartser, Yukio Narukawa, Takashi Mukai, and Axel Scherer. "Surface-plasmon-enhanced light emitters based on InGaN quantum wells". In: *Nature materials* 3.9 (2004), p. 601.
- [65] Jelena Vučković, Marko Lončar, and Axel Scherer. "Surface plasmon enhanced light-emitting diode". In: *IEEE Journal of Quantum Electronics* 36.10 (2000), pp. 1131–1144.
- [66] Rupert F Oulton, Volker J Sorger, Thomas Zentgraf, Ren-Min Ma, Christopher Gladden, Lun Dai, Guy Bartal, and Xiang Zhang. "Plasmon lasers at deep subwavelength scale". In: *Nature* 461.7264 (2009), p. 629.

REFERENCES

- [67] Ren-Min Ma, Rupert F Oulton, Volker J Sorger, Guy Bartal, and Xiang Zhang. "Room-temperature sub-diffraction-limited plasmon laser by total internal reflection". In: *Nature materials* 10.2 (2011), p. 110.
- [68] Malte C Gather. "A rocky road to plasmonic lasers". In: *Nature Photonics* 6.11 (2012), p. 708.
- [69] Gerasimos Konstantatos and Edward H Sargent. "Nanostructured materials for photon detection". In: *Nature nanotechnology* 5.6 (2010), p. 391.
- [70] Rashid Zia, Jon A Schuller, Anu Chandran, and Mark L Brongersma. "Plasmonics: the next chip-scale technology". In: *Materials today* 9.7-8 (2006), pp. 20–27.
- [71] Harry A Atwater and Albert Polman. "Plasmonics for improved photovoltaic devices". In: *Nature materials* 9.3 (2010), p. 205.
- [72] S Pillai, and MA Green. "Plasmonics for photovoltaic applications". In: *Solar Energy Materials and Solar Cells* 94.9 (2010), pp. 1481–1486.
- [73] R Santbergen, TL Temple, R Liang, AHM Smets, RACMM Van Swaaij, and M Zeman. "Application of plasmonic silver island films in thin-film silicon solar cells". In: *Journal of Optics* 14.2 (2012), p. 024010.
- [74] Vivian E Ferry, Jeremy N Munday, and Harry A Atwater. "Design considerations for plasmonic photovoltaics". In: *Advanced materials* 22.43 (2010), pp. 4794–4808.
- [75] Keisuke Nakayama, Katsuaki Tanabe, and Harry A Atwater. "Plasmonic nanoparticle enhanced light absorption in GaAs solar cells". In: *Applied Physics Letters* 93.12 (2008), p. 121904.
- [76] Martin A Green and Supriya Pillai. "Harnessing plasmonics for solar cells". In: *Nature Photonics* 6.3 (2012), p. 130.
- [77] Vivian E Ferry, Luke A Sweatlock, Domenico Pacifici, and Harry A Atwater. "Plasmonic nanostructure design for efficient light coupling into solar cells". In: *Nano letters* 8.12 (2008), pp. 4391–4397.
- [78] Vivian E Ferry, Marc A Verschuuren, Hongbo BT Li, Ruud EI Schropp, Harry A Atwater, and Albert Polman. "Improved red-response in thin film a-Si: H solar cells with soft-imprinted plasmonic back reflectors". In: *Applied Physics Letters* 95.18 (2009), p. 183503.

REFERENCES

- [79] V Giannini, Y Zhang, M Forcales, and J Gómez Rivas. “Long-range surface polaritons in ultra-thin films of silicon”. In: *Optics Express* 16.24 (2008), pp. 19674–19685.
- [80] Xi Chen, Baohua Jia, Jhantu K Saha, Boyuan Cai, Nicholas Stokes, Qi Qiao, Yongqian Wang, Zhengrong Shi, and Min Gu. “Broadband enhancement in thin-film amorphous silicon solar cells enabled by nucleated silver nanoparticles”. In: *Nano letters* 12.5 (2012), pp. 2187–2192.
- [81] Yang Wang, Tianyi Sun, Trilochan Paudel, Yi Zhang, Zhifeng Ren, and Krzysztof Kempa. “Metamaterial-plasmonic absorber structure for high efficiency amorphous silicon solar cells”. In: *Nano letters* 12.1 (2011), pp. 440–445.
- [82] Hairen Tan, Rudi Santbergen, Arno HM Smets, and Miro Zeman. “Plasmonic light trapping in thin-film silicon solar cells with improved self-assembled silver nanoparticles”. In: *Nano letters* 12.8 (2012), pp. 4070–4076.
- [83] Dong Hwan Wang, Do Youb Kim, Kyeong Woo Choi, Jung Hwa Seo, Sang Hyuk Im, Jong Hyeok Park, O Ok Park, and Alan J Heeger. “Enhancement of donor–acceptor polymer bulk heterojunction solar cell power conversion efficiencies by addition of Au nanoparticles”. In: *Angewandte Chemie International Edition* 50.24 (2011), pp. 5519–5523.
- [84] Dong Hwan Wang, Keum Hwan Park, Jung Hwa Seo, Jason Seifter, Ji Hye Jeon, Jung Kyu Kim, Jong Hyeok Park, O Ok Park, and Alan J Heeger. “Enhanced power conversion efficiency in PCDTBT/PC70BM bulk heterojunction photovoltaic devices with embedded silver nanoparticle clusters”. In: *Advanced Energy Materials* 1.5 (2011), pp. 766–770.
- [85] Charlie CD Wang, Wallace CH Choy, Chunhui Duan, Dixon DS Fung, EI Wei, Feng-Xian Xie, Fei Huang, and Yong Cao. “Optical and electrical effects of gold nanoparticles in the active layer of polymer solar cells”. In: *Journal of Materials Chemistry* 22.3 (2012), pp. 1206–1211.
- [86] Chu-Chen Chueh, Chang-Zhi Li, and Alex K-Y Jen. “Recent progress and perspective in solution-processed Interfacial materials for efficient and stable polymer and organometal perovskite solar cells”. In: *Energy & Environmental Science* 8.4 (2015), pp. 1160–1189.

REFERENCES

- [87] Qiaoqiang Gan, Filbert J Bartoli, and Zakya H Kafafi. "Plasmonic-enhanced organic photovoltaics: Breaking the 10% efficiency barrier". In: *Advanced materials* 25.17 (2013), pp. 2385–2396.
- [88] Jingbi You, Xuanhua Li, Feng-xian Xie, Wei EI Sha, Johnson HW Kwong, Gang Li, Wallace CH Choy, and Yang Yang. "Surface Plasmon and Scattering-Enhanced Low-Bandgap Polymer Solar Cell by a Metal Grating Back Electrode". In: *Advanced Energy Materials* 2.10 (2012), pp. 1203–1207.
- [89] Xuanhua Li, Wallace CH Choy, Lijun Huo, Fengxian Xie, Wei EI Sha, Baofu Ding, Xia Guo, Yongfang Li, Jianhui Hou, Jingbi You, et al. "Dual plasmonic nanostructures for high performance inverted organic solar cells". In: *Advanced Materials* 24.22 (2012), pp. 3046–3052.
- [90] Manuel J Mendes, Seweryn Morawiec, Francesca Simone, Francesco Priolo, and Isodiana Crupi. "Colloidal plasmonic back reflectors for light trapping in solar cells". In: *Nanoscale* 6.9 (2014), pp. 4796–4805.
- [91] Gholamhosain Haidari, Morteza Hajimahmoodzadeh, Hamid Reza Fallah, and Mohsen Ghasemi Varnamkhashti. "Effective medium analysis of thermally evaporated Ag nanoparticle films for plasmonic enhancement in organic solar cell". In: *Superlattices and Microstructures* 85 (2015), pp. 294–304.
- [92] Gholamhosain Haidari, Morteza Hajimahmoodzadeh, Hamid Reza Fallah, Andreas Peukert, Alina Chanaewa, and Elizabeth von Hauff. "Thermally evaporated Ag nanoparticle films for plasmonic enhancement in organic solar cells: effects of particle geometry". In: *physica status solidi (RRL)–Rapid Research Letters* 9.3 (2015), pp. 161–165.
- [93] Bjoern Niesen, Barry P Rand, Pol Van Dorpe, David Cheyns, Lianming Tong, Alexandre Dmitriev, and Paul Heremans. "Plasmonic efficiency enhancement of high performance organic solar cells with a nanostructured rear electrode". In: *Advanced Energy Materials* 3.2 (2013), pp. 145–150.
- [94] Kinam Jung, Hyung-Jun Song, Gunhee Lee, Youngjun Ko, KwangJun Ahn, Hoseop Choi, Jun Young Kim, Kyungyeon Ha, Jiyun Song, Jong-Kwon Lee, et al. "Plasmonic organic solar cells employing nanobump assembly via aerosol-derived nanoparticles". In: *ACS nano* 8.3 (2014), pp. 2590–2601.

REFERENCES

- [95] Fiona J Beck, Alexandros Stavriniadis, Silke L Diedenhofen, Tania Lasanta, and Gerasimos Konstantatos. "Surface plasmon polariton couplers for light trapping in thin-film absorbers and their application to colloidal quantum dot optoelectronics". In: *ACS Photonics* 1.11 (2014), pp. 1197–1205.
- [96] Michael Salvador, Bradley A MacLeod, Angela Hess, Abhishek P Kulkarni, Keiko Munechika, Jennifer IL Chen, and David S Ginger. "Electron accumulation on metal nanoparticles in plasmon-enhanced organic solar cells". In: *ACS nano* 6.11 (2012), pp. 10024–10032.
- [97] Daniel Paz-Soldan, Anna Lee, Susanna M Thon, Michael M Adachi, Haopeng Dong, Pouya Maraghechi, Mingjian Yuan, AndreË J Labelle, Sjoerd Hoogland, Kun Liu, et al. "Jointly tuned plasmonic–excitonic photovoltaics using nanoshells". In: *Nano letters* 13.4 (2013), pp. 1502–1508.
- [98] Michael Saliba, Wei Zhang, Victor M Burlakov, Samuel D Stranks, Yao Sun, James M Ball, Michael B Johnston, Alain Goriely, Ulrich Wiesner, and Henry J Snaith. "Plasmonic-Induced Photon Recycling in Metal Halide Perovskite Solar Cells". In: *Advanced Functional Materials* 25.31 (2015), pp. 5038–5046.
- [99] Abhishek P Kulkarni, Kevin M Noone, Keiko Munechika, Samuel R Guyer, and David S Ginger. "Plasmon-enhanced charge carrier generation in organic photovoltaic films using silver nanoprisms". In: *Nano letters* 10.4 (2010), pp. 1501–1505.
- [100] TJ Echtermeyer, L Britnell, PK Jasnos, A Lombardo, RV Gorbachev, AN Grigorenko, AK Geim, AC Ferrari, and KS Novoselov. "Strong plasmonic enhancement of photovoltage in graphene". In: *Nature communications* 2 (2011), p. 458.
- [101] Fang-Chung Chen, Jyh-Lih Wu, Chia-Ling Lee, Yi Hong, Chun-Hong Kuo, and Michael H Huang. "Plasmonic-enhanced polymer photovoltaic devices incorporating solution-processable metal nanoparticles". In: *Applied Physics Letters* 95.1 (2009), p. 182.
- [102] Woo-Jun Yoon, Kyung-Young Jung, Jiwen Liu, Thirumalai Duraisamy, Rao Revur, Fernando L Teixeira, Suvankar Sengupta, and Paul R Berger. "Plasmon-enhanced optical absorption and photocurrent in organic bulk heterojunction photovoltaic devices using self-assembled layer of silver nanoparticles". In: *Solar Energy Materials and Solar Cells* 94.2 (2010), pp. 128–132.

REFERENCES

- [103] Nathan C Lindquist, Wade A Luhman, Sang-Hyun Oh, and Russell J Holmes. "Plasmonic nanocavity arrays for enhanced efficiency in organic photovoltaic cells". In: *Applied Physics Letters* 93.12 (2008), p. 350.
- [104] Yu A Akimov, K Ostrikov, and EP Li. "Surface plasmon enhancement of optical absorption in thin-film silicon solar cells". In: *Plasmonics* 4.2 (2009), pp. 107–113.
- [105] Carl Haillgglund, Gabriel Zeltzer, Ricardo Ruiz, Isabell Thomann, Han-Bo-Ram Lee, Mark L Brongersma, and Stacey F Bent. "Self-assembly based plasmonic arrays tuned by atomic layer deposition for extreme visible light absorption". In: *Nano letters* 13.7 (2013), pp. 3352–3357.
- [106] Sang Eon Han and Gang Chen. "Toward the Lambertian limit of light trapping in thin nanostructured silicon solar cells". In: *Nano letters* 10.11 (2010), pp. 4692–4696.
- [107] C Ciraci, RT Hill, JJ Mock, Y Urzhumov, AI Fernández-Domínguez, SA Maier, JB Pendry, A Chilkoti, and DR Smith. "Probing the ultimate limits of plasmonic enhancement". In: *Science* 337.6098 (2012), pp. 1072–1074.
- [108] Durmus U Karatay, Michael Salvador, Kai Yao, Alex K-Y Jen, and David S Ginger. "Performance limits of plasmon-enhanced organic photovoltaics". In: *Applied Physics Letters* 105.3 (2014), 109_1.
- [109] Mattias Marklund, Gert Brodin, Lennart Stenflo, and Chuan S Liu. "New quantum limits in plasmonic devices". In: *EPL (Europhysics Letters)* 84.1 (2008), p. 17006.
- [110] Jyh-Lih Wu, Fang-Chung Chen, Yu-Sheng Hsiao, Fan-Ching Chien, Peilin Chen, Chun-Hong Kuo, Michael H Huang, and Chain-Shu Hsu. "Surface plasmonic effects of metallic nanoparticles on the performance of polymer bulk heterojunction solar cells". In: *ACS nano* 5.2 (2011), pp. 959–967.
- [111] Mei Xue, Lu Li, Bertrand J Tremolet de Villers, Huajun Shen, Jinfeng Zhu, Zhibin Yu, Adam Z Stieg, Qibing Pei, Benjamin J Schwartz, and Kang L Wang. "Charge-carrier dynamics in hybrid plasmonic organic solar cells with Ag nanoparticles". In: *Applied Physics Letters* 98.25 (2011), p. 119.

REFERENCES

- [112] Soo Won Heo, Eui Jin Lee, Kwan Wook Song, Jang Yong Lee, and Doo Kyung Moon. "Enhanced carrier mobility and photon-harvesting property by introducing Au nano-particles in bulk heterojunction photovoltaic cells". In: *Organic Electronics* 14.8 (2013), pp. 1931–1938.
- [113] Xuanhua Li, Wallace Chik Ho Choy, Haifei Lu, Wei El Sha, and Aaron Ho Pui Ho. "Efficiency Enhancement of Organic Solar Cells by Using Shape-Dependent Broadband Plasmonic Absorption in Metallic Nanoparticles". In: *Advanced Functional Materials* 23.21 (2013), pp. 2728–2735.
- [114] Wanjung Kim, Bong Geun Cha, Jung Kyu Kim, Woonggi Kang, Eun-chul Kim, Tae Kyu Ahn, Dong Hwan Wang, Qing Guo Du, Jeong Ho Cho, Jaeyun Kim, et al. "Tailoring dispersion and aggregation of Au nanoparticles in the BHJ layer of polymer solar cells: Plasmon effects versus electrical effects". In: *ChemSusChem* 7.12 (2014), pp. 3452–3458.
- [115] Zelin Lu, Xujie Pan, Yingzhuang Ma, Yu Li, Lingling Zheng, Danfei Zhang, Qi Xu, Zhijian Chen, Shufeng Wang, Bo Qu, et al. "Plasmonic-enhanced perovskite solar cells using alloy popcorn nanoparticles". In: *RSC Advances* 5.15 (2015), pp. 11175–11179.
- [116] Chao Shen, Hua Tong, Weichuan Gao, Shuanglong Yuan, Guorong Chen, and Yunxia Yang. "Effects of anode structures and fabrication methods on cell efficiencies of CdS/CdSe quantum dot co-sensitized solar cells". In: *Journal of Alloys and Compounds* 644 (2015), pp. 205–210.
- [117] Natalia Kholmicheva, Pavel Moroz, Upendra Rijal, Ebin Bastola, Prakash Uprety, Geethika Liyanage, Anton Razgoniaev, Alexis D Ostrowski, and Mikhail Zamkov. "Plasmonic nanocrystal solar cells utilizing strongly confined radiation". In: *ACS nano* 8.12 (2014), pp. 12549–12559.
- [118] Fiona J Beck, Tania Lasanta, and Gerasimos Konstantatos. "Plasmonic Schottky nanojunctions for tailoring the photogeneration profile in thin film solar cells". In: *Advanced Optical Materials* 2.5 (2014), pp. 493–500.
- [119] Jiang Tang, Kyle W Kemp, Sjoerd Hoogland, Kwang S Jeong, Huan Liu, Larissa Levina, Melissa Furukawa, Xihua Wang, Ratan Debnath, Dongkyu Cha, et al. "Colloidal-quantum-dot photovoltaics using atomic-ligand passivation". In: *Nature materials* 10.10 (2011), p. 765.

REFERENCES

- [120] Xiaoliang Zhang, Jindan Zhang, Jianhua Liu, and Erik MJ Johansson. "Solution processed flexible and bending durable heterojunction colloidal quantum dot solar cell". In: *Nanoscale* 7.27 (2015), pp. 11520–11524.
- [121] Xudong Yao, Yajing Chang, Guopeng Li, Longfei Mi, Shangjing Liu, Hui Wang, Yalan Yu, and Yang Jiang. "Inverted quantum-dot solar cells with depleted heterojunction structure employing CdS as the electron acceptor". In: *Solar Energy Materials and Solar Cells* 137 (2015), pp. 287–292.
- [122] Gi-Hwan Kim, Bright Walker, Hak-Beom Kim, Jin Young Kim, Edward H Sargent, Jongnam Park, and Jin Young Kim. "Inverted colloidal quantum dot solar cells". In: *Advanced Materials* 26.20 (2014), pp. 3321–3327.
- [123] Xinzheng Lan, Silvia Masala, and Edward H Sargent. "Charge-extraction strategies for colloidal quantum dot photovoltaics". In: *Nature materials* 13.3 (2014), p. 233.
- [124] Pouya Maraghechi, André J Labelle, Ahmad R Kirmani, Xinzheng Lan, Michael M Adachi, Susanna M Thon, Sjoerd Hoogland, Anna Lee, Zhijun Ning, Armin Fischer, et al. "The donor–supply electrode enhances performance in colloidal quantum dot solar cells". In: *ACS nano* 7.7 (2013), pp. 6111–6116.
- [125] Zhijun Ning, Oleksandr Voznyy, Jun Pan, Sjoerd Hoogland, Valerio Adinolfi, Jixian Xu, Min Li, Ahmad R Kirmani, Jon-Paul Sun, James Minor, et al. "Air-stable n-type colloidal quantum dot solids". In: *Nature materials* 13.8 (2014), p. 822.
- [126] James M Gee. "The effect of parasitic absorption losses on light trapping in thin silicon solar cells". In: *Photovoltaic Specialists Conference, 1988., Conference Record of the Twentieth IEEE*. IEEE. 1988, pp. 549–554.
- [127] UW Paetzold, F Hallermann, BE Pieters, U Rau, R Carius, and G Von Plessen. "Localized plasmonic losses at metal back contacts of thin-film silicon solar cells". In: *Photonics for Solar Energy Systems III*. Vol. 7725. International Society for Optics and Photonics. 2010, p. 772517.
- [128] Jacob B Khurgin and Alexandra Boltasseva. "Reflecting upon the losses in plasmonics and metamaterials". In: *MRS bulletin* 37.8 (2012), pp. 768–779.

REFERENCES

- [129] U Palanchoke, V Jovanov, H Kurz, R Dewan, P Magnus, Helmut Stiebig, and D Knipp. "Influence of back contact roughness on light trapping and plasmonic losses of randomly textured amorphous silicon thin film solar cells". In: *Applied Physics Letters* 102.8 (2013), p. 083501.
- [130] Peng Du, Pengtao Jing, Di Li, Yinghui Cao, Zhenyu Liu, and Zaicheng Sun. "Plasmonic Ag@ oxide nanoprisms for enhanced performance of organic solar cells". In: *Small* 11.20 (2015), pp. 2454–2462.
- [131] Bo Wu, Nripan Mathews, and Tze Chien Sum. "Ag nanoparticle-blended plasmonic organic solar cells: performance enhancement or detracting?" In: *Physics, Simulation, and Photonic Engineering of Photovoltaic Devices III*. Vol. 8981. International Society for Optics and Photonics. 2014, p. 898111.
- [132] M Magdalena Mandoc, Welmoed Veurman, L Jan Anton Koster, Bert de Boer, and Paul WM Blom. "Origin of the reduced fill factor and photocurrent in MDMO-PPV: PCNEPV all-polymer solar cells". In: *Advanced Functional Materials* 17.13 (2007), pp. 2167–2173.
- [133] Jonathan A Scholl, Ai Leen Koh, and Jennifer A Dionne. "Quantum plasmon resonances of individual metallic nanoparticles". In: *Nature* 483.7390 (2012), p. 421.
- [134] SJ Oldenburg, RD Averitt, SL Westcott, and NJ Halas. "Nanoengineering of optical resonances". In: *Chemical Physics Letters* 288.2-4 (1998), pp. 243–247.
- [135] JJ Mock, M Barbic, DR Smith, DA Schultz, and S Schultz. "Shape effects in plasmon resonance of individual colloidal silver nanoparticles". In: *The Journal of Chemical Physics* 116.15 (2002), pp. 6755–6759.
- [136] Jack J Mock, David R Smith, and Sheldon Schultz. "Local refractive index dependence of plasmon resonance spectra from individual nanoparticles". In: *Nano letters* 3.4 (2003), pp. 485–491.
- [137] Eliza Hutter and Janos H Fendler. "Exploitation of localized surface plasmon resonance". In: *Advanced materials* 16.19 (2004), pp. 1685–1706.
- [138] DAG Bruggeman. "Dielectric constant and conductivity of mixtures of isotropic materials". In: *Ann. Phys.(Leipzig)* 24 (1935), pp. 636–679.
- [139] JC Maxwell Garnett. "VII. Colours in metal glasses, in metallic films, and in metallic solutions.âĀĤII". In: *Phil. Trans. R. Soc. Lond. A* 205.387-401 (1906), pp. 237–288.

REFERENCES

- [140] Hendrik Christoffel Hulst and Hendrik C van de Hulst. *Light scattering by small particles*. Courier Corporation, 1981.
- [141] Qiang Fu and Wenbo Sun. "Mie theory for light scattering by a spherical particle in an absorbing medium". In: *Applied Optics* 40.9 (2001), pp. 1354–1361.
- [142] M Futamata, Y Maruyama, and M Ishikawa. "Local electric field and scattering cross section of Ag nanoparticles under surface plasmon resonance by finite difference time domain method". In: *The Journal of Physical Chemistry B* 107.31 (2003), pp. 7607–7617.
- [143] Weihai Ni, Xiaoshan Kou, Zhi Yang, and Jianfang Wang. "Tailoring longitudinal surface plasmon wavelengths, scattering and absorption cross sections of gold nanorods". In: *Acs Nano* 2.4 (2008), pp. 677–686.
- [144] Bruce T Draine and Piotr J Flatau. "Discrete-dipole approximation for scattering calculations". In: *JOSA A* 11.4 (1994), pp. 1491–1499.
- [145] J-M Jin and Valdis V Liepa. "Application of hybrid finite element method to electromagnetic scattering from coated cylinders". In: *IEEE transactions on antennas and propagation* 36.1 (1988), pp. 50–54.
- [146] DF Swinehart. "The beer-lambert law". In: *Journal of chemical education* 39.7 (1962), p. 333.
- [147] Allen Taflove and Susan C Hagness. *Computational electrodynamics: the finite-difference time-domain method*. Artech house, 2005.
- [148] Christopher JM Emmott, Jason A Röhr, Mariano Campoy-Quiles, Thomas Kirchartz, Antonio Urbina, Nicholas J Ekins-Daukes, and Jenny Nelson. "Organic photovoltaic greenhouses: a unique application for semi-transparent PV?" In: *Energy & environmental science* 8.4 (2015), pp. 1317–1328.
- [149] Philipp Lölper, Michael Stuckelberger, Bjoern Niesen, Jérémie Werner, Miha Filipic, Soo-Jin Moon, Jun-Ho Yum, Marko Topic, Stefaan De Wolf, and Christophe Ballif. "Complex refractive index spectra of CH₃NH₃PbI₃ perovskite thin films determined by spectroscopic ellipsometry and spectrophotometry". In: *The journal of physical chemistry letters* 6.1 (2014), pp. 66–71.

REFERENCES

- [150] Sankara Rao Gollu, MS Murthy, Ramakant Sharma, G Srinivas, Swaroop Ganguly, and Dipti Gupta. "Enhanced efficiency of inverted bulk heterojunction solar cells with embedded silica nanoparticles". In: *Photovoltaic Specialist Conference (PVSC), 2014 IEEE 40th*. IEEE. 2014, pp. 1745–1749.
- [151] NT Fofang, TS Luk, M Okandan, GN Nielson, and I Brener. "Substrate-modified scattering properties of silicon nanostructures for solar energy applications". In: *Optics Express* 21.4 (2013), pp. 4774–4782.
- [152] S Tanev, VV Tuchin, and P Paddon. "Light scattering effects of gold nanoparticles in cells: FDTD modeling". In: *Laser Physics Letters* 3.12 (2006), p. 594.
- [153] Shuang Jiang, Zhe Hu, Zhizhong Chen, Xingxing Fu, Xianzhe Jiang, Qianqian Jiao, Tongjun Yu, and Guoyi Zhang. "Resonant absorption and scattering suppression of localized surface plasmons in Ag particles on green LED". In: *Optics Express* 21.10 (2013), pp. 12100–12110.
- [154] Huanjun Chen, Xiaoshan Kou, Zhi Yang, Weihai Ni, and Jianfang Wang. "Shape-and size-dependent refractive index sensitivity of gold nanoparticles". In: *Langmuir* 24.10 (2008), pp. 5233–5237.
- [155] Kyeong-Seok Lee and Mostafa A El-Sayed. "Dependence of the enhanced optical scattering efficiency relative to that of absorption for gold metal nanorods on aspect ratio, size, end-cap shape, and medium refractive index". In: *The Journal of Physical Chemistry B* 109.43 (2005), pp. 20331–20338.
- [156] Ming Li, Scott K Cushing, Jianming Zhang, Jessica Lankford, Zoraida P Aguilar, Dongling Ma, and Nianqiang Wu. "Shape-dependent surface-enhanced Raman scattering in gold–Raman-probe–silica sandwiched nanoparticles for biocompatible applications". In: *Nanotechnology* 23.11 (2012), p. 115501.
- [157] Xianliang Wang, Xin Liu, Deqiang Yin, Yujie Ke, and Mark T Swihart. "Size-, shape-, and composition-controlled synthesis and localized surface plasmon resonance of copper tin selenide nanocrystals". In: *Chemistry of Materials* 27.9 (2015), pp. 3378–3388.
- [158] Jian Zhu, Liqing Huang, Junwu Zhao, Yongchang Wang, Yanrui Zhao, Limei Hao, and Yimin Lu. "Shape dependent resonance light scattering properties of gold nanorods". In: *Materials Science and Engineering: B* 121.3 (2005), pp. 199–203.

REFERENCES

- [159] Prashant K Jain, Kyeong Seok Lee, Ivan H El-Sayed, and Mostafa A El-Sayed. "Calculated absorption and scattering properties of gold nanoparticles of different size, shape, and composition: applications in biological imaging and biomedicine". In: *The journal of physical chemistry B* 110.14 (2006), pp. 7238–7248.
- [160] Andrea Tao, Prasert Sinsermsuksakul, and Peidong Yang. "Polyhedral silver nanocrystals with distinct scattering signatures". In: *Angewandte Chemie International Edition* 45.28 (2006), pp. 4597–4601.
- [161] Jian Zhu. "Shape dependent full width at half maximum of the absorption band in gold nanorods". In: *Physics Letters A* 339.6 (2005), pp. 466–471.
- [162] David D Evanoff Jr and George Chumanov. "Synthesis and optical properties of silver nanoparticles and arrays". In: *ChemPhysChem* 6.7 (2005), pp. 1221–1231.
- [163] Sol Carretero-Palacios, Mauricio E Calvo, and Hernán Míguez. "Absorption enhancement in organic–inorganic halide perovskite films with embedded plasmonic gold nanoparticles". In: *The Journal of Physical Chemistry C* 119.32 (2015), pp. 18635–18640.
- [164] F Pelayo García de Arquer, Fiona J Beck, and Gerasimos Konstantatos. "Absorption enhancement in solution processed metal-semiconductor nanocomposites". In: *Optics express* 19.21 (2011), pp. 21038–21049.
- [165] Leif AA Pettersson, Lucimara S Roman, and Olle Inganäs. "Modeling photocurrent action spectra of photovoltaic devices based on organic thin films". In: *Journal of Applied Physics* 86.1 (1999), pp. 487–496.
- [166] George F Burkhard, Eric T Hoke, and Michael D McGehee. "Accounting for interference, scattering, and electrode absorption to make accurate internal quantum efficiency measurements in organic and other thin solar cells". In: *Advanced Materials* 22.30 (2010), pp. 3293–3297.
- [167] R Kern, R Sastrawan, J Ferber, R Stangl, and J Luther. "Modeling and interpretation of electrical impedance spectra of dye solar cells operated under open-circuit conditions". In: *Electrochimica Acta* 47.26 (2002), pp. 4213–4225.
- [168] Paul A Basore. "Numerical modeling of textured silicon solar cells using PC-1D". In: *IEEE Transactions on electron devices* 37.2 (1990), pp. 337–343.

REFERENCES

- [169] Jörg Ferber, Rolf Stangl, and Joachim Luther. "An electrical model of the dye-sensitized solar cell". In: *Solar Energy Materials and Solar Cells* 53.1-2 (1998), pp. 29–54.
- [170] Roderick CI MacKenzie, Thomas Kirchartz, George FA Dibb, and Jenny Nelson. "Modeling nongeminate recombination in P3HT: PCBM solar cells". In: *The Journal of Physical Chemistry C* 115.19 (2011), pp. 9806–9813.
- [171] Weiwei Li, Koen H Hendriks, WS Christian Roelofs, Youngju Kim, Martijn M Wienk, and René AJ Janssen. "Efficient small bandgap polymer solar cells with high fill factors for 300 nm thick films". In: *Advanced materials* 25.23 (2013), pp. 3182–3186.
- [172] Ebuka S Arinze, Botong Qiu, Nathan Palmquist, Yan Cheng, Yida Lin, Gabrielle Nyirjesy, Gary Qian, and Susanna M Thon. "Color-tuned and transparent colloidal quantum dot solar cells via optimized multilayer interference". In: *Optics Express* 25.4 (2017), A101–A112.
- [173] Anne Grete Hestnes. "Building integration of solar energy systems". In: *Solar Energy* 67.4-6 (1999), pp. 181–187.
- [174] Andreas Henemann. "BIPV: Built-in solar energy". In: *Renewable Energy Focus* 9.6 (2008), pp. 14–19.
- [175] Zhong Lin Wang, Guang Zhu, Ya Yang, Sihong Wang, and Caofeng Pan. "Progress in nanogenerators for portable electronics". In: *Materials today* 15.12 (2012), pp. 532–543.
- [176] Henrik Davidsson, Bengt Perers, and Björn Karlsson. "Performance of a multifunctional PV/T hybrid solar window". In: *Solar Energy* 84.3 (2010), pp. 365–372.
- [177] T Miyazaki, A Akisawa, and T Kashiwagi. "Energy savings of office buildings by the use of semi-transparent solar cells for windows". In: *Renewable energy* 30.3 (2005), pp. 281–304.
- [178] Hideo Otaka, Michie Kira, Kentaro Yano, Shunichiro Ito, Hirofumi Mitekura, Toshio Kawata, and Fumio Matsui. "Multi-colored dye-sensitized solar cells". In: *Journal of Photochemistry and Photobiology A: Chemistry* 164.1-3 (2004), pp. 67–73.
- [179] Hui Joon Park, Ting Xu, Jae Yong Lee, Abram Ledbetter, and L Jay Guo. "Photonic color filters integrated with organic solar cells for energy harvesting". In: *Acs Nano* 5.9 (2011), pp. 7055–7060.

REFERENCES

- [180] Chu-Chen Chueh, Shang-Chieh Chien, Hin-Lap Yip, José Francisco Salinas, Chang-Zhi Li, Kung-Shih Chen, Fang-Chung Chen, Wen-Chang Chen, and Alex K-Y Jen. "Toward high-performance semi-transparent polymer solar cells: optimization of ultra-thin light absorbing layer and transparent cathode architecture". In: *Advanced Energy Materials* 3.4 (2013), pp. 417–423.
- [181] Young-Hoon Kim, Himchan Cho, Jin Hyuck Heo, Tae-Sik Kim, NoSung Myoung, Chang-Lyoul Lee, Sang Hyuk Im, and Tae-Woo Lee. "Multi-colored organic/inorganic hybrid perovskite light-emitting diodes". In: *Advanced materials* 27.7 (2015), pp. 1248–1254.
- [182] Kyu-Tae Lee, L Jay Guo, and Hui Joon Park. "Neutral-and multi-colored semitransparent perovskite solar cells". In: *Molecules* 21.4 (2016), p. 475.
- [183] Giles E Eperon, Victor M Burlakov, Alain Goriely, and Henry J Snaith. "Neutral color semitransparent microstructured perovskite solar cells". In: *ACS nano* 8.1 (2013), pp. 591–598.
- [184] Cristina Roldan-Carmona, Olga Malinkiewicz, Rafael Betancur, Giulia Longo, Cristina Momblona, Franklin Jaramillo, Luis Camacho, and Henk J Bolink. "High efficiency single-junction semitransparent perovskite solar cells". In: *Energy & Environmental Science* 7.9 (2014), pp. 2968–2973.
- [185] Jae Woong Jung, Chu-Chen Chueh, and Alex K-Y Jen. "High-Performance Semitransparent Perovskite Solar Cells with 10% Power Conversion Efficiency and 25% Average Visible Transmittance Based on Transparent CuSCN as the Hole-Transporting Material". In: *Advanced Energy Materials* 5.17 (2015), p. 1500486.
- [186] Yulia Galagan, Michael G Debije, and Paul WM Blom. "Semitransparent organic solar cells with organic wavelength dependent reflectors". In: *Applied Physics Letters* 98.4 (2011), p. 16.
- [187] Wei Zhang, Miguel Anaya, Gabriel Lozano, Mauricio E Calvo, Michael B Johnston, Hernán Míguez, and Henry J Snaith. "Highly efficient perovskite solar cells with tunable structural color". In: *Nano letters* 15.3 (2015), pp. 1698–1702.
- [188] Kyu-Tae Lee, Masanori Fukuda, Suneel Joglekar, and L Jay Guo. "Colored, see-through perovskite solar cells employing an optical cavity". In: *Journal of Materials Chemistry C* 3.21 (2015), pp. 5377–5382.

REFERENCES

- [189] CeÀşar Omar RamilÀrez Quiroz, Carina Bronnbauer, Ievgen Levchuk, Yi Hou, Christoph J Brabec, and Karen Forberich. "Coloring semitransparent perovskite solar cells via dielectric mirrors". In: *ACS nano* 10.5 (2016), pp. 5104–5112.
- [190] Johannes Krantz, Tobias Stubhan, Moses Richter, Stefanie Spallek, Ivan Litzov, Gebhard J Matt, Erdmann Spiecker, and Christoph J Brabec. "Spray-coated silver nanowires as top electrode layer in semitransparent P3HT: PCBM-based organic solar cell devices". In: *Advanced Functional Materials* 23.13 (2013), pp. 1711–1717.
- [191] Yu-Ying Lee, Kun-Hua Tu, Chen-Chieh Yu, Shao-Sian Li, Jeong-Yuan Hwang, Chih-Cheng Lin, Kuei-Hsien Chen, Li-Chyong Chen, Hsuen-Li Chen, and Chun-Wei Chen. "Top laminated graphene electrode in a semitransparent polymer solar cell by simultaneous thermal annealing/releasing method". In: *ACS nano* 5.8 (2011), pp. 6564–6570.
- [192] Robert Koeppel, Doris Hoeglinger, Pavel A Troshin, Rimma N Lyubovskaya, Vladimir F Razumov, and Niyazi Serdar Sariciftci. "Organic solar cells with semitransparent metal back contacts for power window applications". In: *ChemSusChem: Chemistry & Sustainability Energy & Materials* 2.4 (2009), pp. 309–313.
- [193] Edward H Sargent. "Colloidal quantum dot solar cells". In: *Nature photonics* 6.3 (2012), p. 133.
- [194] Graham H Carey, Ahmed L Abdelhady, Zhijun Ning, Susanna M Thon, Osman M Bakr, and Edward H Sargent. "Colloidal quantum dot solar cells". In: *Chemical reviews* 115.23 (2015), pp. 12732–12763.
- [195] Margaret A Hines and Gregory D Scholes. "Colloidal PbS nanocrystals with size-tunable near-infrared emission: observation of post-synthesis self-narrowing of the particle size distribution". In: *Advanced Materials* 15.21 (2003), pp. 1844–1849.
- [196] Y Wang, A Suna, W Mahler, and R Kasowski. "PbS in polymers. From molecules to bulk solids". In: *The Journal of chemical physics* 87.12 (1987), pp. 7315–7322.
- [197] Jay N Zemel, James D Jensen, and Richard B Schoolar. "Electrical and optical properties of epitaxial films of PbS, PbSe, PbTe, and SnTe". In: *Physical Review* 140.1A (1965), A330.

REFERENCES

- [198] Saim Emin, Surya P Singh, Liyuan Han, Norifusa Satoh, and Ashrafal Islam. "Colloidal quantum dot solar cells". In: *Solar Energy* 85.6 (2011), pp. 1264–1282.
- [199] Xiaoliang Zhang, Carl Hägglund, Malin B Johansson, Kári Sveinbjörnsson, and Erik MJ Johansson. "Fine Tuned Nanolayered Metal/Metal Oxide Electrode for Semitransparent Colloidal Quantum Dot Solar Cells". In: *Advanced Functional Materials* 26.12 (2016), pp. 1921–1929.
- [200] Xiaoliang Zhang, Carl Hägglund, and Erik MJ Johansson. "Highly efficient, transparent and stable semitransparent colloidal quantum dot solar cells: a combined numerical modeling and experimental approach". In: *Energy & Environmental Science* 10.1 (2017), pp. 216–224.
- [201] Olivier Ouellette, Nadir Hossain, Brandon R Sutherland, Amirreza Kiani, F Pelayo GarcilAa de Arquer, Hairen Tan, Mohamed Chaker, Sjoerd Hoogland, and Edward H Sargent. "Optical Resonance Engineering for Infrared Colloidal Quantum Dot Photovoltaics". In: *ACS Energy Letters* 1.4 (2016), pp. 852–857.
- [202] Xiaoliang Zhang, Giles E Eperon, Jianhua Liu, and Erik MJ Johansson. "Semitransparent quantum dot solar cell". In: *Nano Energy* 22 (2016), pp. 70–78.
- [203] Shahab Akhavan, Burak Guzelturk, Vijay Kumar Sharma, and Hilmi Volkan Demir. "Large-area semi-transparent light-sensitive nanocrystal skins". In: *Optics Express* 20.23 (2012), pp. 25255–25266.
- [204] Ebuka S Arinze, Gabrielle Nyirjesy, Yan Cheng, Nathan Palmquist, and Susanna M Thon. "Colloidal quantum dot materials for infrared optoelectronics". In: *Infrared Remote Sensing and Instrumentation XXIII*. Vol. 9608. International Society for Optics and Photonics. 2015, p. 960813.
- [205] James Kennedy. "Particle swarm optimization". In: *Encyclopedia of machine learning*. Springer, 2011, pp. 760–766.
- [206] Kalyanmoy Deb. "Multi-Objective Optimization Using Evolutionary Algorithms. John Wiley & Sons". In: *Inc., New York, NY* (2001).
- [207] Thomas Smith and John Guild. "The CIE colorimetric standards and their use". In: *Transactions of the optical society* 33.3 (1931), p. 73.
- [208] Andrew S Brown and Martin A Green. "Detailed balance limit for the series constrained two terminal tandem solar cell". In: *Physica E: Low-dimensional Systems and Nanostructures* 14.1-2 (2002), pp. 96–100.

REFERENCES

- [209] Xihua Wang, Ghada I Koleilat, Jiang Tang, Huan Liu, Illan J Kramer, Ratan Debnath, Lukasz Brzozowski, D Aaron R Barkhouse, Larissa Levina, Sjoerd Hoogland, et al. "Tandem colloidal quantum dot solar cells employing a graded recombination layer". In: *Nature Photonics* 5.8 (2011), p. 480.
- [210] Joshua J Choi, Whitney N Wenger, Rachel S Hoffman, Yee-Fun Lim, Justin Luria, Jacek Jasieniak, John A Marohn, and Tobias Hanrath. "Solution-Processed Nanocrystal Quantum Dot Tandem Solar Cells". In: *Advanced Materials* 23.28 (2011), pp. 3144–3148.
- [211] Pralay K Santra and Prashant V Kamat. "Tandem-layered quantum dot solar cells: tuning the photovoltaic response with luminescent ternary cadmium chalcogenides". In: *Journal of the American Chemical Society* 135.2 (2013), pp. 877–885.
- [212] MJ Speirs, BGHM Groeneveld, L Protesescu, C Piliago, Maksym V Kovalenko, and MA Loi. "Hybrid inorganic–organic tandem solar cells for broad absorption of the solar spectrum". In: *Physical Chemistry Chemical Physics* 16.17 (2014), pp. 7672–7676.
- [213] Taesoo Kim, Yangqin Gao, Hanlin Hu, Buyi Yan, Zhijun Ning, Lethy Krishnan Jagadamma, Kui Zhao, Ahmad R Kirmani, Jessica Eid, Michael M Adachi, et al. "Hybrid tandem solar cells with depleted-heterojunction quantum dot and polymer bulk heterojunction subcells". In: *Nano Energy* 17 (2015), pp. 196–205.
- [214] Edward H Sargent. "Infrared photovoltaics made by solution processing". In: *Nature Photonics* 3.6 (2009), p. 325.
- [215] André J Labelle, Susanna M Thon, Jin Young Kim, Xinzheng Lan, David Zhitomirsky, Kyle W Kemp, and Edward H Sargent. "Conformal fabrication of colloidal quantum dot solids for optically enhanced photovoltaics". In: *ACS nano* 9.5 (2015), pp. 5447–5453.
- [216] Xinzheng Lan, Oleksandr Voznyy, Amirreza Kiani, F Pelayo García de Arquer, Abdullah Saud Abbas, Gi-Hwan Kim, Mengxia Liu, Zhenyu Yang, Grant Walters, Jixian Xu, et al. "Passivation using molecular halides increases quantum dot solar cell performance". In: *Advanced Materials* 28.2 (2016), pp. 299–304.

REFERENCES

- [217] Mengxia Liu, Oleksandr Voznyy, Randy Sabatini, F Pelayo García de Arquer, Rahim Munir, Ahmed Hesham Balawi, Xinzheng Lan, Fengjia Fan, Grant Walters, Ahmad R Kirmani, et al. “Hybrid organic–inorganic inks flatten the energy landscape in colloidal quantum dot solids”. In: *Nature materials* 16.2 (2017), p. 258.
- [218] Botong Qiu, Yida Lin, Ebuka S Arinze, Arlene Chiu, Lulin Li, and Susanna M Thon. “Photonic band engineering in absorbing media for spectrally selective optoelectronic films”. In: *Optics Express* 26.21 (2018), pp. 26933–26945.
- [219] SB Dworkin and TJ Nye. “Image processing for machine vision measurement of hot formed parts”. In: *Journal of materials processing technology* 174.1-3 (2006), pp. 1–6.
- [220] Drago Bračun, Gašper Škulj, and Miran Kadiš. “Spectral selective and difference imaging laser triangulation measurement system for on line measurement of large hot workpieces in precision open die forging”. In: *The International Journal of Advanced Manufacturing Technology* 90.1-4 (2017), pp. 917–926.
- [221] Joseph J Talghader, Anand S Gawarikar, and Ryan P Shea. “Spectral selectivity in infrared thermal detection”. In: *Light: Science & Applications* 1.8 (2012), e24.
- [222] James A Ratches, Richard H Vollmerhausen, and Ronald G Driggers. “Target acquisition performance modeling of infrared imaging systems: past, present, and future”. In: *IEEE Sensors journal* 1.1 (2001), pp. 31–40.
- [223] Hitosh Hara, Naoki Kishi, Makoto Noro, Hideto Iwaoka, and Kentaro Suzuki. *Fabry-Perot filter, wavelength-selective infrared detector and infrared gas analyzer using the filter and detector*. 2003.
- [224] Peter Werle, Franz Slemr, Karl Maurer, Robert Kormann, Robert Mücke, and Bernd Jänker. “Near-and mid-infrared laser-optical sensors for gas analysis”. In: *Optics and lasers in engineering* 37.2-3 (2002), pp. 101–114.
- [225] Christopher S Goldenstein, R Mitchell Spearrin, Jay B Jeffries, and Ronald K Hanson. “Infrared laser-absorption sensing for combustion gases”. In: *Progress in Energy and Combustion Science* 60 (2017), pp. 132–176.
- [226] Alexis De Vos. “Detailed balance limit of the efficiency of tandem solar cells”. In: *Journal of Physics D: Applied Physics* 13.5 (1980), p. 839.

REFERENCES

- [227] Feng Cao, Kenneth McEnaney, Gang Chen, and Zhifeng Ren. "A review of cermet-based spectrally selective solar absorbers". In: *Energy & Environmental Science* 7.5 (2014), pp. 1615–1627.
- [228] DM Trotter and AJ Sievers. "Spectral selectivity of high-temperature solar absorbers". In: *Applied optics* 19.5 (1980), pp. 711–728.
- [229] Hoyeon Kim, Hui-Seon Kim, Jaewon Ha, Nam-Gyu Park, and Seunghyup Yoo. "Empowering semi-transparent solar cells with thermal-mirror functionality". In: *Advanced Energy Materials* 6.14 (2016), p. 1502466.
- [230] E Radziemska. "The effect of temperature on the power drop in crystalline silicon solar cells". In: *Renewable energy* 28.1 (2003), pp. 1–12.
- [231] Adham Makki, Siddig Omer, and Hisham Sabir. "Advancements in hybrid photovoltaic systems for enhanced solar cells performance". In: *Renewable and sustainable energy reviews* 41 (2015), pp. 658–684.
- [232] BJ Huang, PE Yang, YP Lin, BY Lin, HJ Chen, RC Lai, and JS Cheng. "Solar cell junction temperature measurement of PV module". In: *Solar Energy* 85.2 (2011), pp. 388–392.
- [233] Kevin A Bush, Axel F Palmstrom, J Yu Zhengshan, Mathieu Boccard, Rongrong Cheacharoen, Jonathan P Mailoa, David P McMeekin, Robert LZ Hoye, Colin D Bailie, Tomas Leijtens, et al. "23.6%-efficient monolithic perovskite/silicon tandem solar cells with improved stability". In: *Nature Energy* 2.4 (2017), p. 17009.
- [234] Martin A. Green, Yoshihiro Hishikawa, Ewan D. Dunlop, Dean H. Levi, Jochen Hohl-Ebinger, and Anita W.Y. Ho-Baillie. "Solar cell efficiency tables (version 51)". In: *Progress in Photovoltaics: Research and Applications* 26.1 (), pp. 3–12.
- [235] JC Knight, TA Birks, P St J Russell, and DM Atkin. "All-silica single-mode optical fiber with photonic crystal cladding". In: *Optics letters* 21.19 (1996), pp. 1547–1549.
- [236] Attila Mekis, JC Chen, I Kurland, Shanhui Fan, Pierre R Villeneuve, and JD Joannopoulos. "High transmission through sharp bends in photonic crystal waveguides". In: *Physical Review Letters* 77.18 (1996), p. 3787.
- [237] Philip St J Russell. "Photonic-crystal fibers". In: *Journal of lightwave technology* 24.12 (2006), pp. 4729–4749.

REFERENCES

- [238] Eiichi Kuramochi, Kengo Nozaki, Akihiko Shinya, Koji Takeda, Tomonari Sato, Shinji Matsuo, Hideaki Taniyama, Hisashi Sumikura, and Masaya Notomi. "Large-scale integration of wavelength-addressable all-optical memories on a photonic crystal chip". In: *Nature Photonics* 8.6 (2014), p. 474.
- [239] MR Sprague, PS Michelberger, TFM Champion, DG England, J Nunn, X-M Jin, WS Kolthammer, A Abdolvand, P St J Russell, and IA Walmsley. "Broadband single-photon-level memory in a hollow-core photonic crystal fibre". In: *Nature Photonics* 8.4 (2014), p. 287.
- [240] Yurii A Vlasov, Martin O'boyle, Hendrik F Hamann, and Sharee J McNab. "Active control of slow light on a chip with photonic crystal waveguides". In: *Nature* 438.7064 (2005), p. 65.
- [241] Thomas Volz, Andreas Reinhard, Martin Winger, Antonio Badolato, Kevin J Hennessy, Evelyn L Hu, and Ataç Imamoğlu. "Ultrafast all-optical switching by single photons". In: *Nature Photonics* 6.9 (2012), p. 605.
- [242] John D Joannopoulos, Steven G Johnson, Joshua N Winn, and Robert D Meade. *Photonic crystals: molding the flow of light*. Princeton university press, 2011.
- [243] S Strauf, K Hennessy, MT Rakher, Y-S Choi, A Badolato, LC Andreani, EL Hu, PM Petroff, and D Bouwmeester. "Self-tuned quantum dot gain in photonic crystal lasers". In: *Physical review letters* 96.12 (2006), p. 127404.
- [244] Hong-Gyu Park, Se-Heon Kim, Soon-Hong Kwon, Young-Gu Ju, Jin-Kyu Yang, Jong-Hwa Baek, Sung-Bock Kim, and Yong-Hee Lee. "Electrically driven single-cell photonic crystal laser". In: *Science* 305.5689 (2004), pp. 1444–1447.
- [245] Peter Bermel, Chiyang Luo, Lirong Zeng, Lionel C Kimerling, and John D Joannopoulos. "Improving thin-film crystalline silicon solar cell efficiencies with photonic crystals". In: *Optics express* 15.25 (2007), pp. 16986–17000.
- [246] Antonio Badolato, Kevin Hennessy, Mete Atatüre, Jan Dreiser, Evelyn Hu, Pierre M Petroff, and Ataç Imamoğlu. "Deterministic coupling of single quantum dots to single nanocavity modes". In: *Science* 308.5725 (2005), pp. 1158–1161.

REFERENCES

- [247] Andrew R Parker and Helen E Townley. "Biomimetics of photonic nanostructures". In: *Nature nanotechnology* 2.6 (2007), p. 347.
- [248] Vinodkumar Saranathan, Chinedum O Osuji, Simon GJ Mochrie, Heeso Noh, Suresh Narayanan, Alec Sandy, Eric R Dufresne, and Richard O Prum. "Structure, function, and self-assembly of single network gyroid (I4132) photonic crystals in butterfly wing scales". In: *Proceedings of the National Academy of Sciences* 107.26 (2010), pp. 11676–11681.
- [249] Jeremy W Galusha, Lauren R Richey, John S Gardner, Jennifer N Cha, and Michael H Bartl. "Discovery of a diamond-based photonic crystal structure in beetle scales". In: *Physical Review E* 77.5 (2008), p. 050904.
- [250] John D Joannopoulos, Pierre R Villeneuve, and Shanhui Fan. "Photonic crystals: putting a new twist on light". In: *Nature* 386.6621 (1997), p. 143.
- [251] Zhenlin Wang, Che Ting Chan, Weiyi Zhang, Naiben Ming, and Ping Sheng. "Three-dimensional self-assembly of metal nanoparticles: Possible photonic crystal with a complete gap below the plasma frequency". In: *Physical Review B* 64.11 (2001), p. 113108.
- [252] Ken Xingze Wang, Zongfu Yu, Victor Liu, Aaswath Raman, Yi Cui, and Shanhui Fan. "Light trapping in photonic crystals". In: *Energy & Environmental Science* 7.8 (2014), pp. 2725–2738.
- [253] Alongkarn Chutinan, Nazir P Kherani, and Stefan Zukotynski. "High-efficiency photonic crystal solar cell architecture". In: *Optics Express* 17.11 (2009), pp. 8871–8878.
- [254] Alongkarn Chutinan and Sajeew John. "Light trapping and absorption optimization in certain thin-film photonic crystal architectures". In: *Physical Review A* 78.2 (2008), p. 023825.
- [255] Robert B Withrow and Leonard Price. "Filters for the isolation of narrow regions in the visible and near-visible spectrum". In: *Plant physiology* 28.1 (1953), p. 105.
- [256] Hao Wang and Liping Wang. "Perfect selective metamaterial solar absorbers". In: *Optics express* 21.106 (2013), A1078–A1093.
- [257] Amaresh Mishra and Peter Bäuerle. "Small molecule organic semiconductors on the move: promises for future solar energy technology". In: *Angewandte Chemie International Edition* 51.9 (2012), pp. 2020–2067.
- [258] KF Renk and L Genzel. "Interference filters and Fabry-Perot interferometers for the far infrared". In: *Applied Optics* 1.5 (1962), pp. 643–648.

REFERENCES

- [259] Lifeng Li. “New formulation of the Fourier modal method for crossed surface-relief gratings”. In: *JOSA A* 14.10 (1997), pp. 2758–2767.
- [260] Lifeng Li. “Formulation and comparison of two recursive matrix algorithms for modeling layered diffraction gratings”. In: *JOSA A* 13.5 (1996), pp. 1024–1035.
- [261] Lifeng Li. “Use of Fourier series in the analysis of discontinuous periodic structures”. In: *JOSA A* 13.9 (1996), pp. 1870–1876.
- [262] Valerio Lucarini, Jarkko J Saarinen, Kai-Erik Peiponen, and Erik M Vartiainen. *Kramers-Kronig relations in optical materials research*. Vol. 110. Springer Science & Business Media, 2005.
- [263] Igor A Sukhoivanov and Igor V Guryev. *Photonic crystals: physics and practical modeling*. Vol. 152. Springer, 2009.
- [264] Edward D Palik. “-Gallium Arsenide (GaAs)”. In: *Handbook of optical constants of solids*. Elsevier, 1997, pp. 429–443.
- [265] Hermann A Haus. “Waves and Fields in Optoelectronics Prentice-Hall”. In: *Inc. Englewood Cliffs, New Jersey* (1984).
- [266] Shanhui Fan, Wonjoo Suh, and John D Joannopoulos. “Temporal coupled-mode theory for the Fano resonance in optical resonators”. In: *JOSA A* 20.3 (2003), pp. 569–572.
- [267] Wonjoo Suh, Zheng Wang, and Shanhui Fan. “Temporal coupled-mode theory and the presence of non-orthogonal modes in lossless multi-mode cavities”. In: *IEEE Journal of Quantum Electronics* 40.10 (2004), pp. 1511–1518.
- [268] Shanhui Fan and JD Joannopoulos. “Analysis of guided resonances in photonic crystal slabs”. In: *Physical Review B* 65.23 (2002), p. 235112.
- [269] Gerasimos Konstantatos, Ian Howard, Armin Fischer, Sjoerd Hoogland, Jason Clifford, Ethan Klem, Larissa Levina, and Edward H Sargent. “Ultrasensitive solution-cast quantum dot photodetectors”. In: *Nature* 442.7099 (2006), p. 180.
- [270] Xiwen Gong, Zhenyu Yang, Grant Walters, Riccardo Comin, Zhijun Ning, Eric Beauregard, Valerio Adinolfi, Oleksandr Voznyy, and Edward H Sargent. “Highly efficient quantum dot near-infrared light-emitting diodes”. In: *Nature Photonics* 10.4 (2016), p. 253.

REFERENCES

- [271] Michael M Adachi, André J Labelle, Susanna M Thon, Xinzheng Lan, Sjoerd Hoogland, and Edward H Sargent. "Broadband solar absorption enhancement via periodic nanostructuring of electrodes". In: *Scientific reports* 3 (2013), p. 2928.
- [272] Chin Li Cheung, RJ Nikolić, CE Reinhardt, and TF Wang. "Fabrication of nanopillars by nanosphere lithography". In: *Nanotechnology* 17.5 (2006), p. 1339.
- [273] Alexander H Ip, Susanna M Thon, Sjoerd Hoogland, Oleksandr Voznyy, David Zhitomirsky, Ratan Debnath, Larissa Levina, Lisa R Rollny, Graham H Carey, Armin Fischer, et al. "Hybrid passivated colloidal quantum dot solids". In: *Nature nanotechnology* 7.9 (2012), p. 577.
- [274] Joseph M Luther, Matt Law, Matthew C Beard, Qing Song, Matthew O Reese, Randy J Ellingson, and Arthur J Nozik. "Schottky solar cells based on colloidal nanocrystal films". In: *Nano letters* 8.10 (2008), pp. 3488–3492.
- [275] Ghada I Koleilat, Larissa Levina, Harnik Shukla, Stefan H Myrskog, Sean Hinds, Andras G Pattantyus-Abraham, and Edward H Sargent. "Efficient, stable infrared photovoltaics based on solution-cast colloidal quantum dots". In: *ACS nano* 2.5 (2008), pp. 833–840.
- [276] Dmitri V Talapin and Christopher B Murray. "PbSe nanocrystal solids for n-and p-channel thin film field-effect transistors". In: *Science* 310.5745 (2005), pp. 86–89.
- [277] Maksym V Kovalenko, Marcus Scheele, and Dmitri V Talapin. "Colloidal nanocrystals with molecular metal chalcogenide surface ligands". In: *Science* 324.5933 (2009), pp. 1417–1420.
- [278] Robert D Miller and Josef Michl. "Polysilane high polymers". In: *Chemical Reviews* 89.6 (1989), pp. 1359–1410.
- [279] Rebekka S Klausen, Jonathan R Widawsky, Michael L Steigerwald, Latha Venkataraman, and Colin Nuckolls. "Conductive molecular silicon". In: *Journal of the American Chemical Society* 134.10 (2012), pp. 4541–4544.
- [280] Sravan Surampudi, M-L Yeh, MA Siegler, JF Martinez Hardigree, TA Kasl, HE Katz, and RS Klausen. "Increased carrier mobility in end-functionalized oligosilanes". In: *Chemical science* 6.3 (2015), pp. 1905–1909.

REFERENCES

- [281] Philippe Guyot-Sionnest. "Electrical transport in colloidal quantum dot films". In: *The Journal of Physical Chemistry Letters* 3.9 (2012), pp. 1169–1175.
- [282] Keith T Wong and Nathan S Lewis. "What a difference a bond makes: the structural, chemical, and physical properties of methyl-terminated Si (111) surfaces". In: *Accounts of chemical research* 47.10 (2014), pp. 3037–3044.
- [283] Artem A Bakulin, Stefanie Neutzner, Huib J Bakker, Laurent Ottaviani, Damien Barakel, and Zhuoying Chen. "Charge trapping dynamics in PbS colloidal quantum dot photovoltaic devices". In: *Acs Nano* 7.10 (2013), pp. 8771–8779.
- [284] Yana Vaynzof, Artem A Bakulin, Simon Gélinas, and Richard H Friend. "Direct observation of photoinduced bound charge-pair states at an organic-inorganic semiconductor interface". In: *Physical review letters* 108.24 (2012), p. 246605.

Chapter 5

Engineering Nanostructures for Photon Detection Applications

Over the past decade, solution-processed nanomaterials (such as polymers, hybrid perovskites, colloidal quantum dots and nanowires) are emerging as potential photon detection materials because of their favorable spectral tunability, relative cost, and facile manufacturing and processing techniques [1, 2, 3, 4]. More specifically, the versatility of the fabrication technique makes it possible for relatively easy integration of the active material with read-out integrated circuits [5]. In this chapter, we investigate nanostructured materials for two photon detection systems.

5.1 An Antimony Selenide Molecular Ink for Flexible Broadband Photodetectors

This section is adapted from Ref. [3]. Reprinted with permission from *Advanced Electronic Materials*, 2, no. 9, 1600182, "An Antimony Selenide Molecular Ink for Flexible Broadband Photodetectors," by M. R. Hasan, E. S. Arinze,

A. K. Singh, V. P. Oleshko, S. Guo, A. Rani, Y. Cheng, I. Kalish, , M. E. Zaghoul, M. V. Rao, N. V. Nguyen, A. Motayed, A. V. Davydov, S. M. Thon and R. Debnath, copyright © 2016.

5.1.1 Introduction

As digital imaging devices gain in popularity, the quest for new infrared-sensitive materials that don't depend on epitaxial thin-film deposition techniques has intensified. The ability to deposit semiconducting films from solution has shown great potential for various electronic and optoelectronic applications and emerged as an attractive low-cost approach to fabricating high-quality semiconducting thin films.[6, 7, 8, 9, 10, 11, 12] One can simply employ "soft" non-vacuum processes such as spin-coating,[11, 13, 14, 15, 16] ink-jet printing,[9, 17] and similar techniques to enable high-throughput device fabrication and realize new technologies particularly in the area of flexible optoelectronics.[16, 18, 19]

Research on solution-processed semiconductors has focused on both organic and inorganic systems.[6, 9, 10] However, molecular organic systems have several disadvantages including poor environmental, mechanical and thermal stability as well as poor electronic transport as compared to their inorganic counterparts. On the other hand, inorganic semiconductors can take advantage of covalently-bonded frameworks to achieve desirable electronic transport properties and band gaps.[20, 21, 22] There have been tremendous efforts to deposit inorganic films with excellent properties using chemical bath deposition,[23, 24, 25, 26], spray pyrolysis,[27, 28] and other solution-based

methods.

Among various inorganic semiconductors, metal chalcogenides, particularly, group V-VI compounds have been widely studied for their optoelectrical[29, 30] and thermoelectric properties[31, 32] and successfully utilized in thin film transistors,[10, 11] solar cells,[12, 29, 33] thermoelectric devices,[34, 35] photodetectors (PDs),[36, 37, 38] and phase change memory[39] applications. These films have typically been prepared via sophisticated deposition techniques such as catalyst-assisted chemical vapor deposition,[40] sputtering,[41] thermal evaporation[29, 42] and molecular beam epitaxy[43] that require energy-intensive, high vacuum deposition conditions not amenable to high-throughput mass production.

Although most metal chalcogenides are very difficult to dissolve in common solvents, recent developments in solution-based chemistry of chalcogenides have overcome this limitation, and homogeneous, high-quality semiconductor films derived from true molecular inks have been grown successfully.[39] Typically, an ink is made by dissolving stoichiometric amounts of elemental chalcogens with metal in hydrazine solutions.[11, 44] Unfortunately, hydrazine is highly toxic and explosive, which limits the practicality of production. Some less hazardous and volatile solvents, such as mixtures of amine and thiols, have been used for solution deposition, but their application has been limited to bulk metal chalcogenide thin film growth from their respective compounds.[45, 46, 47]

Antimony selenide (Sb_2Se_3) has emerged from the group V-VI chalcogenides as an excellent candidate for optoelectronics due to its direct band

gap of about 1.1 eV[12] in the NIR regime and p-type semiconductor behavior. One-dimensional (1D) Sb_2Se_3 nanostructures are of particular interest due to their high surface-to-volume ratio and tunable properties that can be used to enhance the performance of optoelectronic devices. Such NWs have been synthesized in the past using solution-based growth methods,[37, 48, 49] but Sb_2Se_3 -based devices, (e.g., PDs) have been fabricated mostly on rigid substrates.[37] The complicated growth methods based on toxic solvents and limited performance to date have hindered Sb_2Se_3 from competing with traditional crystalline PD technologies.

Here, we report on a method for template-free, facile, one-step solution-based and in-situ growth of Sb_2Se_3 nanowires (NWs) on flexible polyimide substrates for fast response and high performance flexible photodetectors. Our one-pot synthesis method is based on a molecular ink prepared by directly mixing elemental antimony and selenium into a solution of ethylenediamine (EDA) and 2-mercaptoethanol (ME).[47] This is the first time, to our knowledge, that this facile synthesis method has been used to fabricate Sb_2Se_3 photodetectors. Chemical, structural and optical properties of the NWs obtained from this technique are characterized. Sb_2Se_3 PDs fabricated on flexible substrates exhibit excellent figures of merit, such as a broadband photoresponse spanning from the ultraviolet (UV) to near-infrared (NIR) range, fast temporal response and superior mechanical stability. Previous studies on Sb_2Se_3 -based flexible photodetectors have primarily focused on using polyethylene terephthalate (PET).[49] However, in this study, we substitute

PET for polyimide, a film with superior resistance to heat and chemical exposure while maintaining excellent performance. Additionally, we demonstrate that the spectral response of our detectors should be tunable by adjusting the nanowire size. Our results indicate that molecular-ink-based flexible, scalable, and tunable systems have the potential to replace conventional broadband and NIR optoelectronic technology.

5.1.2 Results and Discussion

Our deposition method for Sb_2Se_3 films is depicted in Figure 5.1 and involves the following steps: (i) dissolving elemental Sb with excess Se at a molar ratio of 1:3 in EDA and ME to produce the precursor solutions under magnetic stirring for several days in a nitrogen glove box; (ii) spin-casting the resulting dark orange molecular ink onto polyimide substrates and (iii) annealing the as-deposited films. The details can be found in the Experimental section.

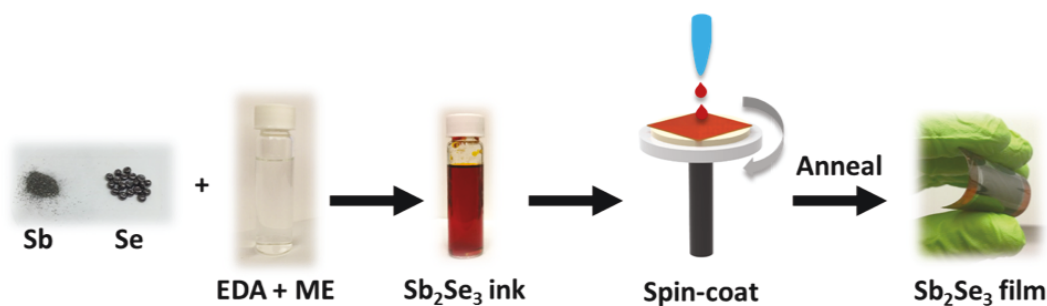


Figure 5.1: Fabrication scheme for Sb_2Se_3 nanostructure formation on flexible substrates utilizing a molecular ink. The process begins with dissolution of elemental Sb and Se in ethylenediamine (EDA) and 2-mercaptoethanol (ME) to produce a molecular ink that is spin-cast onto a flexible substrate and annealed to form a flexible nanowire-based film.[3]

5.1.2.1 Analytical Electron Microscopy of NWs

We used field-emission scanning electron microscopy (FESEM) to image the Sb_2Se_3 nanostructures on flexible polyimides after thermal processing at 350°C in the presence of excess Se, as shown in Figure 5.2a. The FESEM image shows the formation of randomly oriented NWs having a small range of lengths and diameters. The processing temperature and selenium concentration are key fabrication parameters as they dictate the aspect ratio of the nanostructures, which, in turn, affects the device optical properties. Formation of NWs from the as-deposited films takes place at around 200°C in the presence of excess selenium; however, when the concentration of Se is lowered (to near the stoichiometric concentration), the films grow instead with a nanograin-like morphology. Compositional mapping by energy-dispersive X-ray spectroscopy (EDXS) shows the distribution of Sb and Se elements in the film, and one can clearly see the individual nanostructures in the elemental maps. The EDXS spectrum exhibits strong Sb and Se peaks, and there is no discernible sulfur present in the film.

Transmission electron microscopy (TEM) measurements revealed rod-like morphology of $0.1\ \mu\text{m}$ to $1.2\ \mu\text{m}$ long Sb_2Se_3 NWs with diameters ranging from $100\ \text{nm}$ to $300\ \text{nm}$ (Figure 5.2b). The corresponding selected-area diffraction (SAED) pattern (Figure 5.2b, inset) and phase-contrast high-resolution TEM (HRTEM) images (Figure 5.2c) indicate that the Sb_2Se_3 nanostructures are single orthorhombic crystals growing along the $\langle 001 \rangle$ direction of the $Pbnm$ space group. The SAED pattern of an individual NW indexed as the $[430]$ zone shows a 002 point reflection with $0.20\ \text{nm}$ lattice spacing ($d_{002} = 0.19810$

nm) and a 340 point reflection with 0.23 nm lattice spacing ($d_{340} = 0.23431$ nm). More detailed analysis of SAED patterns revealed additional splitting of {341} reflections due to twinning of NWs along the growth direction likely caused by close-packed growth conditions. The latter was supported by examination of corresponding TEM micrographs. The HRTEM image in Figure 5.2c (left) reveals several families of interplanar lattice fringes, including large 0.58 nm (020) spacing ($d_{020} = 0.5885$ nm) parallel to the growth direction, and the inset shows a Fast Fourier Transform (FFT) pattern implying [100] orientation for the Sb_2Se_3 NW sample area indicated by the red box. The enlarged HRTEM fragment (Figure 5.2c, right) shows orthogonal 0.19 nm (022) and (0-22) lattice fringes observed in the vicinity of a partially amorphized NW surface.

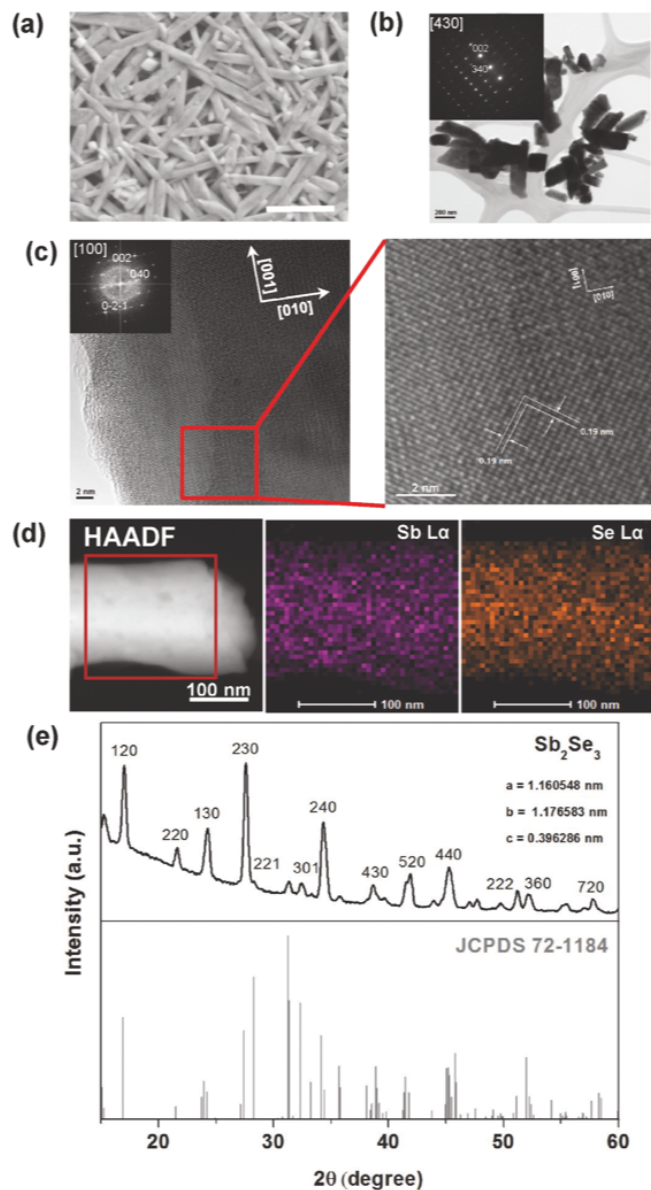


Figure 5.2: Analytical electron microscopy and XRD analysis of Sb_2Se_3 NWs: (a) High magnification FESEM image. The scale bar corresponds to 1 μm . (b) Bright-field (BF) TEM of Sb_2Se_3 NWs with a SAED pattern in the [430] orientation (inset), (c) HRTEM of a single crystalline orthorhombic NW growing along the $\langle 001 \rangle$ direction with the corresponding FFT pattern in the [100] orientation (upper left inset). The right inset shows an enlargement of the area marked by the red box on the left showing the (022) and (0-22) lattice fringes. (d) HAADF-STEM image of a Sb_2Se_3 NW and corresponding Sb L and Se L X-ray maps (right insets). (e) GIXRD pattern of the Sb_2Se_3 NW film, the calculated lattice constants (top) and stick pattern JCPDS card, No. 72-1184 (bottom).[3]

For more accurate evaluation of the nanoscale elemental composition and the spatial uniformities of the Sb and Se elemental distributions, EDXS-FESEM compositional analyses were corroborated with high spatial resolution EDXS and electron energy-loss spectroscopy (EELS). Analyses of randomly selected NWs from the same sample were performed using a 0.2 nm diameter electron probe in scanning transmission electron microscopy (STEM) mode at 300 kV accelerating voltage. Elemental mapping results revealed that Sb and Se were uniformly distributed throughout the analyzed NWs (Figure 5.2d), and elemental line profiles confirmed the same. X-ray spectra acquired during line profiling have been further quantified using a Cliff-Lorimer thin film ratio technique with calculated k-factors for the Sb $\kappa\alpha$ and the Se $\kappa\alpha$ peaks, and absorption (mass-thickness) correction as described elsewhere.[50] Similarly, EELS spectra taken in randomly selected spots on the same sample have been quantified using a thin film ratio technique with 200 eV energy windows for both Sb $M_{4,5}$ - and Se $L_{2,3}$ -edges and corresponding calculated Hartree-Slater ionization cross-sections.[51] Quantification results demonstrate that the Sb/Se atomic ratio in the NWs is close to stoichiometric with excellent agreement between the employed analytical techniques (Table 5.1).

5.1.3 X-ray Diffraction and Optical Properties

We further confirmed the crystal structure of the Sb_2Se_3 NW films using grazing incidence X-Ray diffraction (GIXRD), as shown in Figure 5.2e. All of the diffraction peaks can be indexed to the orthorhombic phase of Sb_2Se_3 (JCPDS Card No. 72-1184) with a space group of $Pbnm$ (62). All of the major

Technique	Accelerating Voltage, kV	Sb/Se atomic ratio, $\pm 2\sigma$ at the 95% confidence limit
EDXS-STEM Cliff-Lorimer thin film ratio method with calculated k-factors for the Sb $\kappa\alpha$ and the Se $\kappa\alpha$ peaks and absorption (mass-thickness) correction	300	0.65 ± 0.09
EELS thin film ratio method with 200 eV integration windows for the Sb $M_{4,5}$ - and the Se $L_{2,3}$ -edges	300	0.65 ± 0.04

Table 5.1: Quantitative EDXS and EELS analyses of Sb_2Se_3 NWs.[3]

planes were indexed, and no secondary phases were detected. Using retrieval analysis, the lattice constants are calculated as: $a = (1.160584 \pm 0.0004)$ nm, $b = (1.176583 \pm 0.0005)$ nm and $c = (0.396286 \pm 0.0002)$ nm, very close to the ideal bulk values for Sb_2Se_3 ($a = 1.162$ nm, $b = 1.177$ nm, $c = 0.3962$ nm) and consistent with previously reported data.[52, 53, 30]

In order to determine the transition type and the optical band gap, a transmission spectrum of the Sb_2Se_3 NW thin films was recorded using UV-Vis absorption spectroscopy. The band gap was estimated by extrapolating the linear region of the Tauc plots of $(\alpha h\nu)^2$ versus $h\nu$ to $h\nu = 0$ (Figure 5.3a), where α is the absorption coefficient and $h\nu$ is the photon energy. A direct transition type with a value of ~ 1.12 eV was confirmed, quite close to previously reported values,[12] as well as those measured by ellipsometry.

We also computed the electronic band structure of bulk Sb_2Se_3 using density functional theory and found good agreement with the measured band gap of the deposited NWs. The calculated minimum gap of 0.90 eV for Sb_2Se_3

was found to be indirect, and the direct gap was 1.05 eV, a difference of 0.15 eV from the indirect gap, making the direct and indirect transitions almost degenerate, as previously reported[54] (Figure 5.3b). Furthermore, the band structure of Sb_2Se_3 exhibits several transitions between the valence band and the conduction band with comparable energy to the fundamental indirect-gap energy, suggesting that Sb_2Se_3 can be considered a direct gap semiconductor for all practical applications. The states at the valence band edge are predominantly associated with Se p-orbitals and those at the conduction band edge are dominated by the Sb p-orbitals. The density of states (DOS) for bulk Sb_2Se_3 shown in Figure 5.3c agrees well with earlier work.[29] The close agreement in the band gap of bulk Sb_2Se_3 and solution-deposited Sb_2Se_3 NWs indicates surface and quantum confinement effects play little role in the electronic structure of the NWs. In addition, Raman spectroscopy performed on Sb_2Se_3 NWs revealed two Raman peaks centered at $(190 \pm 0.3) \text{ cm}^{-1}$ and $(253 \pm 0.3) \text{ cm}^{-1}$ which represent the hetero-polar Sb-Se and non-polar Sb-Sb vibrations[30] (Figure 5.3d). Raman mapping also shows the uniformity of those peaks.

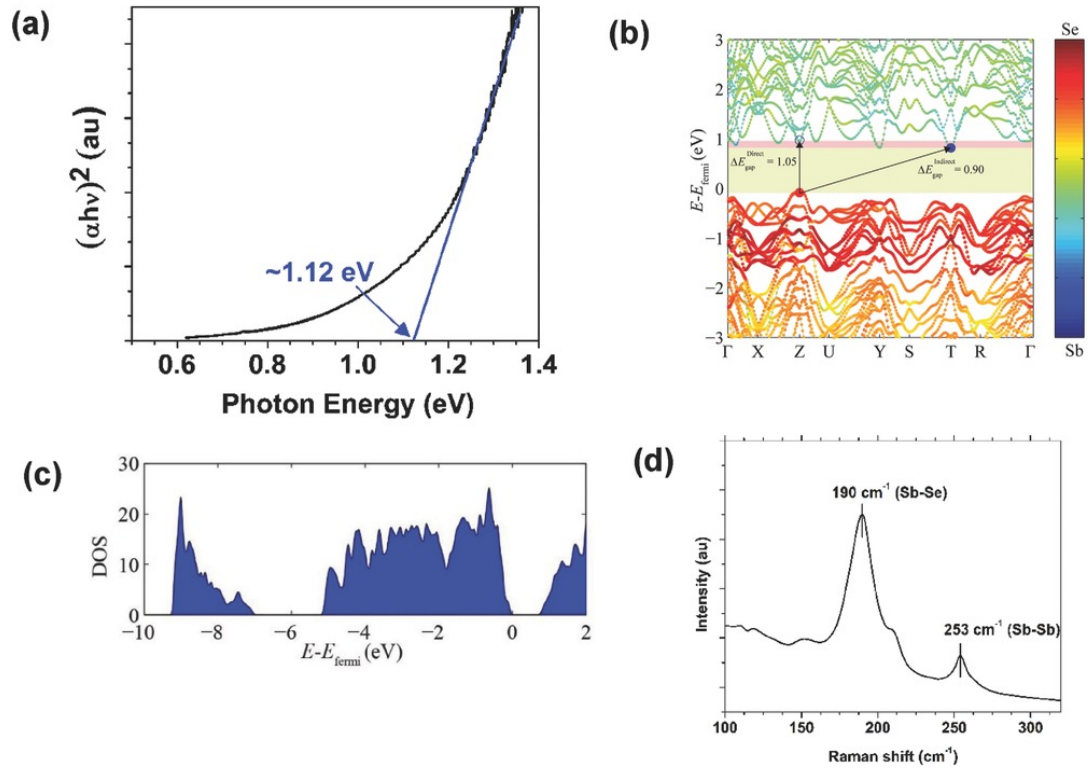


Figure 5.3: Optical properties of Sb_2Se_3 : (a) Tauc plot used to estimate the band gap (~ 1.12 eV) from a linear interpolation. (b) Electronic band structure of bulk Sb_2Se_3 computed using DFT simulations. Sb_2Se_3 has an indirect band gap, $\Delta E_{\text{gap}}^{\text{Indirect}}$, of 0.90 eV and a direct band gap, $\Delta E_{\text{gap}}^{\text{Direct}}$, of 1.05 eV. The valence band maxima and conduction band minima are marked with red and blue circles, respectively. The symbol sizes and colors denote the weights of the Sb or Se contributions to the bands. The valence band maximum is set to zero energy. (c) The calculated DOS vs. $E - E_{\text{fermi}}$ in eV. (d) Raman spectrum showing the heteropolar Sb-Se and non-polar Sb-Sb vibrations.[3]

5.1.4 Flexible Photodetectors: Figures of Merits

After establishing the crystal structure and optical properties of the molecular-ink-based Sb_2Se_3 NWs, we fabricated flexible photoconductive photodetectors by depositing interdigitated Au/Ti/Au electrodes via electron beam evaporation on the NW-polyimide substrates (inset of Figure 5.4a). Figure 5.4a shows

a current-voltage (I-V) characteristic curve for an Sb_2Se_3 NW PD measured in the dark and under 870 nm illumination. At an applied bias ranging from -30 V to 30 V with a very low illumination intensity of $\sim 6.4 \mu\text{W}$, the change in slope of the I-V curve indicates a strong photoresponse, and the linear I-V curve evinces the Ohmic nature of the contact between the metal electrodes and NWs.

The temporal response of the PD under pulsed 365 nm illumination (30 mW/cm^2 , 20 s and 90 s pulse widths) and 10 V bias is presented in Figure 5.4b. Both shorter (20 s pulse width) and longer (90 s pulse width) periods of modulation were performed to demonstrate the photocurrent stability. The PD photocurrent is reproducible and stable with two distinct states: a "low" current state in the dark and a "high" current state under illumination with an on/off ratio of 22. The characteristic rise time (t_r) for the photocurrent to increase from 10% to 90% of its maximum value is (24 ± 2) ms, and the decay time (t_d) for the photocurrent to decrease from 90% to 10% of the peak value is (9 ± 2) ms (as illustrated in Figure 5.4c). This temporal response is significantly faster than in previous Sb_2Se_3 -based photodetector demonstrations with both response and recovery times that are two orders of magnitude smaller than previously reported values (24 and 9 ms vs. 0.18 and 0.20 s).[37, 49]

Device photoresponse is generally governed by complex processes such as carrier generation, trapping, and recombination. Due to the nanostructured nature of the PD active layer, abundant grain boundaries (or junction barriers) are expected to be present in the NW film. This type of defect is generally associated with the formation of deep traps leading to slow temporal response.

Instead, the NW film measured here exhibits fast decay and recovery times. This can potentially be attributed to the high quality crystalline nature of the materials, which leads to efficient optical absorption and photo-carrier generation under illumination. The increased carrier density reduces the junction barrier height between the adjacent NWs, and such light-induced barrier height modulation could lead to the fast response time. Additionally, the large surface-to-volume ratio of the NWs is likely associated with a high density of surface-associated dangling bonds/defects. Thus, when the light is turned off, the carriers can recombine quickly, resulting in short decay times.

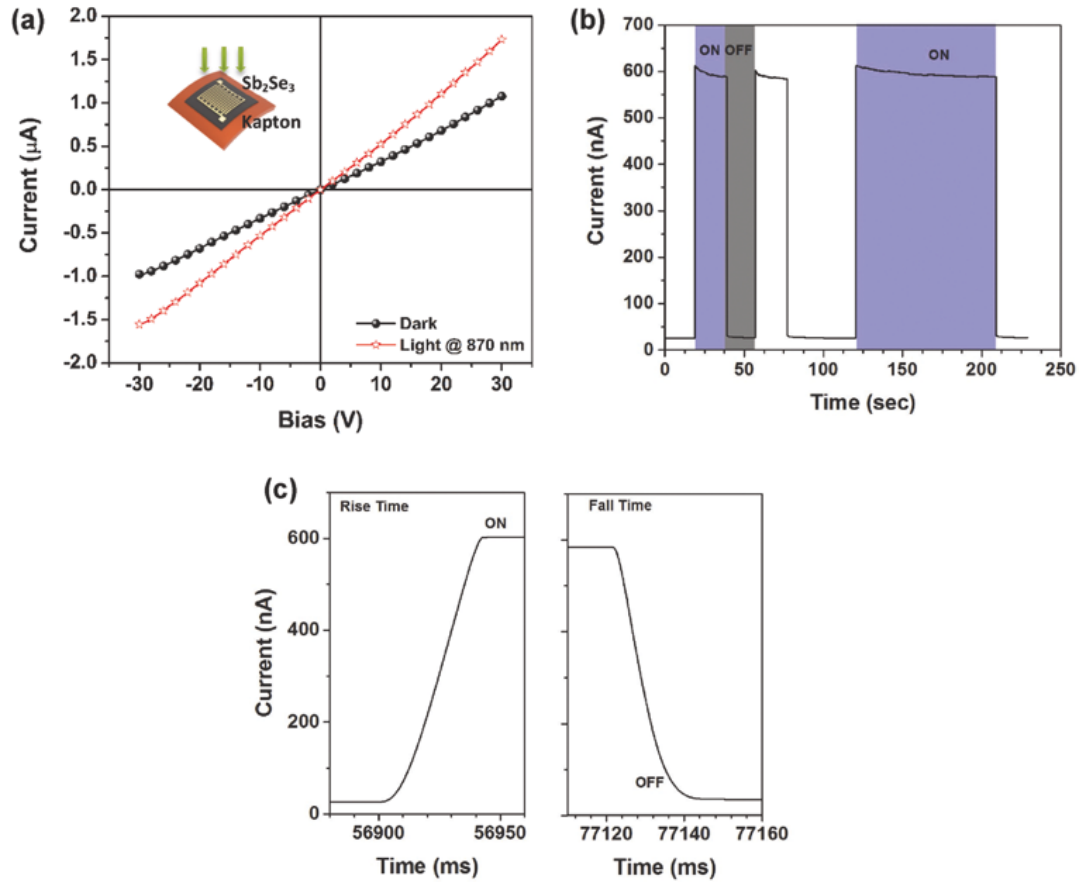


Figure 5.4: Photoconductive device properties: (a) I-V curves measured in the dark and under 870 nm illumination with a light intensity of $6.4 \mu\text{W}$. The inset shows a schematic of the fabricated PD with interdigitated electrodes. (b) Temporal photocurrent response under 365 nm pulsed light ($\sim 30 \text{ mW}/\text{cm}^2$) with periods of 20 s and 90 s (to demonstrate stability) at an applied bias of 10 V. (c) Zoomed-in temporal photocurrent response illustrating the rise ($24 \pm 2 \text{ ms}$) and decay ($9 \pm 2 \text{ ms}$) times measured in one period of modulation.[3]

We also obtained the spectral response of the PD by scaling the measured photocurrent to that of a calibrated Si photodetector. Given nominally identical illumination conditions under applied bias, this measurement can be used to extract the external quantum efficiency (EQE) of the device. Figure 5.5a (top) is a contour plot of the device EQE, which increases monotonically with the

applied bias. It can be seen that the applied bias influences the on/off ratio of the PDs, which is related to the bias dependence of the exciton dissociation and the background current. The EQE at 30 V reaches a maximum of 35% in the NIR (at 1.43 eV) and 51% in the UV (at 4.13 eV); however, it remains lower in the visible regime.

In order to investigate the source of the partial visible transparency present in the EQE spectra, we ran a series of finite-difference time-domain (FDTD) optical simulations of single nanowires and nanowire arrays. The nanowires in the arrays were randomly oriented and modeled as cylinders with a uniform distribution of 250 nm in diameter and 900 nm in length, based on the SEM measurements of the as-grown samples. Their refractive indices were determined from ellipsometry measurements, and absorption and reflection spectra as well as spatial electric field data were obtained for nanowire arrays, planar Sb_2Se_3 control films of comparable total thickness, and single nanowires.

The FDTD single NW absorption results qualitatively reproduce the observed dip in the visible region of the EQE spectra, while the planar device absorption has less of a spectral discrepancy across the same range. The single nanowire results give a potential explanation for this phenomenon: in the visible region, the most common size of nanowire does not support a waveguide mode; however, in the NIR, the nanowire supports a strong mode, leading to enhanced in-coupling and waveguiding in the nanowire array. Nanowire spatial electric field profiles are plotted in Figures 5.5c and d for 1100 nm and 650 nm illuminations, respectively. The small pitch of the interdigitated

electrodes ($100 \mu\text{m}$) leads to a shadowing effect that results in the loss of a fraction of the incoming light (35%). This shadowing could be reduced in future systems by replacing the opaque electrodes with thinner metals or transparent conductive oxides (TCOs) and optimizing their fill fraction.

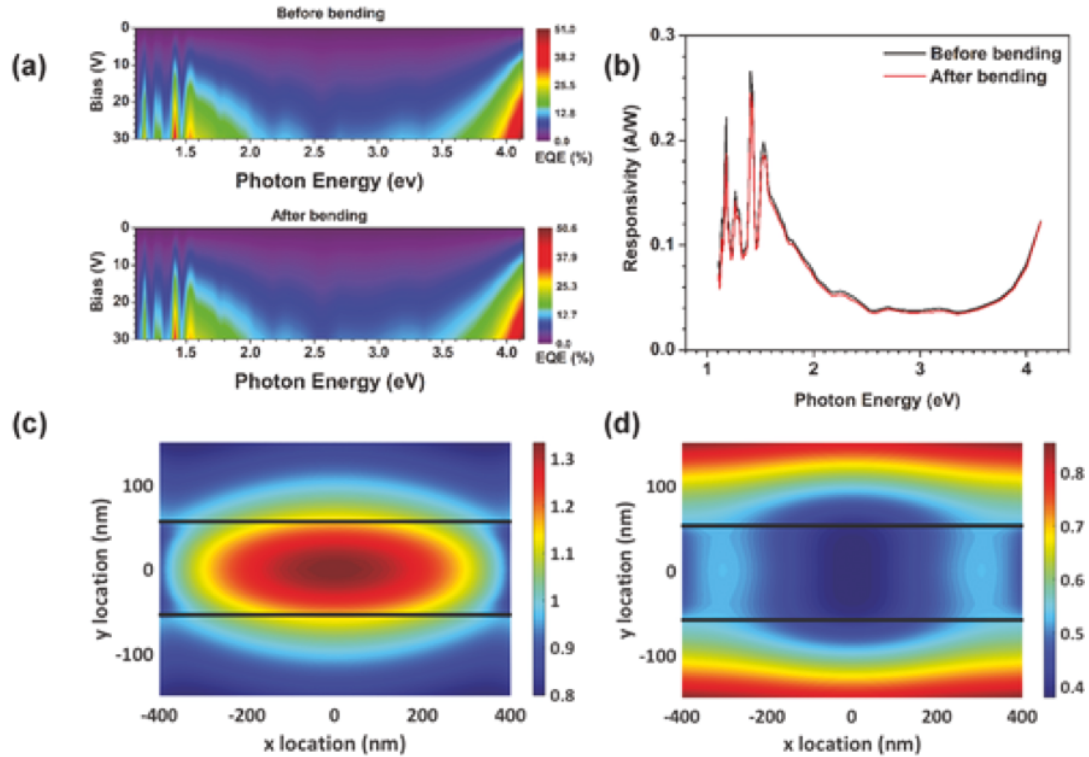


Figure 5.5: Figures of merit of the PDs: (a) EQE data as a function of applied bias: as-made device (before bending: top) and after 40 bending cycles (after bending: bottom) over a radius of curvature of 1 cm. (b) Representative spectral responsivity of the same device at an applied bias of 30 V. The mechanical robustness of the device is evident even after 40 bending cycles. (c)-(d) Calculated FDTD normalized electric field intensity for an average-sized single Sb_2Se_3 nanowire at the plane normal to the incident illumination (s-polarized source) at (c) $\lambda = 1100 \text{ nm}$ and (d) $\lambda = 650 \text{ nm}$. The presence of a waveguide mode in (c) vs. the absence of a confined mode within the NW in (d) demonstrates a possible explanation for the enhanced NIR performance seen in (a) and (b).[3]

These results imply that the spectral responsivity of the photodetectors could be tuned by changing the size of the nanowires in the array. The

nanowire size is controlled by relative precursor concentration during growth and post-annealing conditions. This tuning knob could be used to enable enhanced broadband performance of the molecular-ink based photodetectors. Additionally, controlling the nanowire size would allow for the realization of spectrally-selective detection by enhancing or suppressing performance in specific spectral bands.

Mechanical stability is critical for practical applications of flexible optoelectronics. We measured the device photocurrent after 40 bending cycles over a radius of curvature of 10 mm. As shown in Figure 5.5a (bottom), there is no significant change in the EQE after many bending cycles, demonstrating the robustness of these PDs.

The responsivity (R_λ), another critical measure of PD performance, has also been calculated using the relationship:

$$R_\lambda = \frac{I_{light}}{P_0} \quad (5.1)$$

where I_{light} is the device photocurrent under UV illumination, and P_0 is the light intensity. The calculated responsivities of the devices at 30 V bias are shown in Figure 5.5b before and after bending. The maximum responsivity reaches 0.27 A/W at 880 nm and experiences only a slight decrease to 0.25 A/W after 40 bending cycles, comparable with other broadband PD technologies.

The figures of merit for these molecular-ink-based PDs could be further improved by optimizing the processing conditions and tuning the gap between the two IDEs to optimize the metallized area. Optically, tuning the

nanowire size could target waveguiding and enhanced performance in the visible regime. One could also employ alternative light trapping and optical enhancement schemes such as integration of nanoscale plasmonic structures to improve in-coupling and benefit from local field enhancements.[55] Exploring these approaches is beyond the scope of this paper.

5.1.5 Conclusion

A facile, scalable, template-free route was developed to grow Sb_2Se_3 nanostructures directly on flexible substrates. Our molecular ink was prepared from elemental antimony and selenium dissolved in amine/thiol solvents and deposited at room temperature, employing a chemical method that should be extendable to other technologies. Compositional analysis and structural characterization of the resulting nanowires depict chemically pure, high-quality single-crystalline nanostructures with near stoichiometric composition. The fabricated PDs exhibit fast response and excellent figures of merit. Manipulating the nanowire size is an additional tuning knob that could be used to enhance the broadband performance and build spectrally selective optoelectronics. The negligible change in photoresponse after multiple bending cycles is evidence of excellent mechanical stability which makes the molecular inks a promising platform for low-cost, flexible and portable broadband photon detection, photoelectronic switches and other optoelectronic devices.

5.2 SnO₂/CuO Nanoheterojunctions for Visible-blind Photodetectors

This section is adapted from Ref. [56]. Reprinted with permission from Applied Physics Letters 107, no. 24, 241108, "High-performing visible-blind photodetectors based on SnO₂/CuO nanoheterojunctions," by X. Ting, M. R. Hasan, B. Qiu, E. S. Arinze, N. V. Nguyen, A. Motayed, S. M. Thon, and R. Debnath, copyright © 2015.

5.2.1 Introduction and Background

Transparent oxide semiconductors (TOSs) have attracted considerable attention in recent years, due to their versatile applications in transparent thin-film transistors,[57, 58] transparent electrodes,[59] and optoelectronics.[60, 61, 62] Visible-blind ultraviolet (UV) photodetectors (PDs) are of particular interest, owing to their broad application in digital imaging, missile plume detection, optical communications, and biomedical sensing.[63, 64, 65] Due to its wide bandgap and consequent transparency in the visible spectral region, SnO₂ has been demonstrated as a useful material for visible-blind UV photon detection.[66, 67, 68]

Typical n-SnO₂ PDs work as photoconductors with electrons as the majority carriers. In a photoconductor, absorption of photons with energy larger than the bandgap energy generates free carriers, leading to an increase in conductivity for a period known as the persistence time. The device conducts a single carrier type, and the persistence time can be lengthened by trapping of the non-conducting carrier type, leading to photoconductive gain

and quantum efficiency of greater than 100%. At a specific operation bias, the photocurrent is measured as the response of the PD, which can be used to calculate the EQE (external quantum efficiency) and responsivity of the device.

Current SnO₂ thin-film PD technology is limited by low responsivity, especially at longer UV wavelengths.[69] Efforts to improve device performance have focused on achieving better crystal quality and building one-dimensional SnO₂ nanostructures.[65, 70, 71, 72] The reported ultrahigh responsivity[70] of SnO₂ based PDs indicates that SnO₂ is a promising material for high-performing PDs. Here, we build thin-film SnO₂ PDs using a novel, facile, and scalable approach to fabricate nanoscale p-n heterojunctions with enhanced light absorption in the active material to improve the performance of UV PDs.

Nanorod-based heterojunctions consisting of p-CuO and n-SnO₂ have been previously developed for applications such as gas sensors.[73, 74] Our simplified PD device fabrication method consists of using rf-sputtering to deposit SnO₂ thin films and Cu nanoparticle (NP) clusters. The top layer of Cu NPs oxidizes in ambient to form CuO NP clusters, and the primary role of these clusters is to enhance absorption at the longer wavelength edge of the UV response in the PDs. We used finite-difference time-domain (FDTD) simulations to model the light absorption in devices with and without the CuO NPs and achieved good agreement with the experimental absorption spectra. Our electrical measurements indicated that the inclusion of the CuO NPs improved the responsivity of the PDs more than 5 fold compared to SnO₂-only devices.

5.2.2 Experimental Results and Discussion

The SnO₂ thin films were rf-sputtered using a SnO₂ target on sapphire substrates in a Denton Vacuum Discovery 550 sputtering system. The base pressure was kept at or below 6.7×10^{-4} Pa (5×10^{-6} Torr), and the substrate temperature was maintained at 325 ÅC to yield uniform films. The thickness of the deposited SnO₂ was measured using a J. A. Woollam M2000 ellipsometer and estimated to be (95 ± 2) nm.

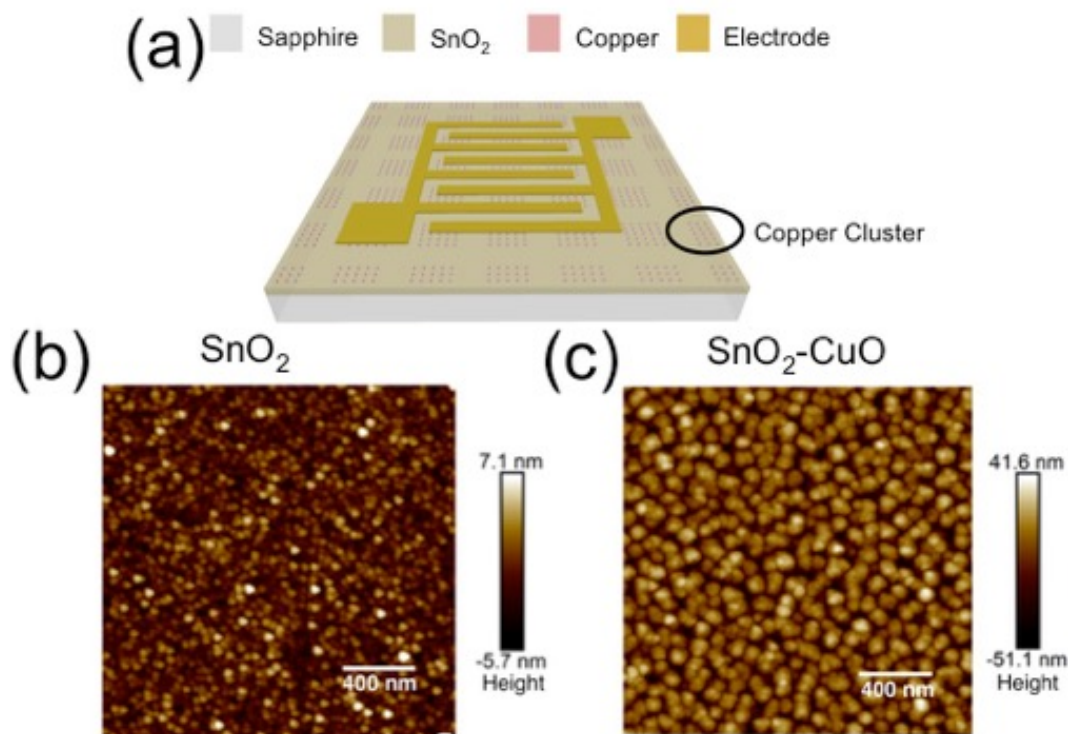


Figure 5.6: (a) Schematic of a SnO₂-CuO nanocluster PD device including the top interdigitated electrodes. Dimensions are not to scale. (b) High-resolution AFM image of an as-deposited SnO₂ film. (c) High-resolution AFM image of a SnO₂ film with a top layer of CuO nanoclusters.[56]

The Cu NP clusters were deposited on the SnO₂ films by rf-sputtering at room temperature. The deposition time was 185 seconds, and a shadow

mask was used to form square-shaped clusters composed of self-assembled nanoparticles with a nominal height of 40-50 nm rather than continuous cluster films. The total areal size of the Cu clusters was $200\ \mu\text{m} \times 200\ \mu\text{m}$, and they were spaced by $200\ \mu\text{m}$, as shown in Figure 5.6a. Oxidation of the Cu nanoparticles occurred spontaneously during and immediately following the deposition, resulting in the formation of CuO NPs. X-ray photoelectron spectroscopy (XPS) measurements indicated that the final NP clusters are primarily (> 95 %) composed of CuO, as shown in Figure 5.7b. Electron beam evaporation was used to deposit Ti/Al/Ti/Au interdigitated electrodes (IDEs) as the final step in the PD fabrication process. Figure 5.6a shows a device schematic of the entire structure.

The surface morphology of the SnO₂ and SnO₂-CuO films was measured using a Bruker Dimension FastScan atomic force microscope (AFM). Figures 5.6b and c show high-resolution AFM images of the bare SnO₂ film and the SnO₂ with a top layer of self-assembled CuO NPs. The measured root mean square (rms) surface roughness of the bare SnO₂ film was 1.8 nm, and the rms value increased to 13.8 nm after the addition of the CuO NPs. The grain sizes of the SnO₂ film and the CuO nanoclusters were estimated as (32.9 ± 13) nm and (74.6 ± 25) nm, respectively. A rough statistical analysis performed on the image in Figure 5.6c resulted in an average CuO NP surface density of $65\ \mu\text{m}^{-2}$ and an average particle height of 45 nm. These estimated parameters were used in the FDTD simulations described below.

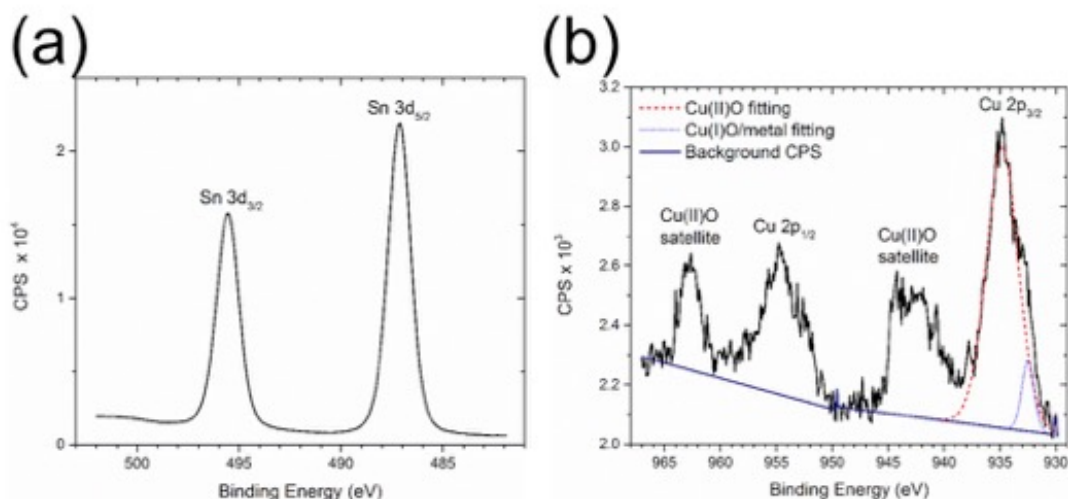


Figure 5.7: High-resolution XPS spectra of (a) the Sn 3d and (b) the Cu 2p regions of a SnO₂-CuO film. CPS is counts per second.[56]

We used XPS measurements to confirm the chemical identity of the SnO₂-CuO films. XPS curve-fitting and analysis was performed using CasaXPS software. The binding energies of the spectra were calibrated to the hydrocarbon peak at 284.8 eV. High-resolution XPS spectra of the Sn 3d and Cu 2p regions of the SnO₂-CuO film are shown in Figures 5.7a and b, respectively. As seen in Figure 5.7a, the Sn 3d 5/2 peak appears at a binding energy of (487.1 ± 0.1) eV with a satellite peak characteristic of Sn 3d 3/2 at (495.5 ± 0.1) eV, which is consistent with previously reported XPS data for SnO₂.^[75] The Cu 2p region of the spectrum shows a combination of Cu-related states that can be identified by referring to published reports.^[76, 77, 78] Curve-fitting of the Cu 2p region peaks (Figure 5.7b) was used to estimate that 95 at.% of the Cu content of the sample is in the form of Cu(II)O and the other 5 at.% is in the form of Cu(I)O or Cu metal. From these measurements, we concluded that the deposited Cu NPs are substantially oxidized to form CuO during and

after the deposition process.

The absorption spectra and absorption coefficients (α) of the SnO₂ and SnO₂-CuO films were measured using an Ocean Optics QE65000 spectrometer and a J. A. Woollam M2000 ellipsometer, respectively. Optical absorbance spectra of the SnO₂ and SnO₂-CuO films are shown in Figure 5.8b. A significant enhancement in the light absorption over the wavelength range of 250 nm to 475 nm is observed in the film decorated with CuO NPs compared to the bare SnO₂ film.

To verify the enhancement mechanism associated with the addition of the CuO NP clusters, we used FDTD simulations to calculate the optical properties of a 100 nm thick SnO₂ film with and without CuO nanoclusters on top. The simulated structure is shown in Figure 5.8a. The CuO NPs were modeled as randomly distributed elliptic paraboloids. The particle shape, dimensions and average surface densities were derived from the analysis of the AFM images (Figure 5.6c). Refractive indices for the SnO₂ film were obtained from ellipsometry measurements, and reported values were used for the refractive indices for the CuO[79] and sapphire[80] substrate. A broadband (200 nm - 1000 nm) plane wave incident from the nanocluster side of the device was used as the excitation source for the simulations.

Figures 5.8b and c show the experimental and simulated absorption spectra for the SnO₂ films with and without CuO NP clusters. The simulated and measured spectra show qualitative agreement in the effect of the CuO NPs on the increase in absorbance across all wavelengths in the plotted range, the apparent red shift of the absorption onset, and the change in shape of the

absorbance curve. Differences in quantitative agreement can be attributed to inhomogeneity in the NP size and density distributions, and uncertainty in the SnO₂ film thickness in the real devices.

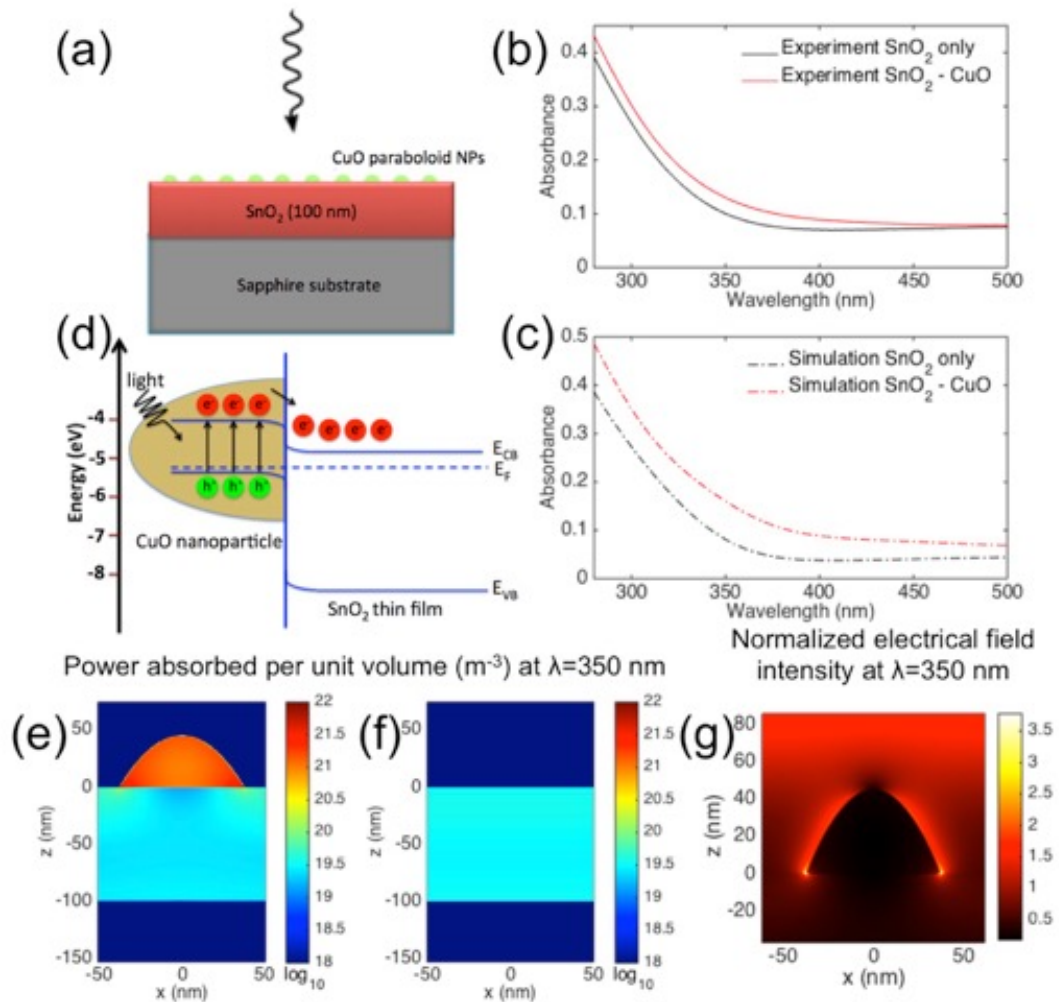


Figure 5.8: (a) Diagram of the setup for the FDTD simulations. A SnO₂ film thickness of 100 nm was used for the simulations with and without CuO NPs. The CuO NP clusters were modeled as elliptic paraboloids with heights of 45 nm and diameters of 75 nm. The CuO NPs were randomly distributed on the SnO₂ film with an average surface density of $65 \mu\text{m}^{-2}$. The size and average density values of the NPs were based on AFM measurements of the real devices. (b) Measured and (c) FDTD simulated absorption spectra of the SnO₂ and SnO₂-CuO films. (d) Schematic band diagram illustrating the hypothesized electron transfer process in the CuO-SnO₂ nanoheterojunctions under irradiation. (e) Spatial cross-section of simulated power absorbed per unit volume at $\lambda = 350 \text{ nm}$ in a single CuO NP on a SnO₂ film and (f) in a bare SnO₂ film. (g) Spatial cross-section of simulated normalized electrical field intensity at $\lambda = 350 \text{ nm}$ for a single CuO NP on a SnO₂ film.[56]

The simulated spatial absorption profiles for a single CuO NP on a SnO₂

film and a bare SnO₂ film at a wavelength of 350 nm are plotted in Figure 5.8e and Figure 5.8f. The normalized electrical field intensity at a wavelength 350 nm is plotted in Figure 5.8g. There is an enhancement of the local electrical field intensity around the NP and strong associated absorption within the NP. We attribute the enhanced absorption in the composite devices to this effect. Our aim was to use this increase in absorption without relying on an increase in SnO₂ film thickness to improve the responsivity of the SnO₂-based photodetectors.

A schematic band diagram for the SnO₂/CuO pn-nanoheterojunctions is depicted in Figure 3(d) using energy levels reported for p-CuO[81] and n-SnO₂[82]. The nanoheterojunction structure takes advantage of the intense absorption in the CuO NPs to transfer a high density of photogenerated electrons from the p CuO NPs to the n-SnO₂ film, while the transfer of holes is hindered by the energy barrier at the junction. The smaller bandgap of CuO (1.35 eV[81]) results in increased absorption at the red edge of the UV spectrum, and the pn-heterojunction nature of the CuO/SnO₂ interface facilitates charge transfer upon illumination to increase the responsivity of the photodetector. Electrons injected into the conduction band of SnO₂ from the CuO increase the free majority carrier density in the photoconductive material, which could lead to a significant increase in photocurrent in the PD. Although the bandgap of CuO is small, the nanoscale structure of the CuO particles are predicted to allow the films to remain "visible-blind" due to poor in-coupling and low absorption in structures that are much smaller than the visible and infrared material photon absorption lengths.

Typical I-V characteristics of the SnO₂-only and CuO-SnO₂ devices measured in the dark and under UV-illumination are shown in Figure 4(a). The photocurrent generated in the PD with CuO NPs was almost double that of the SnO₂-only device under 290 nm wavelength illumination for all tested biases. The measured dark current for the CuO-SnO₂ PD was also larger than that of the SnO₂-only device, indicating that the conductivity of the CuO-SnO₂ composite film was larger than that of the SnO₂-only film.

To quantify the performance of the PDs, we used the photocurrent-to-dark current ratio, defined as:

$$\text{Photocurrent - to - darkcurrentratio} = \frac{I_{UV} - I_{dark}}{I_{dark}} \quad (5.2)$$

where I_{UV} is the current under UV illumination, and I_{dark} is the dark current at the same voltage. The CuO-SnO₂ PDs exhibited a PF of ~ 592 at 1.2 V under 290 nm illumination.

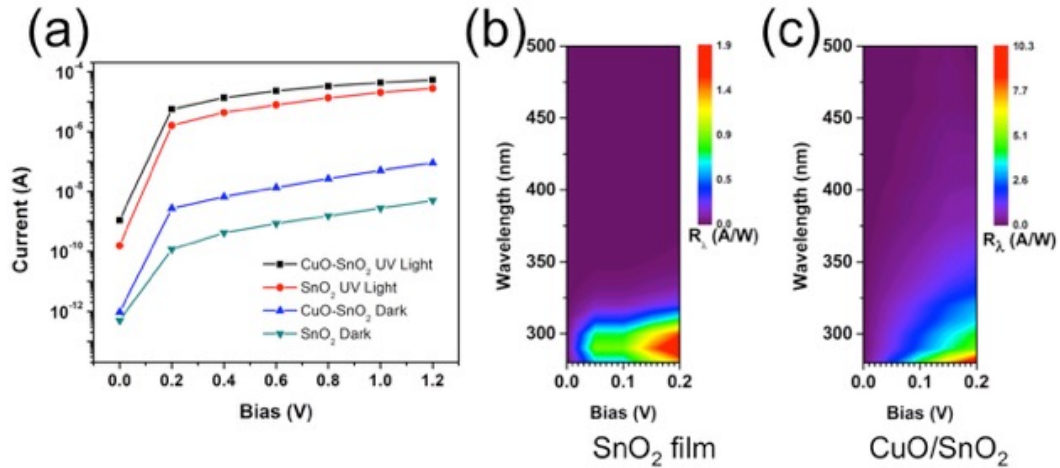


Figure 5.9: (a) ON/OFF I-V curves for SnO₂-only and CuO/SnO₂ PDs under UV illumination at a wavelength of 290 nm. (b) Responsivity as a function of bias and wavelength for SnO₂ and (c) SnO₂-CuO thin film photodetectors.[56]

Responsivities of the SnO₂ and SnO₂-CuO PDs were measured at various bias voltages under a spectrally filtered light source. The measurements, calibrated using a standard NIST silicon photodiode, were associated with a total uncertainty of $\pm 5\%$ (fractional). In order to obtain stable and reliable data, the photocurrent at each wavelength was measured with a delay of 180 seconds with respect to the illumination. The need for stable photocurrent operation precluded higher resolution measurements of the PD response time.

The UV photocurrent response of the PDs was recorded over a voltage range of 0 V to 1.2 V at an illumination wavelength of 290 nm, as shown in Figure 5.9a. In addition to light current enhancements, the dark current also increases after the SnO₂ surface is covered with the CuO NPs, despite the assumed formation of a depletion layer. This increase can be attributed to several potential mechanisms. The small amount of Cu(I)O or Cu metal visible in the XPS spectrum could lead to an increase in the dark current which could be ameliorated in future iterations by including a controlled oxidation step in the fabrication process. Additionally, the presence of defects close to the nanojunction interface could reduce carrier lifetimes, potentially act as dopants, and facilitate leakage paths, contributing to an increase in device dark current.

Figures 5.9b and c illustrate the spectral responsivity of the SnO₂ devices with and without CuO NPs in the low bias regime. The SnO₂-only PDs reached a maximum responsivity of 1.9 A/W at 0.2 V bias under 290 nm illumination, while the devices with CuO NP clusters exhibited a responsivity of 10.3 A/W at 0.2 V bias under 280 nm illumination. The incorporation of the

CuO NPs resulted in a greater than 5 fold improvement of the responsivity. Additionally, the SnO₂-only PD response had a sharp cutoff at around 320 nm in wavelength, whereas the SnO₂-CuO PDs displayed some response out to 340 nm in wavelength at low bias. The broadening of the spectral detection range can be attributed to the drastic enhancement of light absorption and charge transfer facilitated by the SnO₂-CuO nanoheterojunctions in the UVA spectral region. Although the responsivity of these devices is lower than that of PDs based on one-dimensional structures^{9,14}, it is competitive with thin-film based UV PDs made from other traditional semiconductor materials.²⁷ Additionally, this method produces robust structures without complex fabrication processes that operate at low bias, making it suitable for practical applications.

5.2.3 Conclusion

In summary, we have demonstrated high responsivity visible-blind UV PDs based on sputtered SnO₂-CuO nanoheterojunction films. We investigated the properties of the films using AFM and XPS measurements, confirming that the sputtered Cu forms self-assembled nanoparticle clusters that are composed primarily of Cu(II)O after air exposure. The peak responsivity reached a value of 10.3 A/W at a low bias of 0.2 V in the CuO-SnO₂ devices, representing a five-fold increase over the highest responsivity achieved in devices without CuO NPs. The performance enhancement is attributed to the intense local absorption of the CuO NPs and the charge transfer facilitated by the CuO-SnO₂ pn nanoheterojunction structures. Our approach of utilizing

CuO-based pn nanoheterojunctions to enhance the efficiency of visible-blind SnO₂ photodiodes represents a viable path for building UV optoelectronic devices based on cost-effective materials.

References

- [1] Letian Dou, Yang Micheal Yang, Jingbi You, Ziruo Hong, Wei-Hsuan Chang, Gang Li, and Yang Yang. "Solution-processed hybrid perovskite photodetectors with high detectivity". In: *Nature communications* 5 (2014), p. 5404.
- [2] Xiong Gong, Minghong Tong, Yangjun Xia, Wanzhu Cai, Ji Sun Moon, Yong Cao, Gang Yu, Chan-Long Shieh, Boo Nilsson, and Alan J Heeger. "High-detectivity polymer photodetectors with spectral response from 300 nm to 1450 nm". In: *Science* 325.5948 (2009), pp. 1665–1667.
- [3] Md Rezaul Hasan, Ebuka S Arinze, Arunima K Singh, Vladimir P Oleshko, Shiqi Guo, Asha Rani, Yan Cheng, Irina Kalish, Mona E Zaghloul, Mulpuri V Rao, et al. "An Antimony Selenide Molecular Ink for Flexible Broadband Photodetectors". In: *Advanced electronic materials* 2.9 (2016), p. 1600182.
- [4] Steven A McDonald, Gerasimos Konstantatos, Shiguo Zhang, Paul W Cyr, Ethan JD Klem, Larissa Levina, and Edward H Sargent. "Solution-processed PbS quantum dot infrared photodetectors and photovoltaics". In: *Nature materials* 4.2 (2005), p. 138.
- [5] Ethan JD Klem, Chris Gregory, Dorota Temple, and Jay Lewis. "PbS colloidal quantum dot photodiodes for low-cost SWIR sensing". In: *Infrared Technology and Applications XLI*. Vol. 9451. International Society for Optics and Photonics. 2015, p. 945104.
- [6] HE Katz, AJ Lovinger, J Johnson, Ch Kloc, T Siegrist, W Li, Y-Y Lin, and A Dodabalapur. "A soluble and air-stable organic semiconductor with high electron mobility". In: *Nature* 404.6777 (2000), p. 478.
- [7] CR Kagan, DB Mitzi, and CD Dimitrakopoulos. "Organic-inorganic hybrid materials as semiconducting channels in thin-film field-effect transistors". In: *Science* 286.5441 (1999), pp. 945–947.

REFERENCES

- [8] Xiangfeng Duan, Chunming Niu, Vijendra Sahi, Jian Chen, J Wallace Parce, Stephen Empeocles, and Jay L Goldman. "High-performance thin-film transistors using semiconductor nanowires and nanoribbons". In: *Nature* 425.6955 (2003), p. 274.
- [9] H Sirringhaus, T Kawase, RH Friend, T Shimoda, M Inbasekaran, W Wu, and EP Woo. "High-resolution inkjet printing of all-polymer transistor circuits". In: *Science* 290.5499 (2000), pp. 2123–2126.
- [10] Brent A Ridley, Babak Nivi, and Joseph M Jacobson. "All-inorganic field effect transistors fabricated by printing". In: *Science* 286.5440 (1999), pp. 746–749.
- [11] David B Mitzi, Laura L Kosbar, Conal E Murray, Matthew Copel, and Ali Afzali. "High-mobility ultrathin semiconducting films prepared by spin coating". In: *Nature* 428.6980 (2004), p. 299.
- [12] Ying Zhou, Meiyong Leng, Zhe Xia, Jie Zhong, Huaibing Song, Xincheng Liu, Bo Yang, Junpei Zhang, Jie Chen, Kunhao Zhou, et al. "Solution-processed antimony selenide heterojunction solar cells". In: *Advanced Energy Materials* 4.8 (2014), p. 1301846.
- [13] David B Mitzi, Matthew Copel, and S Jay Chey. "Low-voltage transistor employing a high-mobility spin-coated chalcogenide semiconductor". In: *Advanced Materials* 17.10 (2005), pp. 1285–1289.
- [14] Fengjiao Zhang, Chong-an Di, Nikolai Berdunov, Yuanyuan Hu, Yunbin Hu, Xike Gao, Qing Meng, Henning Sirringhaus, and Daoben Zhu. "Ultrathin film organic transistors: precise control of semiconductor thickness via spin-coating". In: *Advanced Materials* 25.10 (2013), pp. 1401–1407.
- [15] AR Brown, A Pomp, CM Hart, and DM De Leeuw. "Logic gates made from polymer transistors and their use in ring oscillators". In: *Science* 270.5238 (1995), pp. 972–974.
- [16] HEA Huitema, GH Gelinck, JBPH van der Putten, KE Kuijk, CM Hart, E Cantatore, PT Herwig, and AJ van Breemen. "JM; de Leeuw, DM". In: *Nature* 414 (2001), p. 599.
- [17] Francis Garnier, Ryad Hajlaoui, Abderrahim Yassar, and Pratima Srivastava. "All-polymer field-effect transistor realized by printing techniques". In: *Science* 265.5179 (1994), pp. 1684–1686.

REFERENCES

- [18] Gerwin H Gelinck. "GH Gelinck, HEA Huitema, E. van Veenendaal, E. Cantatore, L. Schrijnemakers, JB van der Putten, TC Geuns, M. Beenhakkers, JB Giesbers, B.-H. Huisman et al., *Nat. Mater.* 3, 106 (2004)." In: *Nat. Mater.* 3 (2004), p. 106.
- [19] Yanming Sun, Gregory C Welch, Wei Lin Leong, Christopher J Takacs, Guillermo C Bazan, and Alan J Heeger. "Solution-processed small-molecule solar cells with 6.7% efficiency". In: *Nature materials* 11.1 (2012), p. 44.
- [20] David B Mitzi. "Solution-processed inorganic semiconductors". In: *Journal of Materials Chemistry* 14.15 (2004), pp. 2355–2365.
- [21] Jong-Soo Lee, Maksym V Kovalenko, Jing Huang, Dae Sung Chung, and Dmitri V Talapin. "Band-like transport, high electron mobility and high photoconductivity in all-inorganic nanocrystal arrays". In: *Nature nanotechnology* 6.6 (2011), p. 348.
- [22] Andrew M Smith and Shuming Nie. "Semiconductor nanocrystals: structure, properties, and band gap engineering". In: *Accounts of chemical research* 43.2 (2009), pp. 190–200.
- [23] PK Nair, MTS Nair, VM Garcia, OL Arenas, Y Pena, A Castillo, IT Ayala, O Gomezdaza, A Sanchez, J Campos, et al. "Semiconductor thin films by chemical bath deposition for solar energy related applications". In: *Solar Energy Materials and Solar Cells* 52.3-4 (1998), pp. 313–344.
- [24] Olivia Niitsoo, Shaibal K Sarkar, Christophe Pejoux, Sven Rühle, David Cahen, and Gary Hodes. "Chemical bath deposited CdS/CdSe-sensitized porous TiO₂ solar cells". In: *Journal of Photochemistry and Photobiology A: Chemistry* 181.2-3 (2006), pp. 306–313.
- [25] HyoJoong Lee, Mingkui Wang, Peter Chen, Daniel R Gamelin, Shaik M Zakeeruddin, Michael Gratzel, and Md K Nazeeruddin. "Efficient CdSe quantum dot-sensitized solar cells prepared by an improved successive ionic layer adsorption and reaction process". In: *Nano letters* 9.12 (2009), pp. 4221–4227.
- [26] Hyo Joong Lee, Jiwon Bang, Juwon Park, Sungjee Kim, and Su-Moon Park. "Multilayered semiconductor (CdS/CdSe/ZnS)-sensitized TiO₂ mesoporous solar cells: all prepared by successive ionic layer adsorption and reaction processes". In: *Chemistry of Materials* 22.19 (2010), pp. 5636–5643.

REFERENCES

- [27] SA Studenikin, Nickolay Golego, and Michael Cocivera. "Fabrication of green and orange photoluminescent, undoped ZnO films using spray pyrolysis". In: *Journal of Applied physics* 84.4 (1998), pp. 2287–2294.
- [28] E Andrade, M Miki-Yoshida, et al. "Growth, structure and optical characterization of high quality ZnO thin films obtained by spray pyrolysis". In: *Thin Solid Films* 350.1-2 (1999), pp. 192–202.
- [29] Ying Zhou, Liang Wang, Shiyu Chen, Sikai Qin, Xinsheng Liu, Jie Chen, Ding-Jiang Xue, Miao Luo, Yuanzhi Cao, Yibing Cheng, et al. "Thin-film Sb₂Se₃ photovoltaics with oriented one-dimensional ribbons and benign grain boundaries". In: *Nature Photonics* 9.6 (2015), p. 409.
- [30] Yong-Qiang Liu, Meng Zhang, Feng-Xia Wang, and Ge-Bo Pan. "Facile microwave-assisted synthesis of uniform Sb₂Se₃ nanowires for high performance photodetectors". In: *Journal of Materials Chemistry C* 2.2 (2014), pp. 240–244.
- [31] DT Morelli, V Jovovic, and JP Heremans. "Intrinsically minimal thermal conductivity in cubic I-V-VI₂ semiconductors". In: *Physical review letters* 101.3 (2008), p. 035901.
- [32] G Domingo, RS Itoga, and CR Kannewurf. "Fundamental Optical Absorption in SnS₂ and SnSe₂". In: *Physical Review* 143.2 (1966), p. 536.
- [33] Yong Chan Choi, Tarak Nath Mandal, Woon Seok Yang, Yong Hui Lee, Sang Hyuk Im, Jun Hong Noh, and Sang Il Seok. "Sb₂Se₃-sensitized inorganic-organic heterojunction solar cells fabricated using a single-source precursor". In: *Angewandte Chemie* 126.5 (2014), pp. 1353–1357.
- [34] Yunki Kim, Antonio DiVenere, George KL Wong, JB Ketterson, Sunglae Cho, and Jerry R Meyer. "Structural and thermoelectric transport properties of Sb₂Te₃ thin films grown by molecular beam epitaxy". In: *Journal of applied physics* 91.2 (2002), pp. 715–718.
- [35] A Boulouz, S Chakraborty, A Giani, F Pascal Delannoy, Alexandre Boyer, and J Schumann. "Transport properties of V-VI semiconducting thermoelectric BiSbTe alloy thin films and their application to micromodule Peltier devices". In: *Journal of Applied Physics* 89.9 (2001), pp. 5009–5014.

REFERENCES

- [36] Rong Huang, Jie Zhang, Fenfen Wei, Lin Shi, Tao Kong, and Guosheng Cheng. "Ultra-high Responsivity of Ternary Sb–Bi–Se Nanowire Photodetectors". In: *Advanced Functional Materials* 24.23 (2014), pp. 3581–3586.
- [37] Tianyou Zhai, Mingfu Ye, Liang Li, Xiaosheng Fang, Meiyong Liao, Yongfang Li, Yasuo Koide, Yoshio Bando, and Dmitri Golberg. "Single-Crystalline Sb₂Se₃ Nanowires for High-Performance Field Emitters and Photodetectors". In: *Advanced Materials* 22.40 (2010), pp. 4530–4533.
- [38] Donghyeuk Choi, Yamujin Jang, JeeHee Lee, Gyoung Hwa Jeong, Dongmok Whang, Sung Woo Hwang, Kyung-Sang Cho, and Sang-Wook Kim. "Diameter-controlled and surface-modified Sb₂Se₃ nanowires and their photodetector performance". In: *Scientific reports* 4 (2014), p. 6714.
- [39] Matthias Wuttig and Noboru Yamada. "Phase-change materials for rewriteable data storage". In: *Nature materials* 6.11 (2007), p. 824.
- [40] Ren Bin Yang, Julien Bachmann, Eckhard Pippel, Andreas Berger, Jörg Woltersdorf, Ulrich Gösele, and Kornelius Nielsch. "Pulsed Vapor-Liquid-Solid Growth of Antimony Selenide and Antimony Sulfide Nanowires". In: *Advanced Materials* 21.31 (2009), pp. 3170–3174.
- [41] Frédéric Verger, Virginie Nazabal, Florent Colas, P Nĕmec, Christophe Cardinaud, Emeline Baudet, Radwan Chahal, Emmanuel Rinnert, Kada Boukerma, Isabelle Péron, et al. "RF sputtered amorphous chalcogenide thin films for surface enhanced infrared absorption spectroscopy". In: *Optical Materials Express* 3.12 (2013), pp. 2112–2131.
- [42] Miao Luo, Meiyong Leng, Xinsheng Liu, Jie Chen, Chao Chen, Sikai Qin, and Jiang Tang. "Thermal evaporation and characterization of superstrate CdS/Sb₂Se₃ solar cells". In: *Applied Physics Letters* 104.17 (2014), p. 173904.
- [43] Nadezda V Tarakina, S Schreyeck, T Borzenko, C Schumacher, G Karczewski, K Brunner, C Gould, H Buhmann, and LW Molenkamp. "Comparative study of the microstructure of Bi₂Se₃ thin films grown on Si (111) and InP (111) substrates". In: *Crystal Growth & Design* 12.4 (2012), pp. 1913–1918.
- [44] Teodor K Todorov, Kathleen B Reuter, and David B Mitzi. "High-efficiency solar cell with earth-abundant liquid-processed absorber". In: *Advanced materials* 22.20 (2010), E156–E159.

REFERENCES

- [45] David H Webber and Richard L Brutchey. "Alkahest for V2VI3 chalcogenides: dissolution of nine bulk semiconductors in a diamine-dithiol solvent mixture". In: *Journal of the American Chemical Society* 135.42 (2013), pp. 15722–15725.
- [46] Carrie L McCarthy, David H Webber, Emily C Schueller, and Richard L Brutchey. "Solution-Phase Conversion of Bulk Metal Oxides to Metal Chalcogenides Using a Simple Thiol–Amine Solvent Mixture". In: *Angewandte Chemie International Edition* 54.29 (2015), pp. 8378–8381.
- [47] David H Webber, Jannise J Buckley, Priscilla D Antunez, and Richard L Brutchey. "Facile dissolution of selenium and tellurium in a thiol–amine solvent mixture under ambient conditions". In: *Chemical Science* 5.6 (2014), pp. 2498–2502.
- [48] Jianmin Ma, Yaping Wang, Yijing Wang, Qing Chen, Jiabiao Lian, and Wenjun Zheng. "Controlled synthesis of one-dimensional Sb₂Se₃ nanostructures and their electrochemical properties". In: *The Journal of Physical Chemistry C* 113.31 (2009), pp. 13588–13592.
- [49] Guihuan Chen, Wenliang Wang, Chunde Wang, Tao Ding, and Qing Yang. "Controlled synthesis of ultrathin Sb₂Se₃ nanowires and application for flexible photodetectors". In: *Advanced Science* 2.10 (2015), p. 1500109.
- [50] Graham Cliff and G_W Lorimer. "The quantitative analysis of thin specimens". In: *Journal of Microscopy* 103.2 (1975), pp. 203–207.
- [51] Ray F Egerton. *Electron energy-loss spectroscopy in the electron microscope*. Springer Science & Business Media, 2011.
- [52] Nilkamal Maiti, Sang Hyuk Im, Yong Hui Lee, Chong-Hyeak Kim, and Sang Il Seok. "Solvent-assisted growth of Sb₂Se₃ nanocompounds from a single-source precursor under mild reaction conditions". In: *CrystEngComm* 13.11 (2011), pp. 3767–3772.
- [53] Xinsheng Liu, Jie Chen, Miao Luo, Meiyong Leng, Zhe Xia, Ying Zhou, Sikai Qin, Ding-Jiang Xue, Lu Lv, Han Huang, et al. "Thermal evaporation and characterization of Sb₂Se₃ thin film for substrate Sb₂Se₃/CdS solar cells". In: *ACS applied materials & interfaces* 6.13 (2014), pp. 10687–10695.
- [54] Rajasekarakumar Vadapoo, Sridevi Krishnan, Hulusi Yilmaz, and Carlos Marin. "Electronic structure of antimony selenide (Sb₂Se₃) from GW calculations". In: *physica status solidi (b)* 248.3 (2011), pp. 700–705.

REFERENCES

- [55] Pierre Berini. "Surface plasmon photodetectors and their applications". In: *Laser & Photonics Reviews* 8.2 (2014), pp. 197–220.
- [56] Ting Xie, Md Rezaul Hasan, Botong Qiu, Ebuka S Arinze, Nhan V Nguyen, Abhishek Motayed, Susanna M Thon, and Ratan Debnath. "High-performing visible-blind photodetectors based on SnO₂/CuO nanoheterojunctions". In: *Applied physics letters* 107.24 (2015), p. 241108.
- [57] Kenji Nomura, Hiromichi Ohta, Kazushige Ueda, Toshio Kamiya, Masahiro Hirano, and Hideo Hosono. "Thin-film transistor fabricated in single-crystalline transparent oxide semiconductor". In: *Science* 300.5623 (2003), pp. 1269–1272.
- [58] Kenji Nomura, Hiromichi Ohta, Akihiro Takagi, Toshio Kamiya, Masahiro Hirano, and Hideo Hosono. "Room-temperature fabrication of transparent flexible thin-film transistors using amorphous oxide semiconductors". In: *Nature* 432.7016 (2004), p. 488.
- [59] Tadatsugu Minami. "Transparent conducting oxide semiconductors for transparent electrodes". In: *Semiconductor science and technology* 20.4 (2005), S35.
- [60] Ratan Debnath, Ting Xie, Baomei Wen, Wei Li, Jong Y Ha, Nichole F Sullivan, Nhan V Nguyen, and Abhishek Motayed. "A solution-processed high-efficiency p-NiO/n-ZnO heterojunction photodetector". In: *Rsc Advances* 5.19 (2015), pp. 14646–14652.
- [61] Ting Xie, Guannan Liu, Baomei Wen, Jong Y Ha, Nhan V Nguyen, Abhishek Motayed, and Ratan Debnath. "Tunable ultraviolet photoresponse in solution-processed p–n junction photodiodes based on transition-metal oxides". In: *ACS applied materials & interfaces* 7.18 (2015), pp. 9660–9667.
- [62] YY Xi, YF Hsu, AB Djurišić, AMC Ng, WK Chan, HL Tam, and KW Cheah. "NiO/ZnO light emitting diodes by solution-based growth". In: *Applied Physics Letters* 92.11 (2008), p. 113505.
- [63] Ya-Qing Bie, Zhi-Min Liao, Hong-Zhou Zhang, Guang-Ru Li, Yu Ye, Yang-Bo Zhou, Jun Xu, Zhi-Xin Qin, Lun Dai, and Da-Peng Yu. "Self-Powered, ultrafast, visible-blind UV detection and optical logical operation based on ZnO/GaN Nanoscale p-n junctions". In: *Advanced Materials* 23.5 (2011), pp. 649–653.

REFERENCES

- [64] Wei Zhang, Jin Xu, Wei Ye, Yang Li, Zhiqiang Qi, Jiangnan Dai, Zhihao Wu, Changqing Chen, Jun Yin, Jing Li, et al. "High-performance AlGaIn metal–semiconductor–metal solar-blind ultraviolet photodetectors by localized surface plasmon enhancement". In: *Applied Physics Letters* 106.2 (2015), p. 021112.
- [65] Linfeng Hu, Jian Yan, Meiyong Liao, Limin Wu, and Xiaosheng Fang. "Ultrahigh external quantum efficiency from thin SnO₂ nanowire ultraviolet photodetectors". In: *Small* 7.8 (2011), pp. 1012–1017.
- [66] Yujin Chen, Chunling Zhu, Maosheng Cao, and Taihong Wang. "Photoresponse of SnO₂ nanobelts grown in situ on interdigital electrodes". In: *Nanotechnology* 18.28 (2007), p. 285502.
- [67] Sanjay Mathur, Sven Barth, Hao Shen, Jae-Chul Pyun, and Ulf Werner. "Size-dependent photoconductance in SnO₂ nanowires". In: *Small* 1.7 (2005), pp. 713–717.
- [68] Hao Chen, Linfeng Hu, Xiaosheng Fang, and Limin Wu. "General Fabrication of Monolayer SnO₂ Nanonets for High-Performance Ultraviolet Photodetectors". In: *Advanced Functional Materials* 22.6 (2012), pp. 1229–1235.
- [69] Takayoshi Oshima, Takeya Okuno, and Shizuo Fujita. "UV-B sensor based on a SnO₂ thin film". In: *Japanese Journal of Applied Physics* 48.12R (2009), p. 120207.
- [70] Kewei Liu, Makoto Sakurai, Masakazu Aono, and Dezhen Shen. "Ultrahigh-Gain Single SnO₂ Microrod Photoconductor on Flexible Substrate with Fast Recovery Speed". In: *Advanced Functional Materials* 25.21 (2015), pp. 3157–3163.
- [71] Wei Tian, Chao Zhang, Tianyou Zhai, Song-Lin Li, Xi Wang, Meiyong Liao, Kazuhito Tsukagoshi, Dmitri Golberg, and Yoshio Bando. "Flexible SnO₂ hollow nanosphere film based high-performance ultraviolet photodetector". In: *Chemical Communications* 49.36 (2013), pp. 3739–3741.
- [72] Cheng-Hua Lin, Reui-San Chen, Tzung-Te Chen, Hsin-Yi Chen, Yang-Fang Chen, Kuei-Hsien Chen, and Li-Chyong Chen. "High photocurrent gain in SnO₂ nanowires". In: *Applied Physics Letters* 93.11 (2008), p. 112115.

REFERENCES

- [73] Irina Giebelhaus, Elena Varechkina, Thomas Fischer, Marina Rumyantseva, Vladimir Ivanov, Alexander Gaskov, Joan Ramon Morante, Jordi Arbiol, Wieland Tyrra, and Sanjay Mathur. "One-dimensional CuO-SnO₂ p-n heterojunctions for enhanced detection of H₂S". In: *Journal of Materials Chemistry A* 1.37 (2013), pp. 11261–11268.
- [74] Xinyu Xue, Lili Xing, Yujin Chen, Songlin Shi, Yanguo Wang, and Taihong Wang. "Synthesis and H₂S sensing properties of CuO-SnO₂ core/shell pn-junction nanorods". In: *The Journal of Physical Chemistry C* 112.32 (2008), pp. 12157–12160.
- [75] Lilai Liu, Maozhong An, Peixia Yang, and Jinqiu Zhang. "Superior cycle performance and high reversible capacity of SnO₂/graphene composite as an anode material for lithium-ion batteries". In: *Scientific reports* 5 (2015), p. 9055.
- [76] RP Vasquez. "CuO by XPS". In: *Surface Science Spectra* 5.4 (1998), pp. 262–266.
- [77] Dahlang Tahir and Sven Tougaard. "Electronic and optical properties of Cu, CuO and Cu₂O studied by electron spectroscopy". In: *Journal of physics: Condensed matter* 24.17 (2012), p. 175002.
- [78] RP Vasquez. "Cu₂O by XPS". In: *Surface Science Spectra* 5.4 (1998), pp. 257–261.
- [79] ED Palik. "Handbook of Optical Constants of Solids II Academic". In: *New York* 19912 (1991).
- [80] IH Malitson and MJ Dodge. "Refractive-index and birefringence of synthetic sapphire". In: *Journal Of The Optical Society Of America*. Vol. 62. 11. AMER INST PHYSICS CIRCULATION FULFILLMENT DIV, 500 SUNNYSIDE BLVD, WOODBURY, NY 11797-2999. 1972, pp. 1405–1405.
- [81] FP Koffyberg and FA Benko. "A photoelectrochemical determination of the position of the conduction and valence band edges of p-type CuO". In: *Journal of Applied Physics* 53.2 (1982), pp. 1173–1177.
- [82] J Robertson, K Xiong, and SJ Clark. "Band gaps and defect levels in functional oxides". In: *Thin Solid Films* 496.1 (2006), pp. 1–7.

Chapter 6

Earth-Abundant Plasmonic Materials for Energy-Efficient Photocatalytic Systems

6.1 Introduction

Novel realizations of metal nanoparticles (NPs) are of continuing interest due to their unique optical properties and potential applications in optoelectronics, sensing, and catalysis.[1, 2, 3, 4, 5, 6] Plasmonic materials have great appeal as harvesters of visible light, with plasmonic-enhancement promising increased efficiency and spectral sensitivity of catalytic materials.[7, 8, 9, 10] In contrast to bulk metals, metal NPs exhibit localized surface plasmonic resonances (LSPRs) that are tunable via adjustment of particle size, shape, and composition as well as the properties of the surrounding environment.[11, 12] Methods for synthesizing, functionalizing and manipulating gold and silver NPs are well established, and hence their photophysical properties, including narrow and tunable LSPRs across the visible and near-infrared (NIR) regions of the electromagnetic spectrum, are well characterized.[13, 14, 15, 16] However,

large-scale deployment of precious-metal materials is impractical for many applications due to their high cost and relatively low earth abundance. Several alternatives have been proposed and synthesized,[17, 18, 19] but there remains an urgent need to understand their photophysical properties, many of which differ non-trivially from gold and silver due to their unique electronic structures and complex dielectric constants.[20, 21]

6.2 Motivation for Aluminum

Aluminum, in particular, is an inexpensive earth-abundant plasmonic material and a promising alternative to noble metals for applications requiring UV sensitivity and scalability. The plasmon resonance of bulk aluminum metal falls in the ultraviolet, but the LSPRs of aluminum NPs have been tuned successfully to the visible and NIR using size- and shape-modulation[22, 23, 24] and are tunable over an even wider spectral range than those of Au or Ag.[22] Aluminum also forms a native oxide layer at its surface in air[25] that further red-shifts the LSPRs of particles. Unlike the interband transitions of gold (5d-6s) and silver (4d-5s), with threshold energies that overlap with the intraband plasmon resonance, the interband transitions of aluminum fall at 1.5 eV and do not overlap significantly with the intraband transitions.[21] Greater understanding of how these differences in electronic structure affect energy transfer mechanisms is critical for developing optoelectronic and photocatalytic applications[26, 27] based on plasmonic aluminum.

6.3 Dynamics of Energy Transfer in Large Plasmonic Aluminum Nanoparticles

This section is adapted from Ref. [28]. Reprinted with permission from ACS Photonics, Volume 5, Issue 3, Pages 805-813, "Dynamics of Energy Transfer in Large Plasmonic Aluminum Nanoparticles," by K. J. Smith, Y. Cheng, E. S. Arinze, N. E. Kim, A. E. Bragg, and S. M. Thon, copyright © 2017.

6.3.1 Background

The photophysical dynamics of noble-metal plasmonic nanomaterials have been characterized extensively with ultrafast transient absorption spectroscopy over the last two decades.[29, 30] It is now well understood that interaction between a plasmonic NP and a femtosecond laser pulse creates a coherent electronic state (a "plasmon") that rapidly dephases (typically in 5-10 fs) to a highly non-thermal electron distribution.[31, 32] These "excited" non-equilibrium NPs subsequently relax through a sequence of energy-conversion and transfer mechanisms beginning with thermalization via electron-electron (10-100 fs)[33, 34] and electron-lattice (\sim 1-10 ps)[30, 35] scattering followed by lattice relaxation by intraparticle equilibration (10s of ps)[35, 36] and thermal energy transport to the surrounding environment (100s of ps to nanoseconds).[37, 38, 39] The extensive body of work that has explored these processes has also led to an understanding of how energy transfer scales with NP dimensions[32, 35, 37] and shape[40, 41, 42, 43, 44] as well as particle composition[45] and interface properties.[39, 46] Transient optical methods have also been used to demonstrate that hot electrons generated in noble metal NPs are able to

overcome an interfacial Schottky barrier when coupled to TiO_2 , a common and robust semiconductor, thereby facilitating enhanced photocatalytic activity.[47, 48, 49, 50]

In this study, we report the first photophysical characterization of energy-transfer dynamics in aluminum NPs. Time-scales for spectral dynamics are similar to those ascribed for electron-electron, electron-photon, and lattice cooling temperatures for noble-metal particles,[29, 30, 51] although we find that the spectral responses of Al NPs differ qualitatively. Notably, bleaching of the interband transitions is largely isolated from spectral changes to the intraband transition and provides a window into electron-electron thermalization dynamics. Furthermore we find a ~ 250 ps energy transfer to the surrounding medium - comparable to energy transfer rates for a small (< 10 nm in diameter) NPs, but much faster than predicted for the particle size (98 nm in diameter) studied. To understand this phenomenon, we investigated thermal energy transfer dynamics using a two-interface model and find that rapid thermal energy transfer out of the Al core is mediated by the presence of the ~ 4 -nm thick native oxide layer, pointing the way to using surface modifications as a tool to engineer heat transfer rates in applications such as photocatalysis.

6.3.2 Results and Discussion

We synthesized aluminum NPs using modifications of established procedures.[52] Briefly, the particles were formed through decomposition of dimethylethylamine alane under mild heating using titanium (IV) isopropoxide as a catalyst. Morphologies of the synthesized aluminum NPs are shown in the transmission

electron microscope (TEM) image in Figure 6.1a. According to our analysis of the size distribution, the particles are relatively monodisperse with an average diameter of 98 ± 12 nm. The NP shapes are primarily icosahedra and truncated trigonal bipyramids. Figure 6.1b shows a high-resolution TEM image of a single aluminum NP taken using a FEI Talos S200 in which a thin oxide shell with an average thickness of approximately 3.7 nm is visible, consistent with previous observations.[53]

Based on the morphologies obtained from these images, we employed finite difference time-domain (FDTD) simulations to predict the LSPR spatial field intensity distribution (Figure 6.1c) and spectrum (Figure 6.1d) of the aluminum NPs. The blue curve in Figure 6.1d shows the experimental extinction spectrum of the aluminum NPs in 2-propanol measured by UV-Vis spectrophotometry. The solution exhibited a clear broadband absorption peak due to the NP LSPR with a maximum located at 392 nm. We used FDTD simulations to calculate the extinction cross section of an icosahedral aluminum NP 93 nm in diameter with and without an aluminum oxide shell of 3.7 ± 0.8 nm in thickness. The simulated peak extinction cross-sections of the aluminum NPs without (red curve) and with (orange curve) an oxide layer are 389 nm and 393 nm, respectively; the latter matches well with that of the measured extinction peak. We also observe that there is a broad shoulder, both in the measured and the calculated extinction spectra, between 800 nm and 900 nm that is clearer from plots of the first derivative shown in the inset of Figure 6.1d. This shoulder in the experimental spectrum falls at 815 nm and agrees well with the known spectral position of the parallel-band interband transitions in

aluminum (~ 1.5 eV).[21]

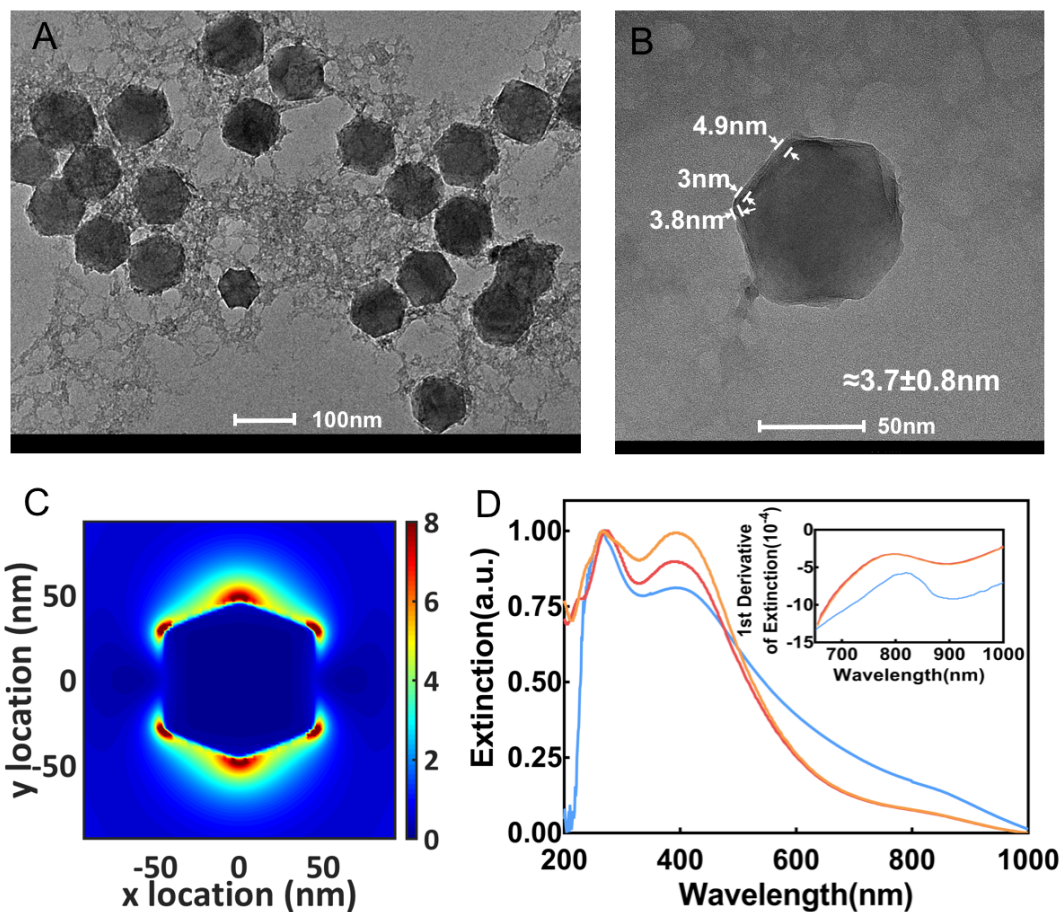


Figure 6.1: (A) TEM image of aluminum NPs. (B) A single aluminum particle surrounded by an oxide layer with an average thickness of 3.7 nm. (C) FDTD-calculated spatial electromagnetic field profile for a 93 nm-diameter aluminum NP at the LSPR wavelength of 393 nm (color scale in a.u.). (D) UV-Vis-NIR extinction (blue curve) of an aluminum NP solution in 2-propanol. FDTD-calculated extinction cross sections for a single bare aluminum icosahedron in a 2-propanol background (red curve) and an aluminum icosahedra with a 3.7 ± 0.8 nm thick aluminum oxide shell (orange curve) in the same background. The inset shows the first derivative of measured (blue) and simulated (red/orange) extinction near the aluminum interband transition (1.5 eV).[28]

Guided by this understanding of steady-state properties, we interrogated

the photophysics of these particles suspended in 2-propanol with transient absorption spectroscopy. Figure 6.2a presents a contour plot of time-dependent changes in optical density (i.e. extinction) from 420 - 1150 nm following interaction with ultrafast laser pulses at 400 nm. "Time zero" can be identified by the sharp line near the bottom of the plot that is associated with ultrafast coherent interactions of the laser pulses with the sample solution that occur during the pulse cross correlation. Spectra collected at various time delays for each spectral region are plotted in Figure 6.2b and 6.2c. In total, Figure 6.2 demonstrates that changes in extinction occur broadly across the visible and NIR.

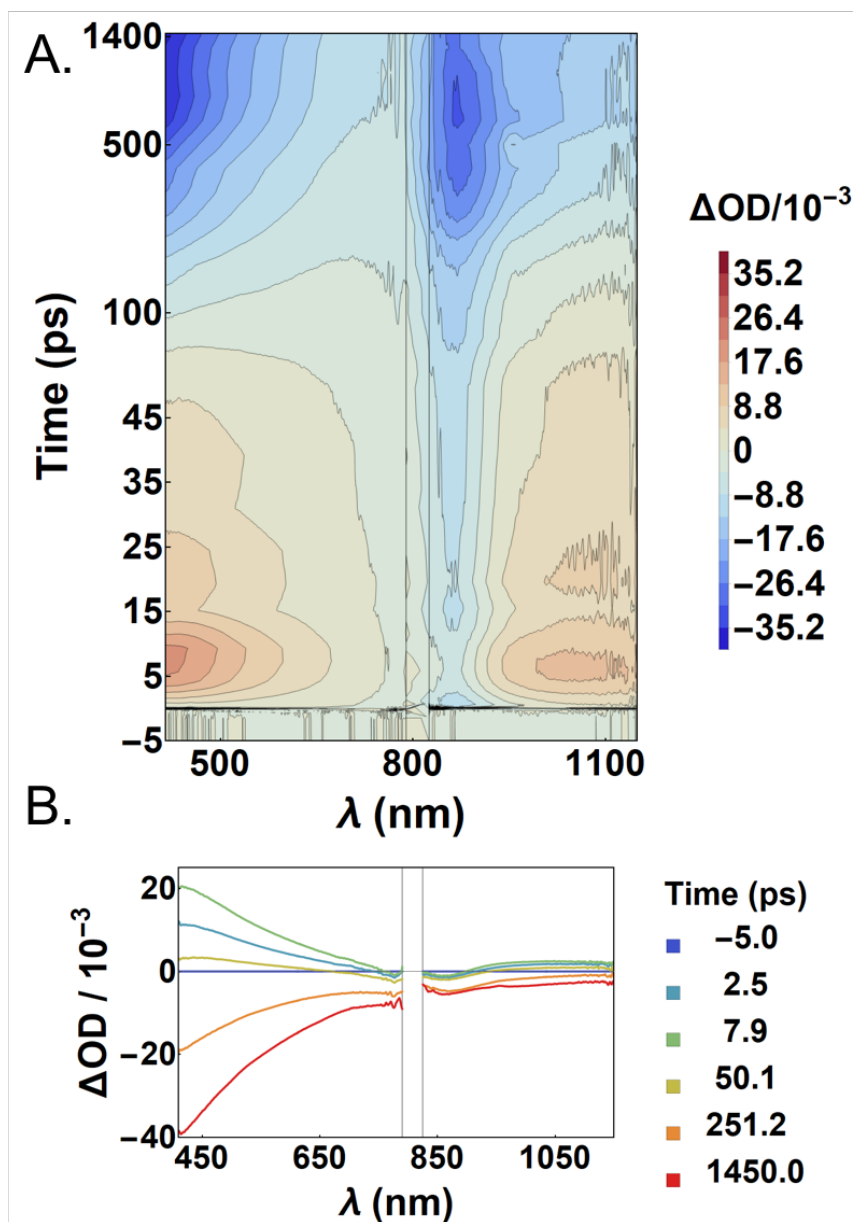


Figure 6.2: Top: Contour plot of transient spectra from 420 - 790 nm and 820-1150 nm. The time axis is linear from 0-50 ps and logarithmic from 50-1450 ps. Signal intensity in the NIR region (820-1150 nm) has been multiplied by a factor of 5 in order to highlight the changes in optical density. Bottom: Visible (left) and NIR (right) transient spectra at selected time delays.[28]

Figure 6.3 plots temporal traces obtained by averaging over three different

spectral regions: a region to the red of the LSPR peak (415-500 nm), near the aluminum interband transition (825-900 nm), and in the NIR beyond the interband transition (1000-1125 nm). Transient spectral dynamics can be summarized as follows: Immediately following excitation, a slow induction to a positive OD occurs broadly across the visible and beyond 900 nm, reaching a maximum positive value by 8 ps. At later time delays, this broad signal decreases in amplitude turning to a negative OD on a timescale of a few hundred picoseconds. The spectral shapes of the broad negative and positive signals in the visible region and at wavelengths longer than 1050 nm appear roughly as mirror images; furthermore the time-dependence of transient signals collected in the visible and longer-wavelength NIR are highly similar.

A different temporal response is observed near the Al interband transition. Here the extinction drops rapidly to negative values within a few hundred femtoseconds after sample excitation (Figure 6.3, blue symbols) - a timescale slower than the experimental time resolution, but faster than the slow induction of extinction observed in other spectral regions. The spectrum in this region exhibits a persistent negative dip that arises from a "bleach" of the Al interband transition. At later delays, the bleach is superimposed upon the broad time-dependent spectral response observed at other wavelengths.

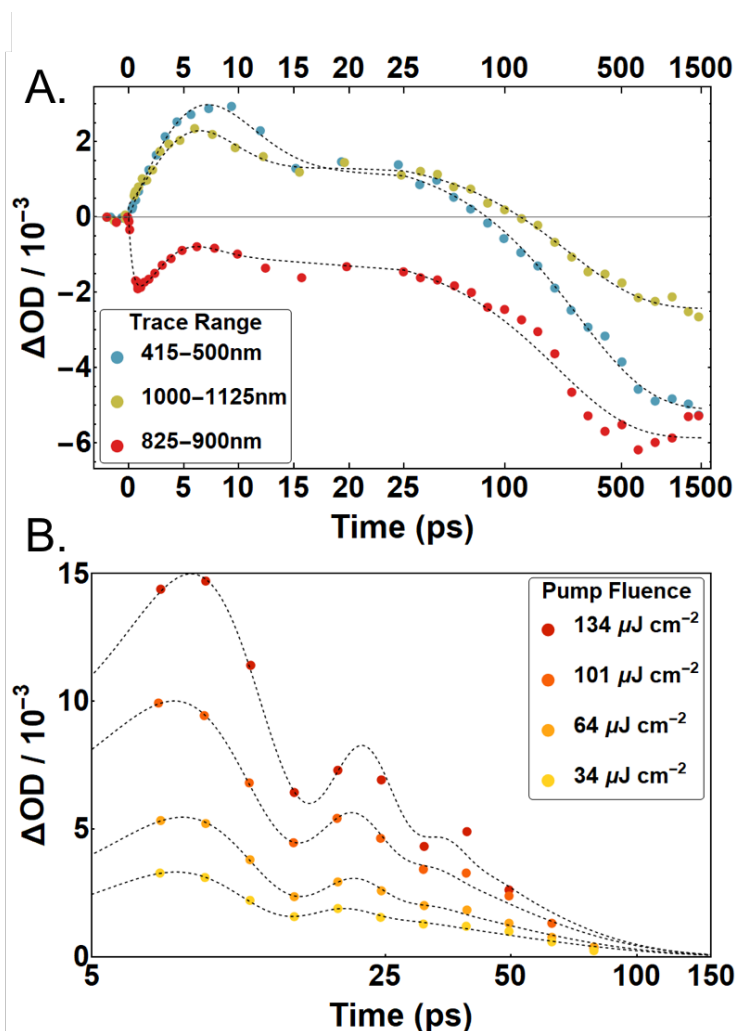


Figure 6.3: Time-dependent traces obtained from three different spectral regions: near the LSPR peak, (415-500 nm) (blue); off the LSPR peak in the NIR (1000-1125 nm) (red); and in the interband transition region of metallic aluminum (825-900 nm) (green). Data from the visible region of the spectrum were scaled in order to display all three data sets on one plot. Fitting curves (described in the text) are displayed in black. The asterisks (**) above the spike in the blue trace mark coherent pulse-interactions that represent the optical temporal resolution of the measurements.[28]

Numerous studies have demonstrated the effects of high-fluence laser excitation on the photophysics of plasmonic NPs, and it is critical to rule these out before ascribing the timescales observed to specific energy-transfer

processes. Non-linear effects can include, but are not limited to, bubble formation by local solvent vaporization,[54] persistent hole burning through particle ablation or melting,[55] and multi-photon absorption.[56] Notably, the broad spectral response we observe long after photoexcitation manifests as a reduction in optical density. In contrast, the formation of large vapor bubbles around photoexcited gold NPs has been shown to increase the probe extinction via increased Mie scattering; additionally, the threshold fluence for bubble formation (5.2 mJ cm^{-2} for 60 nm Au NPs[54]) is much higher (~ 100 fold) than what was used for our transient absorption studies (*vide infra*). To rule out contributions from laser-induced melting, we examined NP morphology using high-resolution TEM (HRTEM) imaging both before and after prolonged exposure to the 400-nm excitation source (4-6 hours of irradiation with continuous sample mixing). Additionally, there was no observable change in the steady-state absorption of the ensemble, indicating no changes in the particle properties with irradiation. The fluence-dependence of the maximum positive and negative extinction appears linear (slope = 1.19 ± 0.119). Together, these control experiments indicate that the spectral responses apparent in Figures 6.2, and 6.3 reflect the intrinsic relaxation dynamics of the plasmonic particles in a linear excitation regime.

As described in the introduction, the photoinduced responses of Au and Ag NPs involve at least four processes that impact their transient spectral dynamics: electron-electron thermalization (100-300 fs), electron-phonon thermalization (1-2 ps), and lattice relaxation dynamics, which include coherent phonon oscillations (\sim few-20 ps period) and thermal energy transfer to the

surrounding medium (10s to 100s of ps). The transient spectra of Al NPs evolve on qualitatively similar timescales as Au and Ag, although the transient spectra have somewhat different characteristics due to the weaker overlap between the intra and interband transitions in Al. The ultrafast induction in the interband bleach region is similar to behavior observed with Ag NPs in a glass matrix;^[33] this induction in the bleach is attributed to electron-electron thermalization that fills states above the Fermi level that serve as terminal states for the interband transition, such that the bleach of this transition increases with electronic relaxation.^[57, 58] The rise in transient spectra broadly across the visible and NIR occurs on timescales consistent with electron-phonon thermalization observed for noble metals and is therefore a direct signature of the particle lattice heating in response to LSPR excitation and subsequent electron thermalization.^[35] This induction can be seen quite clearly for Al NPs, as there is no overlap with the interband transition in the visible spectral region. Importantly, the rapid photoinduced depletion of the interband transition in the NIR provides a direct signature of electron-electron thermalization within the material by which to clock the slow induction in electron-lattice thermalization. Finally, the slower inversion of the broad transient spectrum occurs on timescales consistent with thermal energy transport observed with noble-metal NPs.^[46, 39, 59, 60] The optical response at the latest delays explored in our experiment (~ 1 ns) is characterized by a broadband negative signal that may be attributed to significant temperature dependence of the solvent's dielectric function.

In order to get a better handle on relaxation timescales, we fit the traces

plotted in Figure 6.3 with various time-dependent functions. These traces exhibit induction in the visible and long-wavelength NIR, which we modeled as a Gaussian time-dependent thermal response for heating of the NP lattice by electron-phonon energy transfer. This response is characterized by a breadth related to σ and time delay μ relative to the optical time zero. In this treatment σ^{-1} and μ^{-1} both provide metrics for the rate of electron-to-lattice thermal energy transfer and can be expected to be much longer than the optical instrument response associated with electronic excitation of the NPs (~ 250 fs). The signal intensity after lattice heating was modeled with a single or biexponential decay that was convoluted with the thermal response function as per Equation 6.1 below. Responses in the visible and NIR regions have very similar kinetics and were found to decay with timescales τ_1 of 13.6 ps and 5.3 ps and τ_2 of 297.9 ps and 250.5 ps, respectively, when a biexponential model is applied. The thermal-response parameters σ and μ were found to be $\sigma = 1.96$ ps / $\mu = 2.4$ ps for the visible region and $\sigma = 2.60$ ps / $\mu = 2.22$ ps for the NIR. This analysis therefore indicates an effective electron-to-lattice energy transfer lifetime of ~ 2 -2.5 ps.

The slower of the two single decay timescales (250-300 ps) obtained from these fits is in qualitative agreement with expectations for thermal energy transport to the surrounding solvent medium (*vide infra*).^[39, 59, 46, 60, 61] The faster of the decay timescales, in contrast, is consistent with timescales typically associated with modulation in optical properties as a result of low-frequency "breathing" or coherent phonon displacement that can occur as a result of fast electron-to-phonon energy transfer.^[35, 36] A fit to the data

with a single exponential decay matches the signal rise ($t < 4$ ps) and decay ($t > 40$ ps) quite well and yields an effective electron-to-phonon energy transfer timescale of 1.5 ps, but reveals fit residuals associated with fast intensity changes on intermediate timescales. Given the timescale of this modulation it most likely arises from damped or ensemble-averaged phonon breathing motions following fast electron-to-phonon energy transfer in Al.

A phenomenological two-temperature model (TTM)[62] is commonly used to treat thermal energy transfer from electronic to lattice degrees of freedom in metals. This model involves a rate constant for energy transfer that scales inversely with electronic temperature, which results in a non-exponential rise in the lattice temperature. Using the two temperature model with the Sommerfeld constant $\gamma = 91.2$ ($\text{J}\cdot\text{m}^{-3} \text{K}^{-2}$), and an electron-phonon coupling constant of $g = 1.2 \times 10^{17}$ ($\text{W}\cdot\text{m}^{-3} \text{K}^{-1}$) for Al.[63] We obtain electron-to-lattice energy transfer timescales ($1/e$) between 1.49 ps and 2.18 ps for electronic temperatures ranging from 3000-4500 K, which is qualitatively consistent with timescales obtained from our fits.

The average intensity in the region of the interband transition of metallic aluminum (800-850 nm) exhibits a bleach signal that appears rapidly following the instrument response. This behavior is similar to that exhibited by noble metals while probing in the region of their respective interband transitions.[64] As noted above, transient signals in the region of the interband transition also have contributions from the time-dependent spectral response of the particles observed at other wavelengths; this is clear from the very similar modulations in signal intensity on the picosecond to nanosecond timescales that occur with

a clear offset in spectral intensity between the interband and 1000-1125 nm regions. The superposition of these signals makes it difficult to analyze the time-dependence of the interband bleach feature alone. Therefore, we applied a restricted fit model taken to be the sum of Equations 6.1 and 6.2.

$$f(t)_{Vis/NIR} = (a_1 e^{-\frac{t}{\tau_1}} + a_2 e^{-\frac{t}{\tau_2}} + c) * \left(\frac{1}{\sqrt{2\pi}\sigma} e^{-\frac{(t-\mu)^2}{\sigma^2}} \right) \quad (6.1)$$

$$g(t)_{IB} = (a_3 (1 - e^{-\frac{t}{\tau_{bleach}}})) * \left(\frac{1}{\sqrt{2\pi}\sigma'} e^{-\frac{(t-\mu')^2}{\sigma'^2}} \right) \quad (6.2)$$

For this fit, τ_1 and τ_2 and parameters σ and μ were fixed to values evaluated from signal amplitude evolution in the 1000-1125 nm region; σ' and μ' correspond to the optical instrument response and time zero, respectively, and were evaluated from solvent coherences that appear in transient data. The pre-exponential amplitudes (a_1 through a_3) and a constant offset (c) were left as floating variables. This reveals a bleach induction time, τ_{bleach} , of 400 fs that reflects the slowest phases of electron-electron thermalization. This timescale is slightly longer than the longest electron thermalization timescales observed in large Au and Ag NPs.[33]

Based on precedent with noble-metal NPs, the slowest relaxation timescales observed in our measurements are assigned to thermal energy transport to the surrounding solvent environment. Various models for thermal energy transfer from nanoparticles to the surrounding media have been developed and applied.[39, 59, 60, 61, 64, 65] For example, Vallee and coworkers[60] have

CHAPTER 6. PLASMONIC NANOSTRUCTURES FOR PHOTOCATALYSIS

Material	c ($10^6 \text{ J.m}^{-1}.\text{K}^{-1}$)	Λ ($\text{W.m}^{-1}.\text{K}^{-1}$)
Aluminum (p)	2.43	205
Aluminum Oxide (o)	3.48	30
Isopropanol (m)	2.1	0.16

Table 6.1: Heat capacities and thermal conductivities of aluminum, aluminum oxide and isopropanol.[65, 28]

applied thermal transfer models to fit the time-dependence of transient absorption measurements conducted with Au and Ag in solution and embedded in various glasses.[64, 66] Their model involved a single interface between a NP and the surrounding medium to compute the temperature evolution of both the particle and the medium. Thermal dynamics in this model are governed by the interfacial thermal conductance (G) as well as the thermal conductivity (Λ) and heat capacity (c) of both the metal NP and surrounding medium. Whereas the bulk values of Λ and c are reasonable approximations for NPs, G is generally not known and is varied to fit the temporal behavior observed from optical measurements. Therefore, this line of investigation has also explored the impact of particle size and the chemical composition of interfaces on energy transfer.[37, 39, 46, 60, 61, 64]

We extended our analysis to a two-interface model to incorporate the native aluminum oxide layer on our particles, as described in the Supporting Information. Table 6.1 gives a summary of parameters relevant for the aluminum NP / aluminum oxide shell / isopropanol system.

We used our model to explore the thermal dynamics in aluminum NPs with 93 nm diameters and 3.7 nm aluminum oxide shells suspended in isopropanol. Our results are plotted in Figure 6.4 and indicate that heat dissipates

much more quickly from the aluminum core when an oxide shell is present (blue dashed line) compared to the case without an oxide shell (purple solid line). Notably, the $1/e$ timescale for energy loss from the Al core from these simulations is ~ 300 ps when the oxide is present, in close agreement with the relaxation timescales observed in our experiments. Varying the free parameter G (thermal interface conductance) can control the rate of decay. The value used for the plot in Figure 6.4 was chosen from typical literature values for the thermal interfacial conductance of metal/metal oxide interfaces.[64, 67, 68, 69, 70] Additionally, we predict that large Al NPs (93 nm in diameter) with an oxide layer possess thermal transport properties equivalent to those of much smaller particles (10 nm in diameter, solid blue line in Figure 6.4) with no oxide layer. These results indicate that the native oxide coverage on Al NPs likely provides an intrinsic protection against melting or ablation after interaction with a high intensity laser pulse by facilitating fast and efficient thermal energy transfer to the surrounding solvent.

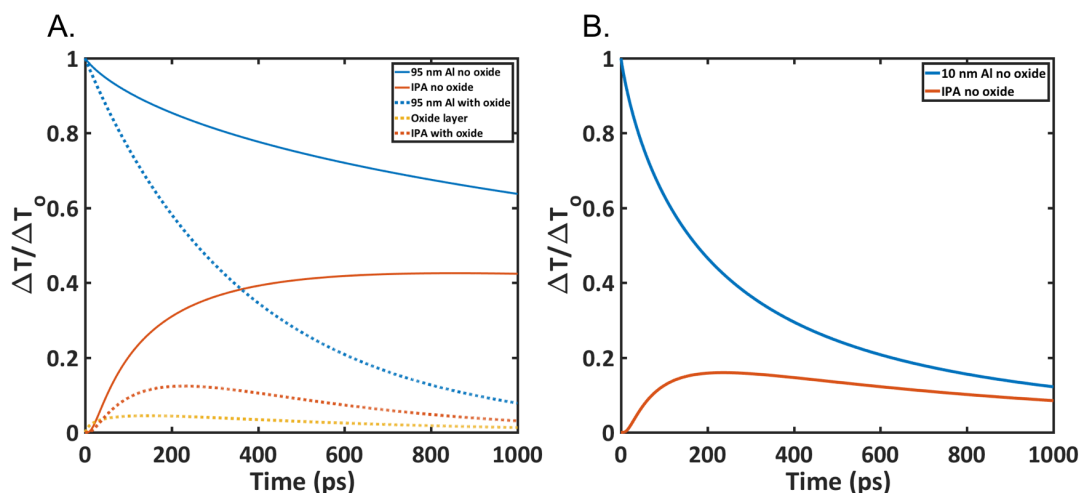


Figure 6.4: Normalized calculated temperature evolutions at the surface of a large (93 nm diameter) aluminum nanoparticle (purple) and 3 nm into the surrounding medium (green) for the case where no oxide is included, where a thin oxide shell layer on the nanoparticle is incorporated into the model (blue, yellow, and orange dotted lines), and where a small (10 nm) nanoparticle is simulated without an oxide layer (blue and orange solid lines).[28]

We also found that the temperature evolution decay timescale ($1/e$) had little dependence on the oxide thickness, indicating that the addition of even a thin oxide shell could be a highly effective means for controlling the lattice temperature of plasmonic NPs. Previous work has demonstrated an increase in thermal energy transfer from Au NPs when encased by a silica shell.[46] This work revealed a dependence on the silica shell thickness, but that the method of shell formation greatly impacted control of thermal energy transport because porous SiO_2 could allow penetration of solvent towards the Au core. In contrast, direct oxidation of the Al surface results in a compact native oxide layer that should prohibit formation of channels through which solvent can directly interface with the metal surface.

6.3.3 Conclusion

We presented the first characterization of the photophysical dynamics of plasmonic aluminum NPs, an emerging earth-abundant materials platform of interest for photocatalysis, optoelectronics, and sensing applications. We found that the response of Al NPs differs qualitatively from noble-metal NPs near the interband transitions, which are largely isolated from spectral changes to the intraband transitions, allowing for study of electron-electron thermalization dynamics. We found that induction timescales matches predictions for electron-lattice relaxation processes in related materials, and energy transfer to the surrounding medium from large particles is comparable to the energy transfer rates predicted for much smaller particles. To understand this phenomenon, we investigated thermal energy transfer dynamics using a two-interface model to account for the presence of a native oxide layer on the aluminum NPs that mediates rapid thermal energy transfer out of the Al core. We propose that using surface modifications, including controlled oxidation, could be an effective tool to engineer heat transfer rates from large particles to the surrounding medium and could be an important strategy for applications in which thermal management is critical for system performance and stability, including in photocatalytic and sensing applications.

References

- [1] Harry A Atwater and Albert Polman. "Plasmonics for improved photovoltaic devices". In: *Nature materials* 9.3 (2010), p. 205.
- [2] Tapan K Sau, Andrey L Rogach, Frank Jäckel, Thomas A Klar, and Jochen Feldmann. "Properties and applications of colloidal nonspherical noble metal nanoparticles". In: *Advanced Materials* 22.16 (2010), pp. 1805–1825.
- [3] Dmitri V Talapin, Jong-Soo Lee, Maksym V Kovalenko, and Elena V Shevchenko. "Prospects of colloidal nanocrystals for electronic and optoelectronic applications". In: *Chemical reviews* 110.1 (2009), pp. 389–458.
- [4] Xiliang Luo, Aoife Morrin, Anthony J Killard, and Malcolm R Smyth. "Application of nanoparticles in electrochemical sensors and biosensors". In: *Electroanalysis* 18.4 (2006), pp. 319–326.
- [5] Shaojun Guo, Sen Zhang, and Shouheng Sun. "Tuning nanoparticle catalysis for the oxygen reduction reaction". In: *Angewandte Chemie International Edition* 52.33 (2013), pp. 8526–8544.
- [6] Royce W Murray. "Nanoelectrochemistry: metal nanoparticles, nanoelectrodes, and nanopores". In: *Chemical reviews* 108.7 (2008), pp. 2688–2720.
- [7] Xuming Zhang, Yu Lim Chen, Ru-Shi Liu, and Din Ping Tsai. "Plasmonic photocatalysis". In: *Reports on Progress in Physics* 76.4 (2013), p. 046401.
- [8] Cesar Clavero. "Plasmon-induced hot-electron generation at nanoparticle/metal-oxide interfaces for photovoltaic and photocatalytic devices". In: *Nature Photonics* 8.2 (2014), p. 95.

REFERENCES

- [9] Ana Primo, Avelino Corma, and Hermenegildo García. "Titania supported gold nanoparticles as photocatalyst". In: *Physical Chemistry Chemical Physics* 13.3 (2011), pp. 886–910.
- [10] Yang Tian and Tetsu Tatsuma. "Mechanisms and applications of plasmon-induced charge separation at TiO₂ films loaded with gold nanoparticles". In: *Journal of the American Chemical Society* 127.20 (2005), pp. 7632–7637.
- [11] Cecilia Noguez. "Surface plasmons on metal nanoparticles: the influence of shape and physical environment". In: *The Journal of Physical Chemistry C* 111.10 (2007), pp. 3806–3819.
- [12] K Lance Kelly, Eduardo Coronado, Lin Lin Zhao, and George C Schatz. *The optical properties of metal nanoparticles: the influence of size, shape, and dielectric environment*. 2003.
- [13] Stephan Link and Mostafa A El-Sayed. "Size and temperature dependence of the plasmon absorption of colloidal gold nanoparticles". In: *The Journal of Physical Chemistry B* 103.21 (1999), pp. 4212–4217.
- [14] Susie Eustis and Mostafa A El-Sayed. "Why gold nanoparticles are more precious than pretty gold: noble metal surface plasmon resonance and its enhancement of the radiative and nonradiative properties of nanocrystals of different shapes". In: *Chemical society reviews* 35.3 (2006), pp. 209–217.
- [15] Traci R Jensen, Michelle Duval Malinsky, Christy L Haynes, and Richard P Van Duyne. "Nanosphere lithography: tunable localized surface plasmon resonance spectra of silver nanoparticles". In: *The Journal of Physical Chemistry B* 104.45 (2000), pp. 10549–10556.
- [16] S Link, Zz L Wang, and MA El-Sayed. "Alloy formation of gold-silver nanoparticles and the dependence of the plasmon absorption on their composition". In: *The Journal of Physical Chemistry B* 103.18 (1999), pp. 3529–3533.
- [17] Alberto Comin and Liberato Manna. "New materials for tunable plasmonic colloidal nanocrystals". In: *Chemical Society Reviews* 43.11 (2014), pp. 3957–3975.
- [18] Gururaj V Naik, Vladimir M Shalaev, and Alexandra Boltasseva. "Alternative plasmonic materials: beyond gold and silver". In: *Advanced Materials* 25.24 (2013), pp. 3264–3294.

REFERENCES

- [19] Urcan Guler, Vladimir M Shalaev, and Alexandra Boltasseva. "Nanoparticle plasmonics: going practical with transition metal nitrides". In: *Materials Today* 18.4 (2015), pp. 227–237.
- [20] Ana M Brown, Ravishankar Sundararaman, Prineha Narang, William A Goddard III, and Harry A Atwater. "Ab initio phonon coupling and optical response of hot electrons in plasmonic metals". In: *Physical Review B* 94.7 (2016), p. 075120.
- [21] H Ehrenreich, HR Philipp, and B Segall. "Optical properties of aluminum". In: *Physical Review* 132.5 (1963), p. 1918.
- [22] Mark W Knight, Nicholas S King, Lifei Liu, Henry O Everitt, Peter Nordlander, and Naomi J Halas. "Aluminum for plasmonics". In: *ACS nano* 8.1 (2013), pp. 834–840.
- [23] George H Chan, Jing Zhao, George C Schatz, and Richard P Van Duyne. "Localized surface plasmon resonance spectroscopy of triangular aluminum nanoparticles". In: *The Journal of Physical Chemistry C* 112.36 (2008), pp. 13958–13963.
- [24] Olivier Lecarme, Quan Sun, Kosei Ueno, and Hiroaki Misawa. "Robust and versatile light absorption at near-infrared wavelengths by plasmonic aluminum nanorods". In: *ACS Photonics* 1.6 (2014), pp. 538–546.
- [25] P Bucher, L Ernst, FL Dryer, RA Yetter, TP Parr, and DM Hanson. "Detailed studies on the flame structure of aluminum particle combustion". In: *Solid propellant chemistry, combustion and motor interior ballistics* 185 (2000), pp. 689–722.
- [26] Qi Hao, Chenxi Wang, Hao Huang, Wan Li, Deyang Du, Di Han, Teng Qiu, and Paul K Chu. "Aluminum plasmonic photocatalysis". In: *Scientific reports* 5 (2015), p. 15288.
- [27] Linan Zhou, Chao Zhang, Michael J McClain, Alejandro Manjavacas, Caroline M Krauter, Shu Tian, Felix Berg, Henry O Everitt, Emily A Carter, Peter Nordlander, et al. "Aluminum nanocrystals as a plasmonic photocatalyst for hydrogen dissociation". In: *Nano letters* 16.2 (2016), pp. 1478–1484.
- [28] Kenneth J Smith, Yan Cheng, Ebuka S Arinze, Nicole E Kim, Arthur E Bragg, and Susanna M Thon. "Dynamics of Energy Transfer in Large Plasmonic Aluminum Nanoparticles". In: *ACS Photonics* 5.3 (2017), pp. 805–813.

REFERENCES

- [29] Gregory V Hartland. "Optical studies of dynamics in noble metal nanostructures". In: *Chemical reviews* 111.6 (2011), pp. 3858–3887.
- [30] Stephan Link and Mostafa A El-Sayed. "Shape and size dependence of radiative, non-radiative and photothermal properties of gold nanocrystals". In: *International reviews in physical chemistry* 19.3 (2000), pp. 409–453.
- [31] F Stietz, J Bosbach, T Wenzel, T Vartanyan, A Goldmann, and F Träger. "Decay times of surface plasmon excitation in metal nanoparticles by persistent spectral hole burning". In: *Physical review letters* 84.24 (2000), p. 5644.
- [32] J Bosbach, C Hendrich, T Vartanyan, F Stietz, and F Träger. "Spectral hole burning in absorption profiles of metal nanoparticles prepared by laser assisted growth". In: *The European Physical Journal D-Atomic, Molecular, Optical and Plasma Physics* 16.1 (2001), pp. 213–217.
- [33] C Voisin, D Christofilos, N Del Fatti, F Vallée, B Prével, E Cottancin, J Lermé, M Pellarin, and M Broyer. "Size-dependent electron-electron interactions in metal nanoparticles". In: *Physical review letters* 85.10 (2000), p. 2200.
- [34] J-Y Bigot, V Halté, J-C Merle, and A Daunois. "Electron dynamics in metallic nanoparticles". In: *Chemical Physics* 251.1-3 (2000), pp. 181–203.
- [35] Jose H Hodak, Arnim Henglein, and Gregory V Hartland. "Size dependent properties of Au particles: Coherent excitation and dephasing of acoustic vibrational modes". In: *The Journal of chemical physics* 111.18 (1999), pp. 8613–8621.
- [36] Rebecca J Newhouse, Haining Wang, Jennifer K Hensel, Damon A Wheeler, Shengli Zou, and Jin Z Zhang. "Coherent vibrational oscillations of hollow gold nanospheres". In: *The Journal of Physical Chemistry Letters* 2.3 (2011), pp. 228–235.
- [37] Min Hu and Gregory V Hartland. "Heat dissipation for Au particles in aqueous solution: relaxation time versus size". In: *The Journal of Physical Chemistry B* 106.28 (2002), pp. 7029–7033.
- [38] Fabrice Vallée. "Ultrafast Non-Equilibrium Electron Dynamics in Metal Nanoparticles". In: *Non-Equilibrium Dynamics of Semiconductors and Nanostructures*. CRC Press, 2005, pp. 105–181.

REFERENCES

- [39] Zhenbin Ge, Youngjong Kang, T Andrew Taton, Paul V Braun, and David G Cahill. "Thermal transport in Au-core polymer-shell nanoparticles". In: *Nano letters* 5.3 (2005), pp. 531–535.
- [40] Anne-Marie Dowgiallo and Kenneth L Knappenberger. "Ultrafast electron–phonon coupling in hollow gold nanospheres". In: *Physical Chemistry Chemical Physics* 13.48 (2011), pp. 21585–21592.
- [41] Damon A Wheeler, Thomas D Green, Haining Wang, Cristina Fernández-López, Luis Liz-Marzán, Shengli Zou, Kenneth L Knappenberger, and Jin Z Zhang. "Optical properties and coherent vibrational oscillations of gold nanostars". In: *Chemical Physics Letters* 543 (2012), pp. 127–132.
- [42] Benoît Dacosta Fernandes, Aurélie Le Beulze, Fabien Morote, Jean Oberle, Mona Treguer-Delapierre, Julien Burgin, and Pierre Langot. "Electron–Phonon Scattering in 2D Silver Nanotriangles". In: *The Journal of Physical Chemistry C* 117.42 (2013), pp. 22041–22045.
- [43] Gerald M Sando, Alan D Berry, Paul M Campbell, Andrew P Baronavski, and Jeffrey C Owrutsky. "Surface plasmon dynamics of high-aspect-ratio gold nanorods". In: *Plasmonics* 2.1 (2007), pp. 23–29.
- [44] Clemens Burda, Xiaobo Chen, Radha Narayanan, and Mostafa A El-Sayed. "Chemistry and properties of nanocrystals of different shapes". In: *Chemical reviews* 105.4 (2005), pp. 1025–1102.
- [45] Wenyu Huang, Wei Qian, Mostafa A El-Sayed, Yong Ding, and Zhong Lin Wang. "Effect of the lattice crystallinity on the electron-phonon relaxation rates in gold nanoparticles". In: *The Journal of Physical Chemistry C* 111.29 (2007), pp. 10751–10757.
- [46] Min Hu, Xuan Wang, Gregory V Hartland, Verónica Salgueiriño-Maceira, and Luis M Liz-Marzán. "Heat dissipation in gold–silica core-shell nanoparticles". In: *Chemical Physics Letters* 372.5-6 (2003), pp. 767–772.
- [47] Luchao Du, Akihiro Furube, Kazuhiro Yamamoto, Kohjiro Hara, Ryuzi Katoh, and M Tachiya. "Plasmon-induced charge separation and recombination dynamics in gold- TiO₂ nanoparticle systems: dependence on TiO₂ particle size". In: *The Journal of Physical Chemistry C* 113.16 (2009), pp. 6454–6462.
- [48] Greg P Maier, Michael V Rapp, J Herbert Waite, Jacob N Israelachvili, and Alison Butler. "Adaptive synergy between catechol and lysine promotes wet adhesion by surface salt displacement". In: *Science* 349.6248 (2015), pp. 628–632.

REFERENCES

- [49] Luchao Du, Akihiro Furube, Kohjiro Hara, Ryuzi Katoh, and Masanori Tachiya. "Ultrafast plasmon induced electron injection mechanism in gold-TiO₂ nanoparticle system". In: *Journal of Photochemistry and Photobiology C: Photochemistry Reviews* 15 (2013), pp. 21–30.
- [50] Akihiro Furube, Luchao Du, Kohjiro Hara, Ryuzi Katoh, and Masanori Tachiya. "Ultrafast plasmon-induced electron transfer from gold nanodots into TiO₂ nanoparticles". In: *Journal of the American Chemical Society* 129.48 (2007), pp. 14852–14853.
- [51] Stephan Link and Mostafa A El-Sayed. "Optical properties and ultrafast dynamics of metallic nanocrystals". In: *Annual review of physical chemistry* 54.1 (2003), pp. 331–366.
- [52] Michael J McClain, Andrea E Schlather, Emilie Ringe, Nicholas S King, Lifei Liu, Alejandro Manjavacas, Mark W Knight, Ish Kumar, Kenton H Whitmire, Henry O Everitt, et al. "Aluminum nanocrystals". In: *Nano letters* 15.4 (2015), pp. 2751–2755.
- [53] Shu Tian, Oara Neumann, Michael J McClain, Xiao Yang, Linan Zhou, Chao Zhang, Peter Nordlander, and Naomi J Halas. "Aluminum nanocrystals: a sustainable substrate for quantitative SERS-based DNA detection". In: *Nano letters* 17.8 (2017), pp. 5071–5077.
- [54] Tetsuro Katayama, Kenji Setoura, Daniel Werner, Hiroshi Miyasaka, and Shuichi Hashimoto. "Picosecond-to-nanosecond dynamics of plasmonic nanobubbles from pump-probe spectral measurements of aqueous colloidal gold nanoparticles". In: *Langmuir* 30.31 (2014), pp. 9504–9513.
- [55] T Ziegler, C Hendrich, F Hubenthal, T Vartanyan, and F Träger. "Dephasing times of surface plasmon excitation in Au nanoparticles determined by persistent spectral hole burning". In: *Chemical physics letters* 386.4-6 (2004), pp. 319–324.
- [56] Tingting Zhao, Xiao-Fang Jiang, Nengyue Gao, Shuang Li, Na Zhou, Rizhao Ma, and Qing-Hua Xu. "Solvent-dependent two-photon photoluminescence and excitation dynamics of gold nanorods". In: *The Journal of Physical Chemistry B* 117.49 (2013), pp. 15576–15583.
- [57] C-K Sun, F Vallée, LH Acioli, EP Ippen, and JG Fujimoto. "Femtosecond-tunable measurement of electron thermalization in gold". In: *Physical Review B* 50.20 (1994), p. 15337.

REFERENCES

- [58] N Del Fatti, C Voisin, M Achermann, S Tzortzakis, D Christofilos, and F Vallée. “Nonequilibrium electron dynamics in noble metals”. In: *Physical Review B* 61.24 (2000), p. 16956.
- [59] Zhenbin Ge, David G Cahill, and Paul V Braun. “AuPd metal nanoparticles as probes of nanoscale thermal transport in aqueous solution”. In: *The Journal of Physical Chemistry B* 108.49 (2004), pp. 18870–18875.
- [60] Tatjana Stoll, Paolo Maioli, Aurélien Crut, Sergio Rodal-Cedeira, Isabel Pastoriza-Santos, Fabrice Vallée, and Natalia Del Fatti. “Time-resolved investigations of the cooling dynamics of metal nanoparticles: impact of environment”. In: *The Journal of Physical Chemistry C* 119.22 (2015), pp. 12757–12764.
- [61] Orla M Wilson, Xiaoyuan Hu, David G Cahill, and Paul V Braun. “Colloidal metal particles as probes of nanoscale thermal transport in fluids”. In: *Physical Review B* 66.22 (2002), p. 224301.
- [62] Jose H Hodak, Ignacio Martini, and Gregory V Hartland. “Spectroscopy and dynamics of nanometer-sized noble metal particles”. In: *The Journal of Physical Chemistry B* 102.36 (1998), pp. 6958–6967.
- [63] Weigang Ma, Haidong Wang, Xing Zhang, and Wei Wang. “Study of the electron–phonon relaxation in thin metal films using transient thermoreflectance technique”. In: *International Journal of Thermophysics* 34.12 (2013), pp. 2400–2415.
- [64] Vincent Juvé, Mattia Scardamaglia, Paolo Maioli, Aurélien Crut, Samy Merabia, Laurent Joly, Natalia Del Fatti, and Fabrice Vallée. “Cooling dynamics and thermal interface resistance of glass-embedded metal nanoparticles”. In: *Physical Review B* 80.19 (2009), p. 195406.
- [65] A Plech, V Kotaidis, S Grésillon, C Dahmen, and G Von Plessen. “Laser-induced heating and melting of gold nanoparticles studied by time-resolved x-ray scattering”. In: *Physical Review B* 70.19 (2004), p. 195423.
- [66] Otto L Muskens, Natalia Del Fatti, and Fabrice Vallée. “Femtosecond response of a single metal nanoparticle”. In: *Nano letters* 6.3 (2006), pp. 552–556.
- [67] Ho-Ki Lyeo and David G Cahill. “Thermal conductance of interfaces between highly dissimilar materials”. In: *Physical Review B* 73.14 (2006), p. 144301.

REFERENCES

- [68] Zhenbin Ge, David G Cahill, and Paul V Braun. "Thermal conductance of hydrophilic and hydrophobic interfaces". In: *Physical review letters* 96.18 (2006), p. 186101.
- [69] Bryan C Gundrum, David G Cahill, and Robert S Averback. "Thermal conductance of metal-metal interfaces". In: *Physical Review B* 72.24 (2005), p. 245426.
- [70] David G Cahill, Wayne K Ford, Kenneth E Goodson, Gerald D Mahan, Arun Majumdar, Humphrey J Maris, Roberto Merlin, and Simon R Phillpot. "Nanoscale thermal transport". In: *Journal of applied physics* 93.2 (2003), pp. 793–818.

Chapter 7

Conclusion and Outlook

7.1 Conclusion

This thesis focuses on engineering nanostructures for energy harvesting by combining modeling, nanofabrication, and advanced optical and electrical characterization techniques (Figure 7.1). It focuses on developing and tuning new semiconducting and metallic colloidal nanoparticle-based materials for various optoelectronic device applications, such as solar cells and photodetectors, and to better understand nanoscale energy transfer and light-matter interaction. With current deployment in applications such as in light emission, sensing, communication, information and computing technology, and energy harvesting and storage, colloidal nanomaterials are gaining significant interest. However, these nanostructures still have ways to go to achieve the necessary robustness and competitive scalability for effective penetration in the commercial markets.

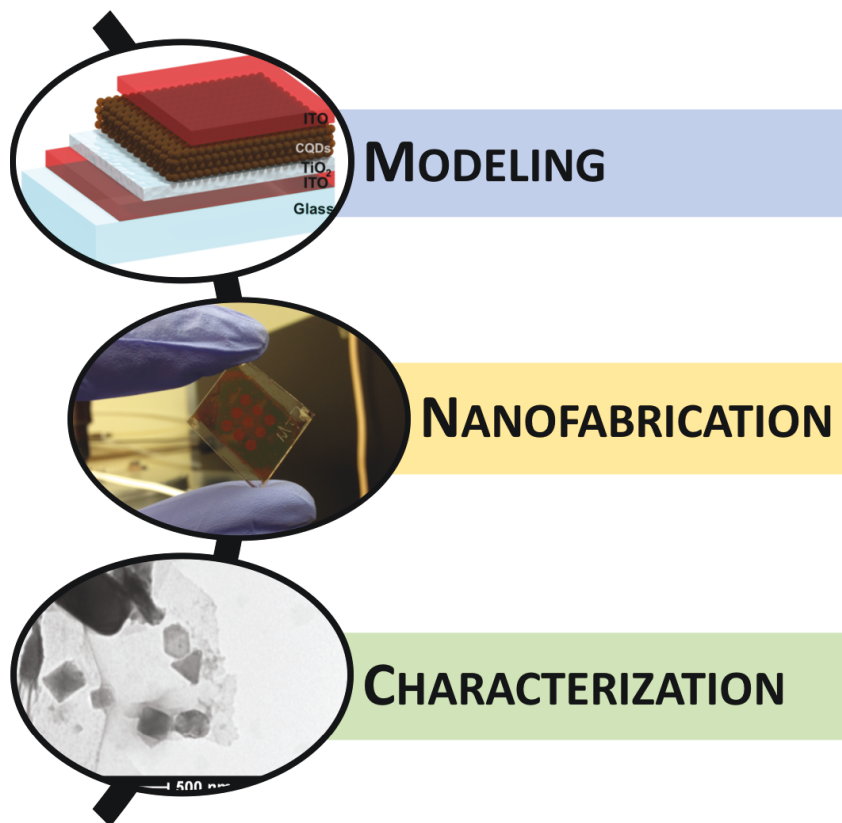


Figure 7.1: Schematic depicting different research topics covered throughout thesis work.

Here we address systems for three light energy harvesting technologies; photovoltaics, photodetectors, and photocatalysts. In photovoltaics, we identified general strategies for designing an effective plasmonic enhancement scheme for solution processed solar cells including adjusting nanoparticle concentration as the most crucial tuning knob in embedded plasmonically-enhanced photovoltaic devices. Additionally, we developed a method for producing arbitrary spectral profiles in layered solar cell structures using thin film interference modeling techniques combined with optimization algorithms and using photonic band engineering in strongly absorbing materials,

we developed and analyzed a new strategy for tuning the spectral selectivity of optoelectronic thin films.

In photon detection, our demonstration of utilizing CuO-based pn nanoheterojunctions to enhance the efficiency of visible-blind SnO₂ photodiodes, and a scalable route was developed to grow Sb₂Se₃ nanostructures directly on flexible substrates show a viable path for low-cost, flexible and portable spectral-tunable photon detection, photoelectronic switches and other optoelectronic devices. In photocatalysis, we presented the first characterization of the photophysical dynamics of plasmonic aluminum NPs, an emerging earth-abundant materials platform of interest for photocatalysis, optoelectronics, and sensing applications, identifying surface modifications as a critical tuning parameter.

7.2 Outlook

To protect the environment, as well as bridge the impending energy demand and supply gap, colloidal nanomaterials provide a sustainable route to addressing the major problems of the 21st century. Maturation of the field, via materials robustness and scalability, will be predicated on three key areas:

1. Identification of novel hybrid materials systems.
2. Optimization of surface engineering strategies.
3. Manipulation of optoelectronic device architectures.

The combination of novel materials can lead to highly desirable hybrid systems for various optoelectronic applications. While there has been a lot of

progress in surface passivation schemes, much is left to be explored regarding complete understanding of trap and defect mechanisms, and continuous development of efficient ligand systems. Advances in device architectures have led to record efficiencies in optoelectronic devices such as solar cells. However, more creative architectural routes like the studies presented in this thesis must be sought to continually push these limits.

Via models, computations, and experimental studies, colloidal nanostructures have emerged in the past few years as beneficial sustainable materials systems in light harvesting applications. Further progress in the materials chemistry and device physics of these optoelectronic technologies is vital in unlocking the vast potential of this dynamic field of study.

Appendix A

Experimental Details

A.1 PbS CQD Synthesis

PbS CQDs were synthesized using a previously published method. The materials used were lead oxide (PbO, Alfa Aesar, >99.99 %), bis(trimethylsilyl)sulphide (TMS, Sigma-Aldrich, synthesis grade), oleic acid (Alfa Aesar, 90 %), 1-octadecene (ODE, Sigma-Aldrich, 90 %) and were used as purchased. All synthesis was performed using standard Schlenk line techniques. In an N₂-filled glovebox, TMS (0.18 mL) was added to ODE (10 mL), which had been dried and degassed by heating to 80 C under vacuum for 16 h. A Pb oleate stock solution was prepared by mixing oleic acid (1.5 mL), PbO (0.45 g), and ODE (3 mL) and heating to 95 C under vacuum for 16 h then placed under nitrogen. 4.5mL of the Pb oleate stock solution and 15mL of ODE were heated to 120 C with constant stirring and nitrogen flow. The TMS/ODE mixture was then injected into the flask. After injection, the flask was allowed to cool gradually to 36 C. The PbS CQDs were then precipitated with distilled acetone (40 mL) and centrifuged. After discarding the supernatant, the precipitate was re-dispersed

APPENDIX A. EXPERIMENTAL DETAILS

in toluene. The PbS CQDs were precipitated again with acetone (5 mL) and methanol (5 mL), centrifuged for 5 min, dried, and finally dispersed in toluene. The yield of PbS CQDs was ~ 0.40 g. The toluene-dispersed PbS CQDs were then stored in sealed vials at ambient conditions until ready to be washed and solvent-exchanged. Conditions such as TMS injection temperature, TMS weight and ODE volume could be varied to achieve different CQD sizes. PbS CQDs in toluene were brought into an N₂-glovebox and precipitated with methanol. The supernatant was discarded and the remaining CQD powder was placed under vacuum until dry. The final redispersion is in octane at a dilution of 50mg/mL. The PbS CQDs were then stored in sealed vials in the N₂-glovebox until ready to be utilized.

A.2 Plasmonic Enhancement Project

A.2.1 Enhancement Model

```
%import k,scat_sigma_slice,total_sigma_slice and corresponding wavelength
%point lambda0 before running

lambda=3e-7:1e-9:1.2e-6; %wavelength in unit of m
e=1.6e-19; %electron charge
alpha = 4.*pi.*k_PCDTBT./lambda; % calculate alpha based on extinction
coefficient k of active layer material
t = 120e-9; %device thickness
sig_scatt=interp1(lambda1,scat_sigma_slice,lambda,'spline');
sig_abs=interp1(lambda2,total_sigma_slice,lambda,'spline');
r=35e-9; %nanoparticle size
sig_phy = pi*r^2;%remember to input the sig_phy
d=(20)^(1/3)*2*r; %calculate the side length of cubic unit cell
rho =1/d; %define 1D density based on side length of cubic unit cell
Qs = sig_scatt/sig_phy;
Qa = sig_abs/sig_phy;

% for rho =2/(t^2):2/(t^2):8/(t^2);
% rho=9/t^2;
A1 = 1 - exp(-alpha*t) - 0*sig_scatt; %absorption before

alpha_new = alpha.*(1 + (sig_phy./d.^2).*((Qs-Qa).*(rho.*t)));
%(sig_phy./d.^2) is to weigh how much impact a single particle has within a
unit cell
%(rho.*t) is to calculate the number of particles in 1D
t_new = t*((1-(4*pi*r^3/3)/d^3))^(1/3);
% define the new thickness by taking out the volume of particles

A2 = 1-exp(-alpha_new.*t_new); %new absorption

plot(lambda,A2./A1) %plot absorption enhancement VS lambda
hold on
% end
ylabel('enhancement','fontsize',16);
xlabel('lambda','fontsize',16);
% legend('rho=2','rho=4','rho=6','rho=8');

%import # of photons per nm, intergrate over lambda and devide by electron
charge to calculate Jsc
J1=trapz(lambda0,A1.*Photonflux)/e;
J2=trapz(lambda0,A2.*Photonflux)/e;
Z=100*(J2-J1)/J1;
```


A.3 Color Tuning Project

A.3.1 Color Computation

```
function Y = ObjectiveColor(x)
n
% Names of layers of materials starting from side light is incident from
t = [0 x(1) x(2) x(3) x(4) x(5)]; % thickness of each corresponding layer in
nm (thickness of the first layer is irrelevant)
% ^changed
%thicknesses = [0 200 300 350 30 200];
%lb [10 50 50 10 10]
%ub [500 300 400 200 200]
lambda=300:1200; % Wavelengths over which field patterns are calculated
%%%%%%%%%%%%%%%%%%%%%%%%%%%%%%%%%%%%%%%%%%%%%%%%%%%%%%%%%%%%%%%%%%%%%%%%%USER-INPUT%%%%%%%%%%%%%%%%%%%%%%%%%%%%%%%%%%%%%%%%%%%%%%%%%%%%%%%%%%%%%%%%%%%%%%%%%
%red
%color = 0.4;
%blue
%color = .19;
%orange
%color = 0.3;
%green
%color = 0.2;
% 0, 10-500, 10-300, 10-400, 10-200, (MoO3) 10-200
% Constants
h=6.626e-34; % Js Planck's constant
c=2.998e8; %m/s speed of light
q=1.602e-19; %C electric charge

%To optimize RGB
xyz_5
%RGB
RefSpec = Reflection(1,61:531);
RefSpec_5=RefSpec(1:5:471)'; % At 5 nm intervals

AM15_5=AM15(1:5:471);

%The reflectance spectrum is a property of the object; by combining
it with
%any arbitrary illumination spectrum, we get the reflected spectrum.

%LumSpec=RefSpec_5.*D65_5; %White Light
LumSpec=RefSpec_5.*AM15_5; %Solar Spectrum

%The objective is to find the XYZ tristimulus values, and the xy
%chromaticity coordinates, using the 1931 CIE color matching
functions.
%That is, we will use the 1931 xyzbar tables

%First, we apply the color functions to the D65 spectrum
%Lum= xyz_5'*D65_5;
Lum= xyz_5'*AM15_5;

%Next, we apply the color functions to the Reflected spectrum
Lum2=xyz_5'*LumSpec;

%We are not going to divide by this middle number ? this is the
reflected
```

APPENDIX A. EXPERIMENTAL DETAILS

```

    %spectrum, not the illumination spectrum. We need to divide by the
previous
    %middle number i.e. by the photopic response to the illumination, not
    %the photopic response to the reflection to get X,Y,Z

XYZ=Lum2/Lum(2);

%xyz values are computed by normalizing the XYZ so that their sum is 1

xyz=XYZ/sum(XYZ);

%Using this transformtation Matrix, we are able to convert from xyz
values
%to the corresponding rgb ratio

ConvMat=[3.240479 -1.537150 -0.498535;-0.969256 1.875992
0.041556;0.055648 -0.204043 1.057311];

rgb = ConvMat*xyz;
Y = -1*(rgb(2,1)-rgb(3,1)-rgb(1,1));
```

A.3.2 Optimization

```
lb =[55];
ub = [80];
numvariables=1;
tic
options=optimoptions('particleswarm','SwarmSize',2000,'TolFun',1E-3);
% objectiveFun=@TMTwolayerITO_TiO2;
% [ITOthicknesses, ITOfvalbest] =
particleswarm(objectiveFun,numvariables,lb,ub,options);
% assignin('base','ITOthicknesses',ITOthicknesses);
% assignin('base','ITOfvalbest',ITOfvalbest);

objectiveFun=@TMTwolayerFTO_TiO2;
[FTOthicknesses, FTOfvalbest] =
particleswarm(objectiveFun,numvariables,lb,ub,options);
assignin('base','FTOthicknesses',FTOthicknesses);
assignin('base','FTOfvalbest',FTOfvalbest);
cd ../
cd ../
cd TransferMatrix
TransferMatrixtwolayer(FTOthicknesses);
toc
```

A.4 Antimony Selenide Project

FDTD calculations were performed using commercial software (Lumerical, Inc.). A broadband plane wave source spanning a wavelength range of 300 to 2000 nm was used as the excitation source. The nanowires were modeled as cylinders with a uniform distribution of 250 nm in diameter and 900 nm in length on a polyimide substrate. The nanowire array was composed of randomly oriented cylinders in all three axes with an angular distribution from 0 to 180 degrees. Refractive index data (n and k) for Sb₂Se₃ was obtained from ellipsometry measurements. Monitors were placed behind the incident source, in front of, and beyond the structure to obtain absorption, reflection and spatial electrical field data.

A.5 Aluminum Project

A.5.1 Two-Interface Model

```
c_m=2.1e6; %ipa c_o=3.48e6; %c_p=2.5e6; c_p=2.43e6; %al
lam_m=0.16; %ipa lam_o=30; lam_p=205; %al
G1=100e6; G2=30e6;
kap1 = lam_o/c_o;
k1= 3*c_o/c_p;
g1=G1/lam_o;
kap2 = lam_m/c_m;
k2= 3*c_m/c_o;
g2=G2/lam_m;
R=62e-9;
r_o=65e-9;
r=r_o+3e-9;
n=1;
t_f= linspace(0,2000e-12,10001);
DT_p=zeros(1,10001);
DT_o=zeros(1,10001);
DT_m=zeros(1,10001);
for t=0:2e-13:2000e-12
fun = @(u) u.^2.*exp(-kap1.*u.^2.*t./(R.^2))./((u.^2.*(1+R.*g1)-
k1.*R.*g1).^2+(u.^3-k1.*R.*g1.*u).^2);
DTp=(2/pi)*k1*(R*g1)^2*integral(fun,0,Inf);
DT_p(1,n)=DTp;
fun2= @(v) v.*exp(-kap1.*v.^2.*t./(R.^2)).*(v.*(1-
v.^2./(k1.*R.*g1)).*cos(v.*(r_o-R)./R)+(1-
v.^2.*(1+R.*g1)./(k1.*R.*g1)).*sin(v.*(r_o-R)./R))./((v.^2.*(1+R.*g1)-
k1.*R.*g1).^2+(v.^3-k1.*R.*g1.*v).^2);
DTo=(2*R/(pi*r_o))*k1*(R*g1)^2*integral(fun2,0,Inf);
DT_o(1,n)=DTo;
fun3= @(w) w.*exp(-kap2.*w.^2.*t./(r_o.^2)).*(w.*(1-
w.^2./(k2.*r_o.*g2)).*cos(w.*(r-r_o)./r_o)+(1-
w.^2.*(1+r_o.*g2)./(k2.*r_o.*g2)).*sin(w.*(r-
r_o)./r_o))./((w.^2.*(1+r_o.*g2)-k2.*r_o.*g2).^2+(w.^3-k2.*r_o.*g2.*w).^2);
DTm=(2*r_o/(pi*r))*k2*(r_o*g2)^2*integral(fun3,0,Inf);
DT_m(1,n)=DTm;
n=n+1;
end
plot(t_f.*1e12,DT_p,t_f.*1e12,DT_m.*DT_p,'-.')
a=(DT_m.*DT_p);
b=find(a==max(a));
t_f(b).*1e12
hold on
```

Ebuka S. Arinze

✉ ebuka.arinze@jhu.edu 🌐 <https://engineering.jhu.edu/nanoenergy/>
☎ (203) 418-0120 📄 <https://orcid.org/0000-0003-4043-4535>

Education

- 2013 – 2018 🎓 **Ph.D., Johns Hopkins University** in Electrical Engineering.
Focus: *Renewable energy conversion and storage, photovoltaics, optoelectronics, nanoengineering and nanophotonics.*
- 2013 – 2015 🎓 **M.S.E., Johns Hopkins University** in Electrical Engineering.
- 2009 – 2013 🎓 **B.S., Fairfield University** in Electrical Engineering. *Summa Cum Laude*

Research

- 2013 – 2018 🧪 **Graduate Student Researcher**, Johns Hopkins University.
Dissertation: *Engineering Tunable Colloidal Nanostructures for Light Energy Harvesting*
Advisor: Professor Susanna M. Thon
- 2012 – 2013 🧪 **Undergraduate Student Researcher**, Fairfield University.
Thesis: *Autonomous Quadcopter Development*
Advisor: Professor Ryan Munden

Teaching

Class Instructor

- Fall 2015 📖 ECE 520.627 – How to Improve Solar Cell Performance using Nanotechnology (undergraduate)




Graduate Course Assistant

- Fall 2014, 2016 📖 ECE 520.270 – Introduction to Renewable Energy Engineering (undergraduate)
- Spring 2015 📖 ECE 520.627 – Photovoltaics and Energy Devices (graduate)

Honors and Awards

- 2018 🏆 Johns Hopkins Diversity Recognition Award Recipient
🏆 Bridge to BCG (Boston Consulting Group), Participant
- 2017 🏆 Microsoft Research Dissertation Grant Recipient
🏆 Best Poster Award Recipient - 44th IEEE Photovoltaic Specialist Conference
🏆 ARPA-E Energy Innovation Summit Student Invitee
- 2015 🏆 Co-founder, JHU ECE Graduate Students Association
🏆 George M.L. Sommerman Engineering Graduate Teaching Assistant Award Recipient
- 2012 🏆 NASA Space Grant Consortium Award Recipient
- 2009 🏆 United States Student Achievers Program (USAP) Scholar

Prior Experience

- 2017 – 2018  **Council Member**, *JHU Homewood Council on Inclusive Excellence*
- Coordinate with University Deans and recommend strategies that enhance retention, advancement and engagement of diverse students, faculty and staff.
 - Institutionalize values of diversity and inclusion into the fabric of academic life (research, education, teaching, policies, and programs).
 - Promote projects and events designed to enrich academic life, broaden the participation of underrepresented groups in academic life.
- 2014 – 2017  **After-School Mentor**, *STEM Achievement in Baltimore Elementary Schools*
- Visit National Science Foundation-funded after-school program in Baltimore City public schools to provide engineering expertise.
 - Lead a team to mentor 20-30 aspiring student engineers in grades 3-5 as they work on science and engineering tasks.
 - Assisted in completion of community-driven projects such as an efficient water-filtration system, a solar-powered cat house, and a robotic waste-pickup machine.
- 2014 – 2016  **Graduate Diversity Fellow**, *JHU Graduate Affairs and Admissions Office*
- Advised the Office of Graduate Affairs and Admissions on matters of policy, graduate student life and issues of diversity.
 - Coordinated on-campus events (e.g. panels, tours) as a representative of the Schools of Engineering.
 - Demonstrated impact with a 27% increase (2016 vs. 2012) in underrepresented minority population of graduate students.

Research Publications

Journal Articles

- 1 Cordero, R. J., Robert, V., Cardinali, G., **Arinze, E. S.**, Thon, S. M., & Casadevall, A. (2018). Impact of yeast pigmentation on heat capture and latitudinal distribution. *Current Biology*, 28(16), 2657–2664.
- 2 Qiu, B., Lin, Y., **Arinze, E. S.**, Chiu, A., Li, L., & Thon, S. M. (2018). Photonic band engineering in absorbing media for spectrally selective optoelectronic films. *Optics Express*, 26(21), 26933–26945.
- 3 **Arinze, E. S.**, Qiu, B., Palmquist, N., Cheng, Y., Lin, Y., Nyirjesy, G., ... Thon, S. M. (2017). Color-tuned and transparent colloidal quantum dot solar cells via optimized multilayer interference. *Optics Express*, 25(4), A101–A112.
- 4 Smith, K. J., Cheng, Y., **Arinze, E. S.**, Kim, N. E., Bragg, A. E., & Thon, S. M. (2017). Dynamics of energy transfer in large plasmonic aluminum nanoparticles. *ACS Photonics*, 5(3), 805–813.
- 5 **Arinze, E. S.**, Qiu, B., Nyirjesy, G., & Thon, S. M. (2016). Plasmonic nanoparticle enhancement of solution-processed solar cells: practical limits and opportunities. *ACS Photonics*, 3(2), 158–173.
- 6 Cheng, Y., **Arinze, E. S.**, Palmquist, N., & Thon, S. M. (2016). Advancing colloidal quantum dot photovoltaic technology. *Nanophotonics*, 5(1), 31–54.

- 7 Hasan, M. R., **Arinze, E. S.**, Singh, A. K., Oleshko, V. P., Guo, S., Rani, A., ..., Rao, M. V. et al. (2016). An antimony selenide molecular ink for flexible broadband photodetectors. *Advanced electronic materials*, 2(9), 1600182.
- 8 Xie, T., Hasan, M. R., Qiu, B., **Arinze, E. S.**, Nguyen, N. V., Motayed, A., ... Debnath, R. (2015). High-performing visible-blind photodetectors based on SnO_2/CuO nanoheterojunctions. *Applied physics letters*, 107(24), 241108.

Conference Proceedings

- 1 **Arinze, E. S.**, Nyirjesy, G., Cheng, Y., Palmquist, N., & Thon, S. M. (2015). Colloidal quantum dot materials for infrared optoelectronics. In *Infrared remote sensing and instrumentation xxxiii* (Vol. 9608, p. 960813). International Society for Optics and Photonics.

Talks and Presentations

- 2018  **10th Biannual Conference on Quantum Dots (QD2018)**, Contributed Talk. Toronto, Ontario, June 2018; *Tuning color and transparency in colloidal quantum dot solar cells via multi-objective optimization*.
-  **MRS Spring Meeting 2018**, Contributed Talk. Phoenix, Arizona, April 2018; *Spectral color-tunability and semitransparency in colloidal quantum dot solar cells through optimized multilayer interference*.
-  **Engineering Sustainability Day (University of Maryland)**, Poster. College Park, Maryland, April 2018; *Multi-objective optimization for color-tunability and transparency in colloidal quantum dot solar cells*.
- 2017  **Electrical and Computer Engineering Department (Johns Hopkins University)**, Proposal Seminar. Baltimore, Maryland, December 2017; *Engineering Tunable Colloidal Nanomaterials for Light Energy Harvesting Applications*.
-  **Optics & Photonics Conference (Johns Hopkins University)**, Poster. Baltimore, Maryland, December 2017; *Color-tunability and semitransparency in colloidal quantum dot solar cells through optimized optical interference*.
-  **Microsoft Research Grant Workshop**, Invited Talk. Seattle, Washington, November 2017; *Nanoengineering for Tunable Energy-Efficient Optoelectronics*.
-  **NOBCChE Annual Meeting 2017**, Contributed Talk. Minneapolis, Minnesota, October 2017; *Probing Energy-Transfer Dynamics in Large Aluminum Nanostructures*.
-  **IEEE Photovoltaic Specialist Conference 2017**, Poster. Washington, D.C., June 2017; *Multi-objective optimization for color-tunability and transparency in colloidal quantum dot solar cells*.
- 2016  **NOBCChE Annual Meeting 2016**, Contributed Talk. Raleigh, North Carolina, November 2016; *Enhancing Solution Processed Solar Cell Photocurrents via Plasmonic Nanoparticles*.
-  **APS Mid-Atlantic Section Meeting 2016**, Contributed Talk. Newark, Delaware, October 2016; *Flexible and Broadband Photodetectors via Solution Processed Antimony Selenide*.
-  **APS March Meeting 2016**, Contributed Talk. Baltimore, Maryland, March 2016; *Limits of Plasmonic Nanoparticle Enhancement in Solution-Processed Solar Cells*.
- 2015  **Green Research and Sustainability Symposium (Johns Hopkins University)**, Poster. Baltimore, Maryland, April 2015; *Demonstration and Characterization of Inexpensive, Earth-Abundant Materials for Efficient Photocatalyzed Synthesis*.

Techniques

Device Fabrication:	<i>Thin film deposition (spin-coating, dip-coating, drop-casting, PVD), flexible device fabrication, surface patterning.</i>
Synthesis:	<i>Colloidal nanomaterials (quantum dots and plasmonic nanoparticles), ligand exchanges.</i>
Thin Film Characterization:	<i>AFM, SEM, TEM, FTIR, UV-Vis spectroscopy, synchrotron-based (XRD, XPS, UPS).</i>
Electronic Measurements:	<i>I-V and C-V measurements, photoluminescence, transient photocurrent and photovoltage.</i>

Service

Conference Activities

2018	Symposium Assistant , <i>Advances in Perovskite Solar Cell Devices and Applications</i> , Materials Research Society Spring Meeting (2018).
2017	Session Chair , <i>Optical Devices and Nanomaterials</i> , Optics & Photonics Conference at Johns Hopkins University (2017). Organizing Committee , Optics & Photonics Conference at Johns Hopkins University (2017).

Technical Peer Reviewer

Reviewer	The Journal of Physical Chemistry Applied Optics Optical Materials Express
----------	--

References

Susanna Thon (Advisor)

Assistant Professor
Electrical and Computer Engineering Department
Johns Hopkins University

✉ susanna.thon@jhu.edu

☎ (410) 516-4120

Jonah Erlebacher

Professor and Department Chair
Department of Materials Science and Engineering
Johns Hopkins University

✉ jonah.erlebacher@jhu.edu

☎ (410) 516-6077

Art Bragg

Associate Professor
Department of Chemistry
Johns Hopkins University

✉ artbragg@jhu.edu

☎ (410) 516-5616

Amy Foster

Associate Professor
Electrical and Computer Engineering Department
Johns Hopkins University

✉ amy.foster@jhu.edu

☎ (410) 516-6434

Frank Johnson

Chief Information Officer & Chief Digital Officer
City of Baltimore
Former Vice President & General Manager
Intel Corporation

✉ frankj351@gmail.com

☎ (410) 396-6648